Alma Mater Studiorum – Università di Bologna

DOTTORATO DI RICERCA IN

ASTROFISICA

ciclo XXX

Settore Concorsuale: 02/C1

Settore Scientifico Disciplinare: FIS/05

Investigating the conclusive phases of galaxy evolution: from star formation to quiescence

Presentata da: Annalisa Citro

Coordinatore Dottorato
Prof. Francesco Rosario Ferraro

Relatore
Prof. Andrea Cimatti

Correlatori:
Dott.ssa Lucia Pozzetti
Dott. Michele E. M. Moresco

Esame finale anno 2018

Sommario

Nonostante i progressi fatti verso una più profonda comprensione dell'evoluzione delle galassie, manca ancora una visione completa di quali siano i meccanismi che regolano la formazione sellare nelle galassie, di come le proprietaà evolutive delle galassie correlino con le loro masse e tassi di formazione stellare e quali processi siano responsabili dello spegnimento della formazione stellare e i loro tempi-scala.
In questo lavoro di tesi, si è cercato di rispondere ad alcune di queste domande aperte, studiando l'evoluzione delle galassie a ritroso nel tempo. In particolare, siamo partiti dallo studio archeologico di galassie passive locali (1), ricostruendo le loro storie di formazione stellare. Abbiamo poi fatto un passo indietro verso la fase in cui le galassie spengono la loro formazione stellare (2), definendo una nuova metodologia che ci permetta di identificare i progenitori delle galassie passive nella fase immediatamente successiva all'interruzione della formazione stellare. Infine, siamo andati ancora più indietro nel tempo, studiando la fase in cui le galassie formano stelle (3), analizzando le proprietà di galassie ad alto redshift che potrebbero essere i progenitori delle galassie passive locali.
I nostri studi si sono basati sull'analisi spettrale delle galassie. In particolare, abbiamo studiato la fase passiva e quella star-forming sfruttando l'informazione contenuta nella totalità degli spettri delle galassie analizzate, la cui forma dipende dalle caratteristiche delle popolazioni stellari. La fase di spegnimento della formazione stellare è stata invece analizzata usando rapporti tra righe di emissione, che sono collegate al mezzo interstellare e al suo stato di ionizzazione durante o subito dopo lo spegnimento della formazione stellare.
I nostri più importanti risultati possono essere riassunti come segue:

1. Riguardo le galassie passive locali, abbiamo analizzato gli spettri stacked mediani di $\sim$ 25000 galassie early-type (ETGs) passive e massive ($\log(\mathrm{M}/\mathrm{M}_{\odot}) \gtrsim 10^{10.75}$) osservate dalla Sloan Digital Sky Survey (SDSS) DR4 a redshift $z < 0.3$, usando la tecnica del full-spectrum fitting (STARLIGHT, Cid Fernandes et al., 2005). Abbiamo trovato che questo methodo è in grado di recuperare le proprietà evolutive delle galassie (i.e. età, metallicità, estinzione da polvere) e le loro storie di formazione stellare con una accuratezza maggiore del 10% a partire da rapporti segnale-rumore $\gtrsim 10 - 20$. Abbiamo trovato evidenze di evoluzione downsizing (Cowie et al., 1996), sia nelle età che nelle storie di formazione stellare. Queste ultime hanno la forma: $\mathrm{SFR}(t) \propto \tau^{-(c+1)} t\, c \exp(-t/\tau)$ e sono più brevi per galassie più massive. Dalle storie di formazione stellare che abbiamo ricostruito, abbiamo dedotto le proprietà dei progenitori delle galassie early-type analizzate, trovando che questi debbano aver avuto un alto tasso di formazione stellare (i.e. $\sim 350 - 400\,\mathrm{M}_{\odot}\ \mathrm{yr}^{-1}$) ed alte masse a redshift $z \sim 4 - 5$, diventando quiescenti a partire da $z \sim 1.5 - 2$.
Questi risultati sono descritti in Citro et al. 2016; Astronomy & Astrophysics, Volume 592, id.A19, 22 pp.

2. Riguardo la fase di spegnimento della formazione stellare, abbiamo proposto una nuova metodologia capace di identificare le galassie star-forming nella fasi immediatamente successive all'interruzione della formazione stellare. Questa metodolo-

gia è basata sull'utilizzo di rapporti tra righe di emissione di alta e bassa ionizzazione. In particolare, ci siamo focalizzati sui due rapporti [O III] λ5007/Hα e [Ne III] λ3869/[O II] λ3727, che sono stati modellati con il codice di fotoionizzazione CLOUDY (Ferland et al., 1998, Ferland et al., 2013). Abbiamo trovato che essi sono ottimi traccianti delle fasi immediatamente successive allo spegnimento della formazione stellare, dato che diminuiscono di un fattore ~ 2 in circa $\sim 80 - 90$ Myr dal momento della sua interruzione. Abbiamo mitigato la degenerazione tra lo stato di ionizzazione/età e la metallicità che compromette il nostro approccio introducendo il nuovo diagramma diagnostico [O III] λ5007/Hα vs. [N II] λ6584/[O II] λ3727. Usando un campione di galassie star-forming selezionate dalla SDSS DR8, abbiamo identificato in questo piano 10 esempi di galassie che stanno spegnendo la loro formazione stellare (i.e. le più estreme), che potrebbero essere i progenitori in fase di spegnimento delle galassie passive studiate precedentemente (che erano passive a $z \lesssim 2$). Abbiamo trovato che queste 10 galassie sono caratterizzate da continui blu e da colori $(u - r)$ più blu di quelli tipici della Green Valley, come ci si aspetta se la formazione stellare in esse si è spenta nel passato molto recente.
Questi risultati sono descritti in Citro et al. 2017; Monthly Notices of the Royal Astronomical Society, Volume 469, Issue 3, p.3108-3124.

3. Riguardo la fase star-forming ad alto redshift, abbiamo analizzato gli spettri stacked mediani ultravioletti di 290 galassie star-forming a $2 \leq z \leq 4$. In particolare, ci siamo focalizzati sul campione ad oggi disponibile della survey spettroscopica ESO-VLT VANDELS (PIs: Ross McLure, Laura Pentericci), della quale faccio attualmente parte. Il nostro scopo principale è stato quello di usare il metodo del full-spectrum fitting per derivare le proprietà evolutive di tali galassie, connettendole allo studio archeologico delle ETGs condotto precedentemente. Abbiamo trovato che, se le righe di assorbimento spettrali che includono anche un contributo di assorbimento dal mezzo interstellare (che non sono modellate dagli attuali modelli di sintesi di popolazioni stellari) vengono escluse dal fit, risultati affidabili sono ancora ottenuti a partire da rapporti segnale-rumore $\sim 10 - 20$, ma con una accuratezza minore rispetto al caso in cui solo le forti righe di emissione vengono escluse dal fit. Dall'analisi spettrale delle galassie VANDELS abbiamo dedotto età più vecchie ed estinzione da polvere più alta per le galassie più massive, mentre non sono emersi andamenti significativi della metallicità in funzione della massa. Inoltre, le storie di formazione stellare sembrano essere più prolungate ad alte masse. Tutti questi risultati saranno confermati da analisi ulteriori condotte sul campione totale di galassie star-forming VANDELS, che ammonterà a ~ 800 spettri.
Questi risultati saranno presentati in Citro et al. 2018, in prep.

Abstract

Despite the progress made towards a more comprehensive knowledge of galaxy evolution, a global picture of the mechanisms regulating the formation of stars in galaxies, of how galaxy evolutionary properties correlate with stellar masses and star formation rates (SFRs) and of the processes suppressing the star formation in galaxies and their timescales is still lacking.
In this thesis work, we attempt to address some of these open questions, inspecting galaxy evolution back in cosmic time. In particular, we start from the archaeological analysis of passive local galaxies (1), reconstructing their past star formation histories. Then we take a step back towards the phase in which galaxies quench their star formation (2), defining a new methodology able to identify the quenching progenitors of passive galaxies. Finally, we move back to the star-forming phase (3), investigating the properties of high-redshift galaxies which could be the star-forming progenitors of the passive local ones.
Our investigations mainly rely on the spectral analysis of galaxies. In particular, we study both the passive and star-forming phase by exploiting the information contained in the galaxy full-spectrum, whose shape depends on the properties of the underlying stellar populations. The quenching phase is instead investigated by means of emission line ratios, which are associated to the Interstellar Medium (ISM) and its ionization state during or just after the star formation has stopped.
The main results obtained from our backward reconstruction of galaxy evolution can be summarized as follows:

1. Concerning passive local galaxies, we analyze the median stacked spectra of $\sim$ 25000 massive ($\log(\mathrm{M}/\mathrm{M}_{\odot} \gtrsim 10^{10.75}$) and passive Sloan Digital Sky Survey (SDSS) DR4 early-type galaxies (ETGs) at $z < 0.3$ by means of the full-spectrum fitting (STARLIGHT, Cid Fernandes et al., 2005). We find that this method is able to retrieve the evolutionary properties (i.e. ages, metallicities, dust extinctions) and the SFHs with an accuracy higher than 10% starting from signal-to-noise ratios (SNRs) $\gtrsim 10-20$. We find evidence of a downsizing evolution (Cowie et al., 1996), both in ages and SFHs. The latter are of the form $\mathrm{SFR}(t) \propto \tau^{-(c+1)} t\ c\ \exp(-t/\tau)$ and are shorter for more massive galaxies than for less massive ones. From the reconstructed SFHs, we place constraints on the properties of the progenitors of the studied ETGs, arguing that they should have been vigorously star-forming – with star formation rates (SFRs) $\sim 350-400\,\mathrm{M}_{\odot}\ \mathrm{yr}^{-1}$ – at $z \sim 4-5$, and quiescent by $z \sim 1.5-2$.
These results can be found in Citro et al. 2016; Astronomy & Astrophysics, Volume 592, id.A19, 22 pp.

2. Concerning the quenching phase of galaxies, we propose a new methodology aimed at finding star-forming galaxies which just quenched their star-formation, based on emission line ratios involving high- and low-ionization potential lines. We focused on the [O III] λ5007/Hα and [Ne III] λ3869/[O II] λ3727 emission line ratios, which are modelled with the CLOUDY photoionization code (Ferland et al., 1998, Ferland et al., 2013). We find that they are very good tracers of the early epochs of quenching, dropping by a factor $\sim$ 2 in $\sim$ 80 – 90 Myr from the

time of the quenching. We mitigate the ionization/age-metallicity degeneracy affecting the proposed methodology by introducing the [O III] λ5007/Hα vs. [N II] λ6584/[O II] λ3727 diagnostic diagram. Using a sample of SDSS DR8 star-forming galaxies, we identify 10 examples of quenching candidates within this plane (i.e. the most extreme ones), which could be the low redshift, quenching progenitors of the ETGs studied earlier on (which are quiescent by $z \sim 1.5 - 2$). We find that the 10 galaxies are characterized by blue dust-corrected continua and by $(u - r)$ colours bluer than the Green Valley ones, as expected if the star formation quenching has occurred in the very recent past.
These results can be found in Citro et al. 2017; Monthly Notices of the Royal Astronomical Society, Volume 469, Issue 3, p.3108-3124.

3. Concerning the star-forming high-redshift phase, we analyzed 6 UV median stacked spectra obtained from a sample of star-forming galaxies at high redshift. In particular, we studied the 290 star-forming and Lyman break galaxies so far available from the on-going ESO-VLT public spectroscopic survey VANDELS (PIs: Ross McLure, Laura Pentericci), where I am involved. These galaxies have $2 \leq z \leq 4$ and $8 < \log(\mathrm{M}/\mathrm{M}_{\odot}) < 11.5$. Our main aim is to derive the evolutionary properties (i.e. ages, metallicities, dust extinctions) and the SFHs of these galaxies by means of the full-spectrum fitting, connecting them to our archaeological study of ETGs. We find that if absorption lines including ISM contributions (which are not modelled by the current evolutionary stellar population synthesis models) are excluded from the spectral fit, reliable results are still retrieved from SNRs $\sim$ 10 – 20, although with a slightly larger dispersion with respect to the case in which only the strongest emission lines are excluded from the fit. The spectral fit of VANDELS spectra provides older ages and larger dust extinctions for more massive galaxies than for less massive ones, while no clear metallicity trend is observed as a function of mass. The SFHs appear to be more prolonged at lower masses than at higher ones. All these results will be confirmed by further analyses performed on the total sample of VANDELS star-forming galaxies, which will amount to $\sim$ 800 spectra.
These results will be presented in Citro et al. 2018, in prep.

Contents

List of Figures

List of Tables

Chapter 1

The "archaeological" reconstruction of the evolution of early-type galaxies

The morphological dichotomy between spiral and elliptical galaxies has been known for years (i.e. since Hubble 1929). Over time, it has been observed that this bimodality can be extended also to other galaxy properties, such as star formation levels and colours (e.g. Strateva et al., 2001, Kauffmann et al., 2003), resulting in a clear separation between star-forming (blue) and quiescent (red) galaxies. Understanding the origin of this dichotomy is one of the key question in the current studies of galaxy evolution.
Generally, two approaches are used to investigate this issue: the *backward approach*, which tries to extrapolate galaxy evolution starting from the evolutionary properties of galaxies at $z = 0$, and the *lookback studies*, which infer galaxy evolution by studying the statistical properties of galaxy samples at different redshifts.
In the currently accepted ΛCDM cosmological model, which predicts a bottom-up or hierarchical formation of cosmic structures, local and massive early-type galaxies (ETGs) represent the endpoints of the evolutionary process, and are therefore fundamental probes to track the galaxy cosmic history backward in cosmic time.
Morevoer, the advent of spectroscopic surveys at intermediate-high redshift (e.g. zCOSMOS and VIPERS at $z > 0.7$, VVDS, VUDS, GMASS, K20, GOODS and VANDELS at $z > 1 - 2$), has allowed in the last years the statistical studies of galaxy samples at different redshifts and thus a more accurate analysis of their evolution across cosmic time.
In this chapter we discuss galaxy evolution in reverse, going from local, passive galaxies to their progenitors at high redshift. We briefly recall the properties and the relations characterizing galaxies through all the evolutionary phases, including the quenching of the star formation.

1.1 Properties of ETGs in the local and high-redshift Universe

ETGs constitute a homogeneus class of galaxies with a spheroidal (E/S0) morphology, old stellar populations, red colours, no (or negligible) star formation and high velocity dispersion (i.e. high masses). These properties are generally used to identify ETGs, and usually correlate between each other. However, it is worth noting that some past studies (e.g. Renzini, 2006, Moresco et al., 2013) have argued that these classifications do not fully overlap, and thus that morphology-, photometry- or spectrum-based selection

criteria can lead to select slightly different ETG samples.
The following sections briefly recall some of the most important ETG properties and scaling relations, both in the local and high-redshift Universe.

1.1.1 Spectral properties

Due to the dominance of old stellar populations and the absence of significant ongoing star formation, ETG spectra are basically red, absorption-line spectra, as it is possible to note from Fig. 1.1. The integrated light of ETGs is dominated by old, low-mass stars (G- and K-type giants) which are still lying on the main sequence, or by stars experiencing advanced evolutionary stages (Red Giant Branch, Asymptotic Giant Branch), which contribute the most to the flux at long wavelengths due to their lower superficial temperature. Apart from the red continuum shape, ETG spectra are also characterized by several absorption features, whose strength is often related to galaxy age, metallicity (Z) and abundance ratios. Trager et al. (1998) e di Worthey & Ottaviani (1997) introduced an ensamble of 25 optical spectral features (i.e. Lick/IDS system), known as Lick indices, as powerful tools to infer galaxy properties. The general approach consists in creating synthetic indices by means of polynomial functions and evolutionary synthesis codes, and comparing them with the observed ones. Although this method is very powerful and independent of resolving power or flux calibration limitations, it is hampered by the fact that age and metallicity may have similar effects on spectral lines and spectral continuum (age-metallicity degeneracy, Worthey 1994). Breaking the age-metallicity degeneracy has thus become one of the primary goals in spectroscopic studies aimed at constrain galaxy stellar population properties, and led to the search for independent indices separately related to age and metallicity.
In this regard, both low- (Hβ) and high- (e.g. Hδ and Hγ) order Balmer absorption lines were proposed in the past as pure age indicators (Worthey & Ottaviani, 1997, Vazdekis & Arimoto, 1999), but several studies have demonstrated that they are not fully independent of metallicity or α-element abundance (Thomas et al., 2004, Korn et al., 2005). Moreover, moderate to high signal-to-noise ratios are required to measure them, limiting their use only to nearby/luminous sources. Concerning Hβ, some authors have also shown that it can be contaminated by nebular emission (Gonzalez, 1993, Concas et al., 2017). Concerning metal abundances, many of the indices proposed by Worthey (1994) as indicators of the global metallicity (e.g. CN2, Ca4455, $C_2$4668, Fe5015, Fe5270, Fe5335, Fe5406, Fe5709, Fe5782, NaD, TiO_2) have been demonstrated to depend on the α-element abundance (Worthey, 1994,Davies et al., 1993a, Carollo & Danziger, 1994), introducing further uncertainties in the Lick indices method. An important step forward to disentangle between age and metallicity effects and to unambiguously determine ages, total metallicities and element abundances has consisted in creating synthetic Lick indices accounting for the effects of the α elements. In particular, Tripicco & Bell (1995) determined the sensitivity of Lick absorption-line indices to individual element abundance variations. Trager et al. (2000) then developed a method to include these results in the analysis of stellar populations, allowing the creation of stellar population models of Lick indices with variable element abundance ratios (Thomas et al., 2003,Thomas et al., 2005, Thomas et al., 2010). However, many uncertainties are still related to the Lick-indices approach. For instance, it is still unclear how to break the degeneracy between young stars and hot horizontal branch stars, whose presence can similarly influence the index strength. Ratios involving different indices (e.g. $H\delta_F/H\beta$), should help to disentangle between the two populations (e.g. Schiavon et al., 2004), but these analyses are hampered by the α elements dependence, which have to be taken into account.

The evolution of the Lick indices as a function of redshift confirm that ETGs have a high formation redshift and thus evolve passively from $z \sim 2-3$. For instance, Bender et al. (1996) and Ziegler & Bender (1997) analyzed the evolution of the Mg_2 index as a function of the galaxy velocity dispersion σ up to $z = 0.375$. They found a weakening of the index with cosmic time and inferred that the age of galaxies at this redshift should be about 2/3 of the age of their local counterparts, implying a $z_F \gtrsim 3$. Similar results have been obtained by studying the evolution of the H_δ and H_γ spectral features (e.g. Kelson et al., 2001). Moreover, the evolution of spectral features in galaxy spectra and the rapid decrease of the number density of massive galaxies with strong Hδ absorption since $z \sim 1$ (Le Borgne et al., 2006, Vergani et al., 2008) gives hints on the formation scenario of ETGs, suggesting a top-down formation (see Sect.1.4).

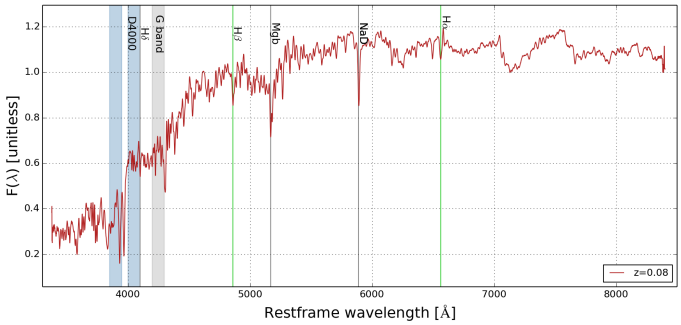

Figure 1.1: Optical stacked spectrum of $\sim$ 2800 SDSS ETGs with $M \sim 10^{10.86} M_\odot$ and median $z \sim 0.11$. Vertical lines mark some absorption features. Black lines are metallic absorptions (from left to right: MgI, NaD); green lines are Balmer absorptions (from left to right: $H\beta$, $H\alpha$); the grey shaded band mark the location of the G Band; blue shaded bands mark the location of the D4000 continuum discontinuity (also known as the D4000 break).

1.1.2 Scaling relations

Due to their homogeneity, early-type galaxies obey to well-defined scaling relations between their physical and evolutionary properties, which can be used to better understand their galaxy structure and evolution. The following sections give a brief summary of the most important among these scaling relations.

The color-magnitude relation

The color-magnitude relation (CMR) links the $(U-V)$ rest-frame color index to the absolute magnitude of elliptical galaxies, and was first discovered by Bower, Lucey & Ellis in 1992 in Virgo and Coma cluster galaxies. Very important information are enclosed in the scatter and slope of this relation, which is illustrated in Fig. 1.2. In particular, assuming that ETGs are passively evolving, the scatter in the CMR allows to constrain their formation redshift (z_f). From the observed color scatter, Bower et al. (1992) concluded that cluster ellipticals are made of very old stars, with the bulk of star formation completed at $z_f \gtrsim 2$. This has been also confirmed by high redshift studies of the CMR. In particular, Ellis et al. (1997) and Stanford et al. (1998) found that cluster ellipticals are passively evolving and have a $z_f \gtrsim 3$; analyzing field, group and cluster galaxies, Tanaka et al. (2005) found that the bright-end of the cluster CMR is already built at $z = 0.83$ while the

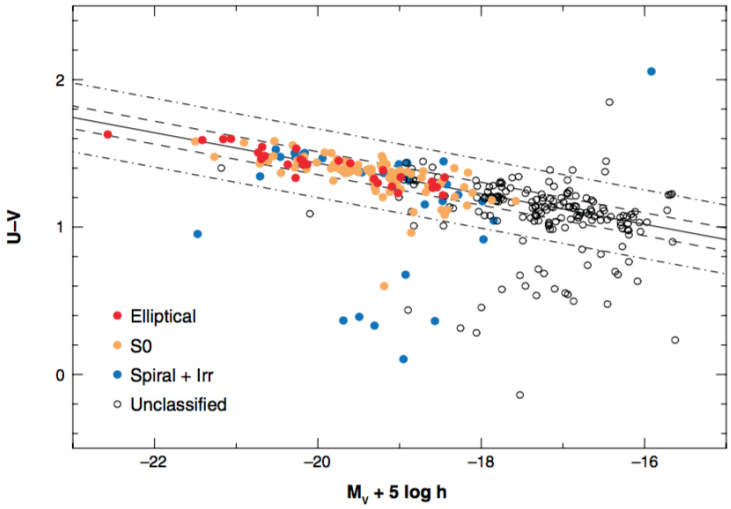

Figure 1.2: The $(U-V)$ – MV color-magnitude relation for galaxies that are spectroscopic members of the Coma cluster (from Bower et al. 1999).

faint-end is possibly still in the process of build-up. They also argued that the built-up of the field CMR appear to be delayed compared to the cluster one. It is worth reminding that useful evolutionary information is also enclosed in the slope of the CMR, which gives clues about the amount of merging galaxies underwent to during their evolution. Indeed, merging events can modify galaxy luminosities and velocity dispersions (dry merging) or also produce a shift in their colors (wet merging).

The fundamental plane

The fundamental plane (FP) is a relation between the structural/dynamical status of elliptical galaxies and their stellar content (Dressler et al., 1987, Djorgovski & Davis, 1987); in particular, it links ETGs effective radius R_e, velocity dispersion σ and surface brightness $I_e = L/2\pi R_e 2$ so that, when ETGs are shown in the 3D space (R_e, σ, I_e), they are not randomly distributed, but cluster close to a plane, as illustrated in Fig. 1.3. The mere existence of the FP implies that elliptical galaxies are virialized systems, have homologous structures and are made of stellar populations which satisfy precise constraints in age and metallicity. However, the observed FP is 'tilted' with respect to the theoretical relation, which implies that trends in the mass-to-light ratio M/L, and hence variations in both structural and stellar properties (metallicity, initial mass function and age) must be present in the ETG population (e.g. Bender et al., 1992, Busarello et al., 1997). However, even if the nature of the small scatter at $z \sim 0$ is not clear yet, it implies that ETGs have a small age dispersion and a high formation redshift. Depending on the IMF slope and the formation redshift z_f, the redshift evolution of the FP provides complementary informations on the ETGs cosmic evolution. In particular, high-z FP studies in clusters led to the conclusion that it shifts nearly parallel to itself, ant thus that no trends in age or IMF with galaxy mass exists (which would produce a rotation of the FP relation); high-z FP observations in the field (Treu et al., 2005) showed, instead, that a rotation with increasing redshift is present and that it could be explained through a systematic trend in the M/L ratio. This trend is consistent with massive objects having a higher z_f than less

massive ones. However, the observed shift of the FP at high z is again consistent with passive evolution of more massive systems that formed at high redshift.

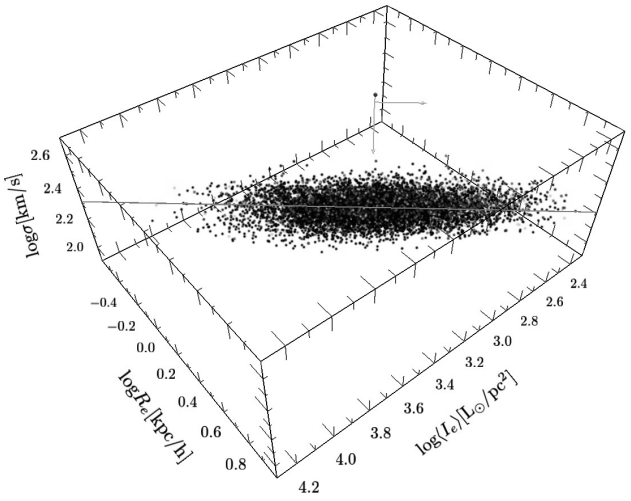

Figure 1.3: The infrared fundamental plane of elliptical galaxies (from Magoulas et al., 2012).

1.1.3 Relations between evolutionary and dynamical properties of early-type galaxies

The relations between the evolutionary and dynamical properties of early-type galaxies in the local Universe have been proved to be particularly useful to reconstruct the galaxy evolutionary path over cosmic time. Moreover, in the past decades, these studies have improved thanks to the developement of full-spectrum fitting techniques and the creation of synthetic Lick indices accounting for the presence of α elements, which makes stellar population properties estimates more and more reliable (see Sect. 1.1.1). In the following, we briefly summarize three of the most important relations linking the galaxy velocity dispersion σ (i.e. mass) with the α elements abundance ([α/Fe]), global metallicity ($[Z/H]$) and age. In particular, we follow the detailed paper by Thomas et al. (2010), who derived these relations analyzing a sample of SDSS ETGs at $0.05 \leq z \leq 0.06$.

[α/Fe] – σ relation. The [α/Fe] – σ relation encloses fundamental information on when and how fast ETGs formed their stars, since the [α/Fe] ratio can be considered an indicator of the timescales of the star formation. α elements are indeed the main product of Type II Supernovae explosions (SN II), while Fe peak elements are produced by the delayed explosion of Type Ia Supernovae. This implies that longer formation timescales correspond to lower [α/Fe], since in this case Type Ia Supernovae have had time to dilute the α-elements released into the interstellar medium (ISM) by SN II explosions. Observations suggest that α elements are more abundant in more massive ETGs (e.g. Worthey et al., 1992, Greggio, 1997, Jørgensen, 1999, Kuntschner, 2000, Terlevich & Forbes, 2002), and several studies employing synthetic Lick indices accounting for

α elements (Proctor & Sansom, 2002, Thomas et al., 2002, Mehlert et al., 2003, Thomas et al., 2010) have confirmed this trend in the past decades.

$[Z/H]-\sigma$ relation. The $[Z/H]-\sigma$ relation links the galaxy velocity dispersion with its global metallicity. It was observed by many authors in the past decades (e.g. Greggio, 1997, Thomas et al., 2005, Thomas et al., 2010), and indicates that more massive galaxies are more metallic than less massive ones. The existence of this relation is commonly related to the galactic wind models (e.g. Arimoto & Yoshii, 1987), according to which more massive galaxies, due to their deeper potential wells, are unable to produce galactic winds, thus retaining more metals and enriching their ISM more than less massive galaxies.

age-σ relation. The existence of a relation between galaxy age and velocity dispersion is still unclear and debated. However, even if early studies did not find any significant correlation between these two quantities (Trager et al., 2000, Kuntschner et al., 2001, Terlevich & Forbes, 2002), some recent works have suggested that a weak trend exists, although with a very large scatter (Proctor & Sansom, 2002; Proctor et al., 2004, Thomas et al., 2005, Thomas et al., 2010). and that it goes in the direction that more massive galaxies are older than less massive ones.

These three relations, which seem also to be independent of the galaxy environment (e.g. Thomas et al., 2010), suggest that more massive galaxies are older and form stars on shorter timescales than less massive ones, paving the way for the development of the so-called downsizing scenario, described in Sect. 1.4.

1.2 Mass-size relation of ETGs

The link between galaxy size and stellar mass has been studied over the past years both at low and high redshift. In the local Universe, the mass-size relation for ETGs has been observed by different authors (e.g. Bernardi et al., 2003), and defined by Shen et al. (2003) using a sample of SDSS galaxies. These authors found that the sizes of local ETGs follow a steep relation, with the median size R scaling as $R \propto M^{0.55}$. Moreover, they argued that the observed relation is consistent with the hypothesis that early-type galaxies are the product of several merging events experienced across cosmic time, in agreeement with the ΛCDM scenario (see Sect. 1.3).
With the advent of deep surveys, this kind of investigations have been pushed towards higher and higher redshifts, and have suggested that ETGs in the past were more compact than their local counterparts. In particular, their effective radii R_{eff} at $z \sim 2-3$ can be by up to a factor $\sim 2-3$ smaller (i.e. their density is ~ 30 times higher) than those in the local Universe (Trujillo et al., 2006, Toft et al., 2007, van der Wel et al., 2008, Cimatti et al., 2012) and their size evolution can be parametrized by $R_{eff} \propto (1+z)^{-1.48}$ (e.g. van der Wel et al., 2014).
It has also become clear over time that high-z ETGs are characterized by old stellar populations (e.g. Cimatti et al., 2008, van Dokkum et al., 2008) and higher velocity dispersions than local ETGs (Cenarro & Trujillo, 2009, van de Sande et al., 2011). These findings imply that most of these objects must increase their sizes and decrease their

velocity dispersions from $z \sim 2$ to $z = 0$ without recent star formation. How this can happen is still debated, but dry (i.e. gas poor, collisionless) merger events are certainly one of the most popular explanations. Alternative scenarios involving the expansion of the stellar system due to a significant mass loss (Damjanov et al., 2009, Ragone-Figueroa & Granato, 2011) have been proposed, but always failed in reproducing the observed size growth. Among dry mergers, minor mergers have been demonstrated to be most effective than major mergers to produce the observed size evolution (Bezanson et al., 2009, Naab et al., 2009). However, N-body numerical simulations have estabilished that dry minor merging events alone are often insufficient to explain the difference between high-z and local ETGs, and that sets of minor and major mergers have to be taken into account (Nipoti et al., 2009a, Nipoti et al., 2009b, Nipoti et al., 2012, Hilz et al., 2012). A further challenge for this kind of studies is to reconcile the dry merger scenario within the ΛCDM model in terms of merger rates and merger fractions (e.g.Guo & White, 2008, Hopkins et al., 2010).

1.3 Evolutionary scenarios for early-type galaxies

The earliest attempts to give a general description of how early-type galaxies form their stars and assemble their mass dates back to the 60s.
In particular, studying the kinematic of stars in the halo of the Milky Way, Eggen et al. (1962) suggested that galaxies form from the collapse of gas clouds (i.e. 'monolithic' collapse), and suggested that the difference between elliptical and spiral galaxies depends on the rapidity of star formation during the collapse. In particular, an elliptical galaxy is formed in the case of dissipationless collapse, when most of the gas turns into stars as it falls and the infall motions are converted into the random motion of stars. This hypothesis was supported by some later works, which demonstrated that the turbolent viscosity generating during the rapid collapse is able to explain most of the observed properties of elliptical galaxies, such as the isophotal shapes, rotation, age and metallicity gradients (Larson, 1975).
At almost the same time, a supplementary formation scenario was proposed by Toomre & Toomre (1972), Toomre (1974), Toomre (1977) (i.e. the 'merger' scenario), who invoked merging events between disc galaxies to explain the tidal disturbances observed in spheroidal systems. This picture became very appealing when modern cosmological models based on dark matter (DM) developed. In particular, this merger hypothesis has been tested by means of numerical simulations, also in the context of the Cold Dark Matter paradigm, which turned out to succesfully explain the observed galactic rotational curves and velocity dispersions (Efstathiou & Silk, 1983, Blumenthal et al., 1984). In this scenario, mergers are a natural consequence of the general shape of the power spectrum. Among merger simulations, the ones involving collisionless (i.e. dry) spheroid-spheroid binary mergers raised a lot of interest over time, especially when it became clear that this kind of mergers can be actually observed in the Universe up to high redshift (Tran et al., 2005; van Dokkum, 2005, Lotz et al., 2008, Jogee et al., 2009). However, it was soon pointed out that dry mergers are unable to explain the observed family of slowly rotating early-type galaxies (White 1979b), and that they can address early-type galaxy evolution, but not their formation (Naab & Ostriker, 2009).
Binary mergers between disc systems followed by the morphological transformation into spheroids have also been considered as an alternative way through which elliptical galaxies can hierarchically grow their mass. However, disc mergers are not able to

produce the observed distribution of masses, ages and metallicities of the bulk of the present-day massive early-type galaxy population (Naab & Ostriker 2009).
Furthermore, recent works have demonstrated that the growth of structures in a hierarchical context involves more complex processes than the single binary mergers classically included in simulations. In particular, mergers are likely to occur on a wide range of masses and on a extended interval of time (De Lucia & Blaizot, 2007, Genel et al., 2008, Feldmann et al., 2010a, Hirschmann et al., 2012).
Although a clear picture of how the stellar mass in early type galaxies grows over cosmic time is still laking, recent high-resolution cosmological zoom-in simulations suggest that the observed properties of ETGs fit with the hierarchical CDM cosmological model. Moreover, the formation and evolution of early-type galaxies seems to involve features of both the monolithic collapse and the merger scenario, and to be characterized by two different phases: a early assembly at $2 < z < 6$, with gas inflows (e.g. Dekel et al., 2009a) and in situ star formation, and a later phase driven by the assembly of stars formed in different galaxies at $3 < z < 0$ (Meza et al., 2003, Naab et al., 2007, Naab et al., 2009, Feldmann et al., 2010b, Oser et al., 2010, Johansson et al., 2012a, Lackner et al., 2012).
In the last decade, it has also become clear that ordinary matter accounts only for the 4.9% of the energy density of the observable Universe, while the remaining 27% and $\sim 68\%$ is constituted by dark matter and by an unknown form of energy, respectively (Planck 2015 results. XIII. Cosmological parameters). This latter, known as "dark energy", is usually parametrized by means of the cosmological constant Λ and acts as a repulsive gravity, able to balance the attractive gravity of matter. Many evidences, such as the accelerated expansion of the Universe (Riess et al., 1998, Perlmutter et al., 1999), the Cosmic Microwave Background anisotropies (Parkinson et al., 2012) and the Large Scale Structure of the Universe have confirmed the existence of the dark energy in the past decades. Since then, the cosmological constant Λ has been considered, together with CDM, the key ingredient of the ΛCDM cosmological model, which describes the formation of cosmic structures.

1.4 The Downsizing scenario

The ΛCDM cosmological model is able to explain many observed phenomena and, as explained in Sect. 1.3, it predicts a hierarchical growth, in which the merging between dark matter halos drives the formation of baryonic structures. However, an ensamble of empirical evidences gathered over the past decades have severely questioned the reliability of ΛCDM, suggesting that galaxy evolution is actually driven by stellar mass, with more massive galaxies forming their stars earlier and on shorter timescales than less massive ones, although the mass assembly proceeds in a hierarchical fashion. This alternative scenario is generally referred to as "downsizing" (Cowie et al., 1996) and has been observed by both backward and lookback studies. In the following, we will describe some of the empirical evidences of the downsizing, following the more comprehensive paper by Fontanot et al. (2009).
Indirect evidences have shown a:

- Chemo-archaeological downsizing. More massive ETGs have higher (up to supersolar) [α/Fe] ratios then low mass ones (e.g. Carollo et al., 1993, Davies et al., 1993b, Trager et al., 2000, Kuntschner et al., 2001, Bernardi et al., 2006, Thomas et al., 2010). This trend could be due to a different initial mass function (IMF) among galaxies or to selective mass losses, as proposed by Faber et al., 1992 and

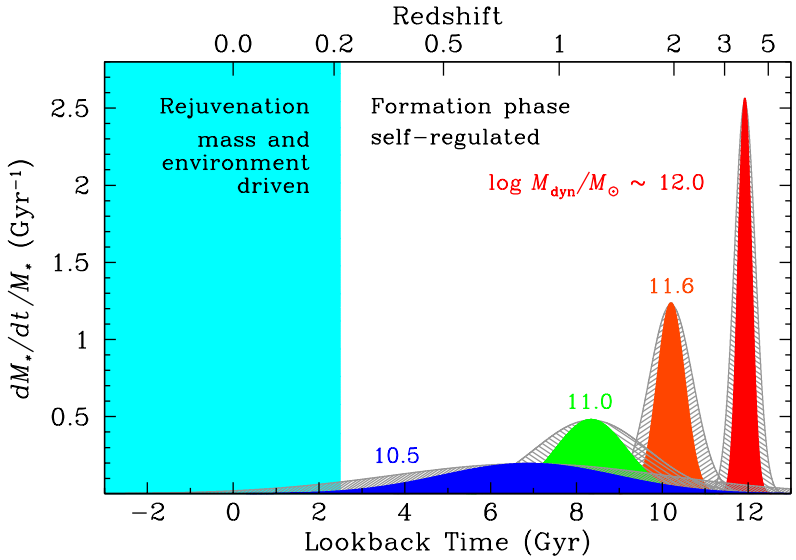

Figure 1.4: Sketch of the downsizing evolution scenario (from Thomas et al., 2010). Specific star formation rate as function of look-back time for early-type galaxies of various masses as indicated by the labels. It is clear that, for higher masses, the peak of the sSFR occurs earlier and the duration of the star formation is shorter.

Worthey et al., 1992. However, since α-elements are produced on shorter time scales by Type II Supernovae explosions of massive stars, a large [α/Fe] can also indicate a shorter duration of the star formation. Several studies in the past years (e.g. Thomas et al., 2005, Thomas et al., 2010) argue that this latter is the most suitable interpretation;

- Archaeological downsizing. The analysis of local elliptical galaxies by means of age-dependent spectral indices or full high-resolution spectrum fitting has shown that less massive galaxies are systematically younger than more massive ones, both in clusters (Nelan et al., 2005, Thomas et al., 2005, Thomas et al., 2010) and in the field (Heavens et al., 2004, Gallazzi et al., 2005, Panter et al., 2007, Conroy et al., 2014, McDermid et al., 2015). Fig. 1.4 shows a sketch of the structure formation according to the downsizing scenario.

Direct evidences obtained by analyzing galaxy samples at different redshifts have instead confirmed the downsizing in star formation as:

- Downisizing in specific SFR. The mass of star forming galaxies declines with decreasing redshift (Cowie et al., 1996), i.e the specific star formation rate (SSFR) declines more rapidly for more massive galaxies towards $z = 0$. Actually, there are conflicting claims in the literature about whether such a trend is in fact seen or not (Juneau et al., 2005, Mobasher et al., 2009);

- Downisizing in metallicity. The redshift evolution of the mass-metallicity (M-Z) relation could be reproduced by a period of star formation that lasts longer in less massive galaxies than in more massive ones (Savaglio et al., 2005, Erb et al., 2006, Maiolino et al., 2008);

- Downsizing in nuclear activity. X-ray (Ueda et al., 2003) and optically (Cristiani et al., 2004) selected AGNs peaks at higher redshift when more massive objects are considered, suggesting that more massive systems experienced the phase of prominent nuclear activity earlier than less massive ones.

- Downsizing in fundamental plane and color-magnitude relations. As already mentioned in Sect. 1.1.2 and 1.1.2, also the evolution of the Fundamental Plane and the CMR relations agrees with the hypothesis that the population of massive ETGs has built up at higher redshift with respect to the population of low-mass ETGs.

- Downsizing in Luminosity function and Galaxy Stellar Mass function. The luminosity function (LF) and the galaxy stellar mass function (GSMF) express the number of galaxies within a luminosity or mass interval. Tracing the distribution of galaxies, they contain fundamental insights on their formation and evolution. In particular, LF provides a cross-check to test the cosmic history of ETGs, since its evolution is related both to the IMF slope and the z_f. Indeed, if ETGs are passively evolving (and were formed at high redshift), then a brightening of the characteristic luminosity $L_\star$ (R-band) of the LF is expected towards higher redshifts. Barrientos & Lilly (2003) confirmed this hypothesis comparing a sample of local cluster ETGs with a sample of 8 cluster at $0.40 < z < 0.48$. de Propris et al. (1999) came to the same conclusion by analyzing the evolution of the observed K-band LF in 38 clusters with $0.1 < z < 1$. They suggested a $z_f \sim 2$, also arguing that not only the star formation but also the mass assembly of massive ETGs could have been accomplished by $z \sim 1$. Cimatti et al. (2006) compared the high redshift LF between $z \sim 0$ and $z \sim 1$ derived from COMBO-17 (Bell et al., 2004), DEEP2 (Faber et al., 2007) and SXDS (Yamada et al., 2005) with the local one (Bell et al., 2004). They deduced that the high luminosity tail of the LF at high redshift perfectly matches the local one, in agreement with the hypothesis of passive evolution, while its faint-end seems to be progressively depopulated going at higher redshift. Moreover, they found that the less luminous/massive ETGs seem to decline in number density as a function of redshift, suggesting that, at each redshift, there is a critical mass above all ETGs are in place.
  Similar evidences come from the studies of the GSMF, whose measurement both in the local and high redshift Universe have significantly improved in the last decades thanks to the advent of deep surveys. In particular, recent observations have shown an increase/decrease in the fraction of red/blue or early/late-type galaxies at intermediate masses since $z \sim 1$ (Fontana et al., 2004, Bundy et al., 2006, Vergani et al., 2008). Moreover, most of the studies exploiting deep surveys such as K20 (Pozzetti et al., 2003, Fontana et al., 2004), VVDS, COMBO17, and DEEP2 (Bell et al., 2004, Cimatti et al., 2006, Faber et al., 2007, Vergani et al., 2008), agree that massive old galaxies were already in place at $z \sim 1$ and that their number density declines rapidly at higher redshift. Another piece of evidence in this regard comes from the discovery of galaxies which look already passive and massive ($M \sim 10^{11} M_\odot$)at $1 < z < 2$ (Glazebrook et al., 2004 and Cimatti et al., 2004). Pozzetti et al. (2010) analysed the GSMF of 8500 galaxies with $I < 22.5$ (AB mag) over 1.4 deg^2 from a zCOSMOS-bright 10k spectroscopic sample (up to $z \sim 1$), observing that the high-mass end of the GSMF has a weak evolution since $z = 1$ and that ETGs increase in number density with cosmic time more rapidly with decreasing mass (see Fig. 1.5). Only higher redshift studies ($z > 1$) (Ilbert et al.,

2010, Ilbert et al., 2013, Muzzin et al., 2013b, Marchesini et al., 2013) have indeed found an evolution for the high mass tail of the mass function.

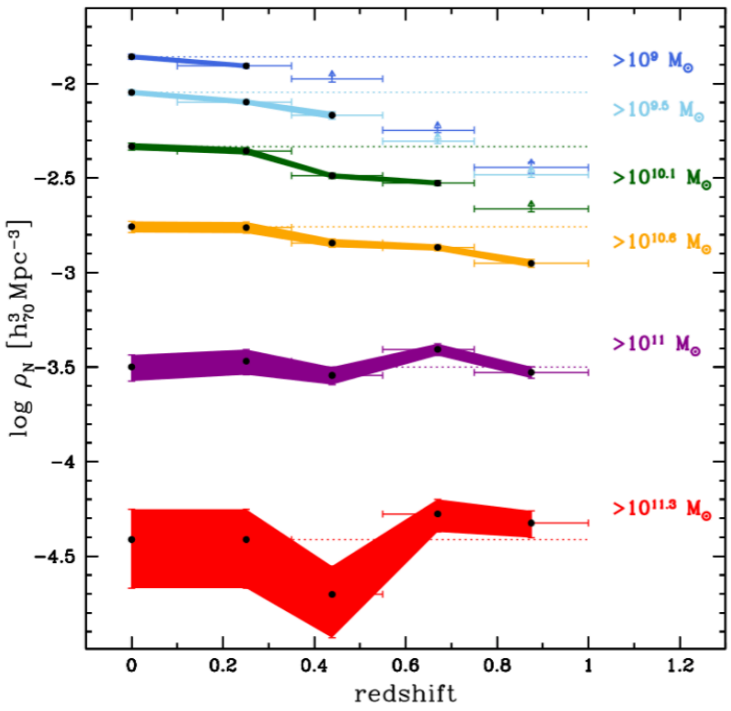

Figure 1.5: Number density evolution of the sample galaxies in various mass bins. The dotted lines correspond to the no-evolution solution normalized at z= 0 (from Pozzetti et al., 2010).

Although a clear picture about the stellar mass assembly across cosmic time is still lacking, all these results suggest that the red sequence of massive galaxies was already in place at $z \sim 1$, and thus that ETGs form the bulk of their stellar mass at higher redshift (i.e. $1.5 < z < 3$). Moreover, it seems that the downsizing trend can be extended from the star formation to the galaxy mass assembly, with more massive galaxies assembling their mass earlier than low massive ones. The physical interpretation of these results on ETG evolution is not trivial in the hierarchial merging scenario of ΛCDM cosmology because the mass downsizing evolution seems anti-hierchical. However, several progresses have been made in the last decades. For instance, the combination of N-body simulations of dark matter halos evolution (Springel et al., 2005, Boylan-Kolchin et al., 2009) with semi-analytic models for galaxy formation (White & Frenk, 1991, Kauffmann et al., 1999, Springel et al., 2005, Lu et al., 2011, Benson, 2012) have allowed a significant advance. For example, De Lucia et al. (2006) were able to reproduce the age-downsizing of elliptical galaxies by invoking AGN feedback to quench the star formation earlier in more massive systems with respect to less massive ones within the standard framework of the hierarchical assembly for stellar mass. The role of AGNs in influencing galaxy evolution and quenching the star formation is supported by several observations (Fabian, 2012 and references therein, Cimatti et al., 2013, Cicone et al., 2014, Förster Schreiber et al., 2014); however, other models are capable to form rapidly ETGs without invoking the AGN feedback (e.g. Naab et al., 2006, 2009, Khochfar & Silk, 2006, Johans-

son et al., 2012b). More recently, Henriques et al. (2013), (2015) found that the early build-up of low mass galaxies predicted by many models could in fact be prevented by assuming less massive systems to reincorporate the gas ejected by supernova-driven winds later than more massive objects. This kind of assumption, although requiring further investigation, would also reproduce the observed *mass assembly downsizing*. However, despite the improvements on the theoretical side, many questions remain still open and the physics of massive galaxy formation is not fully understood.

1.5 Building up the early-type galaxies population: the star-formation quenching

Since Hubble (1929), it is well known that galaxies can be classified in the two distinct populations: the blue cloud, which is populated by blue, star- forming and disc dominated galaxies, and the red sequence, where red, early-type, quiescent and bulge dominated galaxies lie (Strateva et al., 2001). One of the key question in the current studies of galaxy evolution is to understand the origin of this dichotomy, which is clearly visible in the color-mass diagrams, both at $z \sim 0$ (Blanton et al., 2003, Kauffmann et al., 2003, Baldry et al., 2004) and at higher redshifts (Bell et al., 2004, Brammer et al., 2009, Wuyts et al., 2011, Cheung et al., 2012, McIntosh et al., 2014) for $M > 10^{10} M_{\odot}$. In particular, Fig. 1.6 shows the bimodality as observed in the color-mass diagram in the local Universe by Schawinski et al. (2014).

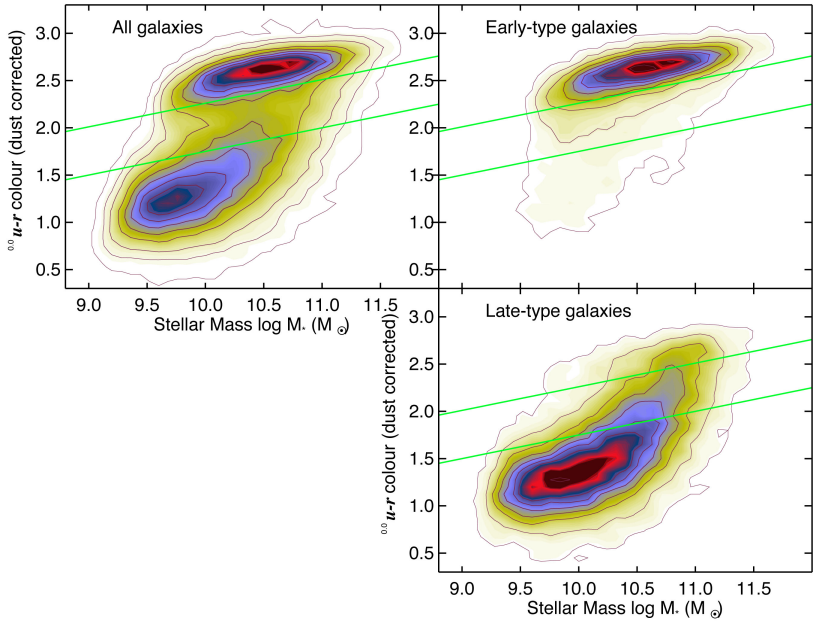

Figure 1.6: The $(u - r)$ color-mass diagram as observed by Schawinski et al. (2014). The top left panel show the whole population of galaxies. The top and bottom right panels show the early-type and late-type galaxies, respectively. Green lines mark the green valley region.

There is a general consensus that the main process underlying the galaxy bimodality is the build-up of the red sequence population at $M < 10^{11} M_{\odot}$, driven by the quenching of the star formation (e.g. Pozzetti et al., 2010). What is still unconstrained are the mechanisms able to modify star-formation and their corresponding time-scales. In the

following sections, we briefly show which are the most common quenching mechanisms invoked to explain this transformation, also describing the properties of the galaxies which are in the quenching phase, transiting from the blue cloud to the red sequence.

1.5.1 Quenching mechanisms

Several hypothesis have been proposed to explain the origin of the SF quenching in star forming galaxies. The mechanisms driving the SF quenching are usually divided into internal or external processes: internal processes are referred to as "mass" quenching and are related to the galaxies themselves (e.g. Peng et al., 2010); external processes are instead identified as "environmental" quenching and are linked to the environment galaxies live in. Concerning internal processes, in more massive galaxies an important role is played by AGNs. Indeed, their capability in influencing galaxy evolution and in halting the star formation is supported by several observations (Hopkins et al., 2005, Cimatti et al., 2013. Cicone et al., 2014, Förster Schreiber et al., 2014), and corroborated by the theoretical results obtained combining N-body simulations of dark matter halos evolution (Springel et al., 2005, Boylan-Kolchin et al., 2009) with semi-analytic models for galaxy formation (White & Frenk, 1991, Lu et al., 2011). However, other mechanisms have been suggested that are capable to rapidly form quiescent galaxies without invoking the AGN feedback (e.g. Naab et al., 2006, 2009, Khochfar & Silk, 2006, Johansson et al., 2012a). For instance, stellar or supernova (SN) feedback is the most likely channel for the star formation quenching in low-mass galaxies (e.g. $< 10^{10} M_{\odot}$).
Among environmental processes, RAM pressure stripping (Gunn & Gott, 1972, Bekki, 2009), tidal stripping (e.g. Diemand et al., 2007), strangulation (e.g. Balogh et al., 2000) or harassment (e.g. Hirschmann et al., 2014) have been proposed as likely mechanisms that can halt the star formation in galaxies. These phenomena are expected to be more evident in satellite galaxies, which orbit around central galaxies residing at the core or their host halo. However, recent studies have demonstrated that also central galaxies can experience quenching beyond their virial radius (e.g. Geha et al., 2012).
Large uncertainties about the quenching of the SF come from the fact that the timescales on which this process occurs are still far to be constrained. The scarcity of galaxies that are in the transition phase (the so-called 'Green Valley' galaxies, see Sect.1.5.2) suggests that, whatever mechanism may be responsible of the star formation shut-off, it has to happen on short time-scales (Tinker et al., 2010, Salim, 2014). The relatively short duration of the quenching process is also suggested by the surprising identification of a significant number of galaxies that look already quiescent at $z \sim 4-5$, when the Universe was only $\sim 1-1.5$ Gyr old. (e.g. Mobasher et al., 2005, Wiklind et al., 2008, Marsan et al., 2015).
Schawinski et al. (2014) found evidences that galaxies with early-type morphologies are characterized by shorter quenching time-scales ($t_{\rm quench} \sim 250$ Myr) with respect to galaxies with late-type morphologies ($t_{\rm quench} > 1Gyr$). They suggest that the SF quenching in late-type galaxies could be due to the inefficiency of the cooling of the hot halo, which slowly moves galaxies towards the red sequence, whilst the SFR gradually declines. Early-type galaxies are instead quenched by the rapid destruction of the galaxy gas reservoir, which brings the SFR to suddenly drop to zero and thus galaxies to rapidly populate the red sequence.
In the case of satellite quenching, Wetzel et al. (2013) introduced the idea of a "delayed than rapid" quenching, to reconcile the longer quenching timescales predicted by semi-analytical models and the short timescales derived from the observations. Another uncertainty is that the time-scales derived observationally are generally shorter than the

ones derived using N-body simulations and semi-analytic models (Muzzin et al., 2012, Taranu et al., 2014).
During the last decade, the hypothesis that the quenching of the SF in galaxies could be driven by a morphological transformation of the galaxies has been suggested by Martig et al. (2009). In this scenario, galaxies quench their SF without loosing their cold gas reservoir: when the gaseous disk turns into a spheroid, star formation can be inhibited by the self-gravity of the gas disk that is left behind. This scenario has also been noted in zoom-in simulations at redshift $z \sim 2$, where the formation of big star-forming clumps is quenched by the bulge growth (e.g. Ceverino et al., 2010). However, very recently, evidences that the quenching of the star formation could be a separated process with respect to the morphological transformation have come from the photometric and spectroscopic investigations of passive spiral galaxies (e.g. Fraser-McKelvie et al., 2016).

1.5.2 Identifying Green Valley galaxies

The 'Green Valley' was first observed by Wyder et al. (2007), who found that the distribution of blue cloud and red sequence galaxies in the $(NUV - r)$ – mass diagram could not be simply described by two gaussians, due to the presence of an excess of galaxies between them. Having intermediate colours between the two populations, galaxies lying on the Green Valley are generally considered as the transiting objects par excellence (Martin et al., 2007, Mendel et al., 2013, Salim, 2014, Schawinski et al., 2014).
Although hampered by the short duration of the quenching process, the search for galaxies in this critical phase of evolution has been carried on by several authors in the past decades. Galaxies characterized by both a tidally disturbed morphology and intermediate colours (e.g. Schweizer & Seitzer, 1992, Tal et al., 2009) or low-level of recent SF (Kaviraj, 2010), young elliptical galaxies (Sanders et al., 1988, Genzel et al., 2001, Dasyra et al., 2006) and very recent post-merger remnants with strong morphological disturbances (Hibbard & van Gorkom, 1996, Carpineti et al., 2012) have been considered as valid "recent time" quenching candidates. Moreover, many attempts aimed at spectroscopically identifying quenching galaxies come from the investigations of the post-starburst (E+A or K+A) galaxies UV and optical spectra, whose strong Balmer absorption lines and missing [O II] λ3727 ([O II], hereafter) and Hα emission lines (Couch & Sharples, 1987, Quintero et al., 2004, Poggianti et al., 2004, Balogh et al., 2011, Muzzin et al., 2012, Mok et al., 2013, Wu et al., 2014) have been interpreted as signs of a recent halt of the SF (Dressler & Gunn, 1983, Zabludoff et al., 1996, Quintero et al., 2004, Poggianti et al., 2008, Wild et al., 2009).
Emission line ratios have been proved to be powerful tools to constrain the ionization state and the properties of galaxies both at $z \sim 0$ and at higher redshift (e.g. Dopita et al., 2000, Kewley et al., 2001, Dopita et al., 2006, Levesque et al., 2010, Kewley et al., 2013, Kashino et al., 2016), but this kind of studies are always hampered by the degeneracies affecting spectra and emission lines, which in many cases make it difficult to disentangle what is the origin of the emission line ratios intensity (e.g. Dopita et al., 2006). However, a general view on how the emission line ratios can help in tracing the quenching phase is lacking, especially if the investigations involve the very early epochs after the quenching.

1.6 Main properties of ETG star-forming precursors

In the past years, a lot of studies aimed at reconstructing the galaxy mass-assembly history across cosmic time have focused on samples of early-type systems at different redshifts (e.g. Gladders et al., 1998, Ferreras et al., 2005). However, as explained in Sect. 1.5, it is well known that the population of ETGs is built up over time by a transformation of star-forming systems into passive ones and that, going towards higher redshift, the population of galaxies as a whole is mainly characterized by star-forming objects (e.g. Pozzetti et al., 2010). This means that not all the present ETGs were early-type systems at high redshift, and that the high-z ETG precursors could actually be star forming objects.[1].
Before describing the main properties of suitable ETG precursors, in the following sections we briefly recall the main properties of the SF galaxy population both in the local and high-redshift Universe.

1.6.1 The main sequence of star-forming galaxies

The star formation main sequence (SFMS) is an approximately linear relation which connects the star formation rate of SF galaxies with their stellar mass, and was first discovered by Daddi et al. (2007) and Noeske et al., 2007 (see Fig. 1.7). This relation has been observed at both low ($z < 1$; Brinchmann et al., 2004, Salim et al., 2007) and high ($z \sim 1$; Daddi et al., 2007) redshift.
There is a general consensus that the tightness of the SFMS is due to the fact that the majority of SF galaxies form stars in a quasi-steady process, in which the fuel for the star formation is continuously replaced by cold, filamentary streams of gas (Kereš et al., 2005, Dekel & Birnboim, 2006, Dekel et al., 2009b). The scatter of the SFMS is instead generally attributed to occasional merger events which can occur in the densest regions (Elbaz et al., 2011, Sargent et al., 2012). In this regard, Rodighiero et al. (2011) found that SFMS outliers, which probably arise from major mergers and are shifted at higher SFRs with respect to the general SFMS relation, represent only the 2 $\%$ of mass-selected star-forming galaxies. This means that major merger events are not the most common way for forming stars in star-forming systems.
The SFMS is generally parametrized by a simple power-law, but the exact value of its slope depends on the sample selection, the SFR indicators and the IMF assumed for its determination. Moreover, the SFMS normalization increases with redshift as $(1+z)^{\sim 3.5}$ due to the increasing of the gas content in galaxies with cosmic time, while its dispersion is constant at all redshifts, amounting to ~ 0.3 dex.
Recent works have claimed that a single power-law is not able to properly describe the SFMS. Indeed, a flattening of the relation at a turnover mass $M > 10^{10} M_{\odot}$ has been observed at all redshift, with a slope variation from $\sim 0.88 \pm 0.06$ to $\sim 0.27 \pm 0.04$ (see Fig. 1.7).

One common explanation for the flattening of the high-mass tail of the SFMS is that galaxies above the turnover mass have already quenched their star formation.
It is still unclear if the turnover mass evolves with redshift, but a disappearence or a weakening of this feature would be expected if galaxies become more and more star-forming going towards earlier cosmic times. However, observations in this regard are controversial: recently, Tasca et al. (2015) and Tomczak et al. (2016) found evidences of

[1]Considering only early-type systems at high redshift as the counterparts of present-day ETGs can introduce the so-called 'progenitor bias', which leads to underestimate the number density of ETG progenitors.

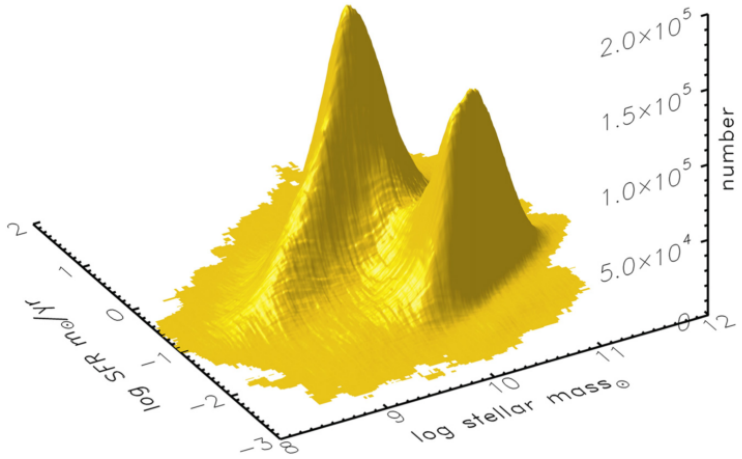

Figure 1.7: The 3D SFR-mass relation for local galaxies in the SDSS database and $0.02 < z < 0.085$ *(From Renzini & Peng, 2015).*

an increasing of the turnover mass with redshift, while other works do not observe any change in the slope at high masses (e.g. Renzini & Peng, 2015). These discrepancies could be related to the differences in the sample selection or in the determination of masses, SFRs, and recipes for dust correction (Wuyts et al., 2011).

1.6.2 Mass-metallicity relation

The mass-metallicity relation (MZR) is a positive correlation between stellar mass and metallicity, and is one of the most important relations observed in galaxies. The interest in the relationship between mass and metallicity dates back to the '70s (Lequeux et al., 1979), when luminosity was generally adopted instead of stellar mass, due to the difficulty in deriving this latter. In particular, the correlation between metallicity and blue luminosity was first observed by Garnett & Shields (1987) and then confirmed by other authors (e.g. Skillman et al., 1989, Brodie & Huchra, 1991, Zaritsky et al., 1994). However, with the advent of more sophisticated models for population synthesis and photoionization, the investigation of the link between metallicities and stellar masses have become more and more accurate. In particular, Tremonti et al. (2004) defined the local MZR using a large sample of SDSS galaxies. They found that this relation spans ~ 3 order of magnitude in mass and a factor ~ 10 in metallicity, and is characterized by a scatter of only ~ 0.1 dex in log(O/H). Gallazzi et al. (2005) found an analogous relation between stellar mass and stellar metallicity, where this latter traces the average history of galaxy metallicity, thus providing important insights on the galaxy chemical evolution (Ma et al., 2016).
The origin of the MZR is debated, and many different explanations have been proposed over time. For instance, a mass-dependent ejection of metal-enriched gas (e.g. Tremonti et al., 2004, Kobayashi et al., 2007, Spitoni et al., 2010), efficiency of star formation (e.g. Brooks et al., 2007, Mouhcine et al., 2008, Calura et al., 2009) or IMF (Köppen et al., 2007) have been suggested as possible mechanisms. Moreover, even if simple theoretical models such as the closed box, leaky-box, and accreting-box ones are generally able to give a qualitative description of this relation, more complex simulations are needed

to explain the MZR in a cosmological context (e.g. Finlator & Davé, 2008, Lu et al., 2015) and to describe the interplay among star formation, infall of metal poor gas and outflow of enrichment material, which are generally considered as the processes on which the MZR relies (e.g. Edmunds, 1990).
The MZR has been observed at different redshifts, showing a strong evolution as a function of cosmic time. In particular, it evolves monothonically, with metallicity decreasing with redshift for a given mass (e.g. Erb et al., 2006, Zahid et al., 2011, Cullen et al., 2014, Sanders et al., 2015). Moreover, Nagao et al. (2008) found that the evolution of the MZR is stronger for lower mass galaxies. This last trend can be considered as another manifestation of the downsizing evolution of galaxies: if more massive galaxies form their stars earlier than less massive ones, then they reach their final chemical state earlier than less massive ones.
The MZR is usually defined using metallicity-sensitive optical emission-line ratios, whose determination relies on theoretical methods based on photoionization models (see e.g. Kewley & Dopita, 2002) or empirical methods based on measurements of the electron-temperature of the gas, (e.g. Pilyugin, 2001, Pettini & Pagel, 2004), or a combination of the two (e.g. Denicoló et al., 2002). Over years, it has been demonstrated that the use of different calibrations can lead to different metallicity estimates, thus influencing the derived MZRs. The reasons for these discrepancies are not clear yet, but deeper investigations are needed to properly characterize the MZR (Kewley & Ellison, 2008) and ensure its robustness both at low and high redshift.

1.6.3 Fundamental metallicity relation

Analyzing a large sample of galaxies in a wide range of redshift ($0 < z < 4$), Mannucci et al. (2010) have recently shown that the MZR is actually a consequence of a more general 3D relation, referred to as the fundamental metallicity relation (FMR), which connects galaxy stellar mass, gas-phase metallicity and SFR. The existence of the FMR can be understood considering that both metallicity and SF are linked to the infall of metal poor gas (which triggers the SF) and to the outflow of enriched material (which is basically a product of the SF). Therefore, besides the already known MZR, a link between metallicity and SFR is expected to exist. This theoretical connection has been confirmed by observations (e.g. Erb et al., 2006, Erb, 2008, Mannucci et al., 2009, Cresci et al., 2010), which, in particular, have claimed the existence of an anticorrelation between metallicity and SFR, at any given mass. One possible explanation for this anticorrelation is that, in the hypothesis that the timescales of gas infalling are shorter than the ones on which the SFR is expected to evolve, the infall of new gas diluites metals inside the galaxy decreasing its metallicity, but triggering the SF at the same time. The FMR evolution with cosmic time indicates that this anticorrelation holds also at higher redshift. In this context, the observed evolution of the MZR described in Sect. 1.6.2 as a function of redshift arises from the fact that we are sampling different parts of the more general FMR relation.
Mannucci et al. (2010) also found that the FMR shows basically no evolution up to $z \sim 2.5$. This suggests that the same physical process drives galaxy evolution on a long interval of cosmic time. On the contrary, at $z > 2.5$, the SFR-metallicity anticorrelation weakens, suggesting that different mechanisms are at play in triggering the SF. The most likely process are merging events, which can inhibit the gas diluition, driving enriched gas into the galaxy and weakening the anticorrelation.

However, it is important to remind that large discrepancies still exist about the size and shape of the SFR-metallicity anticorrelation in the literature. For instance, Mannucci

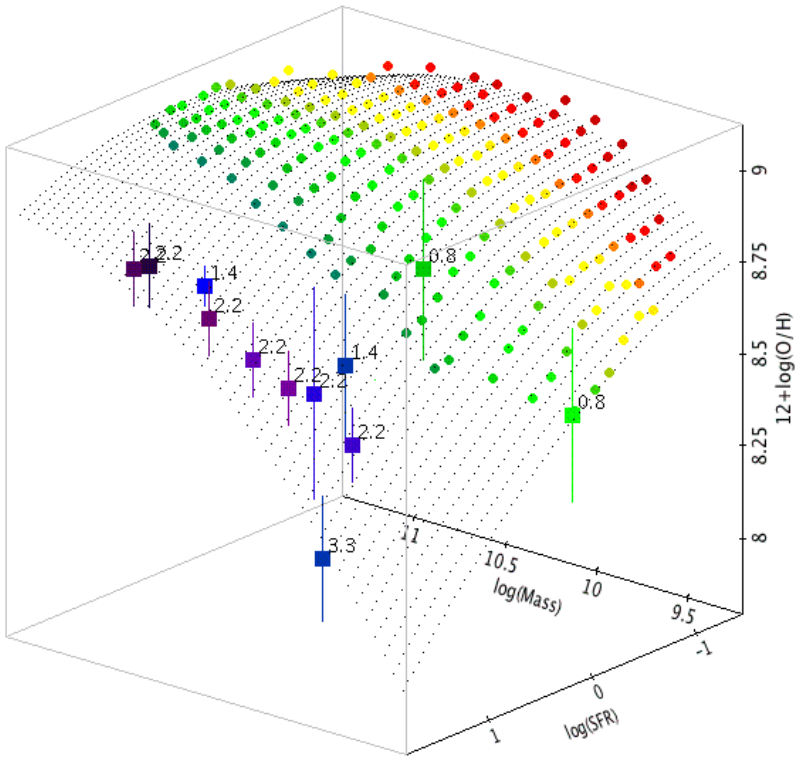

Figure 1.8: Fundametal metallicity relation (from Mannucci et al., 2010). Circles are the median values of metallicity of local SDSS galaxies in bin of M and SFR, with SFR decreasing from blue to red.

et al. (2010) find that for the low-mass end of the FMR the anticorrelation between SFR and metallicity is strong, while it disappears at higher masses. On the contrary, Andrews & Martini (2013) suggest it to be equally strong at all the masses. Furthermore, some authors observe an increasing of the metallicity for increasing SFR at high masses (e.g. Yates et al., 2012). These discrepancies could be due to the different galaxy selection criteria or metallicity indicators used in the various studies.

1.7 Suitable progenitors for early-type galaxies

Linking local ETGs with their progenitors at high redshift is a useful way to get a general view of their evolutionary pattern across cosmic time. Moreover, this investigation offers the chance to get closer to and to better understand the different phases characterizing ETG cosmic history. As argued in the previous sections, both direct and indirect observations have shown that ETGs form the bulk of their stellar mass at $1.5 < z < 3$, becoming passive at $z \sim 1 - 2$. For this reason, ETG progenitors are usually searched among the star forming population at high redshift (i.e. $z \gtrsim 2 - 3$) and the quiescent population at $z \sim 1 - 2$. In the following, we describe the main properties of both the star-forming and quiescent ETG progenitors observed so far.

Star-forming progenitors Thanks to their extreme nature, millimiter (MG) and submillimiter galaxies (SMG) have been regarded as likely ETG progenitors in the past

decades. These objects are indeed outliers in the stellar mass – star formation rate (SFR) relation in the $z \sim 2$ universe (e.g. Daddi et al., 2007), have gas kinematic signatures suggesting ongoing mergers (Tacconi et al., 2006, 2008), are characterized by high star formation efficiencies compared to typical galaxies of similar mass (i.e. SFR $\sim 1000 M_{bigodot}\mathrm{yr}^{-1}$) (Daddi et al., 2008, see also Bouché et al., 2007) and have very short gas-depletion timescales (i.e. hundreds of Myrs) (e.g. Hodge et al., 2015). The existence of these objects has been hypothesized starting from lower redshift observations. Indeed, it has become clear in the past years that populations of passive systems exist at $z \sim 1.5 - 2.5$ (Cimatti et al., 2004, McCarthy et al., 2004, Saracco et al., 2005, Kriek et al., 2008), characterized by large masses (0.5-5 $\times 10^{11} M_{\odot}$) and formation redshifts of $z \gtrsim 3$ (Labbé et al., 2005, Maraston et al., 2006, Longhetti et al., 2007, Cimatti et al., 2008). This implies that a population of galaxies with vigorous star formation (i.e. SFR $\sim$1000 $M_{\odot}$) has to be in place at $z \gtrsim 3 - 4$. Although the uncertainties related to the spectroscopic identification of these objects, several empirical evidences that such a population of SF systems actually exists have been gathered over years. For instance, thanks to ultra-deep optical/near infrared imaging, Dunlop et al. (2004) confirmed the presence of a SMG in the Hubble Deep Field at $z \sim 4.1$. At the same time, Dannerbauer et al. (2004) provided evidences of a group of SMGs at $z \gtrsim 4$. Similarly, Younger et al. (2007) found a population of very dusty starburst at $z \sim 3 - 4$, while more recently, a number of sources at redshift $z \sim 4.5$ have been spectroscopically confirmed to be SMGs with SFR$> 1000 M_{\odot}\mathrm{yr}^{-1}$ (Knudsen et al., 2008, Schinnerer et al., 2009).
The identification of ETG progenitors at very high redshift is hampered by the faintness of their emission. However, pushing the search of these precursors to very high redshifts (i.e. $z \gtrsim 6$) would help in place constraints on galaxy evolution in the very early phases of the history of the Universe. ETG SF progenitors at these high redshifts are generally the ones with the highest Lyα-based SFRs, the so-called Lyα emitters. Several of these objects have been spectroscopically identified at $z > 6.5$ (e.g. Taniguchi et al., 2005, Ouchi et al., 2009), with SFRs of typically $\sim 10 M_{\odot}\mathrm{yr}^{-1}$. Moreover, very recently, Riechers et al., 2013, identified a massive starburst galaxy at redshift 6.34 through a submillimeter color-selection technique. An additional piece of information about ETG SF progenitors comes from the host galaxies of QSOs at $z \sim 6$, which have stellar masses up to $M \sim 10^{11} M_{\odot}$ and high metallicity (e.g. Fan et al., 2003), and also from the surprising identification of a significant number of galaxies at $z \sim 4 - 5$, which have stellar masses up to $M \sim 10^{11} M_{\odot}$ and look already quiescent at these high redshifts (e.g. Mobasher et al., 2005, Wiklind et al., 2008, Juarez et al., 2009, Brammer et al., 2011, Marsan et al., 2015), although their properties are based on photometric redshifts and SED fitting, since they are too faint for spectroscopic identification. Should these galaxies be really ETG analogs at $z \sim 4 - 5$ they would imply that a fraction of massive galaxies formed rapidly at very high redshifts (say $z > 5$) and with an intense star formation, if they are observed already quiescent at $z \sim 4 - 5$.

Quiescent progenitors The observations of high redshift galaxies with suppressed star formation at high redshift is hampered both by the rarity of such objects and by the difficulty to detect them and measure their redshifts. ETGs are characterized by a distinctive spectral feature (i.e. the D4000 break) (see Sect. 1.1.1), which would allow in principle to detect them also at high redshift, where the break is redshifted to the near-infrared. However, since high continuum S/N ratios are required to observe it, the sample of confirmed $z \sim 2$ passive systems is small and poorly constrained. So

far, ETG quiescent progenitors have been spectroscopically confirmed up to $z \sim 2.5$ (van Dokkum et al., 2008). Franx et al. (2003) study a population of red galaxies at $z \sim 2-3$, deducing ages of $\sim$1 Gyr and thus suggesting them as the descendants of galaxies formed at very high redshift; Daddi et al. (2005) find similar old ages in seven early- type galaxies with $M \sim 10^{11} M_{\odot}$ observed in the Hubble Ultra Deep Field at $z \sim 1.4$ and Kriek et al., 2006, analyzing K-selected galaxies at $2.0 < z < 2.7$, find for them very low levels of emission and very low sSFRs (~ 0.0004 Gyr^{-1}). Similar conclusions have also been drawn by Cimatti et al. (2008), who study a sample of spectroscopically selected galaxies at $1.39 < z < 1.99$ using the GMASS spectroscopy and the GOODS multi- band photometry. Beyond $z = 3$, candidate early-type or post-starburst galaxies have been reported, despite uncertainties linked to the degeneracy between age and dust-reddening (e.g. Wiklind et al., 2008, Mancini et al., 2009, Fontana et al., 2009, Stefanon et al., 2013, Muzzin et al., 2013a). Passive galaxies have also been identified at z>1.4 (Onodera et al., 2012, Gobat et al., 2013). Very recently, Straatman et al. (2014) have extended the search for quiescent progenitors at higher redshift, identifying a substantial population of galaxies with suppressed SF at $z \sim 4$ by means of ZFOURGE data. Most of the observed ETG progenitors have compact sizes at $z > 1.5$, with effective radii by a factor $\sim 3-5$ smaller than in the local universe (Daddi et al., 2005, Longhetti et al., 2007, Trujillo & Conselice, 2008). As discussed in the previous sections, a clear picture of what mechanisms would be capable to transform extended starbursts at very high redshift into compact systems is still lacking. Morever, explaining these properties represents a challenge for simulations of galaxy formation (see Sect. 1.2).

1.8 Open questions about the evolution of early-type galaxies

From the previous sections, we learnt that in the past decades several progresses have been made in the direction of a more comprehensive knowledge of galaxy formation and evolution. In particular, the development of more accurate spectral studies and high-resolution numerical simulations, and the advent of high-redshift surveys have allowed to address many questions about how ETGs form and assemble their mass. However, many questions remain open and are far to be addressed.

For instance, the mechanisms regulating the formation of stars in galaxies, how galaxy evolutionary properties correlate with their stellar masses and star formation rates (SFR) are not completely understood. Moreover, the population of star-forming and quiescent progenitors of ETGs at high redshifts is still poorly constrained, mostly because these studies can only rely on photometric redshifts. Explaining the extremely small sizes of ETG precursors represents a further challenge for the current simulations of ETG evolution, as well as understanding what mechanisms could be responsible of the size growth across cosmic time, and if they fit with the hierarchical ΛCMD scenario.

Another critical point is how the quenching of the star formation occurs in star-forming galaxies. In particular, a clear picture of which mechanisms could be able to halt the SF and on which timescales, is still lacking. Although, also the role of AGNs, which are often invoked to explain the SF shut off, is still not understood.

Several uncertainties concern the cosmological evolution scenario itself. Indeed, if empirical evidences suggesting a downsizing trend of the star formation in galaxies can fit with the ΛCDM scenario assuming that the SF is halted earlier in more massive galaxies than in less massive ones, observations suggesting that this trend could also be extended to the galaxy mass assembly are not trivial to explain within the hierarchical cosmological model.

Last but not least, the detailed phases characterizing ETG formation are poorly constrained, although recent high-resolution merger simulations have suggested that they could consist of a mix of monolithic collapse and merging events.
Future studies will be certainly helpful to address these issues and to disentangle between the different mechanisms and processes driving ETG cosmic history.

In this thesis work, we attempt to address some of these debated questions of the field of galaxy evolution, inspecting it back in cosmic time.
In particular, in Chapter 2, we start from the study of passive local galaxies, archaeologically reconstructing their past SFHs. In Chapter 3, we move to the phase in which galaxies quench their star formation, defining a new methodology able to identify the quenching progenitors of passive galaxies. Finally, in Chapter 4 we take a further step back to the star forming phase, analyzing the properties of high-redshift galaxies which could be the star-forming progenitors of the passive local ones. Our investigations mainly rely on the spectral analysis of galaxies. In particular, we study both the passive and star-forming phase by exploiting the information contained in the galaxy full-spectrum, whose shape depends on the properties of the underlying stellar populations. The quenching phase is instead investigated by means of emission line ratios, which are associated to the Interstellar Medium (ISM) and its ionization state during or just after the star formation has stopped. In Chapter 5 we summarize our results and draw our conclusions.

Chapter 2

Inferring the star formation histories of the most massive and passive early-type galaxies at $z < 0.3$

In the ΛCDM cosmological framework, massive galaxies are the end-points of the hierarchical evolution and are therefore key probes to understand how the baryonic matter evolves within the dark matter halos. The backward approach, based on the study of galaxy properties in the local Universe, provides indirect evidences of how galaxies evolve across cosmic time and can be considered as a reliable method to understand their cosmic history.

Since most of the information concerning galaxies is encoded in their integrated light, one of the most successful approaches to derive galaxy evolutionary properties is the spectral analysis. In particular, over time several different techniques have been introduced to extract information from galaxy spectra. As discussed in Sect. 1.1.1, one of the most widely used method is the one based on the Lick indices, which consider the strength of different absorption features relating them to some intrinsic property of the galaxy, such as age, stellar metallicity, and alpha-elements abundance. A complementary approach to the Lick indices, which has been developed in the last decades and has the advantage of not being sensitive to missing data or bad pixels, is the full-spectrum fitting method.

In this chapter, we use the backward approach in order to infer the stellar population properties and star formation histories of the most massive ($M > 10^{10.75} M_{\odot}$) and passive early-type galaxies (ETGs) at $0 < z < 0.3$ (corresponding to a cosmic time interval of ~ 3.3 Gyr) based on stacked, high signal-to-noise ratio (SNR) spectra extracted from the Sloan Digital Sky Survey (SDSS). Our study is focused on the most passive ETGs in order to avoid the contamination of galaxies with residual star formation activity and extract the evolutionary information on the oldest envelope of the global galaxy population. We exploit the information present in the full-spectrum by means of the STARLIGHT public code (Cid Fernandes et al., 2005), adopting different stellar population synthesis models.

The chapter is organized as follows: in Sect 2.1 we briefly describe the full-spectrum fitting technique; in Sect. 2.2 we give information about the full-spectrum fitting code STARLIGHT; in Sect 2.3 we describe some tests performed to verify the reliability of STARLIGHT in retrieving galaxy evolutionary and physical properties (i.e. ages, metallicities, dust extinctions and velocity dispersions) and the SFHs of the input spectra; in Sect. 2.4, 2.5, 2.6 and 2.7 we apply the full-spectrum fitting to the sample of local massive

and passive ETGs and describe the obtained results, interpreting them into a cosmological context. Sect. 2.8 summarizes our main results.

The results shown in this Chapter can be found in *Citro et al. 2016; Astronomy & Astrophysics, Volume 592, id.A19, 22 pp.*

2.1 The full-spectrum fitting technique

The full-spectrum fitting approach uses all the information contained in a galaxy spectrum. Although relatively high signal-to-noise ratios are required to derive the evolutionary properties accurately, this technique has the advantage of being insensitive to extinction or flux calibrating errors. For this reason, it has been widely used in the last decades (e.g. Ocvirk et al., 2006a, 2006b) and its reliability has been assessed on the basis of specifically derived simulations (e.g. Choi et al., 2014).
The full-spectrum fitting approach basically relies on the comparison between galaxy spectra and synthetic stellar populations, according to different algorithms. Being one of the key ingredients of the full-spectrum fitting technique, we devote the following Sections to the description of how synthetic stellar populations are created, also focusing on the properties of the ones adopted in this Chapter.

2.1.1 Evolutionary population synthesis

The first attempts to study galaxy light in terms of their stellar content was based on the trial and error analysis, in which galaxy spectra were fitted with combinations of stellar spectra (e.g. Spinrad & Taylor, 1971, Turnrose, 1976, Pickles, 1985). However, due to the difficulty in constraining the large number of free parameters needed, this technique was abandoned in the early 1980's. With the same purpose of modelling the integrated light of galaxies, Tinsley (1978) introduced the evolutionary population synthesis technique. Here, synthetic models are created starting from stellar evolution tracks and theoretical or empirical stellar spectral libraries, under the assumption of an initial mass function (IMF), a star formation history (SFH) an age and a metallicity.
The two methods which are generally adopted to generate evolutionary population synthesis models are summarized in the following.

Isochrone synthesis technique In this method, the isochrone at time t' of an instantaneous-burst population (Simple Stellar Population, SSP) is computed through the interpolation between consecutive evolutionary tracks, considering all the stages of which they are composed, step by step. The total luminosity is derived by populating each point of the isochrone with an amount of stars dependent on the IMF, while the SSP SED is obtained by summing stellar spectra at each point on the isochrone. This technique is also based on the idea that stellar populations with an arbitrary SFH can be treated as the combination of many SSPs, according to the following equation:

$$F_\lambda(t) = \int_0^t \psi(t-t') S_\lambda[t', \zeta(t-t')]\, dt' \,, \tag{2.1}$$

where $F_\lambda(t)$ is the flux of the total population at time t, $S_\lambda[t', \zeta(t-t')]$ is the power radiated per unit wavelength and per unit initial mass by an SSP of age t' and metallicity $\zeta(t-t')$; $\psi(t-t')$ is instead the star formation rate at the time $(t-t')$, when the SSP was

formed. So, once that S_λ is obtained through the above procedure, one can create a synthetic stellar population with any SFH using eq. 2.1.

Fuel consumption theorem In this case, the total luminosity of synthetic stellar populations is expressed by the following equation:

$$L_{tot}(t, C) = L_{MS}(t, C) + L_{PMS}(t, C) \ , \tag{2.2}$$

where $L_{tot}(t, C)$ is the total luminosity of an SSP of age t and chemical composition C; $L_{MS}(t, C)$ is the total luminosity produced by MS stars and $L_{PMS}(t, C)$ is the total luminosity of post-main sequence (PMS) phases. Actually, while MS is dealt with the already described isochrone synthesis technique, PMS phases are valued by means of the so-called fuel consumption theorem (Renzini & Buzzoni, 1986). In particular:

- Main sequence luminosity. Once that the isochrone corresponding to MS phase is realized, its total luminosity is calculated through the following equation:

$$L_{MS}(t, C) = \int_{M_{in}}^{M_{TO(t,C)}} L(M|t, C) \ , \tag{2.3}$$

  where $L(M|t, C)$ is the light contribution at time t of a star of mass M and chemical composition C, M_{in} is the lowest limit in mass (usually around 0.1 $M_\odot$), M_{TO} is the turn-off mass at time t and $\psi(M)$ is the initial mass function.

- Post-MS luminosity. The study of PMS phases relies on the fuel consumption theorem, which states that the contribution to the integrated bolometric luminosity of an SSP provided by the stars in a given PMS phase is proportional to the amount of fuel burned during that stage. This theorem is based on the fact that, while MS stars have very different masses, the mass of a star at its turnoff (M_{TO}) and that of a star at the end of the AGB phase are practically identical: this implies both that in correspondence of the PMS phases the isochrone of an SSP can be simply approximated by the evolutionary track of a star with $M = M_{TO}$, and that the rate at which stars evolve off the main sequence is comparable to the rate at which they evolve off any PMS phase. Starting from these statements, the luminosity of the PMS can be written as (Renzini & Buzzoni, 1986):

$$L_{PMS}(t, C) = \sum_j n_j L_j \ , \tag{2.4}$$

  where n_j is the number of stars populating each PMS phase j and L_j is the total luminosity of this latter. The term n_j is:

$$n_j = b(t) t_j \ , \tag{2.5}$$

  with $b(t) = \psi(M_{TO})|\dot{M}_{TO}|$ being the evolutionary flux, i.e. the rate at which stars leave MS and hence enter each PMS phase and t_j being the phase duration. Thus:

$$L_{PMS}(t, C) = \sum_j b(t) L_j t_j \ , \tag{2.6}$$

  and hence:

$$L_{PMS} = 9.75 \times 10^{10} b(t) \sum_j F_j(M_{TO}) \ , \tag{2.7}$$

where $F_j(M_{TO}) = L_j t_j = m_H + 0.1 m_{He}$ is the "fuel", i.e. the total energy radiated by a star in each PMS phase j , deriving essentially from nuclear burning. The numerical factors are essential to express luminosity and fuel are expressed in solar units, the evolutionary flux in years.

2.1.2 Main characteristics of synthetic models

From the above descriptions, it is clear that there are two essential ingredients for computing a synthetic population model: stellar evolutionary tracks, which allow to calculate the total luminosity of the synthetic population, and stellar spectra, which are needed to derive its spectral energy distribution.
In this Chapter, we adopt the Bruzual & Charlot (2003) (hereafter, BC03) and the Maraston & Strömbäck (2011) (hereafter, MS11) synthetic models. In the following, we recall the main ingredients used to compute them.

BC03 spectra. BC03 models assume the Padova1994 library (Alongi et al., 1993, Fagotto et al., 1994a, 1994b, Girardi et al., 1996). Its tracks are defined on a large range of metallicities, going from $Z = 0.0001$ to $Z = 0.10$ and contain all the evolutionary phases from the zero age main sequence (ZAMS) to early-AGB. In addition, they supplement the Padova library for post-AGB phases (Vassiliadis & Wood, 1994), and TP-AGB stage (with models of effective temperature and bolometric luminosities by Vassiliadis & Wood (1993)). With these extensions, the Padova1994 library covers all the evolutionary stages from ZAMS to remnant phase for all masses above $0.6 M_{\odot}$ (for less massive stars, models of unevolved main sequence stars are adopted). Regarding stellar spectra, BC03 use two different libraries for the high- and low-resolution cases, i.e. Basel (Bessell et al., 1989, Allard & Hauschildt, 1995, Rauch, 2002) and STELIB (Le Borgne et al., 2003): their main characteristics are summarized in Table 2.1.

Table 2.1: Main characteristics of the stellar spectra libraries adopted to compute BC03 models.

Name	Wavelength range (Å)	Resolving power (R)	Met. range
Basel 3.1	91 to 160 μm	300	$10^{-5} Z_{\odot}$ to $10 Z_{\odot}$
STELIB	3200 to 9500	2000	$-2.0 < [Fe/H] < +0.50$

MS11 spectra. MS11 models adopt the Cassisi et al. (1997) set of isochrones (for MS luminosity) and evolutionary tracks (for PMS luminosity), defined on a large range of metallicities (from $Z_{\odot}/200$ to $2 Z_{\odot}$) and ages (from 1 to 15 Gyr). Moreover, in order to compute higher metallicity populations, a set of Padova isochrones/tracks with $Z = 3.5 Z_{\odot}$ are implemented (Girardi et al., 2000) and, to reach a larger extension in age ($10 - 3 \leq t/Myr < 30$), tracks by Schaller et al. (1992) are implemented. Also in this case semi-empirical solutions are employed for the thermally- pulsating stages. Regarding stellar spectra, MaStro models are realized using four different libraries of stellar spectra, in particular: Pickels library (Pickles, 1998), STELIB library (Le Borgne et al., 2003), MILES

(Sánchez-Blázquez et al., 2006) library and ELODIE (Prugniel et al., 2007) library. Their main characteristics are reported in Table 2.2.

Table 2.2: Main characteristics of the stellar spectra libraries adopted to compute MaStro models.

Name	Wavelength range (Å)	Resolving power (FWHM)	Metallicity range $[Fe/H]$	T_{eff} (K)
Pickles (1998)	1150-25000	11 Å	$[-0.8, +0.6\,]$	2500-3500
STELIB	3200-9300	3.0 Å	$[-2.75, +0.6\,]$	3250-51000
MILES	3500-7430	2.3 Å	$[-2.9, +1.6\,]$	2750-36000
ELODIE v3.1	3900-6800	0.55 Å	$[-3.0, +1.0\,]$	3100-5100

As previously mentioned in Sect. 1.1.1, a problem that affects spectral studies at optical wavelengths is the one of the degeneracies. In particular, one of the most severe degeneracies concerns the three parameters age, dust, and metallicity, which can have similar effects on both the spectral continuum and spectral features. For instance, a spectrum can be redder (i.e. the flux at longer wavelengths is higher than the flux at shorter wavelengths) because of older ages, higher metallicities or larger dust extinction (David Wilkinson, Ph. D Thesis). In more detail, when a stellar population becomes older, the bluer and brighter main sequence stars evolve into the Red Giant Branch stars, which have lower superficial temperatures, reddening the total spectrum.
Moreover, more metallic stellar populations are redder than less metallic ones because higher metallicities imply higher opacities and thus lower effective temperatures of the stars. Also, interstellar dust and gas tend to absorb shorter wavelengths more than longer ones, producing a redder flux.
An attempt to separate these effects consists in using spectral features which become more apparent at high-resolution, such as molecular lines, or also in adding near-infrared or ultra-violet data to the optical ones (e.g. Li & Han, 2007). However, also these other spectral regions are affected by some limitations. For instance, the asymptotic-giant-branch (AGB) phase, which contributes mostly to the near-infrared flux, is not well constrained and, as already mentioned in Sect. 1.1.1, disentangling the effects of young stars and hot horizontal branch stars at short wavelengths is not trivial for the current studies of evolutionary population synthesis.

2.2 The STARLIGHT code

The full-spectrum fitting technique has been used in the last decade as a complementary approach to the one based on the Lick indices to infer the evolutionary properties of ETGs. In the last years, many full-spectrum fitting codes have been developed (e.g. MOPED, Heavens et al., 2000; VESPA, Tojeiro et al., 2007; ULySS, Koleva et al., 2009): starting from different algorithms, these spectral codes explore a well-chosen parameter space in order to find the best possible fit to the data. To study local ETGs, we employ the spectral fitting code STARLIGHT[1] (Cid Fernandes et al., 2005) which have provided excellent results for many different class of objects, from the Low Luminosity AGN, to Seyfert nuclei and normal objects, including the ETGs we are focusing on.
In particular, STARLIGHT provides a best fit model which is obtained from the combination of many SSP spectra defined in user-made libraries, and can be described, at

[1]More informations are available on the website: *www.starlight.ufsc.br*

each wavelength, by the following equation:

$$M_\lambda = \sum_{j=1}^{N_\star} x_j \gamma_j \otimes G(v_\star, \sigma_\star) 10^{-0.4 A_V (q_\lambda - q_{\lambda_0})} \, . \tag{2.8}$$

Here, x_j is the monochromatic flux of the synthetic model j at the normalization wavelength λ_0 extincted by interstellar dust, γ_j represents the spectrum of the synthetic model j at λ_0 and $G(v_\star \sigma_\star)$ is the kinematical kernel. The latter includes a velocity shift $v_\star$, which is basically a fine-tuning for slight errors in the user de-redshifting process, and a velocity dispersion $\sigma_\star$. The last term in the equation is the reddening applied to each synthetic model, parametrized by means of the visual extinction A_V.
Since the best-fit model is normalized at λ_0, the contribution of each synthetic model is ultimately expressed in terms of light-percentages x_j's λ (see Fig. 2.1). From these, the mass contribution m_j of each model to the best fit spectrum can be derived starting from the corresponding x_j and from the mass in stars at the age of the model. In the fit, light- and mass-fractions are derived together with the best fit values for both the stellar velocity dispersion and stellar extinction.

It is worth briefly recalling that the numerical scheme on which STARLIGHT relies to carry out the spectral fit is characterized by a mixture of simulated annealing plus Metropolis plus Markov Chain Monte Carlo techniques, aimed at searching the minimum

$$\chi^2 = \sum_\lambda [(O_\lambda - M_\lambda)/e_\lambda]^2 \, , \tag{2.9}$$

where O_λ is the observed spectrum, M_λ is the best fit model and e_λ is the error associated to the observed flux at each wavelength.

2.3 Testing STARLIGHT with simulated ETGs spectra

One of the most critical aspect of observational astrophysics is that the signal of observed sources, and hence their spectrum, is biased by random contributions of spurious components (generally identified as noise), which can be intrinsic to the employed device or linked with background sources. The relevance of the noise on the effective received signal is quantified through the so-called signal to noise ratio (SNR), where lower SNRs mean larger noise and thus enhanced errors on the observed flux. From this it is clear that, as SNR decreases, both the result and the interpretation of the fits become more and more uncertain; for this reason it can be very useful to investigate how a spectral fitting code reacts to changes in the SNR of the observation, before applying it on data.
In this section we test the STARLIGHT reliability to reproduce the evolutionary properties, such as age, metallicity, star formation histories (SFHs), dust extinction and velocity dispersion of massive and passive galaxies as a function of the signal-to-noise ratio (SNR) of the input spectra. To do this, we simulate spectra with different SNR and known evolutionary and physical properties treating them as STARLIGHT inputs, and then we compare our assumed inputs with the code outputs.
We create an ensemble of simulated spectra from 3500 to 8500 Å with increasing SNR, starting from BC03 theoretical models. These synthetic models are based on the STELIB stellar spectra library (Le Borgne et al., 2003) and assume a Charbrier IMF (Chabrier, 2003). Moreover, they are defined in the wavelength range $3200 - 9500$ Å and have a

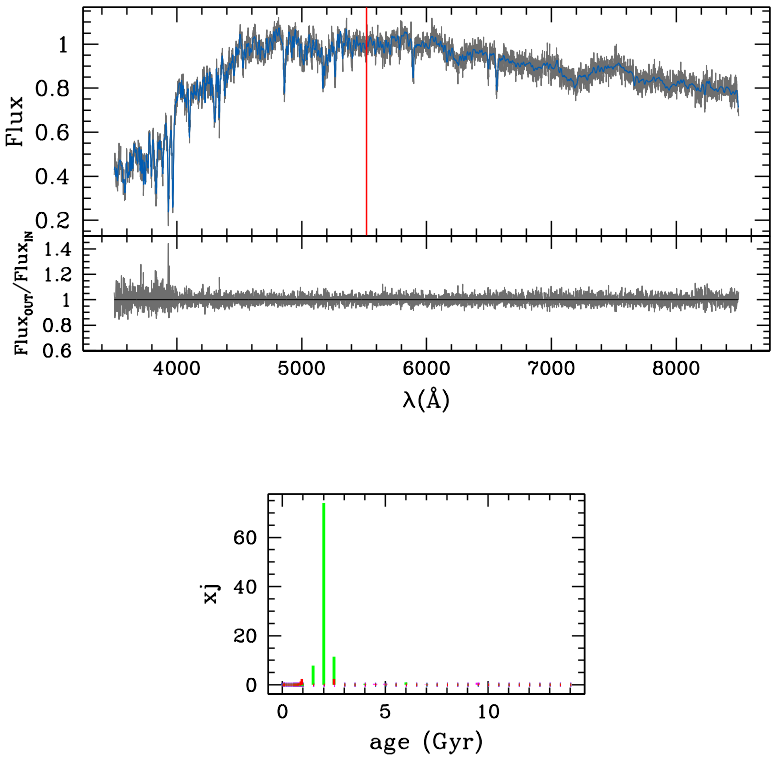

Figure 2.1: STARLIGHT typical output. Top panel. Grey curve: input spectrum; blue curve: best fit model, red vertical line: normalization wavelength. Small panel shows the differences between the input and the best fit model spectrum in function of wavelength. Bottom panel. STARLIGHT light fractions x_j's. The x-axis contains the ages of all the library models, the y-axis contains the light contribution (in percentage) to the best fit model at the normalization wavelength for each library model (in particular: green is for $Z = 0.02$ (solar metallicity), red and magenta stand for $Z = 0.05$ and $Z = 0.008$, respectively).

resolution of $\sim$ 3 Å, which is similar to the resolution of the SDSS spectra analyzed in the second part of this work (see Sect. 2.4.1). We first define an error e_λ for each theoretical spectrum by dividing the median flux of the model in the $6500 - 7000$ Å window by a pre-defined grid of SNR (going from 1 to 10 and from 20 to 500 with step of 10); then, we apply the λ-independent e_λ to the whole model spectrum, generating gaussian random numbers within it and thus producing the simulated flux, as illustrated in Fig. 2.2.We verified that the assumption of a wavelength-independent error is reasonable, since it reproduces the behaviour of the error of individual SDSS spectra, on which we base our subsequent analysis. In particular, within the rest-frame range 3500 – 7000 Å (used to fit our data, see Sect. 2.4.1), the error of SDSS spectra is constant as a function of wavelength, apart from a discontinuity in correspondence of the overlapping of the blue and the red arm of the spectrograph (at $\sim$ 6000 Å).

As a consequence, the SNR in our simulations is wavelength-dependent, as shown in Fig. 2.2.
We assume a composite stellar population (CSP) with an exponentially delayed SFH:

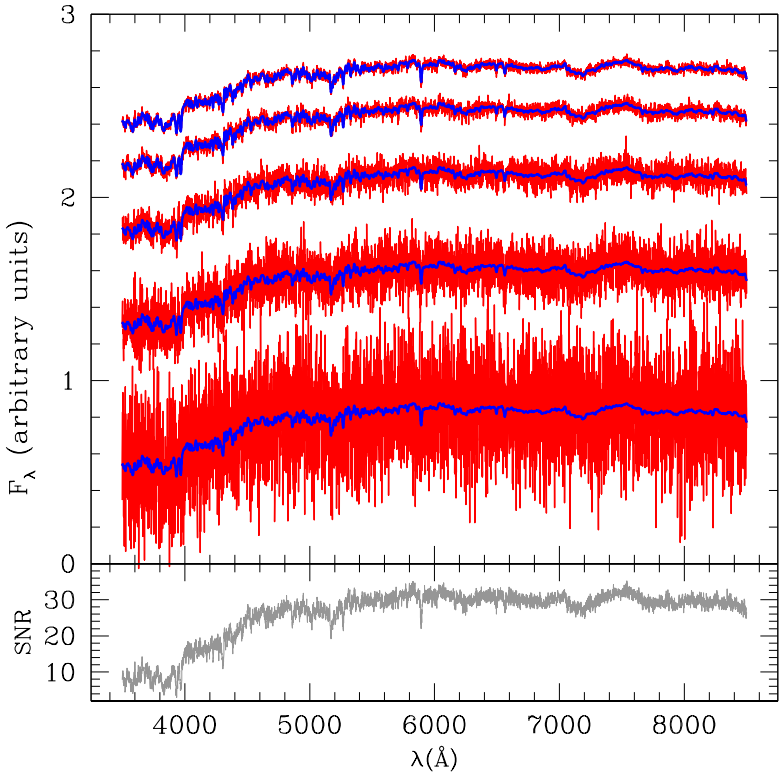

Figure 2.2: Simulated spectra of a CSP at 13 Gyr from the onset of the SFH (exponentially delayed with τ = 0.3 Gyr), with solar metallicity and SNR 2, 5, 10, 20 and 30, increasing form bottom to top. For each SNR, the blue curve is the starting BC03 model used for the simulation, while the red curve is the the simulated spectrum. The lower panel shows the behaviour of the SNR as a function of wavelength for a simulated spectra with SNR $= 30$ in the 6500 – 7000 Å window.

$\psi(t) \propto \tau^{-2}\ t\ exp(-t/\tau)$ and 13 different ages from the beginning of the star formation (going from 1 to 13 Gyr with step of 1 Gyr) as starting theoretical models. We assume solar metallicity ($Z = 0.02$) and a velocity dispersion σ = 200 km s^{-1}. We chose a short e-folding time scale ($\tau = 0.3$ Gyr) in order to reproduce as much as possible old ETGs spectra (Renzini, 2006). It is worth noting that our simulated spectra are also dust-free (i.e. $A_V = 0$ mag). To better quantify the code reliability, we also compute 10 simulations for each age, thus obtaining 130 spectra for each SNR (10 simulations $\times$ 13 models).

To fit the input simulated spectra, we create a spectral library containing 176 BC03 simple stellar population (SSP) spectra. We choose four different metallicities for the synthetic spectra ($Z = 0.004$, $Z = 0.008$, $Z = 0.02$, $Z = 0.05$) and ages going from 0.001 to 14 Gyr. In particular, to produce a well-sampled spectral library which would help in reconstruct the SFH of the input CSPs, we define a smaller time step (0.01 Gyr) for very young ages, to take into account the very different spectral shape of stellar populations younger than 1 Gyr; a larger (0.5 Gyr) time step is instead adopted for older SSPs. We fit the input spectra within the full range $3500 - 8500$ Å and, as required by STARLIGHT, we fix the normalization wavelength for the spectral fitting at the line-free

wavelength of 5520 Å, thus avoiding absorption features which could influence our results. We perform these fits in the two cases of masking or not the input spectral regions related to emission or depending on α-element abundances (all the masked regions are reported in Table 2.3), which are not modelled by the BC03 synthetic spectra. Throughout the chapter, we mainly discuss the results obtained in the second case, since it is more general and easily comparable with the literature.

Table 2.3: Spectral regions masked in the fit.

Emission lines	[O II]3727 [O III]5007 [O I]6302 H_ϵ H_δ H_γ H_β H_α HeI5877 [Ne III]3868 [N II]6584 [S II]6712
α-element dependent lines	[CN1-CN2] Ca4227 G4300 Mg_1 Mg_2 Mgb Fe4383 Fe5335

2.3.1 Definition of the evolutionary properties

Since our tests on STARLIGHT are based on the comparison between input and output quantities, a consistent and accurate definition of them is necessary. In particular, we use mass-weighted properties, instead of light-weighted ones, since they allow to be almost independent of the choice of the normalization wavelength for the fit. Furthermore, mass-weighted quantities have the advantage to offer a more direct probe to the integrated SFH being not biased towards younger ages. Indeed, it is well-known that younger populations can dominate the luminosity of a stellar population, even when they contribute very little to the mass (Trager et al., 2000, Conroy, 2013). Throughout this work, we also compare the retrieved mass-weighted and light-weighted properties (see Sect. 2.5).

- *Age*. Following the definition given by Gallazzi et al. (2005) and Barber et al. (2007), we define the input ages as mass- and light-weighted ages, according to the following equations:

$$\langle t \rangle_{mass} = \frac{\int_0^t SFR(t-t')M(t')t'\mathrm{d}t'}{\int_0^t SFR(t-t')M(t')\mathrm{d}t'}.$$

$$\langle t \rangle_{light} = \frac{\int_0^t SFR(t-t')f_\lambda(t')t'\mathrm{d}t'}{\int_0^t SFR(t-t')f_\lambda(t')\mathrm{d}t'},$$

  where $M(t')$ is the stellar mass provided by an SSP of age t', f_λ is the flux at a given wavelength[2] of an SSP of age t' and $SFR(t-t')$ is the star formation rate at the time $(t-t')$, when the SSP was formed.

[2]Our normalization wavelength is fixed at 5520 Å

These equations account for the fact that a composite stellar population can be treated as the sum of many SSPs of different age. Thus each SSP, with a certain age t', contributes to the global mass- (light-) weighted age of the CSP according to its mass (flux) and to the SFR at the time of its formation.
About the output quantities, we define the retrieved output mass- and light- weighted ages by means of the mass- and light-fraction population vectors, according to the equations:

$$\langle t \rangle_{mass} = \sum_j age_j \cdot m_j \ , \tag{2.10}$$

and

$$\langle t \rangle_{light} = \sum_j age_j \cdot x_j \ , \tag{2.11}$$

where age_j is the age of the model component j, while m_j and x_j are its fractional contribution to the best fit model, respectively, provided by the STARLIGHT code.

- *Age of formation*. Starting from the output mass-weighted ages, we define the "age of formation" age_f (i.e. look-back time) of the analyzed galaxies as:

$$age_f = age_{model} + \Delta t \ , \tag{2.12}$$

where age_{model} is the original age of each model in our spectral library and $\Delta t = [age_U(z = 0) - age_U(z)]$ is the difference between the age of the Universe today and the age of the Universe at the redshift of the galaxy. In other words, age_f allows to consistently scale all the derived ages to $z = 0$.

- *Metallicity*. As said above, we consider solar metallicity ($Z = 0.02$) for the input simulated spectra; we define the output metallicities only as mass-weighted metallicities, employing the following equation:

$$\langle Z \rangle_{mass} = \sum_j Z_j \cdot m_j \ , \tag{2.13}$$

where Z_j is the metallicity of the model component j.

- *Star formation histories.* In general, considering that a CSP can be viewed as the sum of many SSPs (see eq. [1] in Bruzual & Charlot, 2003), the SFH of a stellar population can be understood as the fraction of stellar mass produced as a function of time in the form of SSPs. For this reason, the mass fractions m_j provided by STARLIGHT plotted as function of the library SSPs ages can be considered as a direct proxy for the output SFH. Starting from this, we use the following equation to define the input SFH:

$$SFH_{in} = \frac{SFR(t - t')M(t')\mathrm{d}t'}{\int_0^t SFR(t - t')M(t')\mathrm{d}t'} \ ,$$

where $\mathrm{d}t'$ was introduced to make SFH_{in} dimensionless, just like the output m_j.

- *Extinction and velocity dispersion*. Extinction and velocity dispersion are direct STARLIGHT output, so we compare them directly with the chosen input ones (i.e. $A_V = 0$ mag and σ = 200 km s^{-1}).

2.3.2 Results from the simulations

Age and metallicity

The two top panels of Fig. 2.3 illustrate the results concerning ages and metallicities. In this figure we show the median differences, averaged on all the realized simulations at each SNR, between the output and the input quantites as a function of the mean SNR of the simulated spectra, together with their median absolute deviation (MAD)[3], calculated at each SNR on the available simulations. We found that the differences and the relative dispersions effectively decrease with increasing SNR, as expected. In the case of the ages, only a small systematic shift of about +0.3 Gyr is present at SNR $\gtrsim$ 10. To better quantify our results, we defined the percentage accuracy as the ratio between the dispersion of a given quantity on all the simulations at a given SNR and its true value, calculating the minimum SNR at which the input properties are retrieved with a percentage accuracy higher than $\sim$ 10 %.
We find minimum SNR values of $\sim$ 18 for ages and $\sim$ 9 for metallicities. Table 2.4 lists the and the median dispersions (together with their percentage values) which we find in the case of SNR $= 100$, which is close to the typical SNR of the median stacked spectra which we are going to analyze in Sect. 2.4.1 (results for SNR $=$ 20 are also shown to facilitate the comparison with literature).
We find that, masking the spectral regions associated with emission or depending on α-element abundances, the SNR needed to reach a percentage accuracy larger than the 10% increases to $\sim$ 40 for mass-weighted ages, remaining unchanged for the other quantities. We ascribe this effect to the fact that we are exluding from the fit some spectral regions which are well-known age indicators (e.g. the $H\beta$ line, see Burstein et al., 1984, Worthey et al., 1994).

Dust extinction and velocity dispersion

Dust extinction and velocity dispersion are retrieved with a percentage accuracy higher than the 10 % for SNR $\gtrsim$ 7 and $\gtrsim$ 3, respectively, as illustraded in the two lowest panels of Fig. 2.3 and reported in Table 2.4. The results are in agreement with the ones obtained by Choi et al. (2014), who used another full-spectrum fitting code (developed by Conroy & van Dokkum, 2012) and by Magris et al. (2015), who adopted the STARLIGHT code itself. Indeed, these authors found that age, metallicity, velocity dispersion and dust extinction are recovered without significant systematic offsets starting from SNR $\gtrsim$ 10. In particular, for a SNR of 20, their median percentage shifts are $\lesssim$ 10 % on age and metallicity (Choi et al., 2014) and $\sim$ 8 % on σ (Magris et al., 2015), while their dispersions are $\lesssim$ 10 % on age and metallicity (Choi et al., 2014) and $\sim$ 15 % on σ (Magris et al., 2015). All these values are in agreement with ours at the same SNR (see Table 2.4).
It is worth noting that, if we mask the spectral regions listed in Table 2.3, similar SNR

[3]Given an ensemble of data X_i, the median absolute deviation is defined as: MAD $= 1.48 \times median(|X_i - median(X_i)|$, see Hoaglin et al. (1983).

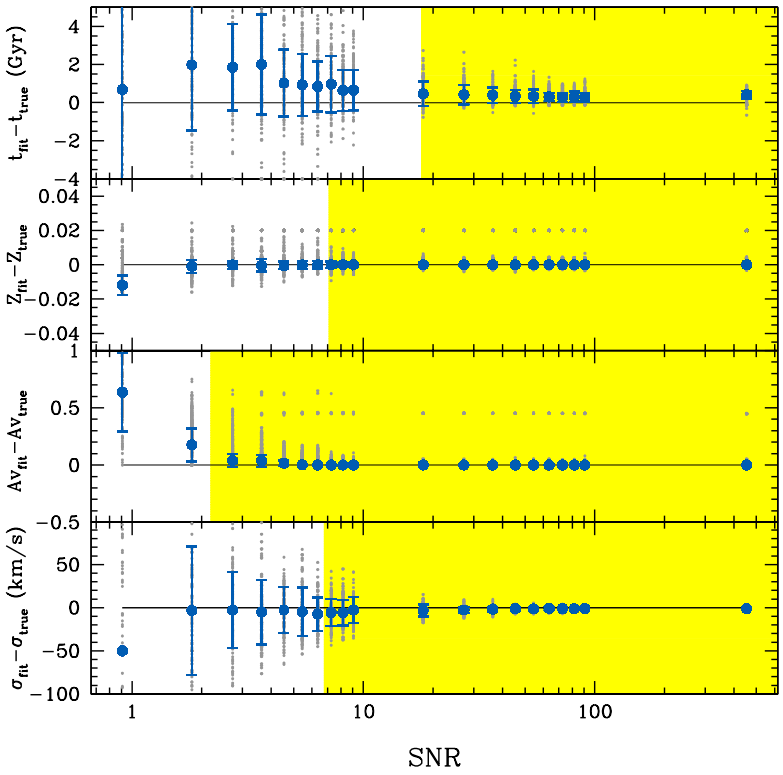

Figure 2.3: Retrieved ages, metallicities, dust extinctions and velocity dispersions as a function of the mean SNR of the input spectra. Blue filled circles are the differences, averaged on all the computed simulations (i.e. 10 × 13 models), between the ouptut and the input mass-weighted ages, mass-weighted metallicities, dust extinctions and velocity dispersions (from top to bottom); blue vertical bars are the median absolute deviations (MAD) on all the computed simulations; grey points are the differences derived from each individual simulation; yellow shaded regions in each panel indicate the minimum SNR from which the accuracy of the input retrieving is better than 10 %.

of $\sim$ 3 and $\sim$ 8 are needed to recover dust extinction and velocity dispersion with a percentage accuracy better than 10 %, respectively.

Star formation histories including a single CSP

To quantify the accuracy with which the SFHs are retrieved, we calculate the percentage of mass gathered around the peak of the SFH, comparing the results with the theoretical expectations, as illustrated in Fig. 2.4. Here, the case of a SNR $=$ 50 CSP input spectrum at four different ages from the onset of the SFH is shown. In particular, we find that the theoretical exponentially delayed SFH assumed for the input spectra (rebinned at the age step of our SSP library models) is narrow, encompassing $\sim$ 100 % of mass within an age interval going from $-$ 1 Gyr to $+$ 0.5 Gyr around its maximum. In comparison, for SNR $\gtrsim$ 10, the retrieved SFHs appear slightly broader with respect to the theoretical one. Indeed, $\sim$ 80 % of mass is gathered within [$-$ 1; $+$ 0.5] Gyr for CSPs younger than 5 Gyr, and an even larger age interval of [$-$ 1.5; $+$ 1] Gyr is necessary to get this same mass percentage in the case of older populations. This dependence is illustrated in a

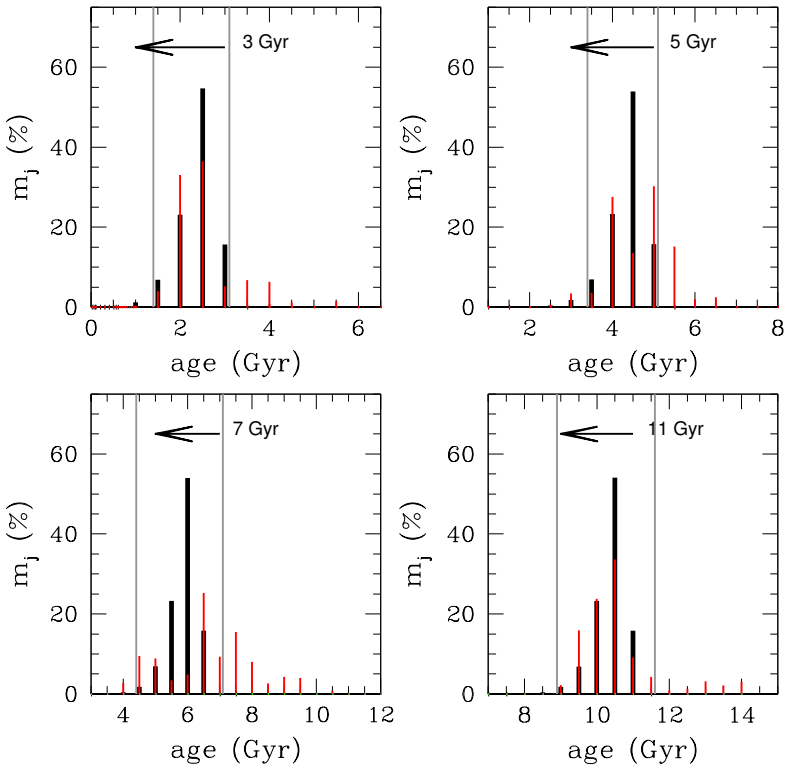

Figure 2.4: Recovery of star formation histories. The four panels show a CSP at 3, 5, 7 and 11 Gyr from the onset of the SFH. Black vertical lines represent the exponentially delayed SFH ($\tau = 0.3$ Gyr) assumed for the input spectra (rebinned according to the age step of our library models), while vertical lines represent the output SFH; horizontal arrows indicate the time from the beginning of the SF (i.e. 3, 5, 7 and 11 Gyr, respectively), while grey vertical lines mark the asymmetric age ranges around the SFH peak defined in the text for CSPs younger or older than 5 Gyr (i.e. $[-1; +0.5]$ and $[-1.5; +1]$, respectively).

more general way in Fig. 2.5, which shows the median mass fractions gathered around the SFH peak as a function of the mean SNR of the simulated spectra, for four CSPs. It is possible to note that CSPs older than 5 Gyr require larger age intervals around the SFH maximum to gather the same mass percentage as younger stellar populations. However, since a significant percentage of mass ($70 - 80$ %) is always reached within $\sim$ 1 Gyr from the peak of the SFH at any age, we conclude that the full-spectrum fitting succeeds in reproducing the input SFH for SNR $\gtrsim$ 10. Finally, we find that STARLIGHT does not have any bias toward young ages, since, at any SNR, no mass is gathered at ages younger than 0.5 Gyr, except in the case of the youngest CSP (these results are valid also when the mask is applied to the input spectra). To summarize, from our tests we can conclude that the full-spectrum fitting with STARLIGHT is reliable if SNR $\gtrsim$ 10 – 20 are considered. These SNRs are lower or equal than the ones of typical SDSS individual spectra (i.e. $\sim$ 20) and well below the typical SNR of stacked spectra, which are mainly used for high redshift studies (see Sect. 2.4.2).

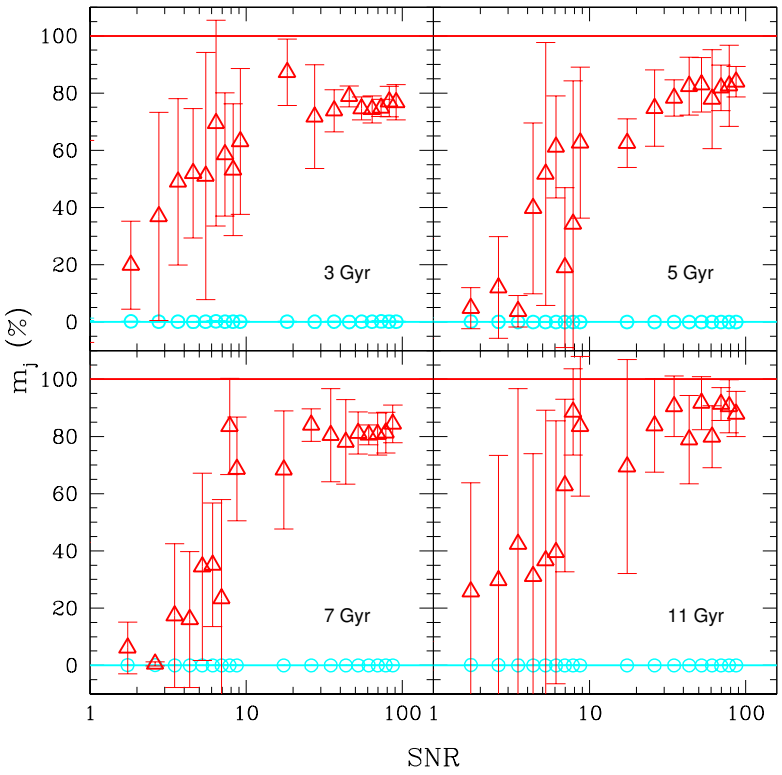

Figure 2.5: Recovery of star formation histories. The four panels show a CSP at 3, 5, 7, and 11 Gyr from the onset of the SFH. In the two top panels, red triangles indicate the median mass fractions retrieved within $[-1; +0.5]$ Gyr from the SFH peak; in the two bottom panels, they are the median mass fractions within $[-1.5; +1]$ Gyr (as described in the text). In all four panels, cyan circles are the median mass fractions relative to stellar populations younger than 0.5 Gyr, while red and cyan horizontal lines mark the expected mass fraction within the defined age ranges and below 0.5 Gyr, respectively.

Table 2.4: Median shift and dispersion from the simulation of ETGs spectra, for SNR $= 20$ and 100 and BC03 spectral synthesis models.

SNR	$\langle t \rangle_{mass}$ (Gyr)		Z		A_V (mag)		σ (km s^{-1})	
	shift	disp	shift	disp	shift	disp	shift	disp
20	0.5 (10 %)	0.6 (10 %)	$\lesssim 10^{-3}$ ($\lesssim 1$ %)	$\lesssim 10^{-3}$ (3 %)	$\lesssim 10^{-3}$	$\lesssim 10^{-3}$	-3.3 (4 %)	6.6 (7 %)
100	0.3 (3 %)	0.3 (3 %)	$\lesssim 10^{-3}$ ($\lesssim 1$ %)	$\lesssim 10^{-3}$ ($\lesssim 1$ %)	0.0001	$\lesssim 10^{-3}$	-1.02 (2 %)	1.3 (1 %)

More complex star formation histories

Since the star formation histories of galaxies (ETGs included, e.g. De Lucia et al., 2006, Maraston et al., 2009) can be stochastic and include multiple bursts, we also verify the full-spectrum fitting capabilities to retrieve more complex SFHs. In particular, we take an 11 Gyr old composite stellar population with an exponentially delayed SF ($\tau = 0.3$

Gyr) as the main SF episode (this age is compatible with the age of the Universe at $z \sim 0.15$, which is the median redshift of our sample, see Sect. 2.4.1). We then define more complex SFHs by combining this single CSP with a burst of SF at different ages (5, 6, 7 Gyr) and with different mass contributions (3, 5, 10 %). In all cases, we consider a solar metallicity for the main SF episode and, according to the results of Maraston et al. (2009), a subsolar metallicity ($Z = 0.004$) for the later one. We do not mask any spectral feature of the input spectra, we assume $A_V = 0.1$ mag for the two components and apply a velocity dispersion of 200 km s^{-1}. We show the results for a SNR of 80, which matches the typical SNR of the SDSS median stacked spectra analyzed in the following (see Sect. 2.4.1). Useful information can be derived from the comparison between the output SFH obtained from these input simulated spectra and the one provided when the single CSP alone is taken as input SFH. Fig. 2.6 shows that the single CSP alone is well recovered by the full-spectrum fitting. In particular, ~ 80 % of the stellar mass is retrieved within ~ 1 Gyr from the SFH peak. When a burst is added to this major episode of SF, the full-spectrum fitting is able to recognize the presence of a more complex SFH, as indicated by the tail appearing at smaller ages, and the total mass percentage of the later burst is retrieved within 1 Gyr from the expected age. However, we note that the main episode of SF is spread on a time interval longer than expected, and 50 % of the stellar mass is retrieved around ~ 1 Gyr from the SFR peak. We also find that, in this case, the mean properties of the global stellar population are well retrieved, with a percentage accuracy larger than 10 % starting from SNR ~ 15 for age, ~ 7 for metallicity, ~ 20 for A_V, ~ 8 for σ and that the metallicities of the two SF episodes are separately recovered. These SNRs are well below the typical ones of the stacked spectra analyzed in the following Sections.
In Fig. 2.7, we analyze the recovery of more complex SFHs as a function of the age and the mass contribution of the later SF burst. In particular, we find that the SFH tail, indicative of the presence of more recent SF episodes, arises for bursts happening $\gtrsim 6$ Gyr after the main SF event and contributing in mass by $\gtrsim 5$ %. Therefore, under these conditions, the full-spectrum fitting is able to recognize the SFH complexity. Furthermore, if mergers have played a role in the galaxy star formation history, these tests suggest that our method would be sensible to variations in SFR produced by mergers among galaxies of different age, but it is intrinsically not able to discern whether or not mergers among galaxies of similar age (coeval mergers), which increase stellar masses and sizes leaving the shape of the SFH unchanged, occurred during the galaxy evolution to build galaxy mass.

2.3.3 Testing different stellar population synthesis models

Having adopted BC03 models to set up both the input simulated spectra and the spectral library, in this Section we verify if this choice can affect the results. This is a simple consistency check to verify the full-spectrum fitting capabilities to retrieve the galaxy evolutionary properties starting from the same input spectra. With this aim, using the procedure described in Sect. 2.3 we simulate, starting from BC03 spectra, 13 simple stellar population (SSP) spectra with solar metallicities and ages going from 1 to 13 Gyr with step of 1 Gyr, within the same SNR range defined in Sect. 2.3, and we fit them with a spectral library of MS11 SSPs models, which are defined in the wavelength range $3200 - 9300$ Å, are based on the STELIB stellar spectra library (Le Borgne et al., 2003), have a resolution of 3 Å, and assume a Kroupa IMF (Kroupa, 2001). We show in Fig. 2.8 the recovery of age, metallicity, velocity dispersion and dust extinction, in analogy with Fig. 2.3. Also in this case, the percentage accuracy of 10 % is reached at similar

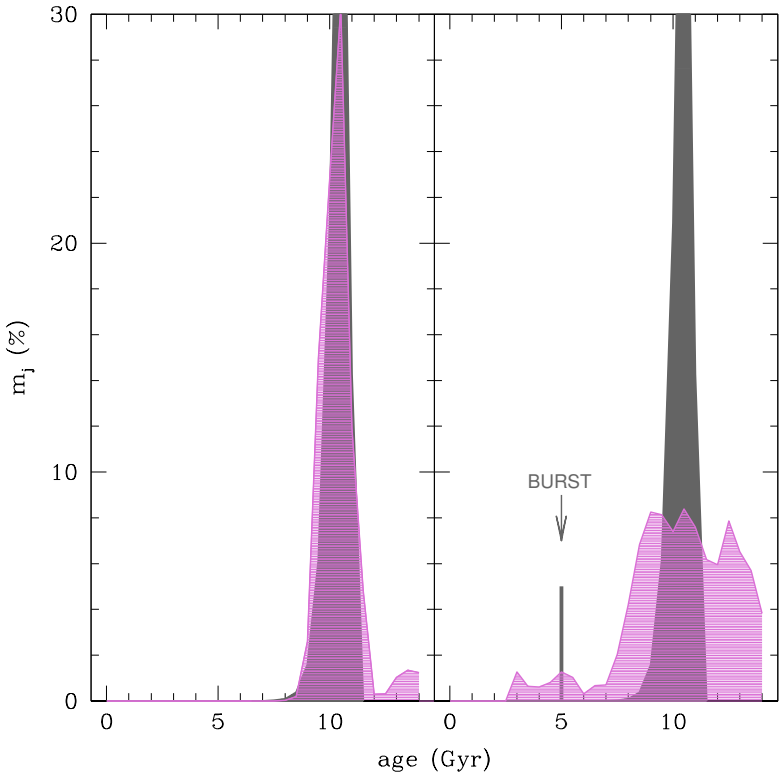

Figure 2.6: Retrieving of more complex SFH. Left panel: output SFH (pink curve) obtained when an input SFH (grey curve) including only a single CSP is considered; right panel: output SFH (pink curve) obtained when an input SFH (grey curve and vertical line) including a single CSP plus a later burst (which happens 6 Gyr after the main SF episode and contributes to the 5 % in mass) is considered.

SNR, which are $\sim$ 5 for age, $\sim$ 7 for velocity dispersion and $\sim$ 3 for dust extinction, while metallicity is retrieved with basically no bias at every SNR. However, as it is possible to note, a difference between the retrieved mass weighted ages and the true ones is present also at high SNR. This overestimation can be explained by the fact that, due to a different treatment of the TP-AGB phase and of the convective overshooting in the stellar interiors, MS11 models are on average bluer than BC03 ones (see Maraston et al., 2006 for further details). This implies that, for the same metallicity, older MS11 models are chosen to best-fit BC03 input spectra, to compensate the bluer colors.

To avoid biases against MS11 models, we also fit an ensamble of 13 MS11 simulated spectra with a spectral library made up of MS11 models themselves (this test is performed using MILES - see Sánchez-Blázquez et al., 2006 - stellar spectra both for the input and the library synthetic models). For computational feasibility, we create in this case a less extended grid of SNR for the input simulated spectra and, to be consistent with the results shown for BC03 models, we do not adopt the mask for the input spectra. In this case, we find that the evolutionary properties are retrieved with a percentage accuracy larger than the 10 % starting from a SNR of $\sim$ 25 for mass-weighted ages, $\sim$ 15 for metallicities, $\sim$ 30 for dust extinction and $\sim$ 6 for velocity dispersion. These values are in general higher than the ones found using BC03 models but, however, it is

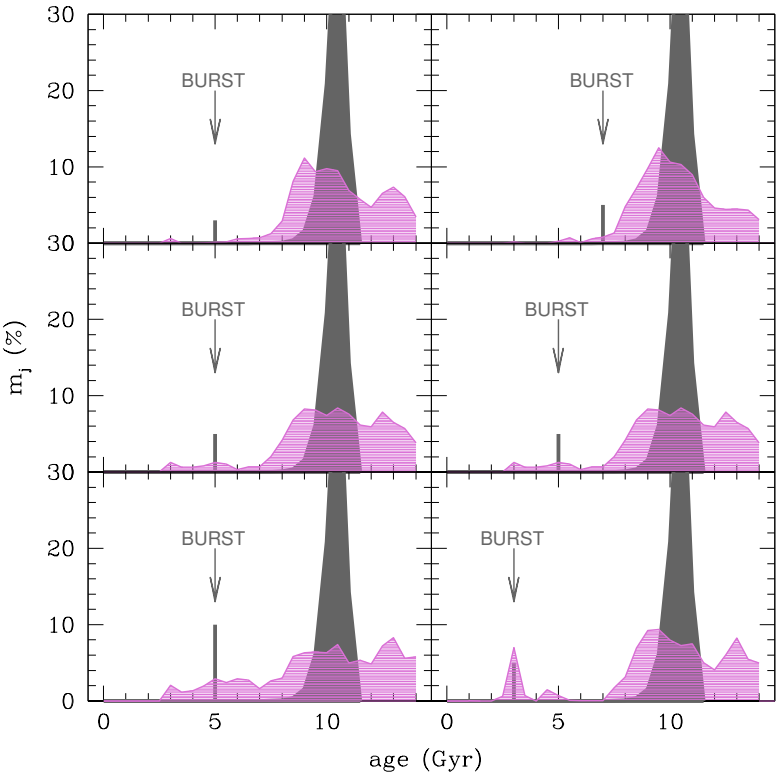

Figure 2.7: Retrieving of more complex SFHs as a function of the age and the mass contribution of the later burst. Left panels show the output SFH (pink curves) obtained when the input SFH (grey curves and vertical lines) includes a single CSP plus a later burst happening 6 Gyr after the main SF episode and contributing in mass by 3, 5 and 10 % (from top to bottom). Right panels show the output SFH (pink curves) obtained when the input SFH (grey curves and vertical lines) includes a single CSP plus a later burst of SF contributing in mass by 5 %, and happening 4, 6, 8 Gyr after the main SF event (from top to bottom).

important to note that they are below the ones of the median stacked spectra analyzed in the following Sections (see Sect. 2.4.1).

2.4 Application to Sloan Digital Sky Survey data

The Sloan Digital Sky Survey or SDSS is a major multi-spectral imaging and spectroscopic redshift survey which uses a dedicated 2.5-meter Telescope at Apache Point Observatory, New Mexico, and exploits two advanced technologies: optical fibers and CCDs. The SDSS has been one of the most successful surveys in the history of astronomy. It has created the most detailed three-dimensional maps of the Universe ever made, with deep multi-color images of one third of the sky, and spectra for more than three million astronomical objects. The SDSS-DR6, from which we selected the data analyzed in this Chapter, spanned $\sim 9583 deg^2$, providing photometry of ∼800000 objects, in the u, g, r, i, z observational bands. The obtained spectra are extracted with a petrosian magnitude $r < 17.77$ and their wavelength coverage goes from 3800 to 9200 with a resolution $\lambda/\Delta\lambda$ of $\sim$ 1800 – 2200. This data release contains 20% more data

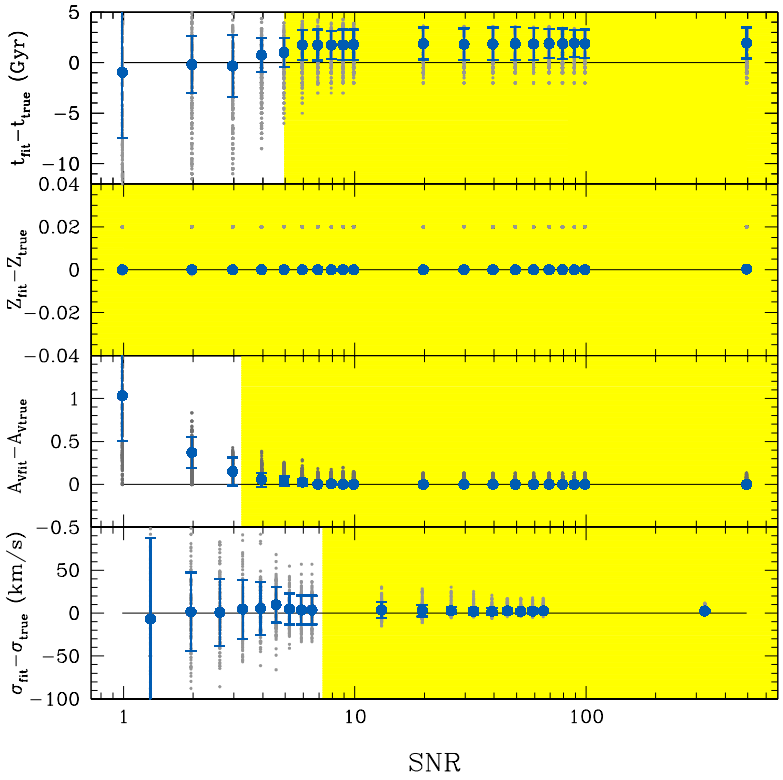

Figure 2.8: The same of Fig. 2.3, but using the MS11 spectral library to retrieve the evolutionary properties.

than the previous ones, provides revised photometric calibration for the imaging data, an improved wavelength and flux calibration for spectra and, above all, higher spectral resolution.

2.4.1 The sample of local early-type galaxies

We analyze a sample of 24488 very massive and passive early-type galaxies with $0.02 \lesssim z \lesssim 0.3$. The restriction to the most passive ETGs is indeed very useful to investigate galaxy evolution, since it allows to address the galaxy mass assembly history in the very early epochs.
The adopted sample was already used by Moresco et al. (2011) (M11) (see this work for more details), who matched SDSS-DR6 galaxies with the Two Micron All Sky Survey (2MASS) (with photometry in the J, H and K bands) to achieve a larger wavelength coverage, thus obtaining better estimates of stellar masses from SED-fitting and photometric data. According to the criteria explained in M11, the analyzed galaxies have no strong emission lines (rest-frame equivalent width EW(Hα)> -5 Å and EW ([OII]λ3727) > -5 Å) and spectral energy distribution matching the reddest passive ETG templates, according to the Ilbert et al. (2006) criteria. Finally, the sample was cross-matched with the SDSS DR4 subsample obtained by Gallazzi et al. (2005), for which stellar metallicity estimates have been performed by means of a set of Lick absorption

indices (see Sect. 2.5.5). Moreover, to deal only with the most massive galaxies, only objects with $log(M/M_{\odot}) > 10.75$ were included in the sample (above this threshold, the galaxy number density is found to be almost constant up to $z \sim 1$, see Pozzetti et al., 2010) which, in addition, was splitted in four narrow mass bins ($\Delta log(M/M_{\odot} = 0.25$): $10.75 < log(M/M_{\odot}) < 11$, $11 < log(M/M_{\odot}) < 11.25$, $11.25 < log(M/M_{\odot}) < 11.5$ and $log(M/M_{\odot}) > 11.5$ (Table 2.5 reports the number of objects contained in each mass bin), in turn divided into various redshift bins of width $\Delta z \sim$ 0.02. It is worth noting that, on average, the difference of the median mass along the redshift range is negligible within the four mass slices in which our sample is divided, showing no significant evolution as a function of redshift (Moresco et al., 2011, Concas et al., 2017). In particular, Fig. 2.9 shows the mass-redshift distribution of the sample. For each mass bin, the median mass has only a very slightly increase with redshift. This trend, although weak, is due to the concurrence of a volume effect, which causes more massive galaxies (less numerous) to be detected only when larger volumes of the Universe are considered, and of a Survey magnitude limit effect, which causes less massive (i.e. less luminous) galaxies to be observed only at lower redshift. The gaps in the sample are due to the fact that galaxies with contamination from sky lines residuals were removed from the sample.
We also assess the morphology of the galaxies in our sample using the Sérsic index ρ_n (Sersic, 1968), which correlates with the morphology because objects with $n < 2.5$ are disky (Andredakis et al., 1995), while those with $n > 2.5$ are bulge-dominated or spheroids (Ravindranath et al., 2004). In particular, the values of ρ_n are taken from the NYU Value-Added Galaxy catalogue (Blanton et al., 2005), which contains photometric and spectroscopic information on a sample of $\sim 2.5 \times 10^7$ galaxies extracted from the SDSS DR7. From this check, we derive that $\sim$ 96 % of the analyzed galaxies are bulge-dominated systems.

2.4.2 Median stacked spectra

In order to increase the SNR of the input spectra, we work on the median stacked spectra derived for each mass and redshift bin. A stacked spectrum is produced by shifting each individual rest-frame spectrum, normalized to a chosen wavelength, to the rest frame and then by constructing, via interpolation, a grid of common wavelengths at which the median (or mean) flux is computed. In our sample, the median stacked spectra were obtained for each mass and redshift bin (see Sect. 2.4.1). We define the error on the median stacked flux as MAD/$\sqrt{N}$, where N is the number of objects at each wavelength. Before stacking them together, we normalized each individual spectrum at rest-frame 5000 Å, where no strong absorption features are present which could influence the final result. It is worth noting that the error on the final stacked spectrum was corrected in order to obtain more reliable values for the χ^2 distribution provided by the spectral fit. In particular, we readjusted the original error e_λ of the spectra making it comparable with the data dispersion of $(O_\lambda - M_\lambda)$ (where O_λ are the observed data, M_λ is the best fit model obtained from the first-round fit). After the error re-definition, the signal-to-noise ratios of the median stacked spectra are $\sim$ 80 (the error e_λ is, on average, increased by a factor of $\sim$ 7).
The main characteristics of the analyzed median stacked spectra are illustrated in Fig. 2.10, where also the fractional differences among the various spectra are shown to better visualize their differences as a function of wavelength. As it is possible to note, median stacked spectra are completely emission lines-free. Moreover, two clear observational trends are present, with spectra getting redder both with cosmic time and increasing mass. In the following, our aim is to investigate these observed trends by means of the

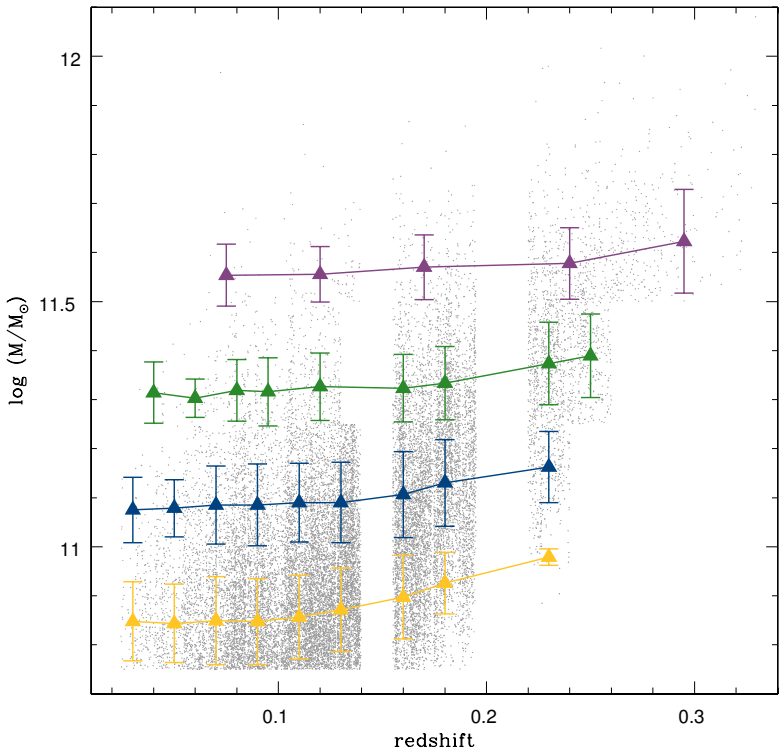

Figure 2.9: Mass-redshift relation of the adopted sample. Each grey point represents a galaxy; colored triangles and vertical bars represent the median masses and corresponding MADs of each mass and redshift bin (with mass increasing from yellow to violet).

full-spectrum fitting technique. In Sect. 2.6, we also verify that the use of stacked spectra does not introduce biases in the results, concluding that they can be employed at high redshift to increase the SNR of the observed spectra.

2.5 Evolutionary properties from the full-spectrum fitting of median stacked spectra

To infer the evolutionary and physical properties of our sample, we fit the median stacked spectra for each mass and redshift bin, mainly using BC03 spectra, but also exploiting a spectral library of MS11 STELIB models. In all cases, we fix the wavelength range for the spectral fitting to $3500 - 7000$ Å for all the mass and redshift bins, in order to avoid redshift-dependent results.Both the BC03 and the MS11 spectral libraries contain spectra with ages starting from 0.01 Gyr and not exceeding the age of the Universe at the redshift of the stacked spectrum itself[4].
We use the metallicities $Z = 0.004, 0.008, 0.02, 0.05$ for the BC03 library and $Z = 0.01, 0.02, 0.04$ for the MS11 one and we assume a Calzetti attenuation curve to account for the pres-

[4]This is a reasonable choice since our study is not aimed at inferring cosmology or cosmological parameters.

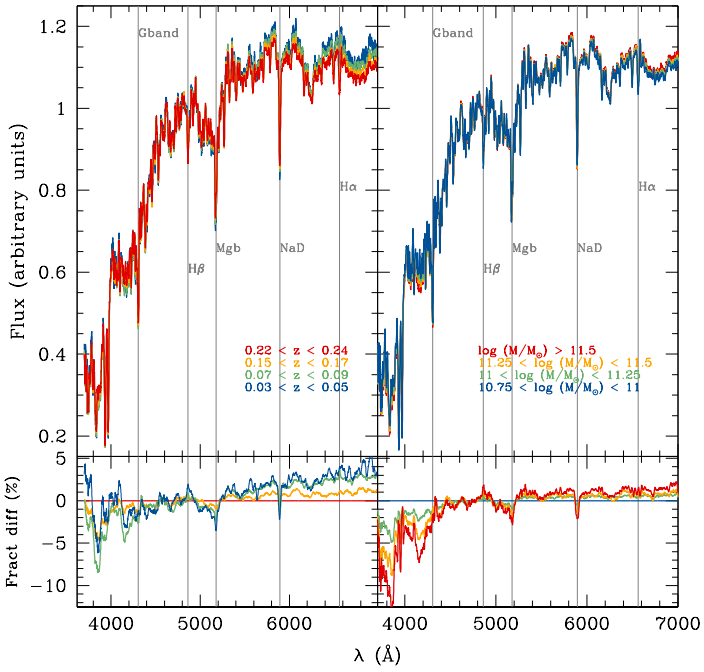

Figure 2.10: SDSS median stacked spectra for the sample of massive and passive ETGs. Left and right upper panels show, respectively, median stacked spectra with a fixed redshift ($0.15 \lesssim z \lesssim 0.19$) and different masses (with mass increasing from blue to red) and with a fixed mass ($11.25 < log(M/M_{\odot}) < 11.5$) and four different redshifts (0.04, 0.08, 0.16, 0.23) (with redshift increasing from blue to red). Lower panels illustrate the fractional differences (defined as $(f_i - f_{REF}/f_{REF}) \times 100$, where f_i is the flux of the i-th spectrum and f_{REF} is the reference one) among the stacked spectra as a function of wavelength. In particular, to show the redshift and the mass dependence we used as reference, respectively, the median stacked spectrum obtained for $11.25 < log(M/M_{\odot}) < 11.5$ and $0.07 < z < 0.09$, and the one corresponding to $10.75 < log(M/M_{\odot}) < 11$ and $0.15 < z < 0.17$. Vertical grey lines mark some of the best-known absorption lines.

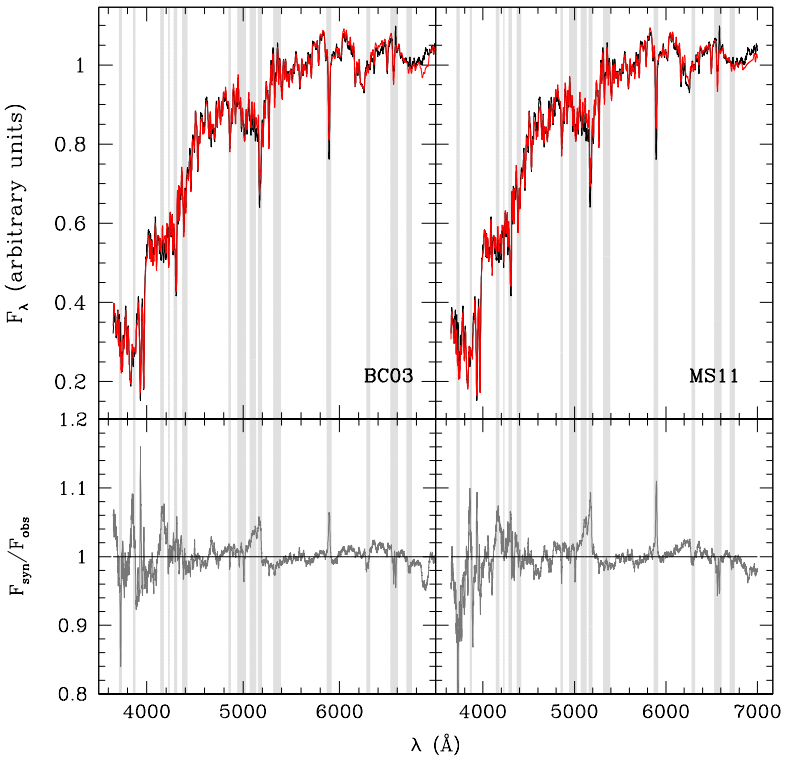

Figure 2.11: Typical output of the full-spectrum fitting procedure using BC03 (left) and MS11 (right) spectral synthesis models. In particular, we show the case of the median stacked spectrum derived for $11 < log(M/M_{\odot}) < 11.25$ *and* $z \sim 0.05$*. In the top panel the black curve is the observed spectrum, the red curve is the best fit model and grey shaded regions are the masked spectral regions (see Table 2.3). In the bottom panel the ratio of the best fit model spectrum to the observed flux is shown.*

ence of dust (Calzetti, 2001). Moreover, contrary to what did in Sect. 2.3, in both cases we mask the spectral regions of the input spectra which are associated with emission lines (Cid Fernandes et al., 2005) and α-element dependent lines (Thomas et al., 2003), since they are not modelled by BC03 and MS11 synthetic spectra (see Table 2.3 and grey shaded regions in Fig. 2.11).
As it is possible to note from Fig. 2.11, the best fit model produced by the spectral fitting matches correctly the input spectrum, both in the case of BC03 and MS11 models. The dispersion on the mean ratio between the synthetic and observed flux on all the not-masked pixels is $\lesssim 2\%$.
From the comparison between the observed and the synthetic spectra, signs of a residual emission in correspondence of the masked spectral regions can be noticed. The presence of this residual emission is discussed in Concas et al. (2017), who focus on the study of the $H\beta$ absorption line.

2.5.1 Error estimates

Throughout the data analysis, the uncertainties on the investigated evolutionary and physical properties are derived in three different ways, defined as follows:

- rms_{sim}: this is the dispersion derived in Sect. 2.3.2 at the typical SNR of the analyzed median stacked spectra (i.e. SNR$\sim$ 100);

- err_{100}: this error is derived by comparing the results obtained from computing 100 realizations of each median stacked spectrum within its error (defined in Sect. 2.4.2);

- rms_{set}: this dispersion is calculated by comparing the results obtained by changing some setting parameters of the spectral fit (e.g. the number of the masked spectral regions, the upper limit for dust extinction, the extension of the library in age or metallicity) (Citro Annalisa, master Thesis).

2.5.2 Ages

Using eq. (2.10), we derive the mass-weighted ages of our galaxies, illustrated in the upper panel of Fig. 2.12. Considering the observed properties of the median stacked spectra with mass and redshift illustrated in Fig. 2.10, we find an evolutionary trend, with mass-weighted ages increasing sistematically with mass (for a fixed redshift), as well as with cosmic time (for a given mass bin). In particular, ages vary from $\sim$ 10 to $\sim$ 13 Gyr, increasing by $\sim$ 0.4 Gyr from the lowest to the highest masses, in agreement with the observational trends shown in Fig. 2.10. The lower panel of Fig. 2.12 illustrates, instead, the retrieved light-weighted ages, which instead increase by $\sim$ 1 Gyr from the lowest to the highest mass. Light-weighted ages are younger than mass-weighted ones, with a difference of $\sim$ 0.6 Gyr in the lowest redshift bins and of $\sim$ 1 Gyr in the highest ones, on average (Table 2.6 lists the three uncertainties estimates rms_{sim}, err_{100} and rms_{set} derived for $< t >_{mass}$).
It is interesting to note that, even when the cosmological constraint is relaxed and the maximum allowed age for the spectral library models is pushed to 14 Gyr at all redshifts, the trend of the mass-weighted age with both mass and cosmic time still holds, and only in few cases the mass-weighted ages exceed the age of the Universe. Fig. 2.13 illustrates our mass-weighted ages as a function of the velocity dispersion (see Sect. 2.5.6). At $z < 0.1$, we find that they are compatible, within the dispersion ($\sim$ 25 %), with the relation derived by McDermid et al. (2015) from the analysis of the ATLAS^{3D} sample ($z \lesssim 0.1$ and $9.5 < log(M_{dyn}/M_{\odot}) < 12$) by means of the PPXF code (Cappellari & Emsellem, 2004). At $z \lesssim 0.06$, for a given velocity dispersion, our mass-weighted ages are instead older than the ones deduced by Thomas et al. (2010). This can be due to the fact that, differently from our approach, they analyzed a sample of $\sim$ 3600 morphologically selected galaxies (i.e. MOSES ETGs at $0.05 \leq z \leq 0.06$, see Schawinski et al., 2007), without restriction to the most passive objects and also to the fact that, using the Lick indices, they derive SSP-equivalent instead of mass-weighted ages.
It is also interesting to note that our average light-weighted ages for $z \lesssim 0.06$ are $\sim$ 11.6 Gyr for all of the four mass bins and that these values are in agreement with the ones obtained at similar redshifts by Conroy et al. (2014), who applied the stellar population synthesis (SPS) model developed by Conroy & van Dokkum (2012) to a sample of nearby ($0.025 < z < 0.06$) SDSS DR7 ETGs, with masses comparable to ours (i.e. $10.70 < log(M/M_{\odot}) < 11.07$).

The derived mass-weighted ages imply a very early epoch of formation. A further

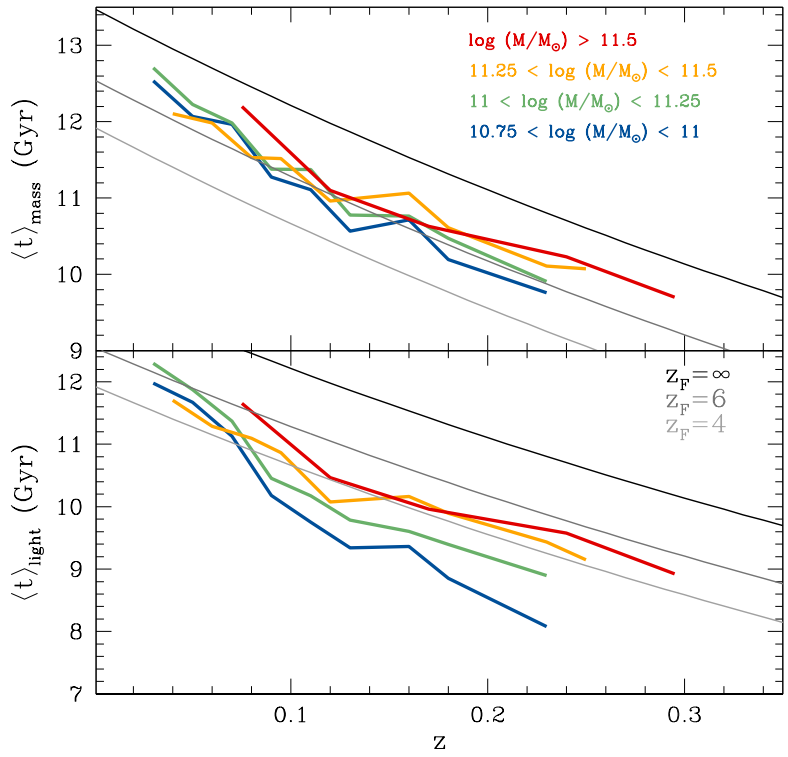

Figure 2.12: Mass-weighted (top) and light-weighted (bottom) age-redshift relations (for BC03 models). Stellar mass increases from blue to red. The black line is the age of the Universe, while grey lines are the age of galaxies assuming different formation redshifts.

confirmation of this comes from Fig. 2.14, which illustrates the ETGs mass-weighted ages of formation (see eq. 2.12) as a function of mass and redshift (in this case, the term $age_U(z)$ in eq. (2.12) is the age of the Universe at the redshift of each of the available median stacked spectra), together with the 1σ dispersions calculated from the 16th and 84th percentiles of the mass fraction cumulative distribution. As it is possible to note, the mass-weighted ages of formation are very high, with an increase of $\sim$ 0.4 Gyr from low to high masses. Taking into account the 1 σ dispersion on the SFHs, we also find that the slopes of the $age_f - z$ relations are compatible with zero, indicating that, at a fixed mass, the analyzed galaxies have similar z_F, especially in the highest mass bins. However, it is important to note that our main results concerning SFHs do not rely on the fact that galaxies in the same mass bin have similar formation epochs, since the spectral fits are realized separately on each mass and redshift bin.

Using MS11 models, we find the same trends of the mass-weighted age_f with mass and redshift. In particular, in this case age_f are only ~ 0.2 Gyr older than the ones provided by BC03 spectra, on average. In all two cases, the independence of age_f of redshift is also an indication that we are not biased towards young galaxy progenitors going to higher redshift, and thus that our sample is not affected by the so-called progenitor bias (van Dokkum & Franx, 1996).

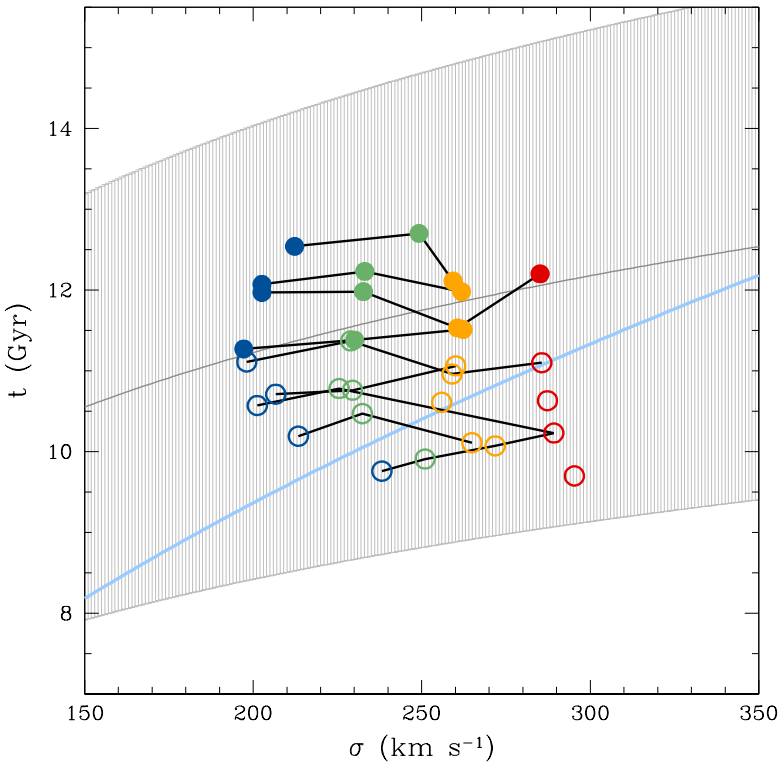

Figure 2.13: Mass-weighted ages as a function of the velocity dispersion σ for BC03 models (symbols are color-coded as in Fig. 2.12). Filled circles are the mass-weighted ages corresponding to $z < 0.1$, matching the redshifts analyzed by McDermid et al. (2015), with black curves linking the mass-weighted ages related to different mass bins but similar redshifts. The grey curve is the age – σ relation inferred by McDermid et al. (2015) with its dispersion (grey shaded region), while the light-blue curve is the Thomas et al. (2010) relation (its dispersion, not shown in the figure, is of the order of $\sim$ 60 %).

2.5.3 Star formation histories

In this Section we investigate the trend with mass of the SFHs by looking at the mass fractions provided by the full-spectrum fitting (m_j) as a function of the mass-weighted age of formation, age_f. In particular, we consider all the redshifts of a given mass bin together, in order to visualize the shape of the SFH as a function of mass. The behaviour of the m_j distribution is illustrated in Fig. 2.15, where asymmetric gaussians - constructed starting from the 50th (P50), 16th (P16) and 84th (P84) percentiles of the mass fraction distribution cumulative functions - are overplotted to the m_j to better visualize the distribution (P16 and P84 allow to compute the dispersion of the distribution within 1σ). Given a mass bin, P50 is the median on the P50 of all the available redshifts, while the asymmetric dispersions are defined as the median differences [P84 – P50] and [P50 – P16], averaged in the same way. Table 2.5 lists the calculated values for the four mass bins. To best retrieve the shape of the SFHs and minimize the dependence on possible

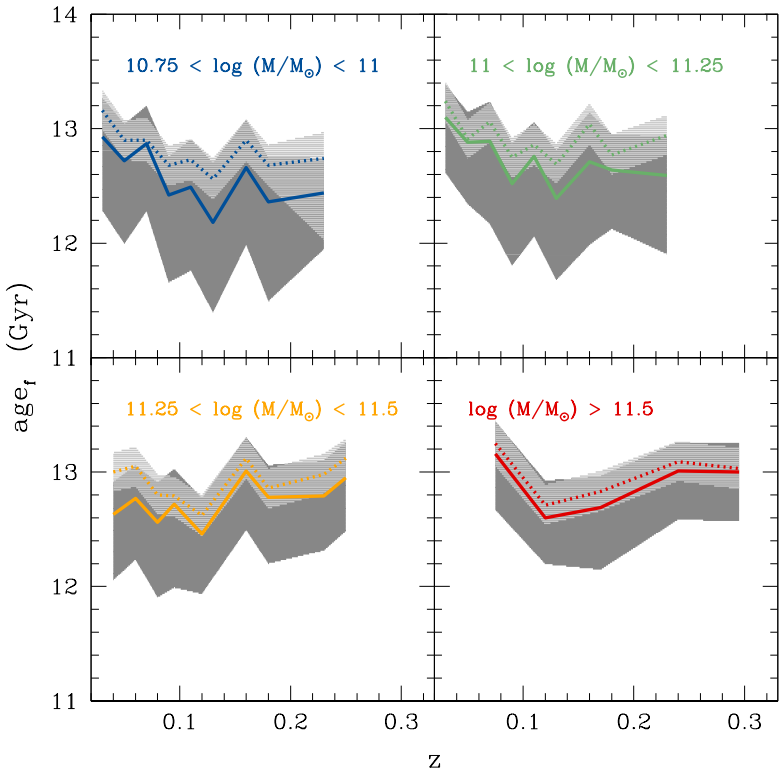

Figure 2.14: age_f-redshift relations for the four mass bins. Solid and dotted curves (color coded as in Fig. 2.12) are the ages of formation as a function of redshift referring, respectively, to BC03 and MS11 spectral synthesis models. Dark-grey and light-grey shaded regions are the 1σ dispersions calculated starting from the 16th (P16) and 84th (P84) percentiles of the mass fraction cumulative function for BC03 and MS11 models, respectively.

small differences in z_F, we decide to put the m_j distributions in phase, by synchronizing the P50 of each redshift bin to the median P50 of each mass bin, in order not to rely on the assumption that galaxies in a given mass bin have the same formation epochs.
From the figure it is possible to note that the median of the asymmetric gaussians slightly increases with mass and that the width of the gaussians decreases from low to high mass. In particular, we find that the width [P84 – P16] decreases from $\sim$ 1 Gyr to $\sim$ 0.7 Gyr from low to high masses, while P50 increases by $\sim$ 0.2 Gyr. MS11 models produce slightly higher P50, which increase by $\sim$ 0.1 Gyr with mass, and dispersions [P84 – P16] of ~ 0.35 Gyr, regardless of mass.

Considering these results and our largest uncertainty on age rms_{set} (see Table 2.6), the derived trends show that massive galaxies have already formed $\sim$ 50 % of the stellar mass by $z \gtrsim 5$ ($z \gtrsim 3$ if the ~ 0.5 Gyr systematic is taken into account, see Sect. 2.6). In addition, this percentage of mass is formed slightly earlier in more massive galaxies than in less massive ones, with the former also having shorter star formation histories than the latter (see Fig. 2.15 and Table 2.5).
We quantify the typical SFR of the analyzed galaxies defining, for each mass bin, the

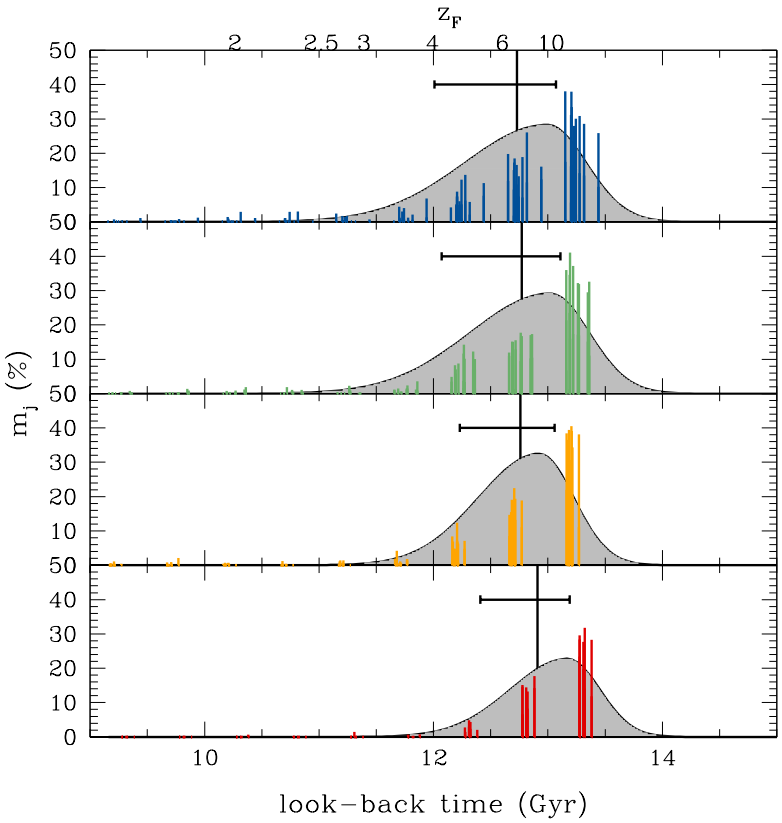

Figure 2.15: Mass fractions m_j as a function of look-back time for the four mass bins, with mass increasing from top to bottom (in the case of BC03 models). Colored vertical lines (color-coded as in Fig. 2.12) are the m_j obtained from the full-spectrum fitting for each mass bin, put in phase according to their P50. In each mass bin, black vertical lines mark the P50 of the distribution, obtained from data as an average on the P50 of all the redshift bins, while black horizontal lines are the median dispersions [P50 – P16] and [P84 – P50]. The corresponding asymmetric gaussians (grey) are overplotted to the m_j distributions. On the top of the figure, the z_F corresponding to each age_f are indicated.

quantity

$$\langle SFR \rangle_{68\ \%} = 0.68 \cdot M/\Delta t\ (68\ \%)\ M_{\odot}\ yr^{-1}\ , \tag{2.14}$$

basing on the assumption that the $68\ \%$ of stellar mass is formed whithin the $68\ \%$ time interval Δt around the peak of the SFH. We find that the typical SFRs increase for increasing mass from $\sim\ 50$ to $\sim\ 370\ M_{\odot}$ yr^{-1} (SFR $\sim\ 140 - 750\ M_{\odot}$ yr^{-1} for MS11 models).

The evolutionary picture emerging from the analysis of the star formation histories can be also deduced from Fig. 2.16, which illustrates the mass fraction relative to the stellar populations older or younger than 5 Gyr. Regardless of redshift and mass, we derive that $\lesssim\ 6\ \%$ of the stellar mass in our galaxies come from stellar populations younger than 5 Gyr ($\lesssim\ 20\ \%$ when we consider light fractions instead of mass fractions) and that this fraction decreases to $\lesssim 4\ \%$ and $\lesssim 1\ \%$ if we consider a threshold of 1 and 0.5 Gyr, respectively. Moreover, the old and the young mass fractions are specular to each other, with the young one decreasing with both mass ad cosmic time, contrary to the old one: this suggests that more massive galaxies assembled a higher fraction of their mass ear-

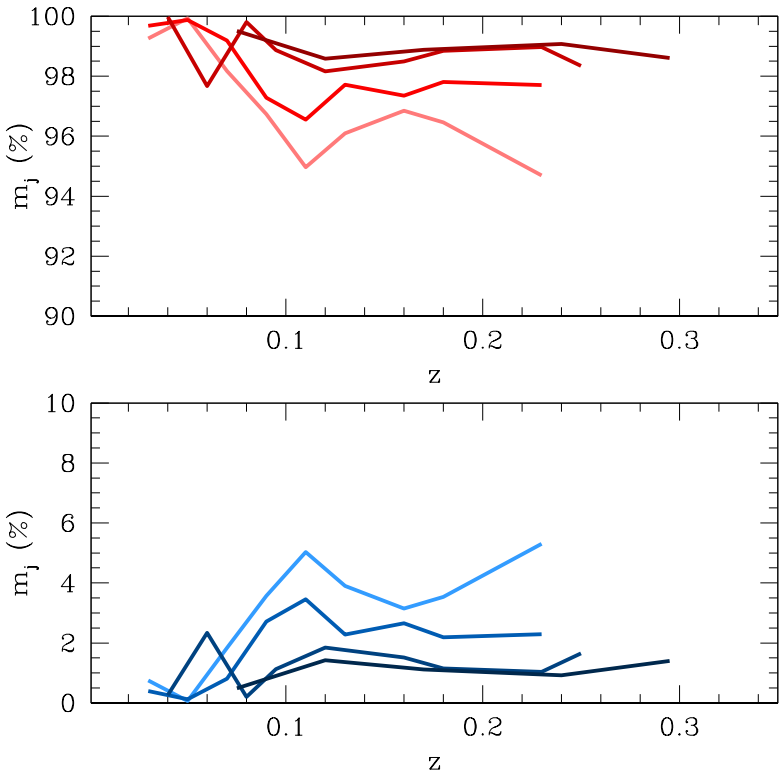

Figure 2.16: Mass fractions m_j recovered from the full-spectrum fitting as a function of redshift in the case of BC03 models. Red and blue curves refer, respectively, to stellar populations older and younger than 5 Gyr, with darker colors standing for higher stellar masses.

lier than less massive systems. The fact that the analyzed galaxies have not experienced significant bursts of star formation in recent times is also shown in Fig. 2.17 (it is worth noting that these bursts would be recognized by the full-spectrum fitting, as discussed in Sect. 2.3.2). MS11 spectral synthesis models confirm these trends, providing a similar low percentage of stellar mass below 5 Gyr (i.e. $< 7\ \%$) and an even smaller contribution ($< 0.1\ \%$) of the stellar populations younger than 1 Gyr to the total mass (which also implies slightly older mass-weighted ages).

Table 2.5: Number of galaxies, statistical, evolutionary and physical properties of the four mass bins of our sample (in the case of BC03 models).

$log(M/M_\odot)$	# Galaxies	P50 (Gyr)	[P84-P16] (Gyr)	τ (Gyr) [Expdel]	τ (Gyr) [Expdelc]	$\langle Z \rangle_{mass}$	A_V (mag)	σ (kms^{-1})
$10.75 - 11$	12462	12.73	1.06	0.44	0.80	0.028	0.13	208
$11 - 11.25$	8064	12.77	1.04	0.44	0.70	0.029	0.1	235
$11.25 - 11.5$	3004	12.76	0.83	0.40	0.65	0.030	0.05	261
> 11.5	990	12.91	0.7	0.37	0.60	0.030	0.03	288

2.5.4 The shape of the star formation history

The SFH of individual galaxies has been often approximated by simple declining exponential functions $SFR(t) \propto exp(-t/\tau)$, where t is the galaxy age and τ is the star formation timescale (*Expdel* hereafter). Despite the success of these models to estimate the stellar masses of nearby spiral galaxies (Bell & de Jong, 2001), recently many results have began to highlight their limitations, especially when applied to higher redshift samples (Papovich et al., 2001, Shapley et al., 2005, Stark et al., 2009). Since then, other functional forms have been considered: for example, delayed-τ (exponentially delayed) models (with τ being the SF timescale), in which $SFR(t) \propto \tau^{-2} t\ exp(-t/\tau)$ (Bruzual A. & Kron, 1980, Bruzual & Charlot, 2003, Moustakas et al., 2013, Pacifici et al., 2013) or 'inverted-τ' models of the form $SFR(t) \propto exp(+t/\tau)$ (Maraston et al., 2010, Pforr et al., 2012) have been suggested to be a better way to represent the SFH of massive galaxies at intermediate or high redshift.
In this Section, we test if these two analytical forms are able to describe the SFH of massive and passive, low redshift ETGs. We also introduce the parametric function (*Expdelc* hereafter):

$$SFR(t) = \tau^{-(c+1)} t^c\ exp(-t/\tau)\ , \tag{2.15}$$

with c being a real number ranging from 0 to 1 with steps of 0.01, which parametrizes how fast the SFR rises at early ages.

The results are shown in Fig. 2.18, in which we illustrate the SFR derived from the mass fractions m_j as a function of the look-back time (age of formation), together with the delayed-τ and the inverted-τ models.
For each mass and redshift bin, the observed SFRs are derived using the following equation:

$$SFR_j = \frac{m_j \times M}{\sum_j m_j \times 0.5 \times 10^9 \times (1-R)}\ (M_\odot\ yr^{-1}), \tag{2.16}$$

where m_j are the mass fractions obtained from the full-spectrum fitting, $\sum_j m_j$ is the sum of the mass fractions of each mass and redshift bin, M is the total stellar mass, the term 0.5×10^9 yr is the time step of our spectral library and R is the 'return fraction', which represents the fraction of mass which is returned to the ISM by supernovae-driven winds and mass losses. In particular, considering both the mass weighted ages of our galaxies (i.e. $\sim\ 10-13$ Gyr) and the Chabrier IMF assumed in this work, we fix the value of R to 0.5 (see Bruzual & Charlot, 2003).
To perform the data-to-model comparison in the case of exponentially delayed SFHs, we define a grid of models $Expdel(\tau)$ with different SF timescales τ (going from 0.2 Gyr to 0.7 Gyr with step of 0.01 Gyr). Then, by minimizing the quadratic differences

$$\sum_j [Expdel(\tau, age_{f\,j}) - SFR_j]^2\ , \tag{2.17}$$

and

$$\sum_j [Expdelc(\tau, c, age_{f\,j}) - SFR_j]^2\ , \tag{2.18}$$

we find the τ and c which best reproduce the observed SFH in each mass and redshift bin, by fixing the P50 of data and models. Then, as already done in Sect. 2.5.3 for the m_j distribution, we put the results obtained for all the redshifts in a given mass

bin together, also putting their P50 in phase according to the median P50. The median values of τ and c on all the redshifts are thus taken as the best fit parameters for that given mass bin (see Fig. 2.18). We find that the standard delayed-τ models with shorter τ's are needed to reproduce the observations for increasing mass. In particular, a value $\tau = 0.44$ (with a dispersion of ± 0.02 Gyr) is compatible with the SFH of less massive galaxies ($10.75 < log(M/M_{\odot}) < 11.25$), while slightly shorter values (i.e. $\tau = 0.37$, with a dispersion of ± 0.02 Gyr) should be adopted to match the SFH at higher masses ($log(M/M_{\odot}) > 11.5$). The $Expdelc$ parametric form provides a much better fit to the data, with quadratic differences which are smaller even by 2 order of magnitude than in the case of the *Expdel* form. Furthermore, slightly higher values of τ are found as best fit, decreasing for increasing mass from 0.8 Gyr (with a dispersion of $\pm$ 0.1 Gyr) to 0.6 Gyr (with a dispersion of $\pm$ 0.1 Gyr), while the best fit c is ~ 0.1 (with a dispersion of $\pm$ 0.05) regardless of mass, and reproduces the very fast rise of the SFR (see Table 2.5). The derived values are compatible with the SF timescale $\Delta t \sim 0.4$ Gyr derived by Thomas et al. (2010) from the measure of the α-element abundance[5]. However, it needs to be mentioned that, also using the $[\alpha/Fe]$ ratios, Conroy et al. (2014) obtained longer SF timescale ($\Delta t \sim$ 0.8 Gyr) for similar masses. In addition, it is worth noting that, as shown in Sect. 2.3, the full-spectrum fitting tends to broaden the SFH for old stellar populations in the case of BC03 models (see Fig. 2.2) and thus the derived SF timescales could be effectively overestimated.
However, in agreement with the BC03 analysis, also the best fits with MS11 models confirm the short e-folding times, which are $\tau \sim 0.25$ Gyr (with a dispersion of ± 0.0016 Gyr), regardless of mass ($\tau \sim 0.39$ Gyr – with a dispersion of $\pm$ 0.03 – and $c \sim 0.1$ – with a dispersion of $\pm$ 0.02 – in the case of $Expdelc$, regardless of mass).
Fig. 2.18 also illustrates 'inverted-τ' models with $\tau = 0.3$ Gyr, normalized at the SFR maximum in each mass bin. The increased difficulty in matching these models with the observations may be linked to our poor sampling of the SFH at very early ages.
Fig. 2.18 confirms that the SFHs derived from our analysis are smooth and concentrated at high redshift. However, we are not able to distinguish whether these smooth SFHs are the result of a rapid collapse at high redshift or derive from coeval mergers. An important consideration is that the smoothness of the derived SFHs could be due to the fact that they derive from median stacked spectra, which represent the average behaviour of the sample. Therefore, the stochastic SF episodes related to the individual galaxies involved in the stack can be washed out and diluted within the stack. Our results have to be taken with a statistical meaning because are based on the analysis of stacked spectra. High SNR spectra of individual ETGs are required to better assess their evolution and star formation histories.

2.5.5 Metallicities

From the fit to the median stacked spectra, we also analyze the trends with mass and redshift of the retrieved mass-weighted metallicities $\langle Z \rangle_{mass}$, derived from eq. (2.13). On average, we find supersolar metallicities, with $\langle Z \rangle_{mass} \sim 0.029 \pm 0.0015$, as illustrated in Fig. 2.19 (a median value $\langle Z \rangle_{light} \sim$ 0.025 is obtained in case of light-weighted metallicities). Our $\langle Z \rangle_{mass}$ have no clear trend with redshift in a given mass bin, and also do not show a significant dependence on mass (metallicities increase on average by only 0.0025 from the lowest to the highest masses). The independence of metallicities of cosmic time is a suggestion that the analyzed galaxies are very old systems, which

[5] $[\alpha/Fe] \approx (1/5) - (1/6) \cdot log\Delta t$, see Thomas et al. (2005).

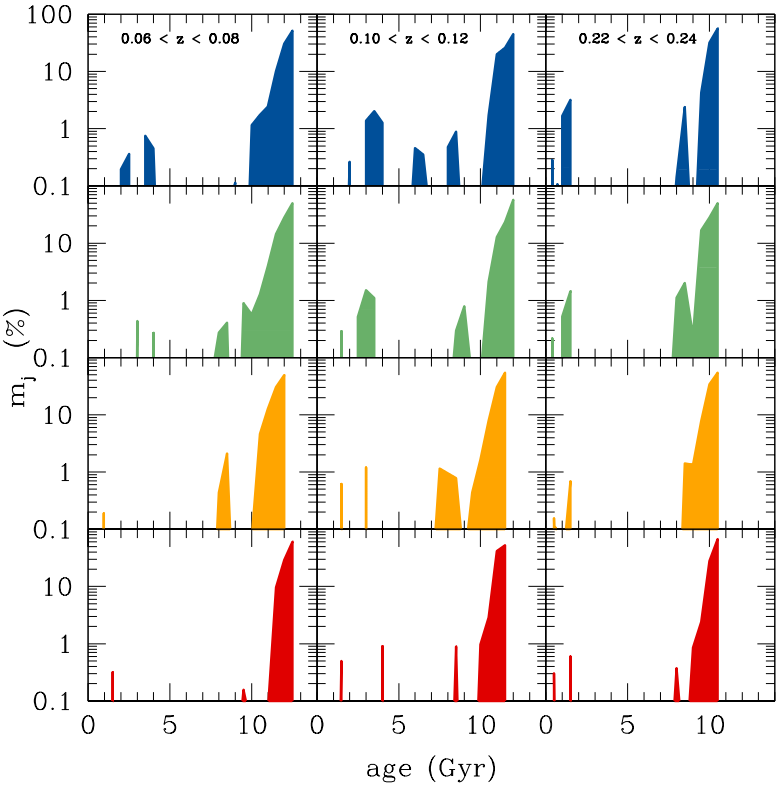

Figure 2.17: SFHs derived from median stacked spectra. Mass increases from top to bottom, redshift increases from left to right, as indicated. Note that no significant episodes of SF occurred after the main SF event. The mass fractions relative to stellar population younger than 5 Gyr is very low (i.e. $\lesssim 5$ %).

have depleted all their cold gas reservoir, with no further enrichment of their interstellar medium with new metals (however, we remind that the analyzed interval of cosmic time is not much extended, amounting to $\sim$ 3.3 Gyr). The dependence on mass suggests that more massive galaxies are able to retain more metals thanks to their deeper potential wells (Tremonti et al., 2004).
We find that MS11 models also provide slightly supersolar metallicities ($\langle Z \rangle_{mass} \sim 0.027 \pm 0.0020$, on average), with a more remarkable dependence on mass (metallicity increases by $\sim$ 0.005 from the lowest to the highest mass). The three uncertainty estimates rms_{sim}, err_{100} and rms_{set} calculated on the mass-weighted metallicities are reported in Table 2.6.
In Fig. 2.20, instead, we show a comparison between our metallicity estimates and the ones reported in the literature. In particular, we illustrate the scaling relation provided by Thomas et al. (2010) obtained from their sample of nearby ETGs[6], with its observed average scatter. We also show the median metallicities measured on our sample by Gallazzi et al. (2005), together with their MADs. These metallicities are, in all two cases, measured by fitting individual spectral features (Lick indices, Burstein et al., 1984). In particular, Thomas et al. (2010) derived their values from the measure of 24 Lick indices,

[6]We convert the [Z/H] values given by Thomas et al. (2010) following the conversion of Caputo et al. (2001): $logZ = [Z/H] - 1.7$.

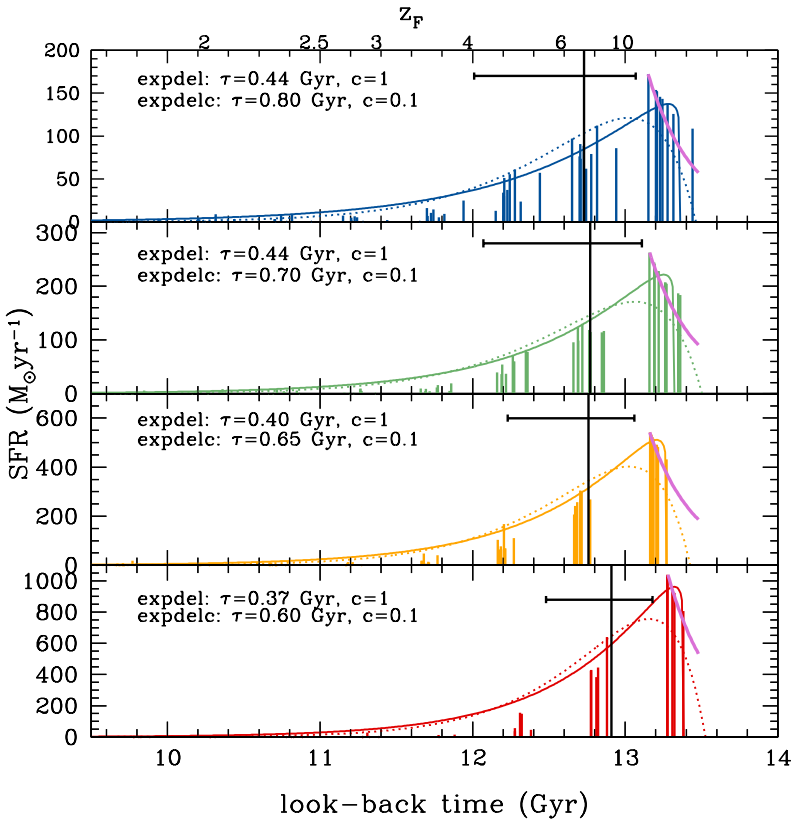

Figure 2.18: SFH for the four mass bins of our sample, with mass increasing from top to bottom (in the case of BC03 models). Colored vertical lines are the SFR ($M_{\odot}$ yr^{-1}) derived from the m_j provided by the spectral fitting (colors are coded as in Fig. 2.12). In each mass bin, black vertical and horizontal lines are defined as in Fig. 2.15. In each panel, we show the two best fit models deriving from the assumption of an $Expdel$ (dotted curves) or an $Expdelc$ (solid curves) parametric function to describe the derived SFHs. The best fit parameters are also reported. Pink curves are the inverted-τ models with τ = 0.3 Gyr described in the text, extended up to 13.48 Gyr (which corresponds to the age of the Universe in the assumed cosmology).

while Gallazzi et al. (2005) used a set of 5 specific Lick indices, including Hβ, Hδ_A, Hγ_A, $[Mg_2Fe]$ and $[MgFe]'$[7].

It is possible to note that the metallicity estimates are broadly consistent, with a difference $\Delta\langle Z\rangle_{(This\ work-Gallazzi)}$ ∼+0.0036 and $\Delta\langle Z\rangle_{(This\ work-Thomas)}$ ∼ −0.0032. The figure also illustrates the McDermid et al. (2015) mass-weighted metallicity – velocity dispersion relation, which they derive by means of another full-spectrum fitting code (i.e. PPXF), using the Vazdekis synthetic models (Vazdekis et al., 2012). We find that their metallicities are closer to the solar value (i.e. $Z \sim 0.02$), with $\langle\Delta Z\rangle_{(This\ work-McDermid)} \sim -0.01$.

We ascribe the discrepancies among these various results mainly to the use of different sets of Lick indices or synthetic models (in the case of full-spectrum fitting). Therefore, even if there is agreement among the majority of the reported results in predicting su-

[7]Where $[MgFe]' = \sqrt{Mgb\,(0.72\,Fe5270 + 0.28Fe5335)}$ and $[Mg_2Fe] = 0.6\,Mg_2 + 0.4\,log(Fe4531 + Fe5015)$.

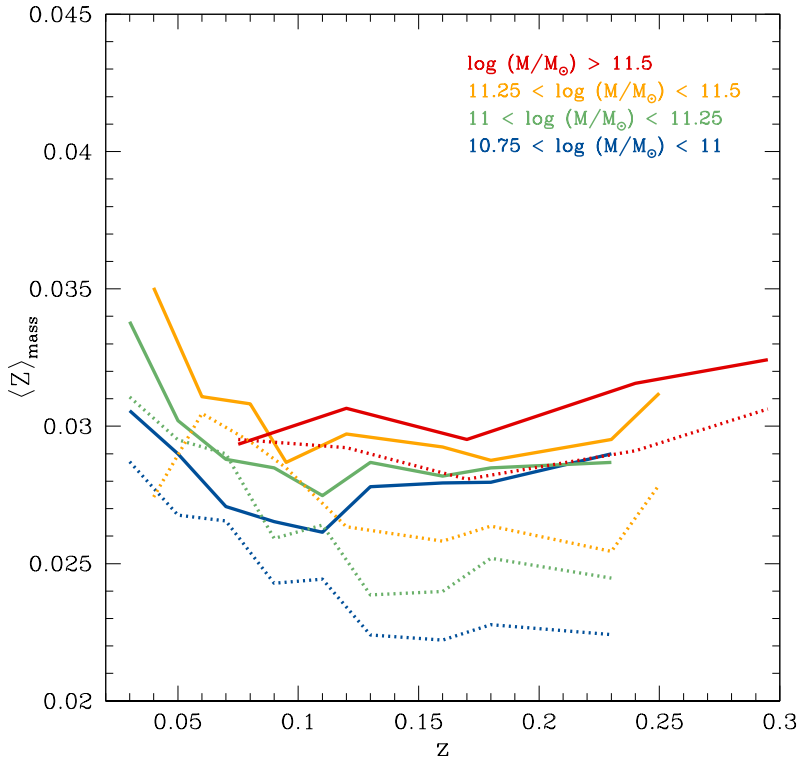

Figure 2.19: Mass weighted metallicities as a function of mass and redshift. Solid and dotted curves refer to BC03 and MS11 models, respectively. Stellar mass increases from blue to red, as indicated in the top right of the figure.

persolar metallicities (i.e. $Z \gtrsim 0.025$), which also increase with σ, it is evident that the absolute values of metallicities depend on the method and the assumptions used for their estimate.

2.5.6 Velocity dispersions and dust extinction

In Fig. 2.21 we illustrate the trend of the velocity dispersion with stellar mass. In particular, we show the values obtained for all the redshift bins available for a given mass. We find velocity dispersions $\sigma \sim 200 - 300$ km s^{-1}, increasing for increasing stellar mass. Our results are compared with the median values derived on the same sample by the Princeton group[8], who have provided a re-reduction of a subsample of SDSS data. It is possible to note that there is a good agreement between the two estimates. Indeed, the differences $\Delta\sigma_{(This\ Work-Princeton)}$ are $\lesssim 12$ %. Furthermore, it is worth noting that the largest discrepancies occur only in correspondence of the extreme low or high redshift bins, which have fewer statistics (i.e. which contain fewer objects), and that MS11 models provide velocity dispersions which are in agreement with the BC03 ones, being only ~ 3.5 km s^{-1} lower than them, on average.
As it is possible to note in Fig. 2.22, the visual extinction A_V obtained from the spectral

[8]More information are available on the website $http://spectro.princeton.edu/$

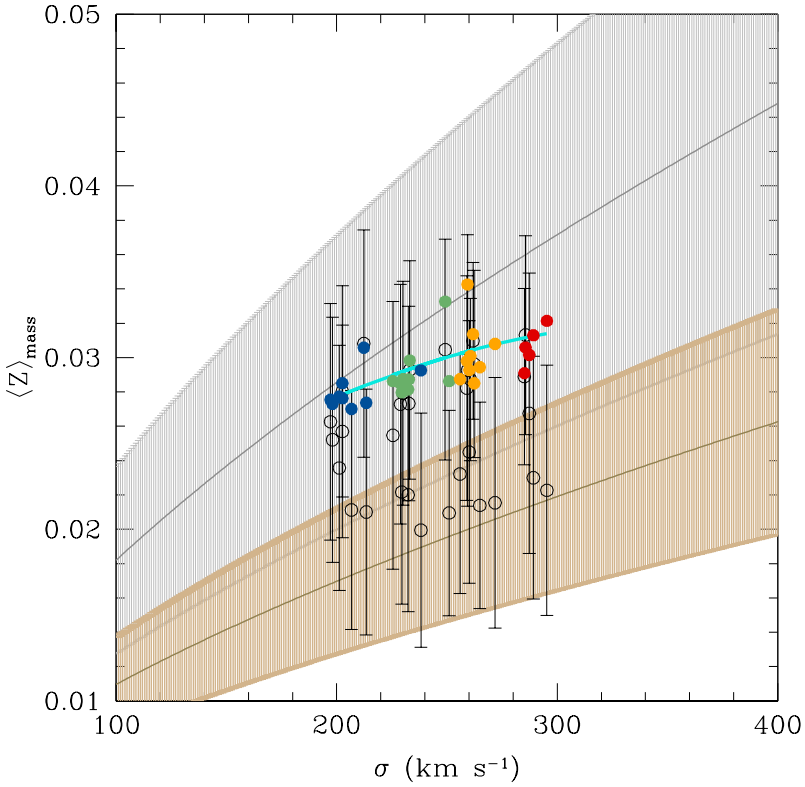

Figure 2.20: Comparison between our mass-weighted metallicities (in the case of BC03 models) and the values reported in the literature. In particular, colored filled circles (color-coded as in Fig. 2.12) are our results (the cyan curve is a second order fit to our data); the grey curve is the scaling relation provided by Thomas et al. (2010), with its dispersion (grey shaded region), while black open circles and vertical bars are the measures (and dispersions) performed on our sample by Gallazzi et al. (2005). The light-brown curve is the relation derived by McDermid et al. (2015), together with its dispersion (light-brown shaded region).

fit with BC03 models is always < 0.2 mag and on average $\sim$ 0.08 (averaging on the four mass bins), in agreement with the typical view of early-type galaxies being old and dust-free objects (Wise & Silva, 1996, Saglia et al., 2000, Tojeiro et al., 2013). MS11 models also produce very low A_V (< 0.25 mag) which, however, are higher by $\sim$ 0.08 mag than the BC03 ones, on average. Moreover, in the BC03 case, more massive galaxies have lower A_V with respect to less massive ones, while this trend is much less remarkable when MS11 models are used. Although further investigations are needed to confirm the reliability of this trend, it may suggest that more massive galaxies are able to clear their interstellar medium more efficiently, probably due to more intense feedback processes linked with star formation or AGN activity. As usual, the value of rms_{sim}, err_{100} and rms_{set} for both the velocity dispersions and dust extinction are reported in Table 2.6.

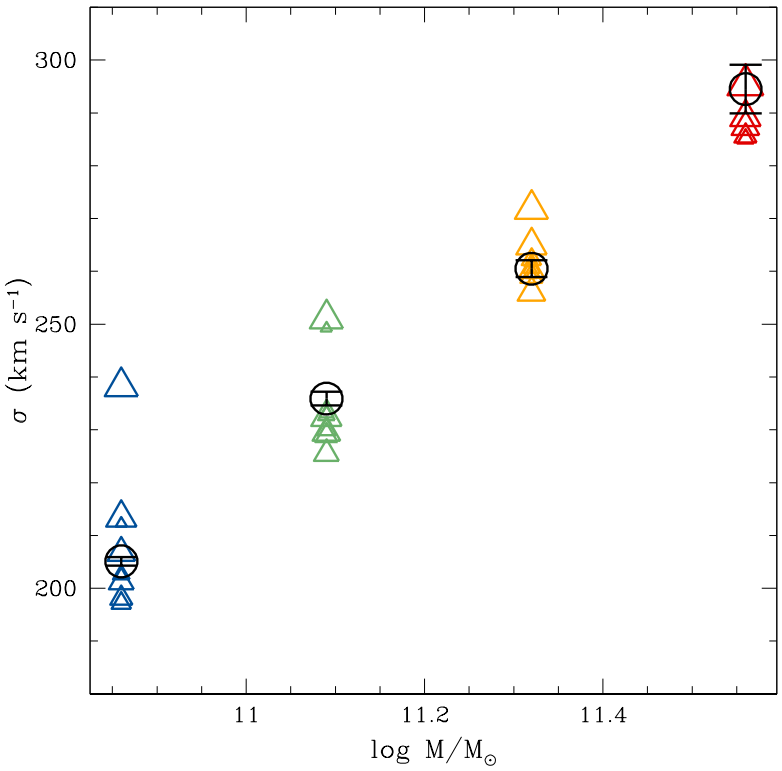

Figure 2.21: Velocity dispersions σ as a function of mass (for BC03 models). Colored triangles represent our observed values at different redshift for each mass bin (the values of σ are illustrated together with the errors MAD/$\sqrt{N}$), with the size of the triangles increasing for increasing redshift; black open circles are the velocity dispersions derived from the re-reduction of SDSS spectra performed by the Princeton Group, used for comparison.

2.6 Testing the fitting of individual spectra

Since median stacked spectra are very useful to increase the SNR of the observed spectra, in this Section we verify if the results obtained using median stacked spectra are consistent with the ones derived by fitting individual spectra (we performed this check in the case of BC03 models). In particular, we compare the $\langle t \rangle_{mass}$, $\langle Z \rangle_{mass}$, A_V and σ derived so far through the median stacked spectra, with the median of their distributions obtained studying individual objects. We restrict our analysis only to the two most massive bins (i.e. $< 11.25 < log(M/M_{\odot}) < 11.5$ and $log(M/M_{\odot}) > 11.5$), both because they are the most interesting ones to investigate galaxy formation and evolution and for computational feasibility (since they contain fewer objects, see Table 2.5).
Fig. 2.23 illustrates what derived for $\langle t \rangle_{mass}$, $\langle Z \rangle_{mass}$, σ and A_V at $< 11.25 < log(M/M_{\odot}) < 11.5$ and $log(M/M_{\odot}) > 11.5$.
As it is possible to note, in most of the cases the results of median stacked spectra are overlapped to the ones of individual spectra within the dispersion of these latter. We found that ages, metallicities and velocity dispersions are higher in the case of median stacked spectra of $\lesssim 10$ % (the average age differences between individual and stacked

Table 2.6: Uncertainties on ages, metallicities, velocity dispersions and dust extinction provided by the three different estimates described in the text (in the case of BC03 models).

Uncertainty	$\langle t \rangle_{mass}$ (Gyr)	Z	σ (km s^{-1})	A_V (mag)
rms_{sim}	$\pm$ 0.3	$\pm$ 0.0001	$\pm$ 1.3	$\lesssim 10^{-4}$
err_{100}	$\pm$ 0.05	$\lesssim$ 0.0002	$\pm$ 0.3	$\pm$ 0.002
rms_{set}	$\pm$ 0.6	$\pm$ 0.0015	$\pm$ 1.75	$\pm$ 0.030

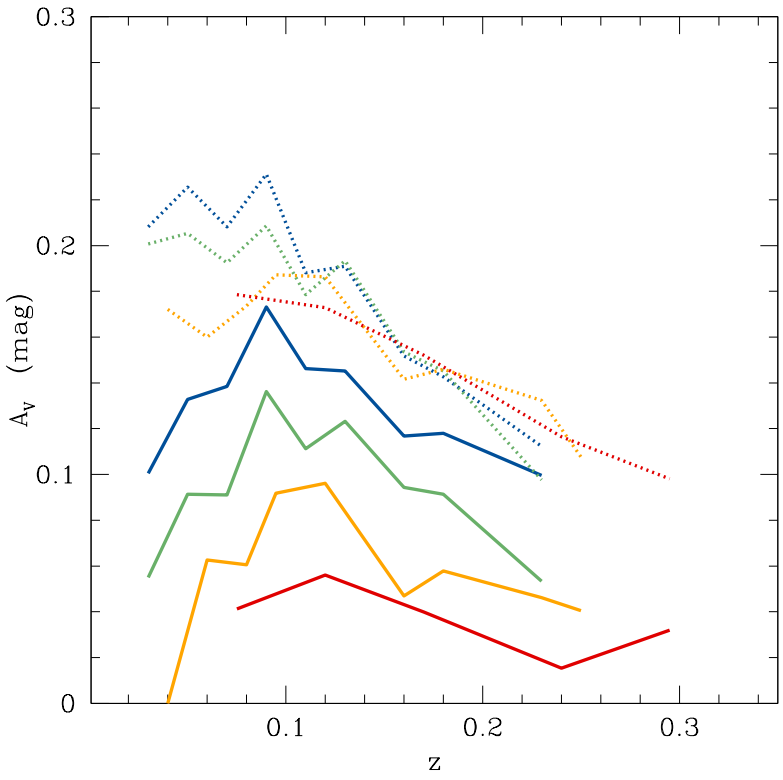

Figure 2.22: Dust extinction A_V as a function of redshift and mass. Solid and dotted curves refer to BC03 and MS11 models, respectively. Colors are coded as in Fig. 2.12.

spectra are smaller than the uncertainty produced on age by the full-spectrum fitting method, i.e. $\pm$ 0.6 Gyr), $\lesssim 15$ %, $\lesssim 3$ % and $\lesssim 15$ % respectively.
Moreover, taking into account the systematic errors derived for the various quantities under analysis (see Table 2.6), we find that the bias between the quantities inferred from median stacked and individual spectra is not significant, with a significance of $\sim 0.5\,\sigma$ for age, $\sim 1.1\,\sigma$ for metallicity, $\sim 0.05\,\sigma$ for dust extinction. In the case of velocity dispersion, it is $\sim 2.2\,\sigma$ for $11.25 < log(M/M_{\odot}) < 11.5$ and $\sim 0.5\,\sigma$ for $log(M/M_{\odot}) > 11.5$. The discrepancy between individual and median stacked spectra is thus small, confirming that our sample is selected to be homogeneus. For this reason, we expect the properties of the median stacked spectra to be similar to ones of each individual spec-

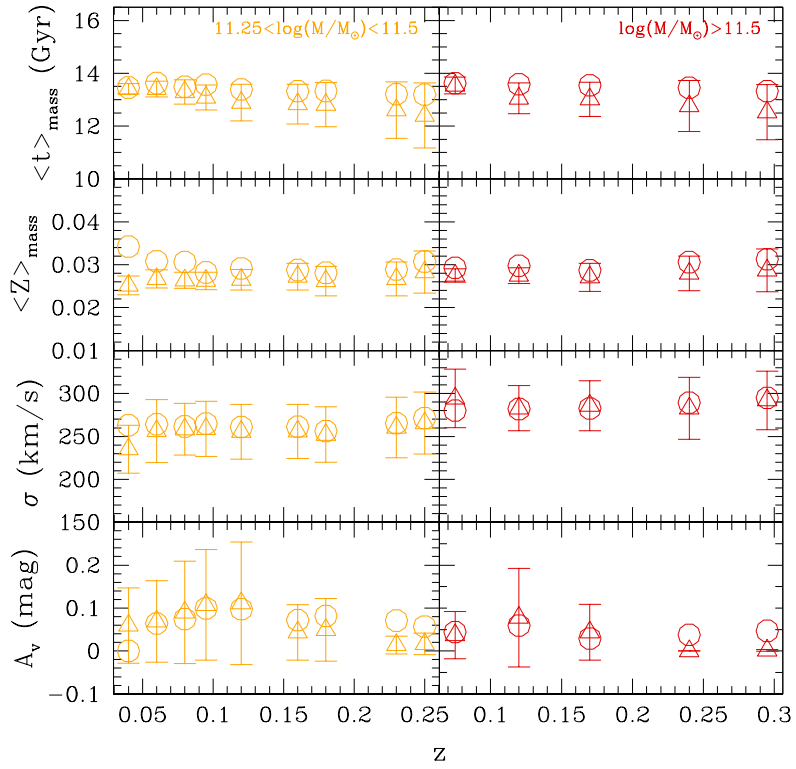

Figure 2.23: Comparison between the median ages, metallicities, velocity dispersions and dust extinction derived from median stacked spectra (open circles) and individual spectra (open triangles) in the case of BC03 models (vertical bars are the MADs on the results from individual spectra) for the two mass bins $11.25 < log(M/M_{\odot}) < 11.5$ *(left) and* $log(M/M_{\odot}) > 11.5$ *(right).*

trum entering the stack. This test demonstrates that the procedure of stacking spectra do not introduce significant bias on the retrieved evolutionary and physical properties, since the produced shifts mostly lie within the dispersion produced by the fit to individual spectra. Therefore, analyzing stacked spectra is essentially equivalent to analyze individually each spectrum that contributed to the stack.
Finally, an important consideration is that, if we consider the small 0.4 – 0.5 Gyr systematic introduced by stacked spectra, the formation redshifts derived from this analysis decrease to $z \gtrsim 3$.

2.7 The question of progenitors

Linking galaxies at $z \sim 0$ with their progenitors back in cosmic time is essential to derive a coherent evolutionary pattern and understand the formation process of different galaxy types. In this work, we attempt to place constraints on the progenitors of nearby ($z \lesssim 0.3$), very massive ($log(M/M_{\odot}) > 10.75$) and passive ETGs by exploiting their SFH, reconstructed from the full-spectrum fitting analysis described in previous Sections. The aim is to verify if the inferred properties of the progenitors fit into an evo-

lutionary path consistent with other observational constraints. In this regard, we first infer the properties of the star-forming progenitors from which today's massive ETGs originated, and then follow their evolution until they terminate the star formation activity and become quiescent descendants at later cosmic times.
As already said, our method is not able to distinguish if the analyzed massive and passive galaxies formed with a monolithic-like collapse at high redshift or if coeval mergers occurred to build their stellar mass. In this regard, it is important to clarify that the results described in the following sections implicitly assume that no coeval merger events have happened during the formation history of the analyzed galaxies. Furthermore, we illustrate the results derived assuming the $Expdelc$ as the parametric form describing the observed SFHs.

2.7.1 The star-forming progenitor phase

Starting from the shapes of the SFHs illustrated in Sect. 2.5.4 (Fig. 2.18), we display the inferred evolutionary path of our sample ETGs in the SFR – stellar mass plane. Fig. 2.24 shows the evolutionary tracks separately for the four mass bins of our sample as a function of cosmic time, together with the main sequences (MS) of star-forming galaxies available in the literature as a function of redshift. All the MS relations have been normalized to the Chabrier (2003) IMF adopted in this work.

Several important results emerge from Fig. 2.24 (which illustrates the case of BC03 models). The inferred SFRs were high in the past, with typical levels $\langle SFR \rangle_{68\ \%}$ up to $350 - 400\ M_{\odot}$ yr^{-1} for the most massive bin, but broadly consistent with those of MS galaxies at the same redshifts and masses. At early epochs ($z \sim 3-6$), the SFRs increase with mass and, for a given redshift, the slope of the SFR–mass correlation is similar to that of the MS. An example is represented by the comparison with the results of Salmon et al. (2015), who used CANDELS data to derive the MS relation at $3.5 \lesssim z \lesssim 6$. Our results suggest that the progenitors of our ETGs were already forming stars at very high rates at $z > 3 - 4$. It is worth noting that such early formation epochs ($3 \lesssim z \lesssim 10$) are also derived by McDermid et al. (2015) for ATLAS^{3D} ETGs with masses comparable to those of our sample. Fig. 2.24 also shows that after ~ 400 Myr, the SFRs of our ETGs decrease rather rapidly to a few $M_{\odot}$ yr^{-1} at $z \sim 2$, and that this tends to occur slightly earlier for the galaxies in the highest mass bin (where a deviation from the slope of the SFR – mass relation is present). The complete quiescence is achieved at later cosmic times. In particular, if the SFR at which a galaxy of a given mass is considered quiescent is defined as SFR(M) $\sim 10^{-11}$ yr^{-1} $\cdot$ $M/M_{\odot}$, our sample ETGs become inactive at $z \sim 1.5 - 2$.
These evolutionary trends are apparent in the complementary Fig. 2.25, which illustrates the specific star formation rate (sSFR, i.e. SFR per unit mass) for the four mass bins as a function of look-back time, together with the literature values (derived from the SFRs of Fig. 2.24). This shows that the peak of star formation activity of the very massive and passive ETGs occurred at $4 \lesssim z \lesssim 7$. It is worth noting that MS11 models provide a similar evolution for the sSFR at $z > 6$ (with SFR up to $\sim 700 - 750\ M_{\odot}$ yr^{-1}), even if a steepening with respect to the BC03 predictions occurs at lower redshifts, suggesting slightly higher redshifts for the beginning of the quiescent phase ($z \sim 1.5 - 2$). Either case, we find that the studied galaxies have already formed $\gtrsim 75\ \%$ (i.e. $M \gtrsim 10^{10.62} M_{\odot}$) of the total stellar mass by $z \sim 5^{+3.8}_{-1.4}$, thus we expect their progenitors at this redshift to be also very massive – in the hypothesis of no coeval mergers. If these systems are dusty and follow the same star formation scaling relations present at lower redshifts, the inferred SFRs imply infrared luminosities in the range of the so called

luminous to ultra-luminous infrared galaxies ($11 \lesssim log(L_{\rm IR}/L_{\odot}) \lesssim 13$).

Clearly, the question is whether galaxies with very high SFRs and substantial stellar masses have been observed at such high redshifts (if no mergers occurr). The answer is probably yes, although the information is still limited and fragmentary. Examples are represented by high redshift millimeter/submillimeter galaxies at $z \sim 4-5$ (Schinnerer et al., 2008; Daddi et al., 2009; Hodge et al., 2015) and massive starbursts at $z \sim 5-6.3$ (Walter et al., 2012; Riechers et al., 2013; 2015). Also the existence of galaxies at $z > 3$ with simultaneous substantial stellar masses and high SFRs is suggestive of systems that could evolve rapidly towards a quiescence phase (Béthermin et al., 2015; see also Pozzi et al., 2015). In this regards, also the massive and mostly quenched galaxies at $z \sim 3$ discovered by Taniguchi et al. (2015) could fit well into a scenario of earlier star formation as inferred from the SFHs of our sample of ETGs. Last but not least, the mere existence of QSOs at $z \sim 6$ with massive and evolved host galaxies (e.g. Fan et al., 2003, Dietrich et al., 2003, Freudling et al., 2003, Goto et al., 2009, Bañados et al., 2014, Wu et al., 2015) may be consistent with this scenario.

2.7.2 The quiescent descendent phase

According to the inferred SFHs (Fig. 2.18), the progenitors of our sample ETGs are expected to be already quiescent by $z \sim 1.5-2$ ($z \sim 2.5-3$ in the case of MS11 models), with this phase lasting without other major episodes of star formation at later cosmic epochs. This implies that a population of massive and passive galaxies ($M \gtrsim 10^{10.75} M_{\odot}$) should already be in place at $z \sim 2-4$.

Such kind of galaxies have been indeed spectroscopically identified up to $z \sim 3$ (Dunlop et al., 1996, Cimatti et al., 2004, McCarthy et al., 2004, Kriek et al., 2006, Gobat et al., 2012), and subsequently studied in more detail (e.g. Cimatti et al., 2008, Saracco et al., 2009, Onodera et al., 2015, Belli et al., 2015, Lonoce et al., 2015, see also Newman et al., 2015). Their properties are broadly consistent with those expected in the evolutionary scenario inferred in this work. As a matter of fact, these galaxies are massive ($M \sim 10^{10.5-11} M_{\odot}$), dominated by old stars ($\gtrsim$ 1 Gyr), passive or weakly star-forming, with low sSFR, and characterized by spheroidal morphologies and surface brightness profiles typical of early-type galaxies. However, at fixed mass, their sizes are, on average, smaller than in present-day ETGs, implying a substantially higher stellar mass density (Daddi et al., 2005, Cimatti et al., 2008, 2012, Trujillo et al., 2011).

The archaeological results of our work imply that if the complete quiescence is achieved by $z \sim 2^{+0.5}_{-0.3}$ ($z \sim 3^{+1}_{-0.6}$ for MS11 models) on average, nearly quiescent galaxies (sSFR $\sim 10^{-11}$ yr^{-1}, up to 10^{-10} yr^{-1}) should be present also at higher redshifts. This possibility is now strongly supported by the detection of several massive quiescent galaxy candidates at $3 < z < 7$ (Mobasher et al., 2005, Rodighiero et al., 2007, Wiklind et al., 2008, Mancini et al., 2009, Fontana et al., 2009, Brammer et al., 2011, Muzzin et al., 2013a, Straatman et al., 2014, Caputi et al., 2015, Marsan et al., 2015). Although these galaxies are too faint for the current spectroscopic sensitivity, their photometric SEDs suggest that they are massive (up to $M \sim 10^{11} M_{\odot}$), old (often with ages close to the age of the Universe at their redshifts) and have low sSFRs. We note that the existence of massive galaxies at high redshifts is also a crucial test for the structure formation in the ΛCDM cosmological context (Steinhardt et al., 2015).

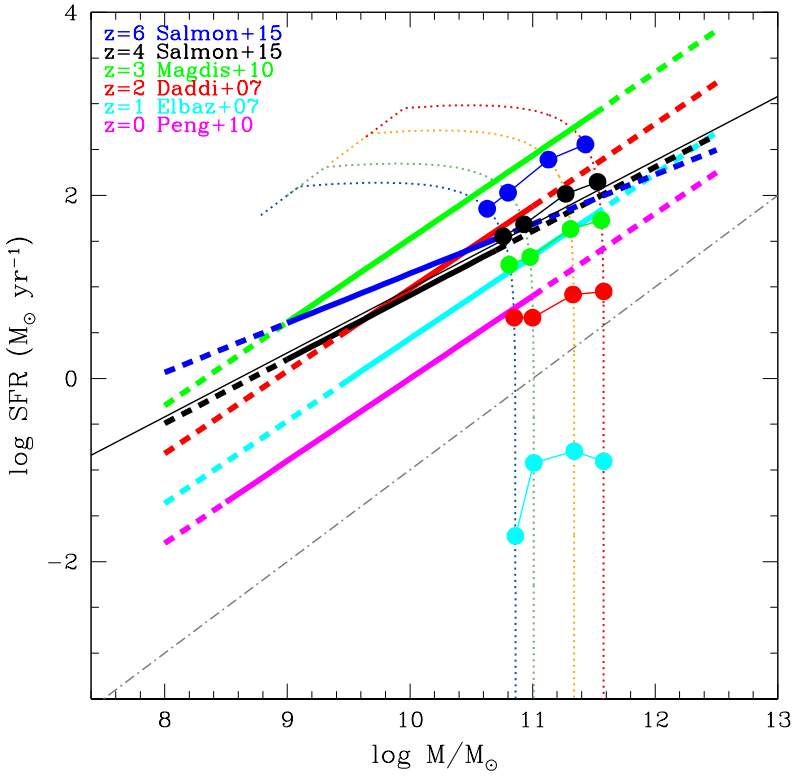

Figure 2.24: Evolving SFR – mass curves (in the case of BC03 models and for the $Expdelc$ parametric form). The four dotted curves are the evolving SFR – mass relations for the four mass bins of our sample (deduced from the SFHs of Fig. 2.18) as a function of cosmic time (from left to right), color coded as in Fig. 2.18. Blue, black, green, red, cyan and magenta lines are the SFR – mass relations deduced by different authors at various redshifts (as indicated in the top left of the figure), within their observed mass ranges (solid lines). Filled circles are the SFR for the four mass bins at various z, corresponding to the ones reported in the top left of the figure (note that, at $z \sim 0$, we derive $log(SFR) < -3$, thus the values at this redshift are not included in the plot). The grey dashed-dotted line represents the level of SFR at which the galaxies can be considered completely quiescent.

2.7.3 The size of the progenitors

More information comes from the the sizes of our passive ETGs. Fig. 2.26 shows a comparison between the effective radii R_e of the analyzed galaxies and the ones of the parent population, which we define as the ensamble of SDSS DR4 ETGs with $log(M/M_{\odot}) > 10.75$ (Kauffmann et al., 2003)[9]. In particular, R_e are taken from the NYU Value-Added Galaxy catalogue (Blanton et al., 2005). Moreover, since the majority of our passive, massive ETGs are bulge-dominated systems (see Sect. 2.4.1), we restrict this analysis only to galaxies with this kind of morphology, both in the passive and the parent sample.
Fig. 2.26 shows that the median R_e increases for increasing mass (from $\sim$ 5 Kpc to $\sim$ 20 Kpc) and, given a stellar mass, our passive ETGs have median sizes smaller than the

[9]We rescaled the stellar masses of the parent population, estimated by Kauffmann et al. (2003), to M11 stellar masses, by subtracting 0.2 dex to the former.

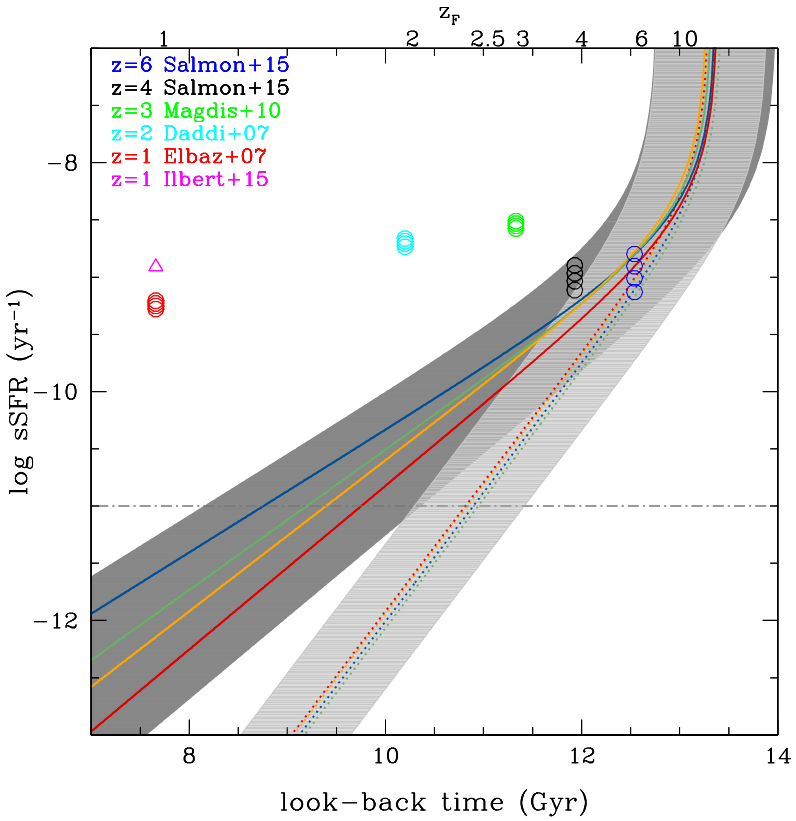

Figure 2.25: Evolving sSFR – z relations for the $Expdelc$ parametric form. Solid and dotted curves are the sSFR – z relations for the four mass bins (color coded as in Fig. 2.18) for BC03 and MS11 models, respectively. Blue, black, green, cyan and red open circles (and violet open triangle) are the sSFR estimates obtained by various authors at different redshifts (for the four mass bins), as indicated in the top left of the figure. The grey horizontal dashed-dotted line marks the level of sSFR at which a galaxy is in general considered completely quiescent (sSFR $\lesssim 10^{-11}$ yr^{-1}). Dark-grey and light-grey shaded regions represent the uncertainty on the look-back time, associated to the results from BC03 and MS11 models, respectively.

ones of the parent sample even by $\sim 15\,\%$ (at the highest masses). Furthermore, also the entire R_e distribution is extended to smaller radii in the case of passive ETGs, especially for $log(M/M_{\odot}) \gtrsim 11.5$. Reminding that small differences in galaxy size imply large differences in stellar mass density, the derived trends suggest that the ETGs analyzed in this work should have formed from higher density progenitors which, in the hypothesis of no coeval mergers, do not increase their mass during the evolution. On the other hand, we cannot exclude that galaxies in the parent sample have experienced more dry mergers than our massive and passive galaxies, which have increased their size across cosmic time (Naab et al., 2009, Johansson et al., 2012a). The observed trend is also in agreement with some literature studies at low redshift which also suggest that more compact galaxies contain older stellar populations than larger ones (e.g. Saracco et al., 2009, Shankar & Bernardi, 2009, Williams et al., 2010, Poggianti et al., 2013, McDermid et al., 2015). In general, this is qualitatively consistent with the high z_F inferred by our analysis ($z > 5$) since, according to the cosmological evolution of the baryonic matter density, gas was denser at these cosmic epochs. These findings also agree with recent

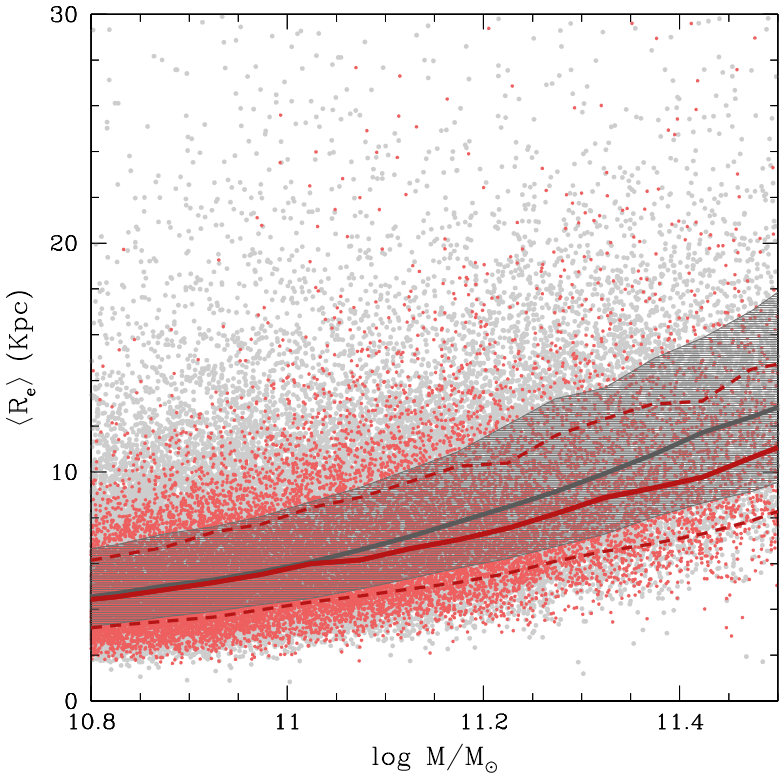

Figure 2.26: Size – mass relation derived for our sample of massive, passive ETGs (red) and for the parent sample of local galaxies with $log(M/M_{\odot}) > 10.75$ (grey) (Kauffmann et al., 2003 stellar masses are rescaled to the M11 ones). Colored points represent the two samples; solid curves are the P50 of the R_e distribution at each mass. The dashed red curves and the shaded grey region includes the 68 % of the R_e distribution of the passive and the parent sample, respectively.

observations of compact systems (with various level of SF) at $z \sim 2-3$, which could be identified as local massive ETGs progenitors (e.g. Daddi et al., 2004, Cattaneo et al., 2013, Finkelstein et al., 2013, Marchesini et al., 2014, Nelson et al., 2014, Williams et al., 2015). Moreover, recent models of elliptical galaxy formation also predict the formation of compact and dense progenitors at high redshifts (e.g. Johansson et al., 2012a, Naab et al., 2014 and references therein).

2.7.4 The number density of progenitors

The number density (ρ_n) of our ETGs can be used as another consistency check in the comparison between the low redshift galaxy population and their progenitors at earlier epochs. To do that, we first derived the mass function (MF) of the analyzed galaxies at $z \sim 0$ by rescaling the local Baldry et al. (2008) MF[10] (of all galaxy types) to the percentage of galaxies of each mass bin towards the parent population (which increases from $\sim 23\%$ to $\sim 70\%$ from the lowest to the highest masses), which is defined as in

[10]We rescaled Baldry et al. (2008) stellar masses (which are derived from an average on four stellar mass estimates, which include the Kauffmann et al. (2003) ones) to M11 ones.

the previous section, but now including galaxies of any morphology. Then, we evolve this local MF back in cosmic time following the decrease of the stellar mass predicted by the derived SFHs, inferring, at each cosmic time, the number density of galaxies above $log(M/M_{\odot}) = 10.75$. We verified that the mass completeness of our subsample of massive and passive galaxies is consistent with the one of the global sample of galaxies above $log(M/M_{\odot}) = 10.75$ and at $z \lesssim 0.3$, on which the V_{max} correction was already applied (see Baldry et al., 2008), and that our mass subsamples show no significant mass evolution as a function of redshift.

At $z \sim 0$, we obtain $log(\rho_n) \sim -3.98 \pm 0.1$ Mpc^{-3}.
Fig. 2.27 shows a comparison between the ρ_n obtained from this procedure and the literature[11], as a function of both the look-back time and the spectral synthesis models used for the fit (BC03 and MS11 models). In the case of BC03 models we find that, when the analyzed ETGs are completely quiescent and have already formed the totality of their stellar mass ($0 \lesssim z \lesssim 2$), the ρ_n inferred by us is independent of look-back time and is compatible with the literature, not exceeding the total number of passive galaxies per unit volume observed above the same mass threshold. Moreover, the redshift at which we have no more quiescent galaxies (since they are turning into star-forming systems, $z \sim 2$) is consistent with the one at which the ρ_n of quiescent galaxies observed in literature starts to rapidly decline. At earlier epochs, when the ETGs are still forming stars, the ρ_n of the SF progenitors starts to turn down, as the stellar mass formed by the ETGs decreases, and its value at $2 \lesssim z \lesssim 3$ (i.e. $log(\rho_n) \sim -4.1$ Mpc^{-3}) is in agreement with the literature observations at the same redshifts. Going towards the beginning of the SF ($z > 3$), ρ_n rapidly decreases and, within the uncertainty on the look-back time ($\pm$ 0.6 Gyr, see Table 2.6), this decline is in agreement with the one observed in the literature for the global population of SF and quiescent galaxies.
In the case of MS11 models, the drop of ρ_n occurs at slightly earlier times due to the shorter derived SFH. However the results are, also in this case, in agreement with the low redshift observations, and a marginal consistency with the literature is still present at high z.

Finally, for each mass bin, we also calculate the star formation rate density (SFRD) of the SF progenitors at $z \sim 5$ by multiplying the typical star formation rates $\langle SFR \rangle_{68\ \%}$ defined in Sect. 2.7.1 by the ρ_n of the considered mass bin. From this, we infer a global SFRD log(SFRD) $\sim -1.71\ M_{\odot}$ yr^{-1} Mpc^{-3}, which is totally consistent, within the uncertainties, to the Madau & Dickinson (2014) SFRD at the same redshift, which amounts to log(SFRD) $\sim -1.72 \pm 0.27\ M_{\odot}$ yr^{-1} Mpc^{-3} (the uncertainties on the Madau & Dickinson (2014) SFRD are taken from Behroozi et al., 2013). It is however worth noting that, in the case of MS11 models, a higher SFRD, i.e. log(SFRD) $\sim -1.22\ M_{\odot}$ yr^{-1} Mpc^{-3}, is derived at the same redshift.

[11] The literature MF have been all rescaled to a Chabrier (2003) IMF and to BC03 stellar masses (M11 stellar masses rely on these spectral synthesis models).

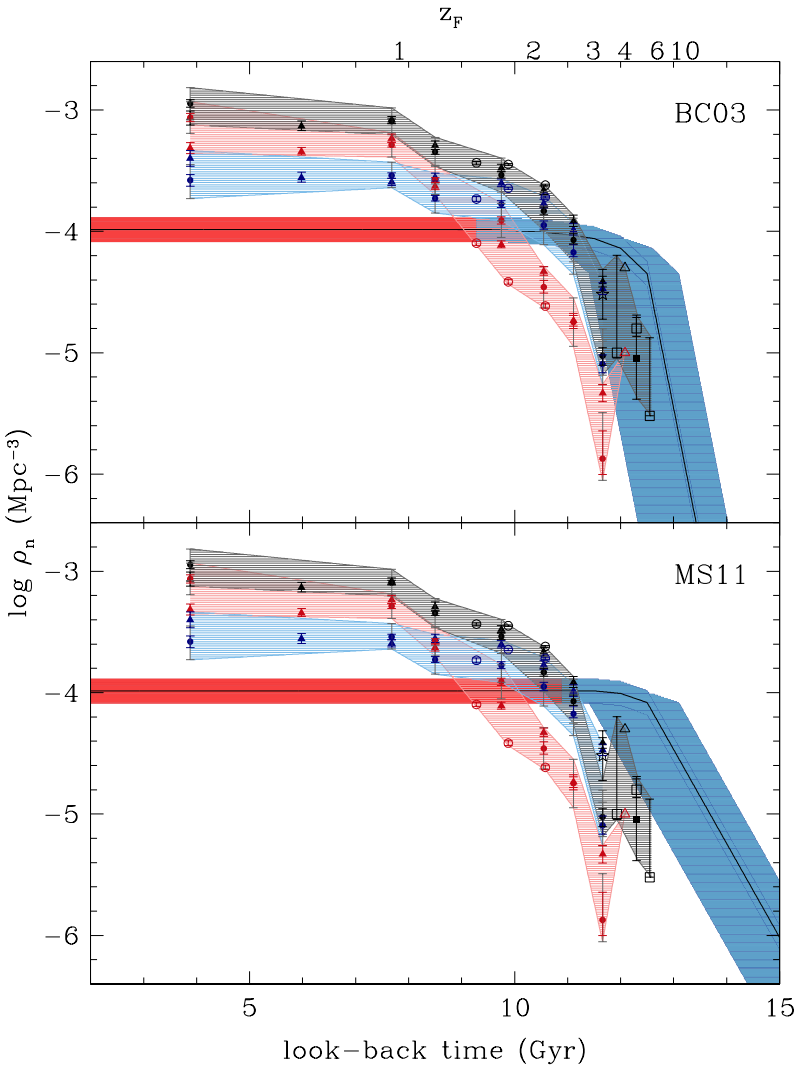

Figure 2.27: Number density above $log(M/M_{\odot}) = 10.75$. The central colored bands are the ρ_n of the ETG progenitors as a function of the look-back time in the case of BC03 (upper panel) and MS11 (lower panel) models, derived from the SFHs of the analyzed ETGs, together with its uncertainty ($\pm$ 0.1 dex) and the uncertainty on the look-back time (i.e. $^{+0.6}_{-1.1}$ Gyr, considering the small $\sim$ 0.5 Gyr systematic introduced by median stacked spectra, see Sect. 2.6). The red and the blue parts cover, respectively, the redshift interval within which ETGs are completely quiescent or star-forming. At each cosmic epoch, the literature results are illustrated with red, blue and black symbols, which refer to the ρ_n of the quiescent, the star-forming and the global galaxy population (i.e. star-forming + quiescent galaxies), respectively (all above the same mass threshold). In more detail, closed triangles and cirlces are the Ilbert et al. (2013) and the Muzzin et al. (2013a) ρ_n, respectively; open triangles and circles are the Mancini et al. (2009) and the Domínguez Sánchez et al. (2011) values, respectively; open square and star are the Grazian et al. (2015) and the Caputi et al. (2015) values, respectively. The shaded colored regions emphasize the uncertainties on the literature number densities (at each cosmic time, we consider the outermost envelope which includes all the literature estimates, taking into account their uncertainties). It is important to note that the literature ρ_n and their associated errors are derived by integrating the GSMF inferred through the $1/V_{max}$ method, and by computing the quadrature sum of its errors. The Muzzin et al. (2013a) error estimates (obtained from the best fit Schechter functions) are also shown in grey.

2.8 Summary of Chapter 2

In this work we analysed the median stacked spectra of a sample of 24488 SDSS DR4 ETGs at $z < 0.3$ in order to derive the properties of their stellar populations and to reconstruct their star formation histories. This study focused on the extreme cases of passive ETGs with the highest stellar masses ($log(M/M_{\odot}) > 10.75$) which, in turn, represent the passive envelope of the galaxy population at $0 < z < 0.3$. The sample was divided into four bins with increasing stellar mass. The stacked optical spectra were analysed by means of the full-spectrum fitting technique using the public code STARLIGHT in order to derive constraints in a way complementary to the traditional method of Lick indices based on a few absorption lines. Using this archaeological approach, we also inferred the properties of the progenitors of massive and passive ETGs. Our main results can be summarized as follows.

- First of all, STARLIGHT was tested against stellar population synthesis models in order to assess its reliability in the case of spectra similar to those of ETGs. It was found that the software retrieves the stellar population main properties (age, metallicity, SFH, dust extinction) and the velocity dispersion with a percentage accuracy higher than 10 % for SNR $\gtrsim$ 10 – 20, even if more complex SFHs are considered. In order to minimize the uncertainties, the STARLIGHT analysis was applied to stacked spectra with typical SNR $\sim$ 80.

- Mass-weighted stellar ages are very old, increasing with cosmic time from $\sim$ 10 to $\sim$ 13 Gyr, and show a clear tendency to increase with mass despite the rather limited mass leverage of our sample, which is selected to include only the most massive systems ($log(M/M_{\odot}) > 10.75$). This result provides an additional support to the downsizing evolutionary scenario where more massive galaxies are older than less massive ones. The derived ages are broadly compatible with those found with different full-spectrum fitting codes (e.g. McDermid et al., 2015 and Conroy et al., 2014) and with the Lick indices approach (e.g. Thomas et al., 2010; Graves & Schiavon, 2008). The bottom line is that the most massive and passive ETGs represent the oldest galaxies in the present-day Universe, with ages close to the age of the Universe itself in the most extreme cases.

- Mass-weighted metallicities are slightly supersolar, with a median $Z \sim 0.029 \pm 0.0015$ ($Z \sim 0.027 \pm 0.0020$ for MS11 models), increase with stellar mass, and do not show any significant trends with redshift. This supports the interpretation that the analyzed galaxies are very old objects which formed the bulk of their stars much earlier and did not enrich significantly their interstellar medium with new metals at later epochs (however, we remind that we have a limited leverage in cosmic time, i.e. ~ 3.3 Gyr). This contrasts with the metallicity evolution of star-forming galaxies (e.g. Maiolino et al., 2008, Mannucci et al., 2009, Foster et al., 2012, Zahid et al., 2013, De Rossi et al., 2015). Although our metallicities are broadly consistent with other results at a fixed stellar mass, a large scatter is present amongst the estimates of the metallicity (Z) obtained with different methods.

- The SFHs inferred with the full-spectrum fitting suggest that the star formation

occurred during an extended period of time. The SFHs are globally compatible with a parametric function of the form $SFR(t) \propto \tau^{-(c+1)} t^c \, exp(-t/\tau)$, where the typical value of τ and c are always short, with τ decreasing from 0.8 to 0.6 Gyr (with a dispersion of $\pm$ 0.1) from lower to higher masses and $c \sim 0.1$ (with a dispersion of $\pm$ 0.05) regardless of mass, reproducing the fast rise of the SFR at the beginning of the SFH. Other works highlighted a stronger dependence of the star formation timescale on the mass (e.g. Thomas et al., 2010, McDermid et al., 2015).

- Based on the inferred SFHs, we derive that the ETGs of our sample formed about 50 % of their stellar mass at early epochs, i.e., on average, at $z \gtrsim 5$ (which decrease to $z \gtrsim 3$ if the small 0.5 Gyr systematic introduced by median stacked spectra is taken into account). Moreover, the most massive galaxies formed it $\sim$ 0.2 Gyr ($\sim$ 0.1 Gyr for MS11 models) before than less massive systems.

- Low dust extinction ($A_V \lesssim 0.2 - 0.25$ mag) are required to fit the spectra. In addition, in the case of BC03 models, a trend is present showing that A_V tends to decrease for increasing stellar mass. The reliability, the significance and the interpretation of this trend requires further analysis beyond the scope of this thesis work, but a qualitative interpretation may be that the most massive galaxies were able to "clear" their interstellar medium more efficiently probably due to more intense feedback processes due to star formation and/or AGN activity.

- The stellar velocity dispersions $200 \lesssim \sigma \lesssim 300$ km s^{-1} estimated with STARLIGHT are consistent with estimates by other groups within the uncertainties, and increase with stellar mass.

- Based on the SFHs, we reconstructed the mass assembly history and the properties of the progenitors of the most massive ETGs of the present-day Universe, assuming that no coeval mergers have occurred during the evolution of the analyzed galaxies. The SFHs imply that these galaxies were vigorously forming stars and assembled large stellar masses ($\gtrsim 75$ % of the total stellar mass) by $z \sim 5^{+3.8}_{-1.4}$, with SFR up to $50 - 370 \, M_\odot$ yr^{-1} (SFR $\sim$ $140 - 750 \, M_\odot$ yr^{-1} for MS11 models). Possible star-forming progenitors with these characteristics have indeed been found in samples of galaxies at $4 < z < 6.5$ selected in the submm/mm. The inferred SFHs also predict the existence of quiescent galaxies at $2 < z < 4$ characterized by large stellar masses and low specific star formation rate. Galaxies with these properties have been spectroscopically identified at $z \sim 2 - 3$, and photometric candidates at higher redshifts also exist.

- The R_e of our sample ETGs are significantly smaller than those of the parent sample of SDSS DR4 ETGs with $log(M/M_\odot) > 10.75$. This implies higher stellar mass densities and suggest that they should have formed from high density progenitors

- Based on the number density of the analyzed galaxies in the present-day Universe ($log(\rho_n) \sim -3.98 \pm 0.1$ Mpc^{-3}), the inferred number densities of the progenitors are consistent with the literature, within the uncertainties. Moreover, the mean

star formation rate density implied by the star-forming progenitors does not violate the Madau & Dickinson (2014) relation at high redshift ($z \sim 5$), in the case of BC03 models.

- We find a good agreement among our results concerning ages, metallicities and SFHs and the ones obtained using the fit to individual spectral features (Lick indices) and α-elements abundances. We thus suggest the full-spectrum fitting to be a complementary and valid approach to derive the stellar population properties and the star formation histories of early-type galaxies.

Chapter 3

A methodology to select star forming galaxies just after the quenching of star formation

While in Chapter 2 we analyzed in detail the SFHs and the evolutionary and physical properties (i.e. ages, metallicities, dust extinctions and velocity dispersions) of massive and passive galaxies, in this Chapter we aim to get more insights about the processes involved in quenching by dissecting the crucial phase that links read and dead galaxies to blue star forming ones.

Understanding the origin of the dichotomy of star-forming and passive galaxies is one of the key questions in modern astrophysical studies. Over time, it has been argued that this bimodality is due to the quenching of the star formation in galaxies, which turns star-forming into passive objects. One common method used to investigate the SF quenching consists to analyze the properties of galaxies which are in the transition phase. In this regard, galaxies characterized by both a tidally disturbed morphology and intermediate colours (e.g. Schweizer & Seitzer, 1992; Tal et al., 2009) or low-level of recent SF (Kaviraj, 2010), young elliptical galaxies (Sanders et al., 1988; Genzel et al., 2001; Dasyra et al., 2006) and very recent post-merger remnants with strong morphological disturbances (Hibbard & van Gorkom, 1996; Rothberg & Joseph, 2004; Carpineti et al., 2012) have been considered as valid 'recent time' quenching candidates. The classification of the quenching population has also been performed through the investigation of galaxy spectroscopic properties, such as the fluxes and the equivalent widths of the emission/absorption lines produced in their Ionized atomic Hydrogen regions (H II regions) (e.g. Balmer lines). However, these studies have generally brought to identify transition galaxies in more advanced phases of the quenching process (Couch & Sharples, 1987, Quintero et al., 2004, Poggianti et al., 2004, Balogh et al., 2011, Muzzin et al., 2012, Mok et al., 2013, Wu et al., 2014), i.e $\sim 0.5 - 1$ Gyr after the SF halt. It has also been proved that H II region emission lines are useful to assess the ionization state or metallicity of galaxies both at $z \sim 0$ and at higher redshift (e.g. Dopita et al., 2000, Kewley et al., 2001, Dopita et al., 2006, Levesque et al., 2010, Kewley et al., 2013, Kashino et al., 2016). Unfortunately, this kind of studies are always hampered by the degeneracies affecting spectra and emission lines, which in many cases make it difficult to disentangle what is the origin of the emission line ratios intensity (e.g. Dopita et al., 2006).

In this Chapter, we propose and discuss a new method to select galaxies just after the quenching of star formation based on the emission lines originating in H II regions, and

emission line ratios. The knowledge in this field is indeed still fragmentary, especially when one tries to push the limit to the very early epochs after the SF quenching. The chapter is organized as follows: in Sect. 3.1 we review the main properties of the H II regions; in Sect. 3.2 we describe what are the main ingredients and equations used by photoionization codes to produce photionization models; in Sect. 3.3 we discuss how we can use photoionization models to study the quenching phase; in Sect. 3.4 and 3.5 we present our photoionization models to simulate the quenching phase and we test their reliability; in Sect. 3.6 we propose two quenching diagnostics and show our time evolution and their properties; in Sect. 3.7 we discuss how to mitigate the ionization/age – metallicity degeneracy which affects our models; while in Sect. 3.8 we present how our methodology can be used to identify quenching galaxies and present our results. Sect. 3.9 summarizes our main results.

The results shown in this Chapter can be found in *Citro et al. 2017; Monthly Notices of the Royal Astronomical Society, Volume 469, Issue 3, p.3108-3124.*

3.1 H II regions

H II regions are created when the extreme UV radiation (i.e. photons with energies larger than 13.6 eV and wavelength shorter than 912 Å) from a star ionizes and heats the surrounding gas. In particular, these energetic photons creates a spherical region of ionized hydrogen (H II) between the star and the neutral gas (H I) further out (Stromgrën Sphere, see Sect. 3.1.2). The physics of an H II region is basically driven by two processes: the *photoionization equilibrium* and the *thermal balance*. H II regions are not in thermodynamical equilibrium, therefore the population of the energetic levels of atoms and ions can be only determined by a detailed study of the microphysical processes happening in the photoionized region. However, due to the large number of collisions, the electrons inside H II regions generally follow an equilibrium, maxwellian velocity distribution and the photoionized regions can be therefore considered in *kinetic equilibrium*.

3.1.1 Photoionization equilibrium

The photoionization equilibrium is the balance between photoionization and recombination and is valid at each radius of the nebula. This condition determines the structure of the nebula and the rough spatial distribution of ionic states of the elements in the ionized zone.
In the very simplified case of a pure-hydrogen nebula, the photoionization equilibrium can be described by the following equation:

$$n_{H^0} \int_{\nu_0}^{\infty} \frac{4\pi J_\nu}{h\nu} a_\nu \mathrm{d}\nu \; = n_e \, n_p \, \alpha_{TOT}(H^0, T) \;\; , \tag{3.1}$$

where n_{H^0} is the neutral hydrogen density, ν_0 is the hydrogen ionization frequency (corresponding to an energy of 13.6 eV), α_ν is the photoionization cross section at a given frequency ν, $4\pi J_\nu = L_\nu / 4\pi r^2$ is the flux of ionizing photons at a radius r from the central star, and α_{TOT} is the recombination coefficient on all the energetic levels, which is proportional to the temperature as $\alpha_{TOT} \propto T^{-1/2}$.
This equation is valid when only the ionizing source is taken into account, while the diffuse emission from the photoionized cloud itself is neglected. Moreover, eq. 3.1 relies

on the so-called *Nebular approximation*, which states that, to the first order, all H I atoms are in the ground state (i.e. recombinations of electrons to excited levels are followed by a rapid cascade to the ground level).
To understand the ionization structure of an H II region, the photoionization equilibrium equation must be computed at each radius of the nebula, by means of the *radiative transfer* equation (which is valid both for lines and continuum). This latter can be written as follows:

$$\frac{dI_\nu}{ds} = -n_{H^0}\, a_\nu\, I_\nu \;+\; j_\nu \;\;, \tag{3.2}$$

where $\frac{dI_\nu}{ds}$ is the variation of the specific intensity of the radiation field within a thickness ds in the propagation direction, a_ν is the absorption coefficient per unit wavelength and j_ν is the local emission coefficient. At each radius, the first term of this equation accounts for the intensity of the ionizing source attenuated by the absorptions occurring within the nebula, while the second term represents the intrinsic emissivity of the cloud at each radius.
Applying eq. 3.2 to eq. 3.1, it is possible to derive that the equation for the photoionization equilibrium can be divided into a stellar part:

$$4\pi J_{\nu_s} = \pi F_{\nu_s}(r) = \pi F_{\nu_s}(R^\star)\,(\frac{R^\star}{r})^2 e^{-t_\nu(r)} \;\;, \tag{3.3}$$

where $F_{\nu_s}(r)$ is the flux of the star at a distance r from the central source, $R^\star$ is the radius of the central ionizing source, $\tau_\nu(r)$ is the optical depth at the radius r; and a diffuse part (analogue to eq. 3.2):

$$\frac{dI_\nu}{ds} = n_{H^0}\alpha_\nu I_{\nu d} + j_{\nu d} \;\;. \tag{3.4}$$

In the case of an optically thin nebula (case A recombination), the diffuse part is negligible and the only contribution to the photoionization equilibrium is given by the processes related to the central ionizing source. For optically thick nebulae (case B recombination, which is closer to observations of real nebulae), the usual assumption is instead the "on-the-spot" approximation, for which the diffuse radiation produced by cascades on the ground level is immediately and locally reabsorbed (Osterbrock 1989).
Taking account of the radiative transfer equation, the photoionization equilibrium equation becomes:

$$n_{H^0}\frac{{R_\star}^2}{r}\int_{\upsilon_0}^{\infty}\frac{\pi F_\nu(R_\star)}{h\nu}a_\nu e^{-\tau_\nu}d\nu = n_e n_p \alpha_B(H^0,T) \;\;, \tag{3.5}$$

where $\alpha_B(H^0,T)$ is the total recombination coefficient less the contributions from recombinations directly into the ground state (according to the on-the-spot approximation). Its general meaning is that, in optically thick nebulae, the ionizations caused by stellar photons are balanced by recombinations to excited levels of H. The recombinations to the ground level generate instead ionizing photons that are immediately absorbed, having no net effect on the overall ionization balance.
As mentioned before, the photoionization equilibrium described so far is valid in the ideal case of pure Hydrogen nebula. In real nebulae, several different phenomena have instead to be taken into account. First of all, they contain Helium and metals. This implies that a tight coupling between the ionizations and recombinations due to these different elements can arise, strongly affecting the ionization structure. Moreover, in real

nebulae, the shape of the ionization radiation field, and thus the ionization structure, can be heavily affected by dust, since dust grains can redistribute the photon energies, re-emitting the UV radiation at longer wavelengths.

3.1.2 Thermal balance

The thermal balance in H II regions describes the interplay between all the heating and cooling phenomena which happen inside the photoionized cloud. In the time-steady limit, where atomic processes occur much faster than other changes in the system (e.g. the dynamics of the flow or changes in the central stars radiation field), the thermal balance equation can be written as:

$$G_{pi} = L_r + L_{ff} + L_C \ , \tag{3.6}$$

where:

- G_{pi} represents the energy input from photoionizations, which are the principal source of heating in ionized regions. In particular, when a free electron is injected into the plasma by a photoionization, it has a certain kinetic energy which adds to the plasma.

- L_r represents the energy lost by recombinations when electrons recombine with protons to form neutral hydrogen.

- L_C is the energy lost by collisional cooling. This phenomenon is linked to collisional excitations, which happen via electron-ion impacts. These excitations are indeed very probable in H II regions, since energies in the ground state fine structure levels of metal ions (especially O^+, O^{++}, N^+) have typical excitation potentials of a few electronVolts, comparable with the thermal energy of the electrons that excite them. In particular, if the ISM electron density is lower than the threshold density (the so-called critical density)[1] of a given transition, the excited electron radiatively de-excites before the next collision, emitting a photon that escapes from the nebula. This leads to a net loss of energy from the free-electron plasma, since electron kinetic energy is converted into photons that escape from the cloud. On the contrary, for hydrogen densities higher than the critical density, the de-excitation takes place via collisions and no energy loss occurs.

Fig. 3.1 shows the heating (due to photoionization) and cooling (due to recombinations and collisional processes) curves for an optically thin cell of gas (from Ferland, 2003). Fig. 3.1, allows to understand how heating and cooling depend on temperature, metallicity and dust grains. As it is possible to note, the photoionization heating declines as a function of temperature ($G_{pi} \sim T^{-1}$), reflecting the temperature dependence of the recombination coefficient (see eq. 3.1).
About the cooling curve, at low temperatures and densities, the gas mainly cools by emitting the far-infrared lines that arise from split ground terms of the heavy elements. The peak at $\sim 10^5$ K occurs when the gas becomes hot enough to excite permitted lines of the abundant heavy elements. These lines have very high transition probabilities, and thus a little density dependence, so that the cooling curves for different densities

[1]The critical density is defined as $n_{crit} = A_{ul}/q_{ul}$, where A_{ul} and q_{ul} are the radiative and collisional de-excitation rates, respectively.

are similar. Finally, at very high temperatures ($T \gtrsim 10^6$), the abundant elements have lost most of their electrons, and only other less efficient coolants, such as the free-free emission, remain.
About the metallicity Z, its effect basically consists in raising or lowering the cooling curve. In particular, whereas the heating, which is mainly due to the photoionization of hydrogen, does not change by much, the gas coolants are strongly affected by Z. In particular, for very low Z, the most important coolant is the hydrogen. On the contrary, when Z exceeds several times solar, the temperature falls to $\sim 10^3$ K, and the infrared fine-structure lines dominate the cooling. At even higher Z, the ionized gas has reached room temperature (~ 300 K), and most of the cooling comes from infrared fine-structure lines. Concerning the condition of the galaxy H II regions we are interested in, at their typical temperatures (i.e. 10^4 K) and metallicities (i.e. $0.1Z_{\odot} < Z < Z_{\odot}$), the collisional cooling can be considered as the main cooling mechanism.
Dust grains also influence the H II regions spectra, especially if Z increases and the grains-to-metals ratio is kept constant. In general, H II regions become an increasingly stronger infrared source as the grains become more abundant and absorb more of the stellar continuum. Moreover, the luminosity produced by the hydrogen, which is proportional to the number of hydrogen photoionizations, decreases as heavy elements and dust increase, since they remove larger fractions of the stellar continuum.

The effects of metallicity, temperature and dust on the final spectra of H II regions also depends on the starting ionization state/degree of ionization of the ions inside the photoionized region. This initial structure is linked to the number of ionizing photons with energies able to ionize different ions. In particular, highly-ionized metals, which have lost most of their electrons and thus have high ionization potential, can be only produced by very energetic ionizing photons (with energies larger than 13.6 eV and wavelengths shorter than 912). These latter are provided only by very hard continua, i.e. by young and low-metallicity ionizing sources.

3.1.3 The size of the H II regions

Due to the photoionization equilibrium described above, we expect the size of an H II region to be limited, since the photons from the central source can ionize the material around it only within a certain radius. This hypothesis was first quantified by Stromgrën in 1939, who defined the radius of an H II region as:

$$r_{strom} = \left(\frac{3Q_{\star}}{4\pi\alpha_{TOT} n_{H^0}^2}\right) \tag{3.7}$$

(Strömgren, 1939), where $Q_{\star}$ is the number of ionizing photons emitted per second by the central source.
According to the Strömgren theory, UV photons from a central star ionizes the material which, after a first phase of expansion, halts once that the Strömgren radius is reached. Therefore, H II regions are static and in pressure equilibrium. The assumption that H II regions are static is reasonable, considering that the time scales on which their dynamical state can change are much longer than those associated to atomic or molecular processes. However, several studies in the last decades have shown that a number of physical effects can lead to departures from the simple Strömgren sphere model. Among these, particular attention has been payed to the H II regions dynamical expansion, which occurs if the pressure in the surrounding neutral medium cannot

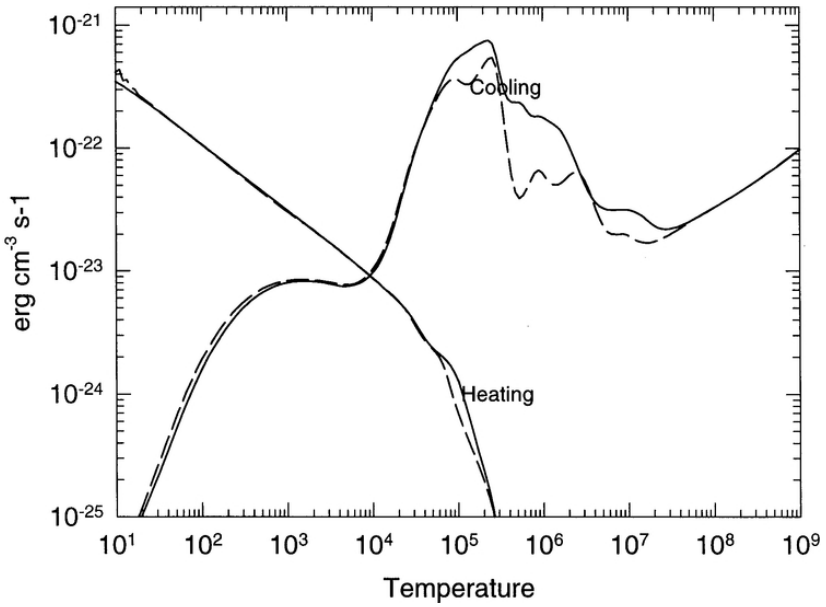

Figure 3.1: Heating and cooling rates for two photoionized cells of gas. The solid curves show results for low-density ($10^2 cm^3$) gas with abundances similar to the Orion Nebula. Grains exist and refractory elements have depleted abundances. The dashed curve shows a higher-density gas ($10^8 cm^3$) with solar abundances and no grains. Both volume heating and cooling rates have been divided by the square of the density to bring out the homology relations between the heating and cooling quantities (From Ferland (2003)).

confine the ionized gas (see Draine, 2011). Understanding the cause of this expansion has been the object of a number of studies, starting with the pioneering investigations by Kahn (1954) and Savedoff & Greene (1955). So far, a clear picture about the origin of this phenomenon is still lacking. Indeed, even if several studies have argued that the expansion is mainly wind-driven (e.g. Dopita et al., 2000, 2006), recent observations of nearby galaxies have motivated to revisit the question, and suggested that radiation pressure can be important to explain this process, especially in the giant H II regions which surround clusters and contain many O-type stars (Krumholz & Matzner, 2009, Yeh & Matzner, 2012, Verdolini et al., 2013).

3.2 How photoionization models work

Since H II regions are not in thermodynamical equilibrium, their physical conditions derive from the combination of many microphysical processes, and their spectra are the result of the radiative transfer along the photoinized nebula. This implies that no analytical solutions exist to predict the properties of H II region spectra, and large-scale numerical simulations must be performed to accurately simulate them. Photoionization codes are able to perform these simulations, by applying the ionization and thermal equilibrium at each radius of the photoionized cloud. As described in Morisset (2017), the main ingredient to feed into a photoionization code is a description of the photoionized region in terms of both the ionizing radiation field and of the properties of the ionized gas. About the ionizing radiation, the intensity and the shape of the ionizing stellar continuum (which is mainly determined by its age and stellar metallicity)

need to be specified. Concerning the ionized gas, its hydrogen density, elemental abundances, dust-to-gas ratio and dust composition must be provided.
The general idea of photoionization codes is that a slab of material is illuminated by a central ionizing source, with a geometry which can be both plane parallel (when $thickness\ of\ the\ slab \lll distance\ from\ the\ ionizing\ source$) or spherical. Additional ingredients can also be specified, such as the optical thickness of the cloud, the filling factor (i.e. the percentage of the photoionized cloud which is filled) and the covering factor (i.e. the percentage of ionizing photons which are intercepted by the gas).
The scheme which is usually followed by the photoionization codes to derive the final spectrum of a H II region, consists in the following steps:

- assume a geometry;
- determine the ionizing flux at the incident face of the cloud;
- divide the cloud into zones and calculate the reduction of photons as you move into the cloud;
- use the on-the-spot approximation (all diffuse ionizing photons are absorbed locally) in the first series of calculations to determine: temperature, ionization fractions, emissivities, and reduction of ionizing photons in each zone;
- in subsequent iterations, determine the diffuse field as you go to deeper zones in the cloud.

A fundamental parameter which helps to parametrize the starting ionization state of a H II region at the inner shell of the nebula (see Sect. 3.1.2), is the adimensional ionization parameter U, which is defined as the ratio between the mean intensity of the radiation field and the density of the ionized gas. In the plane parallel case, U can be written as (Tielens, 2010):

$$U = F_0/n_{\rm H}c \ , \tag{3.8}$$

where $n_{\rm H}$ is the hydrogen number density of the photoionized gas, c is the speed of light and F_0 is the flux of the UV ionizing photons ($\lambda < 912$ Å) striking the photoionized cloud. F_0 is proportional to the number of UV hydrogen ionizing photons $Q(H)$, which in turns depends on the stellar metallicity, the stellar mass, the star-formation rate, the age and the IMF of the ionizing central source. For instance, higher masses, higher star formation rates (SFRs), younger ages, top-heavy IMFs or lower metallicities, which all imply an higher number of massive stars, lead $Q(H)$ to increase. Moreover, F_0 depends on the proximity of the central stars to the photoionized nebula. As explained in Sect. 3.3, when a galaxy quenches its star formation, $Q(H)$ declines due to the aging and the softening of the ionizing SED. As a consequence, F_0 decreases and so does the ionization parameter.

Historically, the first generation of codes including the basic features of modern photoionization codes have appeared by the late 1960's (Harrington, 1968, Rubin, 1968, Tarter & Salpeter, 1969). These codes were applicable only to low density nebulae, and were not able to properly treat processes such as the charge exchange or low-temperature dielectronic recombination. A second generation of codes was developed in 1980's, with the attempt to extend their use to higher densities, and also higher photon energies and optical depths. In the last years, a great efforts have been made to obtain more and more accurate predictions from the photoionization codes, but much

work remains to be done (e.g. Ferland et al., 2013). For instance, the knowledge of all the heating and cooling agents, of the transition probabilities and photoionization cross sections of all the elements, and of the dust grains composition/structure, is still fragmentary. The current advances in photoionization codes mainly concern the inclusion of atomic data updates, time dependent effects (e.g. shock ionization, see Allen et al., 2008), dust radiative transfer, expansion to Photo-Dissociation Regions, 3-D geometry. This latter ingredient requires very long computation times, but it will be very useful to properly understand the spectra of observed nebulae, especially the spatially resolved ones.

3.3 What can we learn on star-formation quenching from H II regions

In the previous Sections it has been mentioned that the presence of specific emission lines in H II region spectra depends on the intensity and shape of the ionizing source (see Sect. 3.1.2), and also on the metallicity and the dust properties of the ionized gas. Since the stellar populations and the gas properties in galaxies evolve as a function of time, we expect the emission lines in H II region spectra to reflect galaxy evolution and also dramatic phenomena like the interruption of the star-formation (i.e. star-formation quenching). Starting from these considerations, in this Chapter we propose a methodology able to identify galaxies which are transiting from the star-forming to the read and dead phase, quenching their star-formation. In particular, our aim is to identify galaxies just after the quenching of the star formation. The approach we are going is based on the use of emission line ratios, and is illustrated in Fig. 3.2.

If the star formation is quenched in a star-forming region, the number of UV hydrogen ionizing photons (i.e. $\lambda < 912$ Å) provided by the central ionizing source declines. In particular, since massive O stars are the first to disappear, the harder UV photons are the first to drop, leading to a softening of the UV ionizing spectrum. As a consequence, high-ionization lines, which can be excited only by the hardest ionizing photons, rapidly disappear; low-ionization lines, which can be produced also by colder O stars and B stars, remain strong at later times.

This allows us to devise a new methodology for identifying quenching galaxies. We search for galaxy spectra characterized by very faint high-ionization lines, like [O III] and [Ne III], but still strong low-ionization lines, like Hα and [O II]. We put into practice our methodology by looking for galaxy spectra with high signal-to-noise (S/N) Hα emission but very low values of the [O III]/Hα and the [Ne III]/[O II] emission line ratios. These lines are observable in a wide range of redshifts (e.g. $0 < z < 2$) with optical and near infrared spectroscopy. In particular, [Ne III]/[O II], despite involving a very faint emission line like [Ne III] λ3869 ([Ne III], hereafter), has the advantage of being basically unaffected by dust extinction, including emission lines which are very close in wavelength. We also investigated the possibility to use a line ratio less affected by dust extinction correction such as the [O III] λ5007/Hβ ([O III]/Hβ, hereafter), which has also the advantage of involving stronger emission lines than [Ne III]/[O II].

In the following, we assume a sharp quenching of the SF as extreme case. Moreover, we illustrate the results obtained if a more realistic, smoother but still short decline of the SF is adopted. This is in agreement with recent studies arguing that quenching processes occurring on 100 – 200 Myr time-scales can be modelled by a sudden interruption of the SF (e.g. Schawinski et al., 2014, Ciesla et al., 2016, Schaefer et al., 2017).

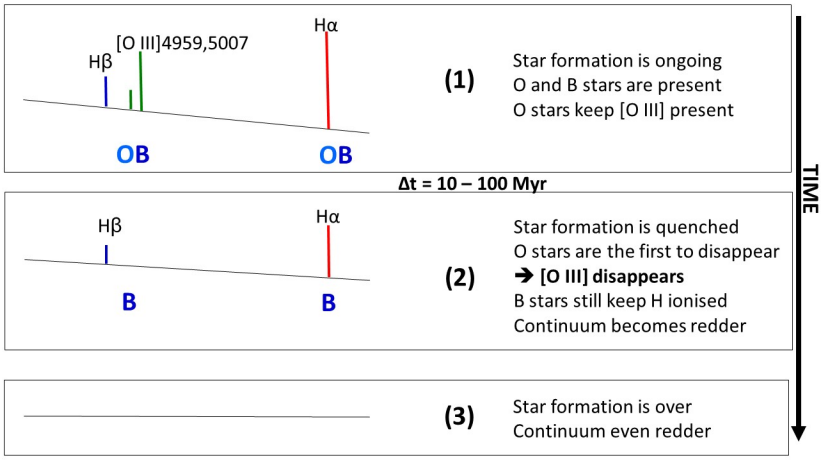

Figure 3.2: Sketch describing the effect of the star-formation quenching on high- and low-ionization potential lines. When the SF is halted, the most massive O stars die on timescales of 10 – 100 Myr. As a consequence, the high-ionization lines, which can be only produced by these stars, disappear from the galaxy spectrum. On the contrary, low-ionization lines, which need the softer photons provided by B stars to be produced, survive at longer times in the spectra (from Quai et al. 2017, submitted).

3.4 Modelling the quenching phase

In order to investigate the behaviour of the proposed emission line ratios during the quenching phase, we simulate star-forming regions until their quiescent phase. Here we describe the main ingredients of our photoionization models.

We consider a star-forming region as formed by a central source of energy, with a given spectral energy distribution (SED) and intensity, surrounded by a spherical cloud. We simulate its final spectrum by means of the photoionization code CLOUDY (Version 13.03, Ferland et al., 1998, Ferland et al., 2013), adopting a plane-parallel geometry (i.e. the simplest geometry allowed by the code), in which the thickness of the photoionized nebula is very small compared to the distance to the photoionizing source.

The shape of the ionizing source is simulated by means of different stellar synthetic spectra, such as the Leitherer et al., 1999 (Starburst99) and Bruzual & Charlot, 2003 (BC03) models.

The adopted Starburst99 synthetic spectra are simple stellar populations (SSPs) with a fixed mass of $M = 10^6\ M_{\odot}$, metallicities Z = 0.004, 0.008, 0.02, 0.04 and a Salpeter initial mass function (IMF) (with $m_{\rm low}$=1 and $m_{\rm up}$=100 $M_{\odot}$). They are computed using Lejeune – Schmutz stellar atmospheres (Lejeune et al., 1997; Schmutz et al., 1992) and Geneva-HIGH 1994 evolutionary tracks (Meynet et al., 1994, Leitherer et al., 1999). This set of ingredients is in agreement with the ones generally used in the literature (e.g. Levesque et al., 2010, Kewley et al., 2001, Dopita et al., 2006).

For BC03 synthetic spectra, we adopt SSPs with metallicities Z = 0.004, 0.008, 0.02, 0.04. In particular, since the default BC03 highest metallicity is Z = 0.05, we interpolate the metallicities to create BC03 models with Z = 0.04, in order to be consistent with the Starburst99 results. These models are normalized to $M = 1\ M_{\odot}$ and assume a Chabrier IMF with $m_{\rm low}$=0.1 and $m_{\rm up}$=100 $M_{\odot}$. The slope of these two IMFs differs at $M < 1\ M_{\odot}$, but we expect this difference not to influence the shape of the final SED, since very low mass stars contribute mostly to the mass of a stellar population rather than to its UV spectral properties. Moreover, since we are interested in emission line ratios, we can neglect the

different mass normalization of the two models.

We parametrize the intensity of the ionizing source by means of the ionization parameter, as described in Sect. 3.2. We adopt two different kind of models, which account for the decrease of the ionization parameter and the decline of the number of ionizing photons due to the quenching process.

1. *Fixed-age models*. To fit with the majority of the literature studies (e.g. Dopita et al., 2006, Levesque et al., 2010, Kashino et al., 2016), we assume the central source to be an SSP with a given metallicity (Z = 0.004, 0.008, 0.02, 0.04) and a fixed age of 0.01 Myr. Moreover, we adopt a grid of decreasing ionization parameters in order to simulate different ionization levels. We assume a grid of fixed-age ionization parameters $\log(U)_0$ going from -3.6 to -2.5 with steps of 0.1 dex, to be consistent with the observations of unresolved star-forming H II regions ($\log(U) \lesssim -2.3$, see Yeh & Matzner, 2012), local H II regions ($-3.2 < \log(U) < -2.9$, see Dopita et al., 2000) and star-forming galaxies (see Moustakas et al., 2006; Moustakas et al., 2010). In these models, given a metallicity, the shape of the ionizing source is fixed, regardless of the ionization parameter, and models with the lowest $\log(U)_0$ can describe star-forming regions, but with very low densities of ionizing photons.

2. *Evolving-age models*. We also construct models which take account of the shape variation of the ionizing SED as a function of time after SF is stopped. This evolution is illustrated in Fig. 3.3 for an SSP of solar metallicity. The UV ionizing flux decreases as a function of time, with harder energies disappearing first, due to the sudden disappearence of the most massive O stars able to produce them. This behaviour is also visible in Fig. 3.4, which shows the time evolution of the number of ionizing photons below different energy thresholds (i.e. the ones relative to the emission lines studied in this Chapter: H and O^+, 13.6 eV; O^{++}, 35 eV and Ne^{++}, 41 eV) and for different metallicities. The number of ionizing photons decreases with time, and its decline is more pronounced for harder energies and higher metallicities. Moreover, the effect of the increased metallicity is more visible at the harder energies, which are more absorbed due to the larger stellar opacities. To account for the softening of the UV ionizing spectrum as a function of time after the SF quenching, in these models we simulate the central ionizing source using an SSP with given metallicity (Z = 0.004, 0.008, 0.02, 0.04) and age going from 0.01 to 10 Myr. In particular, the youngest SSP of 0.01 Myr is taken as representative of a still star-forming region (this kind of assumption is often used in literature, e.g. Kewley et al., 2001, Dopita et al., 2006, Levesque et al., 2010), while older SSPs are used to describe the epochs subsequent to the SF quenching. The still star-forming region can have a ionization state described by one of the fixed-age ionization parameters $\log(U)_0$ defined before, which then evolves with time according to the $Q(H)$ time evolution (see Rigby & Rieke, 2004). Since $Q(H)$ decreases after the SF quenching, we expect the ionization parameter to get lower as a function of time. For this reason, each model with a given age will be characterized by an evolving-age ionization parameter $\log(U)_t$.

For the ionized nebula, we adopt an hydrogen density $n_{\rm H} = 100$ cm^{-3}, which is in agreement with the typical densities in observed star-forming regions (Dopita et al.,

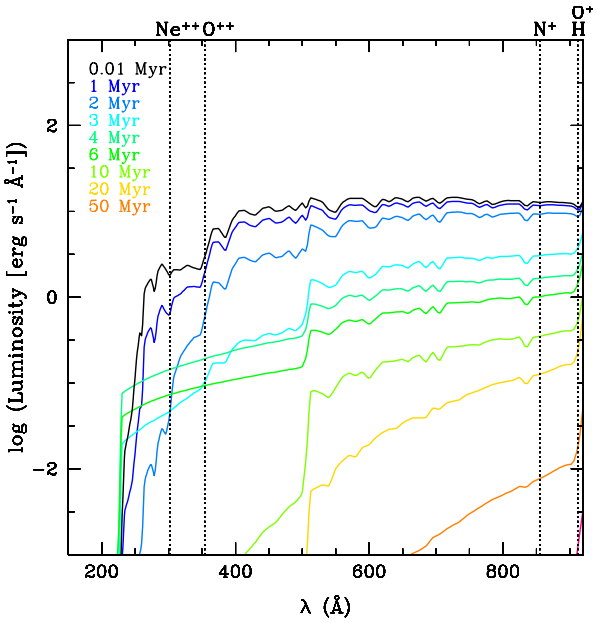

Figure 3.3: Time evolution of a Starburst99 SSP SED with solar metallicity (spectra get older from blue to orange, as reported in the top left of the figure). Black dotted vertical lines indicate the wavelengths corresponding to the ionization energies of the emission lines analysed in this Chapter, as indicated.

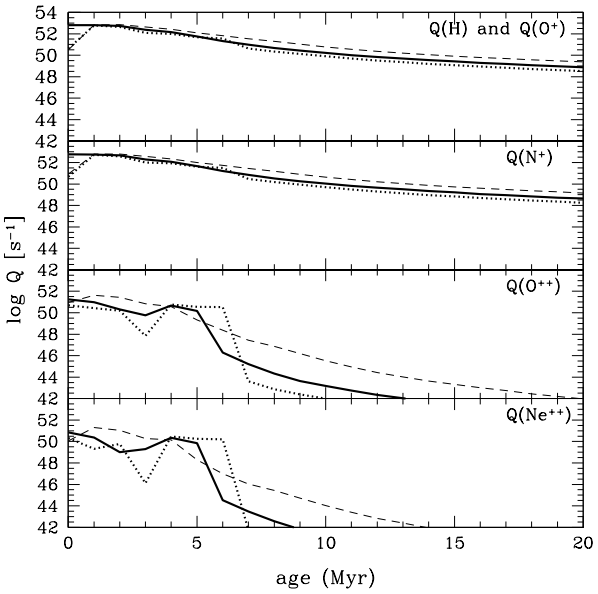

Figure 3.4: Time evolution of the number of photons able to ionize H and O^+, N^+, O^{++} and Ne^{++}, from top to bottom. Note that H and O^+ have the same ionization potential (i.e. 13.6 eV) and thus are illustrated within the same panel. Curves are relative to a Starburst99 SSP with $log(M/M_{\odot}) = 10^6$ and three different metallicities (Z = 0.004, dashed; Z = 0.02, solid; Z = 0.04, dotted).

2000, Kewley et al., 2001, Dopita et al., 2006), and the solar chemical composition by Asplund et al., 2005 (the abundances of the various elements adopted in this Chapter are listed in Table 1 of Dopita et al., 2006). In particular, we match the metallicity of the ionized nebula with the metallicity of the ionizing stellar population[2]. For non-solar metallicities, we linearly rescale the abundance of each element, except for He, C and N, for which we assume the metallicity dependences reported in Dopita et al. (2006). Depletion factors are fixed at the same values regardless of metallicity (e.g. Dopita et al., 2006, Nakajima & Ouchi, 2014). This implies that the dust-to-metal ratio is fixed regardless of metallicity, and that the dust-to-gas ratio is proportional to metallicity (e.g. Issa et al., 1990; Lisenfeld & Ferrara, 1998; Draine et al., 2007; da Cunha et al., 2010). To account for the presence of dust, we adopt the default ISM grain distribution implemented in CLOUDY. However, throughout this Chapter we always use the intrinsic fluxes provided by the CLOUDY code for all the analysed emission lines, i.e. those that not require any correction for the dust extinction.
Finally, since the emission lines we are interested in require very high gas kinetic temperature (i.e. $T > 20,000$ K) to be produced, we stop the calculation at the point in which the kinetic temperature of the gas has fallen down to $T \sim 4,000$ K, since at this temperature not even the hydrogen can be ionized.

3.5 Testing the reliability of the photoionization model

Before describing the behaviour of the proposed quenching diagnostics, in this section we verify the reliability of our models comparing them with data and literature.

3.5.1 Comparison with data

We perform the comparison with data using the Baldwin, Phillips & Terlevich diagram (BPT; Baldwin et al., 1981), which is generally adopted to distinguish star-forming from AGN ionization sources (Veilleux & Osterbrock, 1987, Kewley et al., 2001, Kauffmann et al., 2003, Stasińska et al., 2006). To verify the consistency of our models with real data, we use a sample of $\sim 174,000$ star-forming galaxies extracted from the Sloan Digital Sky Survey Data Release 8 (SDSS DR8, Eisenstein et al., 2011, see Quai et al. 2017, submitted, for details), classified as star-forming on the basis of the BPT diagram itself, using the definition by Kauffmann et al. (2003). Galaxies in this sample have $0.04 \lesssim z \lesssim 0.21$, $9 \lesssim \log(M/M_{\odot}) \lesssim 12$, signal-to-noise ratio (S/N) of the Hα flux > 5 and of the Hβ flux > 3. The threshold of S/N (Hα) has been adopted because we expect just quenched galaxy spectra to be still characterized by relatively strong low-ionization lines (see Sect. 3.3).
The emission line measurements for each object are derived from the MPA-JHU group (Brinchmann et al., 2004) and are corrected for dust extinction assuming the Calzetti extinction curve (Calzetti et al., 2000) and using the Hα/Hβ ratio to estimate the nebular colour excess E(B − V). Starting from the selected sample, in the following sections we consider different subsamples of objects, selected according to the signal-to-noise ratio (S/N) of the emission lines under analysis. Throughout the Chapter, emission lines characterized by a S/N < 2 are regarded as not-detected lines, thus their fluxes are treated as upper limits and set to 2σ. We consider, in particular, upper limits for objects with [O III] λ5007 ([O III], hereafter) and [Ne III] undetected. On the contrary, S/N >

[2] It is important to note that the solar metallicity of the Starburst99 (and BC03) models is slightly higher (Z = 0.02) than the Asplund et al., 2005 one (i.e. Z = 0.016).

2 are associated to emission lines like [O II], [N II] λ6584 ([N II], hereafter) and [S II] $\lambda\lambda$6717,6731 ([S II], hereafter).
As illustrated in Fig. 3.5, models are able to reproduce the bulk of the data distribution in the BPT star-forming branch, with galaxies spanning the entire range of ionization parameters and metallicities considered in our study. The discrepancy of the uppermost envelope of the SF region could be also due to residual contamination by AGN or composite sources (e.g. Stasińska et al., 2006) or to shortcomings related to models. For instance, recent works have argued that, at the present state, many of the synthetic spectra generally used in the literature can produce too soft UV ionizing fluxes, especially at high metallicities (e.g. Levesque et al., 2010). Moreover, first evidences that local galaxies can have higher N/O ratios and/or higher dust-to-metal ratios especially at high metallicities have been found in the very last years (Brinchmann et al., 2013, Pérez-Montero et al., 2013, Wu et al., 2014, Morisset et al., 2016), suggesting that they could help in filling the gaps between models and data. At Z > 0.02, models with different metallicities and ionization parameters overlap between each other. This can be mainly attributed to the fact that the [N II] λ6584/Hα ([N II]/Hα, hereafter) ratio has not a smooth increase with Z, flattening at supersolar metallicities (see Sect. 3.7 for further details). However, defining more sophisticated models able to explain the BPT diagram is beyond the aims of this Chapter and would not influence our studies on the galaxy quenching phases.
It is important to note that the adopted SDSS data are sensitive enough for our methodology, which basically relies on the detection of variations in emission line ratios. Our assumptions of S/N (Hα) > 5 and S/N ([O III]) $\leq$ 2 allow to detect differences between these two lines (and thus variations in their ratio) by up to a factor $\sim$ 10. More precisely, the limiting fluxes for [O III] and Hα in our sample are $\sim 0.32 \times 10^{-16}$ erg s^{-1} cm^{-2} and $\sim 1.8 \times 10^{-16}$ erg s^{-1} cm^{-2}, respectively, and the lowest detected log([O III]/Hα) is $\sim$ –1.5, which corresponds to a difference by a factor $\sim$ 30 between the two lines (cfr. Quai et al, 2017, submitted). Furthermore, the analyzed SDSS individual spectra have a continuum S/N around the [O III] line > 5, which has been proved to be sufficient to provide reasonable measurements of emission line fluxes (e.g. Thomas et al., 2013). This further implies a good sensitivity to variations in ratios involving emission lines in this spectral region.

3.5.2 Comparison with other models

We verify the reliability of our models comparing them with other predictions available in the literature: i.e. those presented in Kewley et al. (2001) (Kew01, hereafter) and those by Levesque et al. (2010) (Lev10, hereafter). In Table 1 we summarize the main parameters characterising Kew01, Lev10, and our model. Fig. 3.6 shows the results within the BPT plane. Note that, to be consistent with the literature, this comparison is performed only in the case of fixed-age models.
Our models are in reasonable agreement with the literature ones, at each metallicity. However, at Z $\geq$ 0.02, the dispersion among different predictions is more pronounced, and in some cases (e.g. Kew01) models produce too high [N II]/Hα values with respect to the data. We also find that, at Z = 0.04, a difference in the [O III]/Hβ vs. [N II]/Hα slope is present. This can be due to the different dust-prescriptions adopted, which lead our models to be dustier than those of Kew01 and Lev10. The discrepancy is larger at higher metallicities, where our models have an higher dust-to-gas ratios with respect to those of the literature (see Sect. 3.4). In particular, when many ionizing photons are provided by the central source (i.e. at high log(U)$_0$ ~ -2), the larger amount of dust

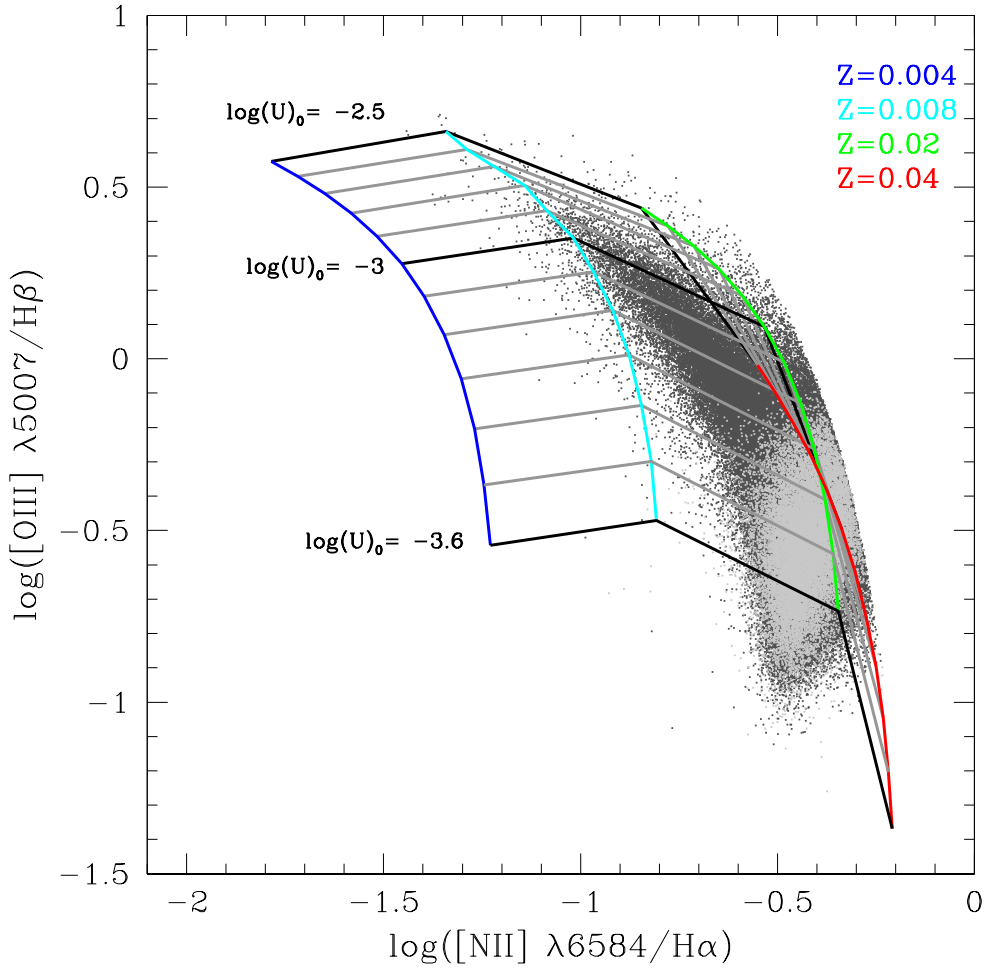

Figure 3.5: Comparison between our models and observations. Dark grey points are galaxies extracted from the SDSS DR8 with S/N(Hα) > 5, S/N(Hβ) > 3 and S/N([N II]), S/N([O III]) > 2, while light grey points are galaxies with S/N([O III])< 2. The superimposed grid is our set of fixed-age models with different metallicities (Z = 0.004 blue; Z = 0.008 cyan; Z = 0.02 green; Z = 0.04 red) and different log(U)$_0$ (going from -3.6 to -2.5 with steps of 0.1 dex from bottom to top). Black curves mark the levels log(U)$_0$ $= -3.6, -3, -2.5$, from bottom to top, as indicated.

in our models amplifies grain photoelectric heating processes, which produce free electrons able to collisionally- excite the [O III]. This increases the [O III]/Hβ ratio more than the Kev01 and Lev01 models, hence producing a steeper slope for our models. At lower $\log(U)_0$, when grain photoelectric heating processes decrease because of the very low number of ionizing photons, there is instead a better agreement among different models.
Note that this does not affect the lowest $\log(U)_0$ regimes (i.e. $\log(U)_0 \lesssim -3.5$), which are the ones relevant in our study. More generally, the discrepancies among different models are related to the different ingredients and photoionization codes adopted for the simulations. In particular, as already mentioned in Sect. 3.5.1, different stellar atmospheres can produce UV SEDs with different slopes, affecting the emission line ratios which are more sensitive to the UV hardness (Schmutz et al., 1992, Hillier & Miller, 1998, Dopita et al., 2000, Pauldrach et al., 2001, Kewley et al., 2001, Levesque et al., 2010). Furthermore, Kew01 models adopt higher depletion factors for some elements (e.g. C and Fe) and thus higher dust-to-metal ratios for a given metallicity. This produces an increase of the gas electron temperature, which favours the cooling from metal optical lines like [O III] and [N II] (e.g. Shields & Kennicutt, 1995, Charlot & Longhetti, 2001; Brinchmann et al., 2013), increasing their fluxes and thus the emission line ratios in which they are involved.

Table 3.1: Main ingredients of our models, Kewley et al. (2001)'s and Levesque et al. (2010)'s ones.

	Our assumptions	Kew01	Lev10
Code	CLOUDY 13.03	MAPPINGS III	MAPPINGS III
Evolutionary tracks	Geneva High 1994	Geneva High 1994	Geneva High 1994
Stellar atmospheres	Lejeune-Shmutz	Lejeune-Shmutz	Paldruach-Hillier
$\log(U)_0$	$-3.6 < \log(U)_0 < -2$	$-3.7 < \log(U)_0 < -2$	$-3.5 < \log(U)_0 < -1.9$
Ionizing source SFH	SSP	SSP	SSP
Ionizing source age	0.01 Myr	0.01 Myr	0.01 Myr
Metallicity	0.001, 0.004, 0.008, 0.02, 0.04	0.004, 0.008, 0.02, 0.04	0.004, 0.008, 0.02, 0.04

3.6 Quenching diagnostics

Before describing how the two emission line ratios mentioned above can help in identifying galaxies which are quenching their SF, in the following sections we describe in more details their behaviour as a function of time, ionization parameter and metallicity, and the relative degeneracies.

3.6.1 Emission lines ratios and their evolution with time

The two proposed emission line ratios are expected to suddenly react to the halt of the SF within a star-forming region. In this regard, Figs. 3.7 and 3.8 show the percentage variation of the emission lines as a function of time from the SF quenching, for different metallicities and initial $\log(U)_0$. Regardless of the initial $\log(U)_0$, high-ionization lines

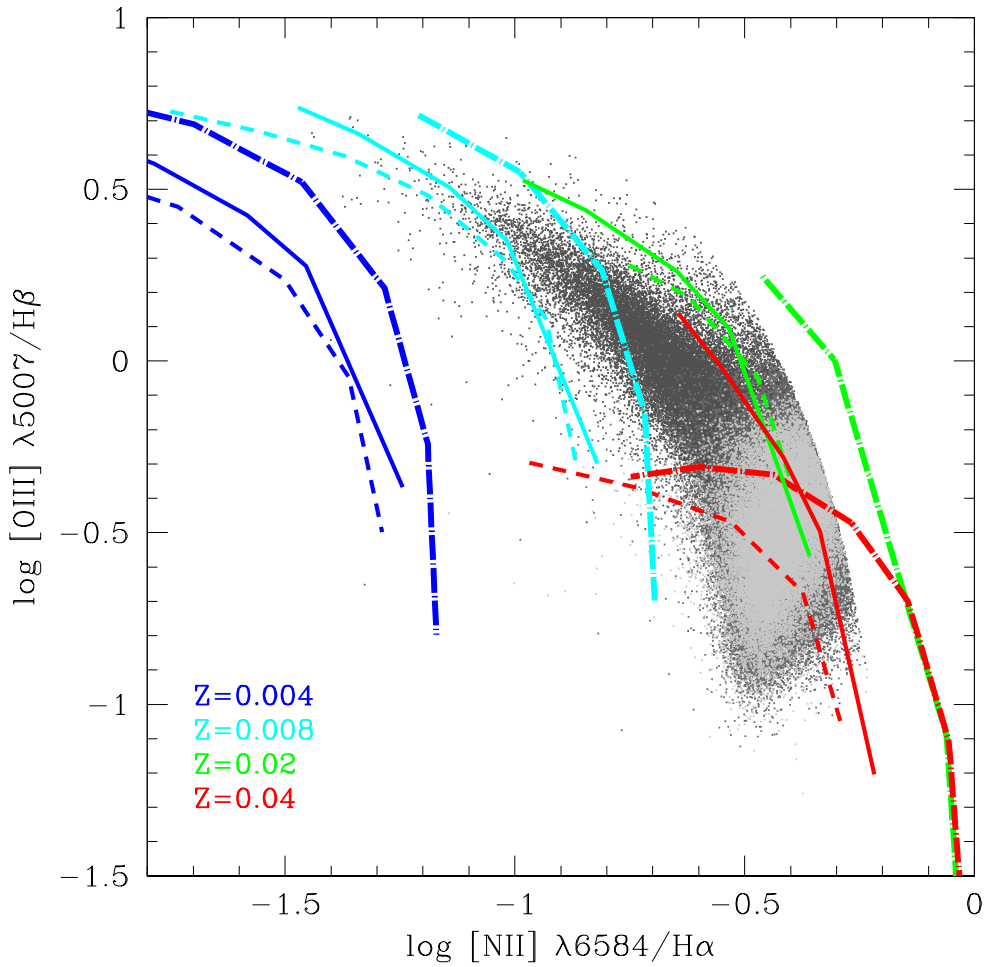

Figure 3.6: Comparison among our models (solid curves), Levesque et al. (2010) (dashed curves) and Kewley et al. (2001) (dotted-dashed curves) predictions, for $-3 < log(U)_0 < -2$. Grey points are the sample extracted from the SDSS DR8, colour coded as in Fig. 3.5. Different colours indicate different metallicities (Z = 0.004, blue; Z = 0.008 cyan; Z = 0.02, green; Z = 0.04, red).

behave differently from low-ionization ones, with the former changing more significantly as a function of the various parameters. For instance, [O III] and [Ne III] drop by more than a factor 10 within the first $2-3$ Myr after the SF quenching, especially at the highest metallicity and the lowest $\log(U)_0$. Moreover, they experience a temporary rise at ~ 4 Myr, which is particularly pronounced at the highest metallicities. This rise can be attributed to Wolf-Rayet (WR) stars, which are more numerous at higher metallicities (Schaller et al., 1992; see also Levesque et al., 2010) and can supply, on short time intervals, very energetic photons able to re-ionize O^{++} and Ne^{++}, producing a temporary increase of the line fluxes. After $5-6$ Myr from the SF quenching, for all metallicities, both [O III] and [Ne III] have declined by a factor ~ 100 with respect to their values in the star-forming phase and, at ~ 10 Myr they are more than a factor ~ 1000 lower than their initial value.
Compared to [O III] and [Ne III], Hα and [O II] have a slower decline as a function of time, which is also delayed with respect to high-ionization lines. [O II], which differently from Hα depends on metallicity, is also less dependent on it than [O III] and [Ne III]. At $5-6$ Myr, when the high-ionization lines definitely drop, [O II] and Hα have declined by a factor ~ 10 less, regardless of metallicity. In particular, it takes $\sim 10-15$ Myr for the low-ionization lines to decline by a factor $\sim 100-1000$. These predictions confirm that just quenched galaxies could lack of high-ionization emission lines, still having relatively strong low-ionization lines in their spectra.

The behaviour of individual emission lines is reflected in the two emission line ratios considered in our study, as illustrated in Fig. 3.9. In particular, both [O III]/Hα and [Ne III]/[O II] decrease for increasing age and metallicity, at each $\log(U)_0$. For both emission line ratios, the decline is more pronounced at higher metallicities, since for a given age, more metallic massive stars have softer UV spectra. Indeed, at $\log(U)_0 = -3$ and at the lowest Z, [O III]/Hα and [Ne III]/[O II] decrease by ~ 0.1 dex and ~ 0.2 dex within ~ 2 Myr from the SF quenching respectively, while at the highest Z they drop by ~ 1.3 dex and ~ 1 dex, within the same time interval. However, regardless of metallicity, the two emission line ratios are characterized by a decline by a factor ~ 10 within ~ 10 Myr from the epoch of the SF quenching. Although fixed-age models assume a fixed shape for the SED of the ionizing source, the ones which are characterized by the lowest $\log(U)_0$ can in some sense describe star-forming regions that are quenching their SF, since low-ionization parameters are related to low numbers of ionizing photons and then to low levels of star formation. For this reason, it can be interesting to investigate the behaviour of the emission line ratios under analysis as a function of both $\log(U)_0$ and $\log(U)_t$. Fig. 3.10 illustrates the case of [O III]/Hα. For Z=0.02, a decline by a factor ~ 10 of this ratio corresponds to a decrease in $\log(U)_t$ by 0.1 dex (starting from an initial $\log(U)_0 = -3$), within a time interval of ~ 2 Myr, while only a more pronounced decrease by ~ 1 dex in $\log(U)_0$ can produce the same effect. Therefore, the decline of [O III]/Hα is more rapid for evolving-age models than for fixed-age ones. This is due to the fact that the former include the additional effect of the UV softening as a function of time.

3.6.2 The influence of different hydrogen densities

The typical hydrogen densities of H II regions are of the order of $n_{\rm H} \sim 100$ cm^{-3}, and are therefore well below the critical densities of the forbidden lines considered in our

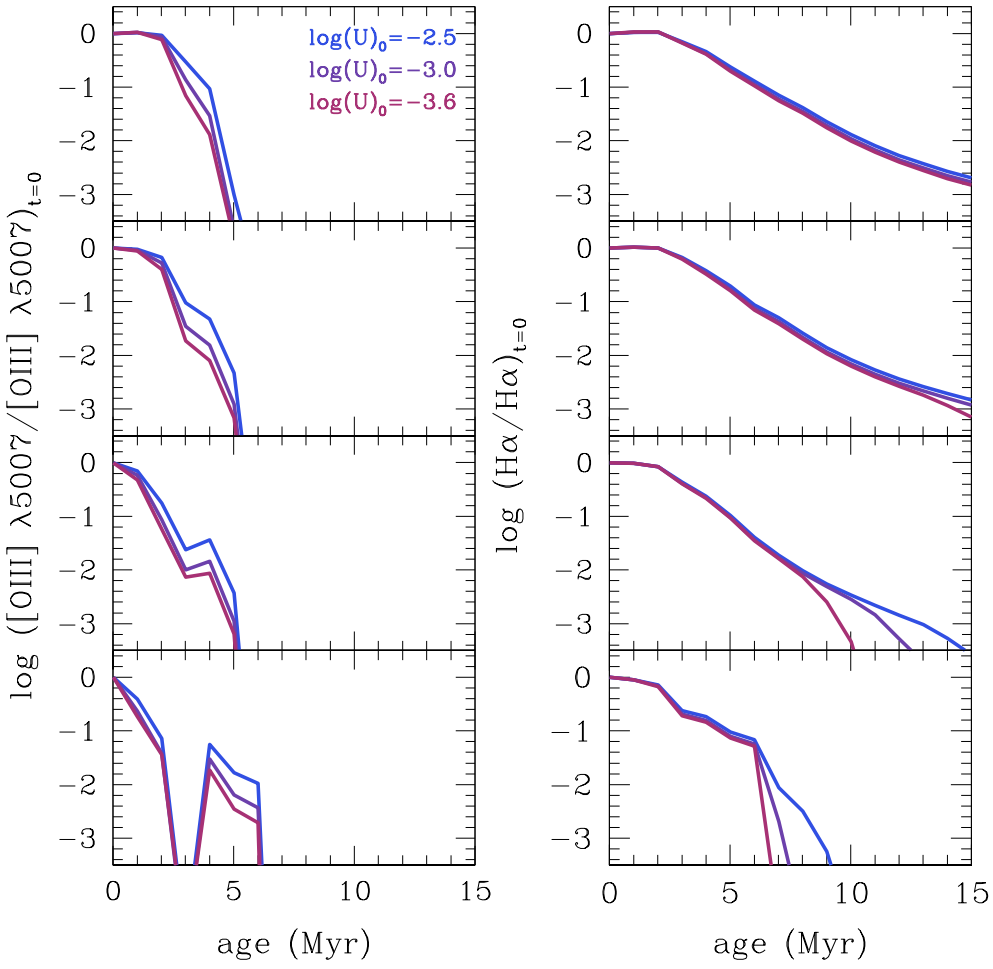

Figure 3.7: Evolution of the line luminosity relative to the initial one at $t = 0$ for [O III] (left) and Hα (right) as a function of time, metallicity and log(U)$_0$. Metallicity (Z = 0.004, 0.008, 0.02, 0.04) increases from the top to the bottom panel. In each panel, we show the results for log(U)$_0$ –2.5, –3, –3.6, with log(U)$_0$ decreasing from blue to red, as indicated.

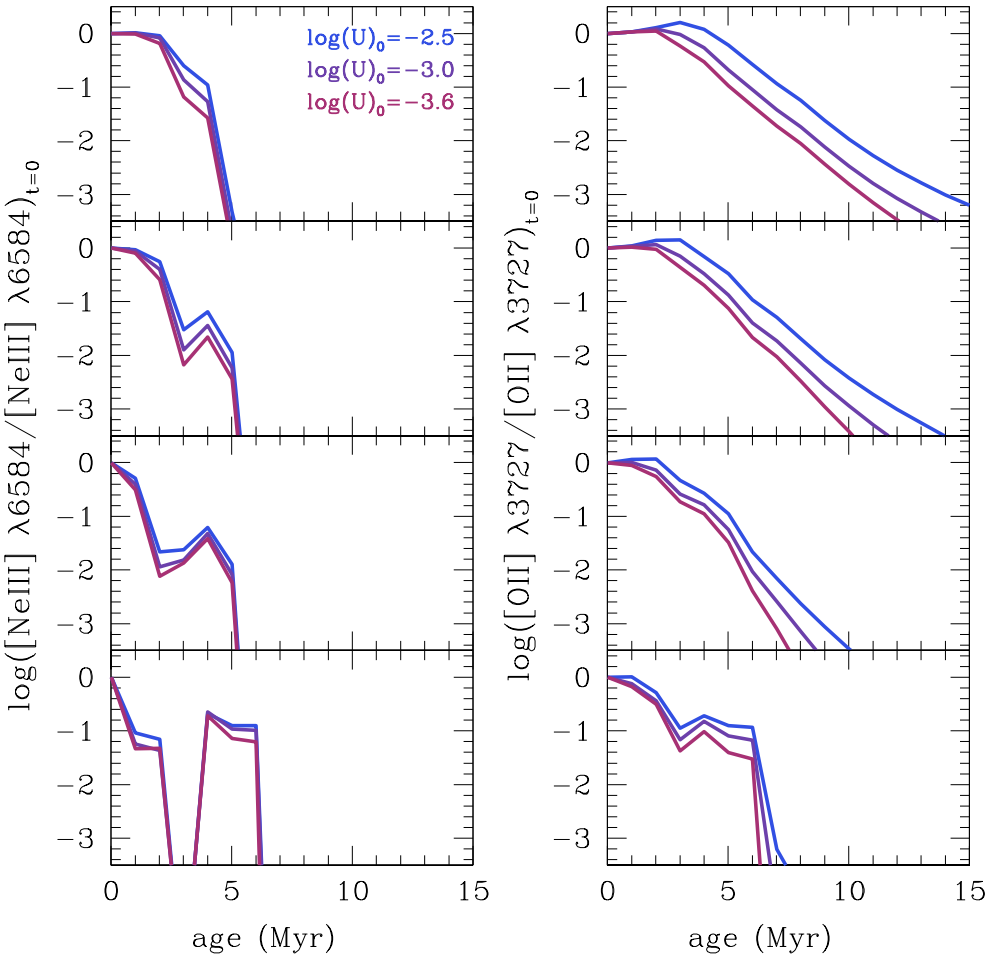

Figure 3.8: Percentage evolution of [Ne III] (left) and [O II] (right) as a function of time, metallicity and log(U)$_0$. Metallicity (Z = 0.004, 0.008, 0.02, 0.04) increases from the top to the bottom panel. In each panel, we show the results for log(U)$_0$ –2.5, –3, –3.6, with log(U)$_0$ decreasing from blue to red, as indicated.

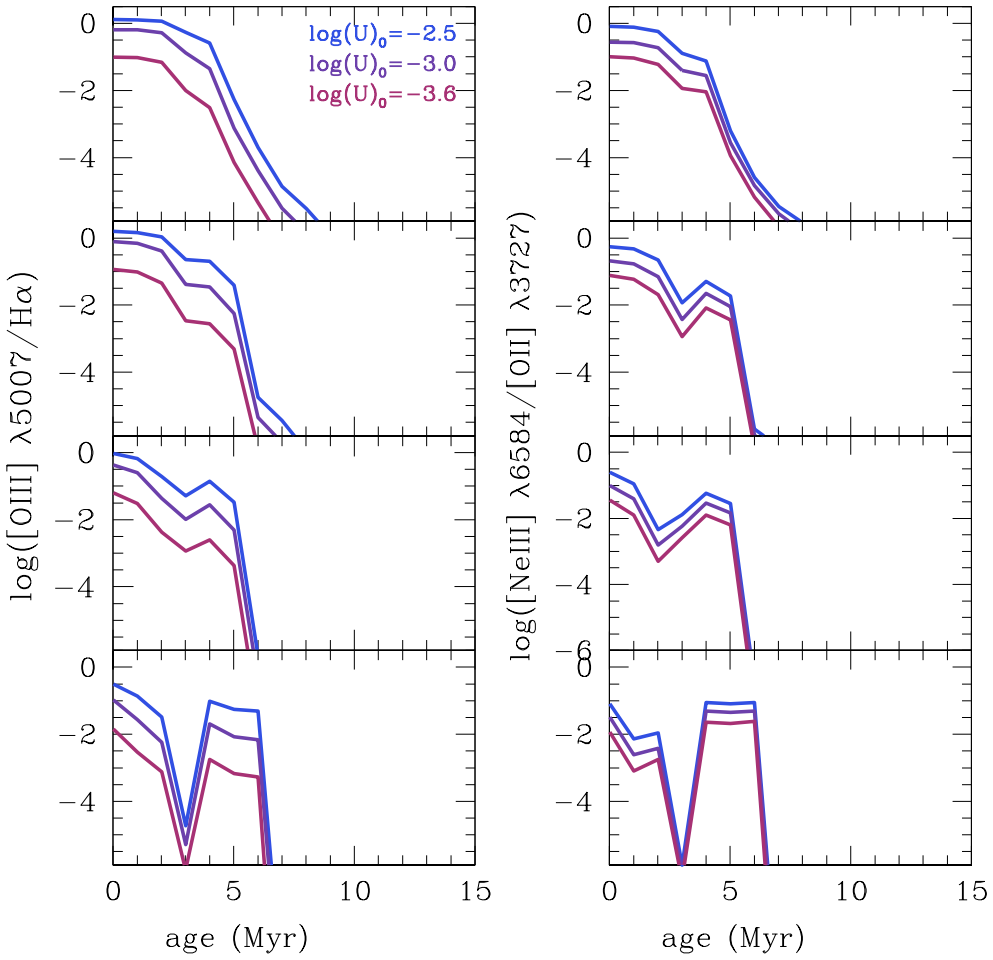

Figure 3.9: [O III]/Hα (left) and [Ne III]/[O II] (right) evolution as a function of time, metallicity and $\log(U)_0$. Metallicity (Z = 0.004, 0.008, 0.02, 0.04) increases from the top to the bottom panel. In each panel, we show the results for $\log(U)_0$ –2.5, –3, –3.6, with $\log(U)_0$ decreasing from blue to red, as indicated.

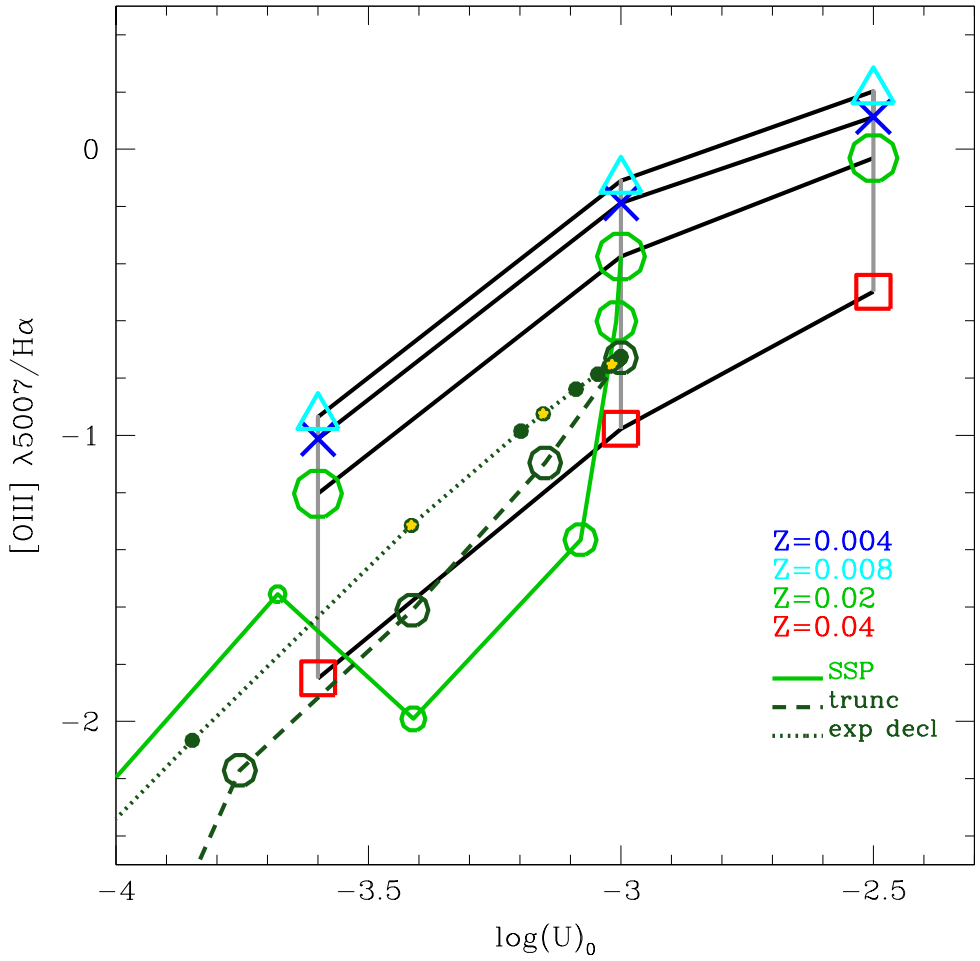

Figure 3.10: [O III]/Hα as a function of log(U)$_0$ and log(U)$_t$. Grey curves connect models with the same log(U)$_0$, for the three log(U)$_0$ $= -3.6, -3, -2.5$ and different metallicity (Z = 0.004 blue; Z = 0.008 cyan; Z = 0.02 green; Z = 0.04 red), while black curves connect models with the same metallicity. For Z = 0.02, evolving-age models for SSP (light green empty circles), truncated (dark green empty circles) and the exponentially declining (dark green filled circles) SFHs are shown (see Sect. 3.6.4 for further details), for an initial log(U)$_0$ $= -3$. The emission line ratio evolution is illustrated with a time step of 1 Myr within the first 10 Myr after quenching, ∼ 20 Myr from 10 to 100 Myr after quenching, and 100 Myr even further. For the exponentially declining SFH, gold small stars mark the values of the emission line ratios corresponding to 10, 80, and 200 Myr after the SF quenching, from the highest to the lowest value of [O III]/Hα.

analysis[3]. However, it can be interesting to investigate how [O III]/Hα and [Ne III]/[O II] are affected by an increase of n_H towards the critical densities (n_{crit}) of [O III], [Ne III] and [O II].
As illustrated in Fig. 3.11, we find that [O III]/Hα increases by only $\sim$ 0.2 dex for n_H < n_{crit}([O III]), i.e. when Hα and [O III] are both increasing due to the increment of ionized hydrogen and free electrons able excite metal ions. On the contrary, when n_H > n_{crit}([O III]), [O III]/Hα rapidly drops, due to the prevalence of collisional on radiative de-excitations for the [O III] line.
The [Ne III]/[O II] ratio has a more complex behaviour, since it involves two forbidden lines. In particular, it increases by $\sim$ 0.5 dex for n_H < n_{crit}([O II]), while it starts to rapidly increase when n_{crit}([O II]) is reached and [O II] saturates. This trend is inverted when also n_{crit}([Ne III]) is reached.
In general, we find that zero-age models with high-n_H can produce the same [O III]/Hα values as quenching ones with low-n_H (and zero age models with low-n_H can produce the same [Ne III]/[O II] values as quenching ones with high-n_H), at each metallicity. This means that our models can in principle be affected by the n_H degeneracy. However, this holds true for $n_H \gtrsim 4$, which is much larger than the typical n_H in H II regions. This allows to exclude the very low [O III]/Hα and [Ne III]/[O II] found in this Chapter to be related to density rather than quenching effects. Finally, we notice that the sudden drop of the emission line ratios after a few Myr from the SF quenching is present regardless of n_H.

3.6.3 The influence of different synthetic stellar spectra

In this section we verify if the results illustrated in Sect. 3.6 are influenced by the use of different synthetic spectra to describe the central ionizing source. Fig. 3.12 illustrates a comparison between Starburst99 and BC03 models, in the case of $\log(U)_0 = -3$ and for the four metallicities considered in this Chapter. The general behaviour of [O III]/Hα and [Ne III]/[O II] obtained using BC03 models is in agreement with the ones resulting from Starburst99 spectra. Both emission line ratios decline by a factor $\sim$ 10 within $\sim$ 10 Myr from the quenching of the SF, at each metallicity. After the SF shutdown, the behaviour of the two emission line ratios is more uneven in the case of BC03 models than for Starburst99 ones. This is probabily due to the different stellar atmospheres (see Charlot & Longhetti, 2001) and evolutionary tracks (see Bruzual & Charlot, 2003) used to compute the models. For instance, BC03 models are based on the Padova1994 evolutionary tracks (Bressan et al., 1994), which are characterized by a higher number of WR stars with respect to the Geneva-HIGH 1994 ones (as discussed in Bruzual & Charlot, 2003). This can give more pronounced discontinuities in the emission line ratios at the very early ages after the SF quenching. The time at which the two emission line ratios begin to definitely drop is the same in the case of BC03 and Starburst99 spectra. After this epoch, the time required to have a decrease by a factor $\sim$1000 is slightly higher for BC03 models, with a shift of $\sim 1-3$ Myr for both emission line ratios. Apart from these small differences, we can conclude that our methodology is valid also when BC03 models are adopted. This is an interesting result, since BC03 models are generally used only to describe more advanced evolutionary phases of galaxy evolution (e.g. Leitherer et al., 1999, Bruzual & Charlot, 2003, Chen et al., 2010).

[3]($n_{crit\,[OIII]} \sim 7 \times 10^5$ cm^{-3}, $n_{crit\,[NeIII]} \sim 1.1 \times 10^7$ cm^{-3}), $n_{crit\,[OII]} \sim 1 \times 10^4$ cm^{-3}).

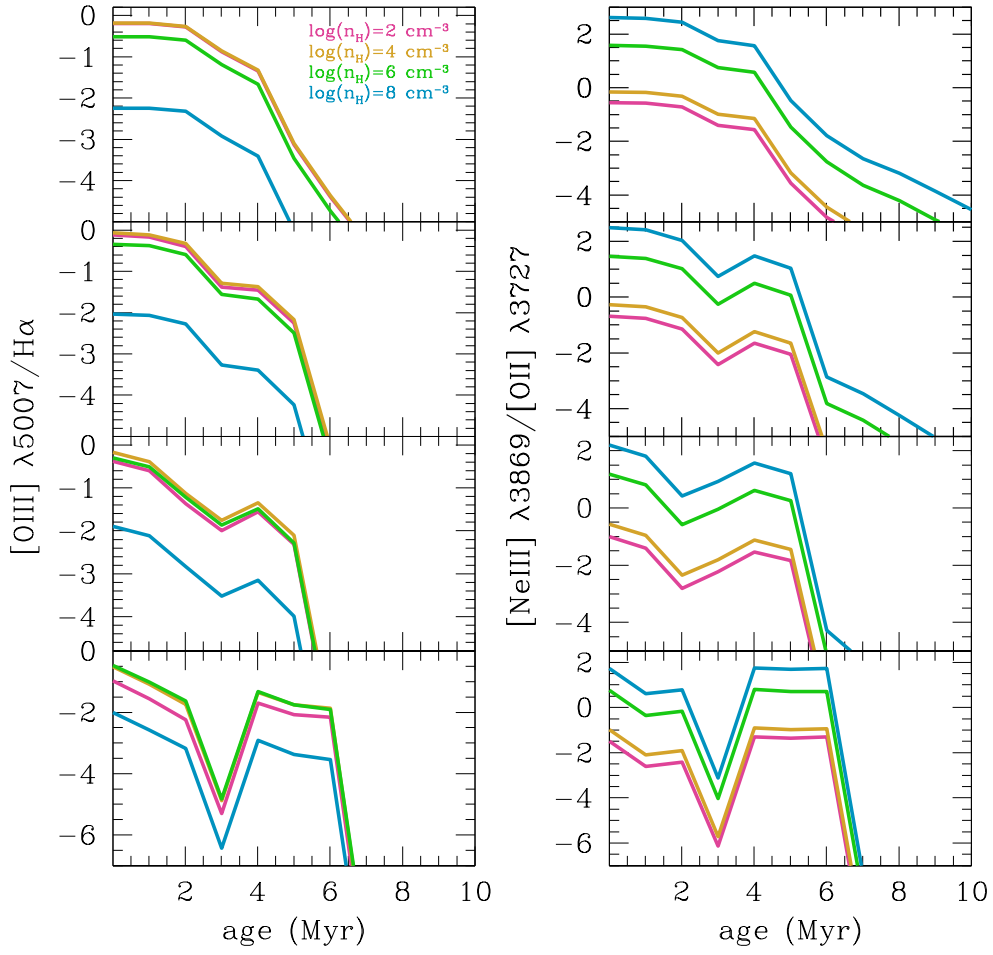

Figure 3.11: [O III]/Hα and [Ne III]/[O II] time evolution for different values of $n_{\rm H}$, and log$(U)_0$= − 3. The hydrogen density increases from log$(n_{\rm H})$=2 (which is our default value) to log$(n_{\rm H})$=8, from pink to cyan, as labelled. Metallicity (Z = 0.004, 0.008, 0.02, 0.04) increases from the top to the bottom panel.

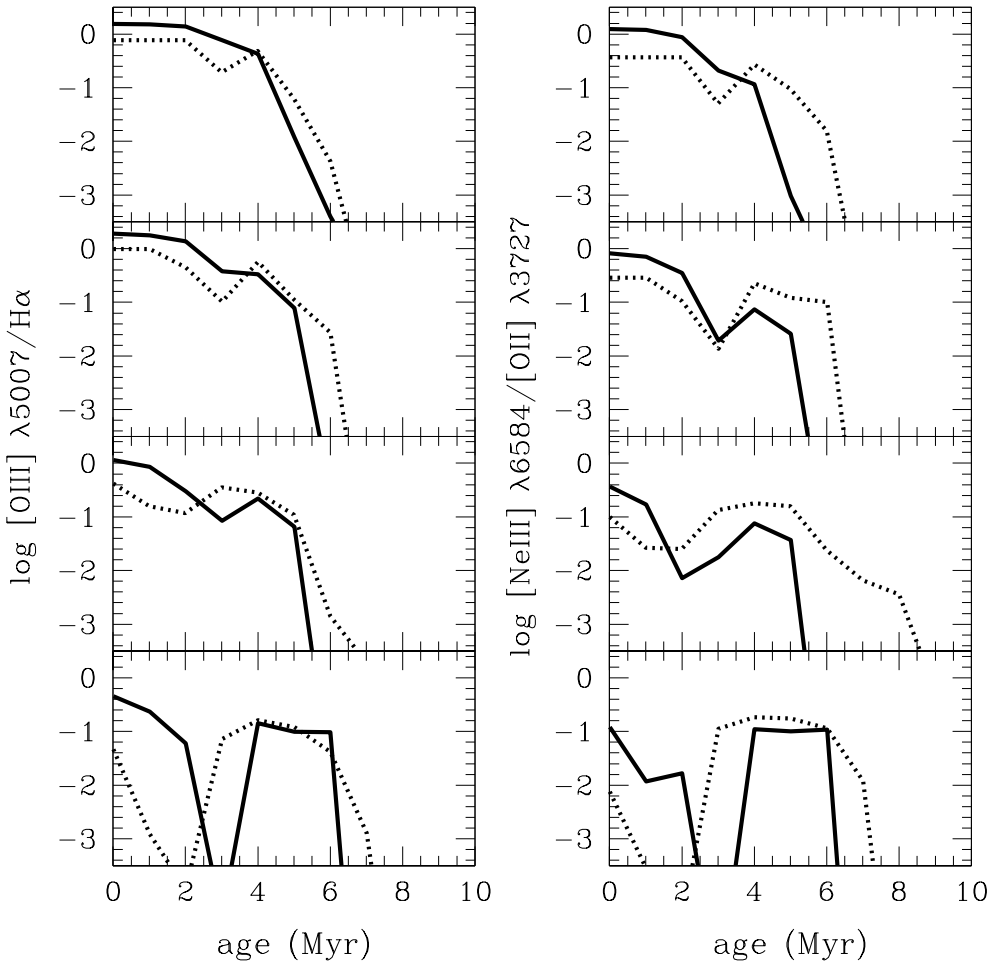

Figure 3.12: Comparison between [O III]/Hα and [Ne III]/[O II] obtained assuming Starburst99 (solid curves) and BC03 (dotted curves) models to simulate the central ionizing source, assuming $\log(U)_0 = -3$. Metallicity (Z = 0.004, 0.008, 0.02, 0.04) increases from the top to the bottom panel.

3.6.4 The influence of different star formation histories

The instantaneous SF quenching modelled so far can be considered an extreme case, which allows to better show the strength of our approach to probe SF quenching on very short time-scales. In this section we investigate how the behaviour of [O III]/Hα and [Ne III]/[O II] changes if different star-formation histories (SFHs) and if a more realistic and smoother SFHs are assumed. In particular, using Starburst99 models, we analyse the case of a truncated SFH, with SFR = 1 $M_{\odot}$ yr^{-1} up to 200 Myr and zero at older ages, and the case of a smoother decline described by an exponentially declining SFR (i.e. SFR $\propto e^{-t/\tau}$), with $\tau = 200$ Myr, since this is the SFH shape generally assumed to describe local star-forming galaxies (e.g. Bell & de Jong, 2001). For the truncated SFH, a SFR = 1 $M_{\odot}$ yr^{-1} is chosen to match the typical SFRs of SDSS star-forming galaxies (Brinchmann et al., 2004, Whitaker et al., 2014) at stellar masses comparable with the ones of our sample. For the exponentially declining SFH, models are normalized to 10^6 $M_{\odot}$. Moreover, we do not consider very high values of $\tau > 200$ Myr, since in this case the SFH would extend at much larger times, incompatible with our assumption that galaxies are quenching their SF. Furthermore, larger τ's have been demonstrated to produce galaxies which never leave the blue cloud (e.g. Schawinski et al., 2014).
For both SFHs, we consider Z = 0.02 and an initial ionization level log(U)$_0 = -3$. In particular, to be consistent with the SSP case (see Sect. 3.6), for the truncated SFH we attribute log(U)$_0 = -3$ at the time corresponding to the last act of SF (i.e. 200 Myr in this case). For the exponentially declining SFH, log(U)$_0 = -3$ is instead associated to the age at which $Q(H)$ begins to drop (~ 10 Myr), since we are interested in the epochs at which the SF starts to quench. Moreover, these choices allow to avoid, at very early times $t < t_{\rm MS}$(O stars) (i.e. $\sim 2 \times 10^7$ yr), the short transient phase during which a rapid rise of ionizing photons characterizes both SFHs (see Madau et al., 1998), also reflecting on the two emission line ratios under analysis (see Fig. 3.13).
Fig. 3.14 shows the time evolution of [O III]/Hα and [Ne III]/[O II] for the three assumed SFHs, starting from the time of quenching. For the truncated SFH stopping at 200 Myr, the two emission line ratios drop by a factor ~ 10 within ~ 2 Myr and by more than a factor ~ 1000 within ~ 10 Myr from the quenching of the SF, similarly to the SSP case.
In the case of an exponentially declining SFR, instead, they decrease following the decline of the SFR. In particular, we find that the star-forming region takes ~ 80 Myr to become quiescent, reaching specific star-formation rate (sSFR) $\sim 10^{-11}$ yr^{-1} (which are typical of quiescent galaxies) and, within this time interval, both [O III]/Hα and [Ne III]/[O II] decrease by a factor ~ 2. This decline corresponds to a decrease in log(U)$_t$ by only ~ 0.2 dex, as illustrated in Fig. 3.10, implying that, when smoother SFHs are considered, log(U)$_t$ has a smoother decline. Moreover, ~ 500 Myr are necessary for the two emission line ratios to decline by a factor $\sim$10.
It is interesting to note that the value of the two emission line ratios at the age at which the SF stops (200 Myr for the truncated and ~ 10 Myr for the exponentially declining SFH) is lower by a factor ~ 2 for more complex SFHs than for a 0.01 Myr SSP with the same log(U)$_0 = -3$. Therefore, if an ionizing stellar population forms stars continuously on a longer time interval, its SED at the time of quenching is softer than the SED of a stellar population which forms all its stars into a single burst. This can be due to the accumulation of long lived stars contributing mostly to the flux at longer wavelengths. Moreover, the temporary increase of [O III]/Hα and [Ne III]/[O II] due to Wolf-Rayet stars is less evident for more complex SFHs than for the SSP case, since, even after the SF quenching, the evolution is dominated by the numerous generations of stars formed

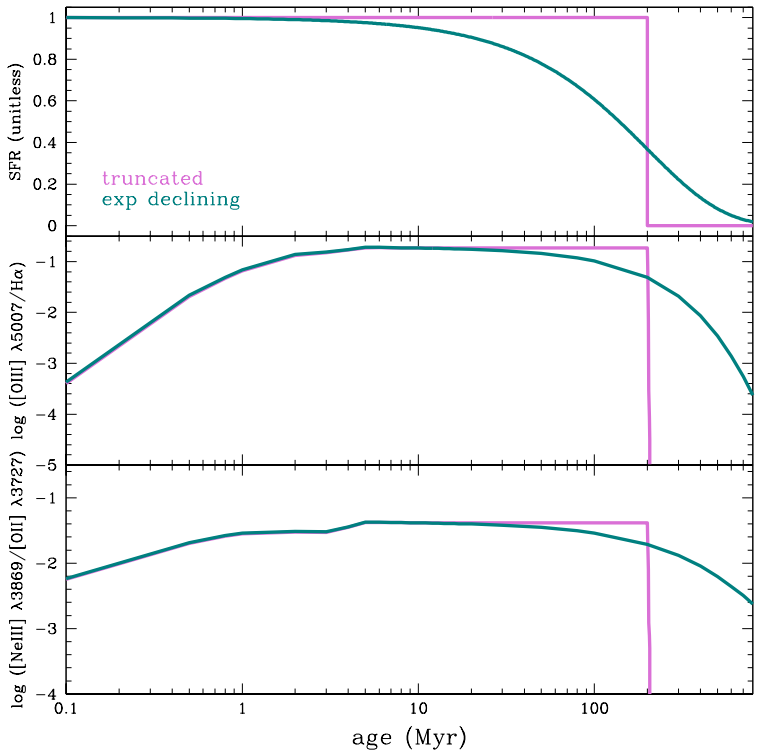

Figure 3.13: SFR, [O III]/Hα and [Ne III]/[O II] emission line ratios as a function of time for the truncated and the exponentially declining SFHs, Z = 0.02 and $t = 0$. In the top panels, the SFRs have different scales due to the different definitions of the two SFHs (described in the text). In both cases of truncated and exponentially declining SFH, the fast rise before the time of quenching is visible, as described in the text.

during time rather than by the short lived WR stars.
All these trends confirm that the decline of [O III]/Hα and [Ne III]/[O II] takes place regardless of the shape of the assumed SFH and that very low values of these emission line ratios are expected whether galaxies have abruptly quenched their SF or they have gradually reached low levels of SF.

3.6.5 The time evolution of optical colours

The softening of the SED associated to the SF quenching also implies an evolution of galaxy colours with time. Since we are analyzing optical SDSS spectra, in this section we focus on the intrinsic $(u - r)$ optical colour, showing its evolution as a function of time in Fig. 3.15. In particular, the three analyzed quenching SFHs are compared to a continuous SFH with SFR = 1 $M_\odot$ yr^{-1} and to a quenching SFH with SFR = 1 $M_\odot$ yr^{-1} until 500 Myr and zero at later ages. The colour reddening is fast for the quenching SFHs, and colours are always redder than the colours of a continuous SF model even when a significant population of old stars has already been built up (i.e. after $\sim$ 500 Myr - 1 Gyr). We find that the typical $(u - r)$ colours of green valley ($1.5 \lesssim (u - r) \lesssim 2.5$,

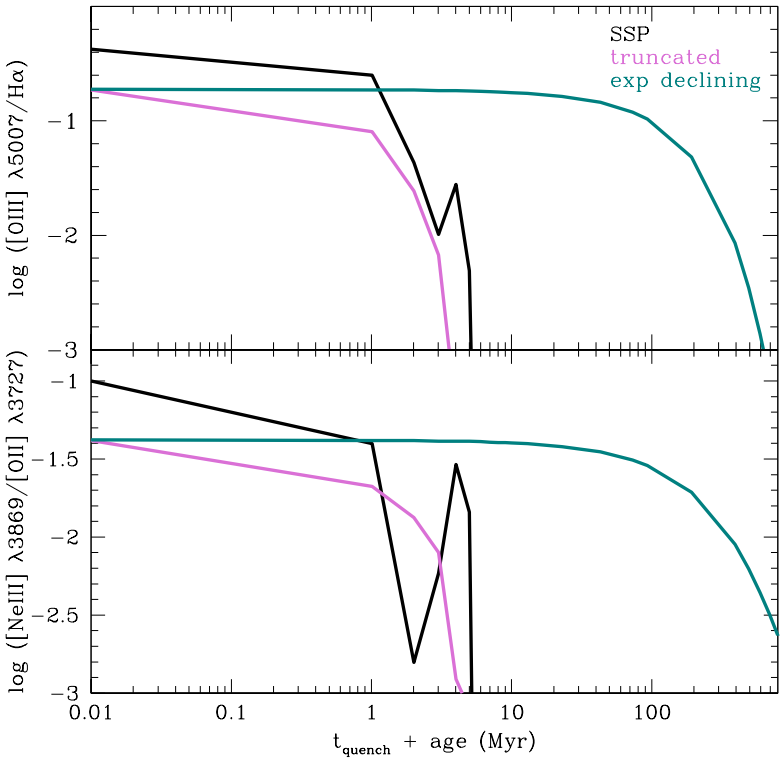

Figure 3.14: [O III]/Hα and [Ne III]/[O II] emission line ratios as a function of time for different SFHs and Z = 0.02. The SSP (black curve), truncated (violet curve) and the exponentially declining (green curve) SFHs are shown up to $\sim$ 800 Myr from the time of quenching (indicated as $t_{\rm quench}$).

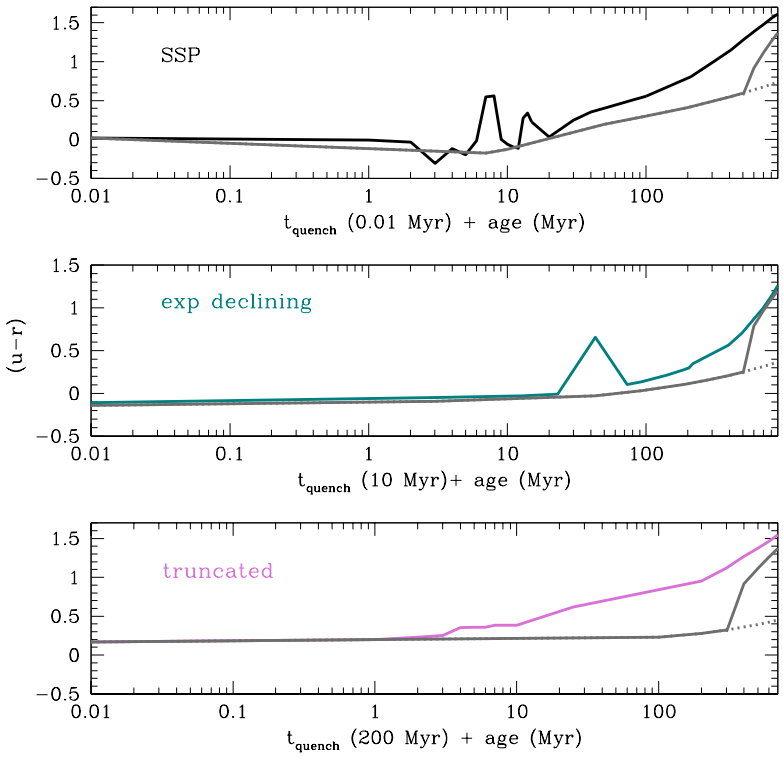

Figure 3.15: Time evolution of the optical $(u-r)$ colour, for solar metallicity and different SFHs. Black, violet and green curve refer to the SSP, truncated and exponentially declining SFHs considered in this Chapter. Grey dotted and solid curves refer to a continuous SFH with SFR = 1 $M_{\odot}$ yr^{-1} and to a truncated SFR with SFR = 1 $M_{\odot}$ yr^{-1} until 500 Myr and zero at later ages, respectively. From top to bottom, we show the colour evolution within 900 Myr from the quenching time of the SSP (i.e. 0.01 Myr), exponential ($\sim$ 10 Myr) and truncated ($\sim$ 200 Myr) SFHs considered in this Chapter.

depending on mass) or red sequence ($(u-r) \gtrsim 2-3$) galaxies (Schawinski et al., 2014) are reached at later times (i.e. $\sim$ 1 Gyr) with respect to the time-scales considered so far (i.e. $\sim$ 10 – 100 Myr). This happens even when an old stellar population is already present for a continuous SF model at the time of the SF halt (as in the case of the 500 Myr-truncated SFH). It is important to note that all these trends refer to an individual quenching stellar population and could thus be diluted by the mutual effects of the multiple stellar populations inside a galaxy which are experiencing different evolutionary stages.

3.6.6 The expected fractions of quenching candidates

In the previous sections we found that [O III]/Hα and [Ne III]/[O II] are very sensitive to the SF quenching and that star-forming galaxies characterized by low values of these two emission line ratios might be objects caught in the act of quenching. However, the precise time-scales that the emission line ratios are able to trace depend on the SFH of the central ionizing source. Deriving these time-scales can be useful to understand what is the physical phenomenon associated to the SF quenching and to estimate the

fraction of galaxies observed in the phase of quenching. In particular, the faster the SF is quenched, the faster the galaxies move from the blue cloud to the red sequence, and the less they clump in the transition zone. To estimate the percentages of objects which are expected to be in the quenching phase, we use the following eq. 3.9:

$$F_{QG} = t_Q / t_{DM} = t_Q \times sSFR \ , \tag{3.9}$$

where F_{QG} is the expected fraction of quenching galaxies, t_Q is the time needed for the emission line ratios to decrease by a factor ~ 10 (i.e. ~ 10 Myr for the SSP/truncated case and ~ 500 Myr for the exponentially declining SFH, see Sect. 3.6) and t_{DM} is the doubling-mass time (e.g. Guzmán et al., 1997, Madau & Dickinson, 2014), which we consider as a proxy of the typical life-time of a SF galaxy (Guzmán et al., 1997 and Greis et al., 2016). In particular, since the typical sSFRs of SF galaxies with redshift and masses comparable to ours (i.e. $0.2 < z < 0.4$ and $9 < \log(M/M_{\odot}) < 12$) range from $\sim 10^{0.3}$ Gyr^{-1} to $\sim 10^{0.1}$ Gyr^{-1} (e.g. Karim et al., 2011), we can deduce that the typical t_{DM} for our sample range from ~ 3 Gyr to ~ 10 Gyr, increasing for increasing mass.
The expected fractions of quenching galaxies are ~ 0.06 % – 0.2 % for the SSP/truncated SFHs and to ~ 5 % – 15 % for the exponentially declining one, respectively, decreasing for increasing mass. It is interesting to note that, once that a complete sample of quenching candidates is selected from a SF galaxy sample, the observed fractions F_{QG} derived from data can help in disentangling what are the effective time-scales of the quenching mechanism at Chapter. However, degeneracies (see Sect. 3.7) and especially observational limits (e.g. the limiting fluxes of the analyzed emission line) can hamper the detections of the whole population of existing quenching candidates. Therefore, the derived percentages should be considered as lower limits, as well as the inferred quenching time-scales.

3.7 Mitigating the ionization - metallicity degeneracy

One of the limitations of our methodology is the metallicity degeneracy. Indeed, since higher metallicity ionizing SEDs are softer than lower metallicity ones due to the larger opacity of the ionizing stars (see Fig. 3.4), they can have the same effects on the emitted spectrum and emission line ratios as quenched, low-ionization ones. Reducing this degeneracy is extremely important for our analysis, in order to exclude objects whose [O III]/Hα and [Ne III]/[O II] are low because of high metallicities rather than low ionization. The main effect of the metallicity degeneracy is illustrated in Fig. 3.16, for $\log(U)_0 = -3$. The same value of an emission line ratio can be produced by different combinations of age (i.e. $\log(U)_t$) and metallicity. In particular, younger star-forming regions with higher metallicity can produce the same results as older star-forming regions with lower metallicity. This occurs for both [O III]/Hα and [Ne III]/[O II].

To mitigate the effects of the metallicity degeneracy, we suggest the use of independent pairs of emission line ratios, depending separately on ionization and metallicity as much as possible. In particular, we combine [O III]/Hα and [Ne III]/[O II] with the [N II] λ6584/[O II] λ3727 ([N II]/[O II], hereafter) emission line ratio, whose behaviour in our model as a function of the stellar metallicity is illustrated in Fig. 3.17, for a fixed age of 0.01 Myr. Here we also compare [N II]/[O II] with other two metallicity indicators, i.e. [N II]/Hα (e.g. Pettini & Pagel, 2004; Denicoló et al., 2002, Nagao et al., 2006) and [N II] λ6584/[S II] $\lambda\lambda$6717,6731 (e.g. Nagao et al., 2006) ([N II]/[S II], hereafter). While the [N II]/Hα and [N II]/[S II] ratios flatten at high metallicities (Kewley & Dopita, 2002, Levesque et al., 2010) and have a larger dependences on the ionization level, [N II]/[O

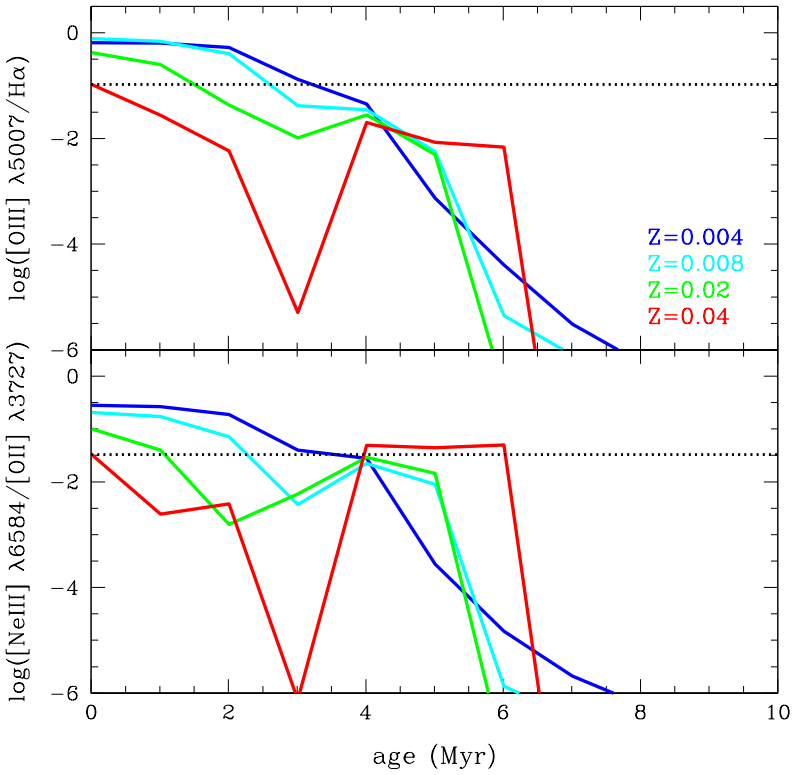

Figure 3.16: [O III]/Hα (top) and [Ne III]/[O II] (bottom) as a function of time, for $\log(U)_0 = -3$, and different metallicities (Z = 0.004, blue; Z = 0.008, cyan; Z = 0.02, green; Z = 0.04, red). In each panel, the black dotted line marks the initial value of the emission line ratios for Z = 0.04.

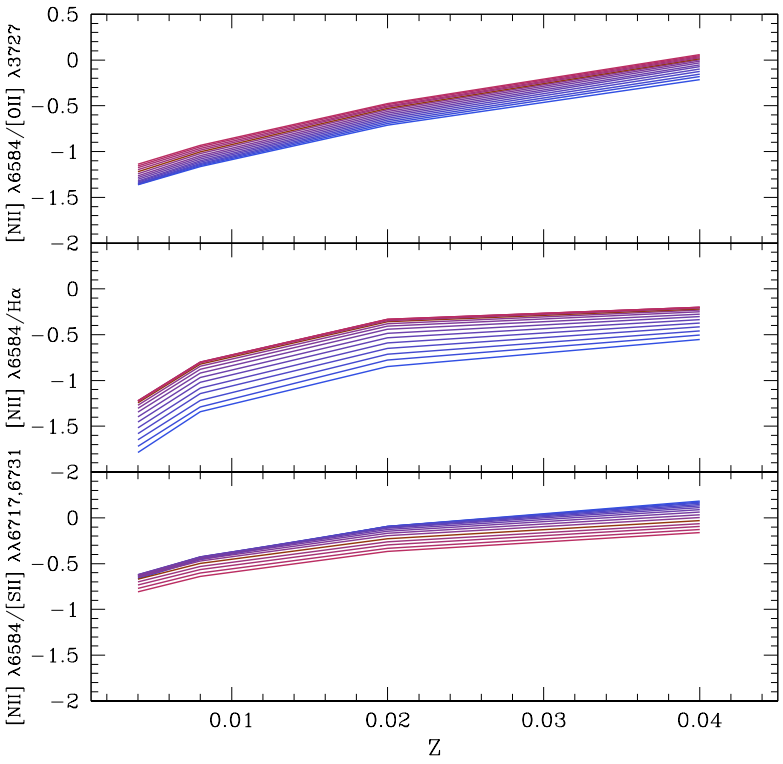

Figure 3.17: Comparison between [N II]/[O II], [N II]/Hα and [N II]/[S II] as a function of metallicity and log(U)$_0$. Colours are coded as in Fig. 3.7.

II] scales smoothly from low to high abundances and has a little dependence on log(U)$_0$ (e.g. van Zee et al., 1998, Dopita et al., 2000, Kewley & Dopita, 2002). Moreover, even if the [N II]/[S II] ratio is less affected by reddening effects (it involves emission lines which are closer in wavelength), it has a weaker dependence on metallicity with respect to [N II]/[O II], which has also the advantage of including stronger, and thus more easily detectable, emission lines. Therefore, it can be preferable once that the observed emission lines are corrected for dust extinction. In the following, in order to mitigate the metallicity degeneracy, we combine the two proposed quenching diagnostics with the [N II]/[O II] ratio.

3.8 Identifying galaxies in the quenching phase

In the previous sections we found that galaxies which have quenched their SF in the recent past can be characterized by low values of the [O III]/Hα and the [Ne III]/[O II] emission line ratios. In this section, we test the reliability of our approach by applying it to the SDSS sample described in Sect. 3.5.1, and analyzing the properties of some of the extreme candidates selected. However, it is important to remind that it is beyond the scope of this Chapter to identify a complete sample of quenching candidates and to investigate their detailed properties, for which we refer to Quai et al. (2017, submitted). Our methodology consists in selecting galaxies with high S/N Hα in their spectra and

lying at the lowest envelope (i.e. lowest $\log(U)_0$) of the SF galaxy distribution within the [O III]/Hα vs. [N II]/[O II] diagnostic diagram. Following the results discussed in Sect. 3.7, this plane is able to mitigate the metallicity degeneracy. Since [O III]/Hα and [N II]/[O II] are affected by dust extinction, we corrected the involved emission lines adopting the Calzetti extinction curve (Calzetti et al., 2000) and using the Hα/Hβ ratio to estimate the nebular colour excess $E(B-V)$. It is worth noting that, since the metallicity degeneracy strongly affects the [O III]/Hβ vs. [N II]/Hα plane, we do not use it to identify possible quenching candidates, although all the objects lying below log([O III]/Hβ)< – 0.5 would fulfill our selection criterion (see Fig. 3.5).

As it is possible to note from Fig. 3.18, the bulk of the data distribution lies within a range of fixed-age ionization parameters going from $\log(U)_0 = -3$ to $\log(U)_0 = -3.6$, and spans the entire metallicity range of our models (the discrepancy between data and models at high values of [N II]/[O II] can be explained as in Sect. 3.5.1). The median of the data distribution can be described by $-3.2 \lesssim \log(U)_0 \lesssim -3$ decreasing for increasing metallicity, in agreement with the literature results concerning star-forming galaxies at low redshifts (e.g. Dopita et al., 2006, Nakajima & Ouchi, 2014, Shirazi et al., 2014, Hayashi et al., 2015, Kashino et al., 2016, Onodera et al., 2016). Given this latter consideration, we also show evolving-age models characterized by $\log(U)_0 = -3$ at the time in which the SF stops, both in the SSP and the smoother SFHs cases (see Sect. 3.6.4), for Z = 0.02. We find that the initial value of the [O III]/Hα ratio is lower for smoother SFHs than for SSPs, as already discussed in Sect. 3.6.4. Furthermore, for the exponentially declining SFH, the decrease of [O III]/Hα is very slow, with the [O III]/Hα values corresponding to the first 10 Myr after the SF quenching accumulating within $\lesssim 0.1$ dex.
Since within this diagnostic diagram metallicity effects are separated from ionization ones, at each [N II]/[O II] (i.e. at each metallicity), objects with the lowest [O III]/Hα ratios could be considered as quenching candidates. Starting from this, we select a subsample of 10 extreme objects with [O III]/Hα below the values corresponding to the lowest $\log(U)_0 = -3.6$ and with S/N([O III]) < 2. This ionization level is consistent with the quiescent phase of SSP evolving-age models, reached ~ 2 Myr after quenching and corresponding to $\log(U)_t \sim -3.2$. If smoother SFHs are assumed, these very low levels of [O III]/Hα are instead reached ~ 200 Myr after the SF quenching, at $\log(U)_t \sim -3.4$.
The 10 selected objects are not detected in [O III] and they have upper limits $\lesssim$ – 1.1 on the OIII/Halpha ratio. Moreover, basing on our models of [N II]/[O II] and on Tremonti et al. (2004) models, they have intermediate metallicities (i.e. log([N II]/[O II]) ranging from $\sim$ – 1 to $\sim$ – 0.4), and a faint [Ne III] emission line with S/N([Ne III]) < 2 (see Sect. 3.5.1). This is compatible with our suggestion that galaxies that have quenched their SF in the recent past can be characterized by the absence of high-ionization lines. Moreover, it confirms that the two proposed emission line ratios are complementary in the identification of quenching candidates.
Fig. 3.19 illustrates the 10 objects in the [Ne III]/[O II] vs. [N II]/[O II] diagnostic diagram. Within this plane, the candidates have apparently high [Ne III]/[O II] ratios but, since [Ne III] is undetected, these values are actually upper limits, thus the real [Ne III]/[O II] ratios of the 10 objects can be much lower than the illustrated ones. The same holds for all the objects lying in the upper right or outside the model grid in Fig. 3.19, which are characterized by 2 < S/N([Ne III]) < 4.

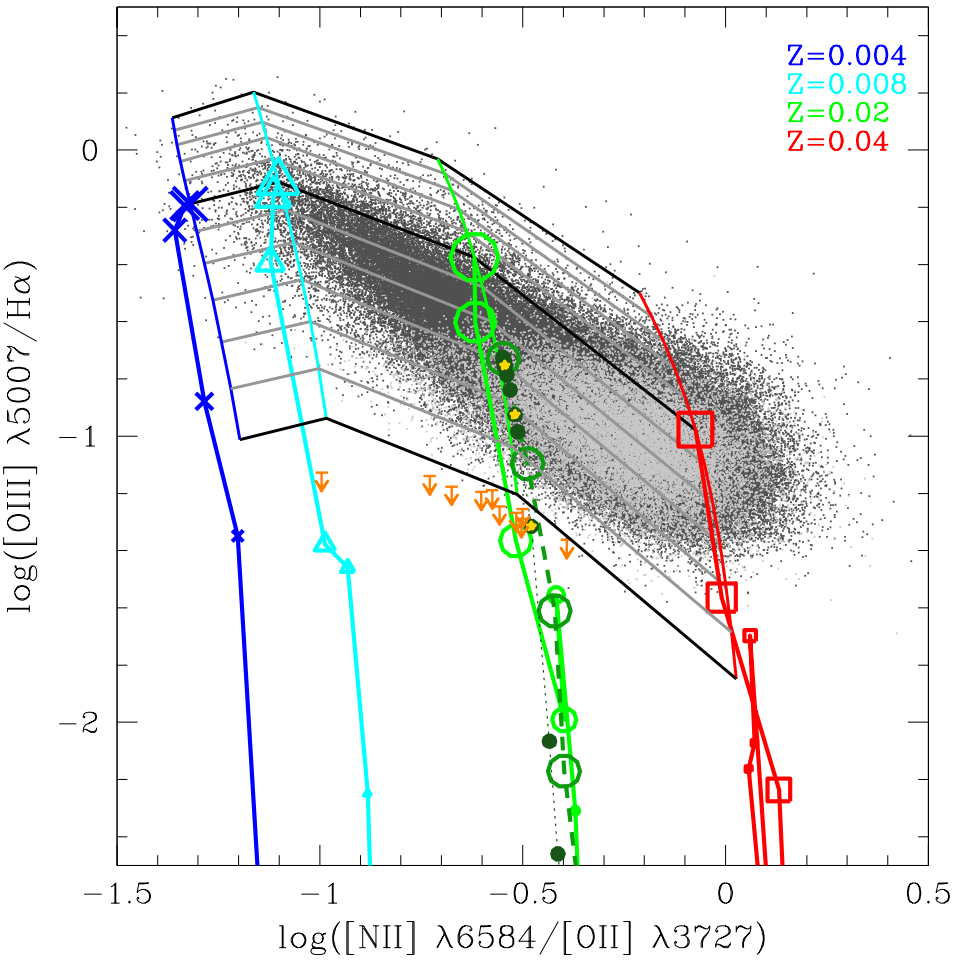

Figure 3.18: Quenching candidates within the [O III]/Hα vs. [N II]/[O II] plane. Dark grey points are galaxies extracted from the SDSS DR8 with S/N(Hα) > 5, S/N(Hβ) > 3 and S/N([N II]), S/N([O II]), S/N([O III]) > 2, while light grey points are galaxies with S/N([O III]) < 2. The superimposed grid is our set of fixed-age models with different metallicities, as in Fig. 3.5. Colored curves associated to different symbols are evolving-age models with an initial $\log(U)_0 = -3$ (with symbol size decreasing for increasing mass) for the four considered metallicities and with a time step of 1 Myr. For Z = 0.02, evolving-age models obtained for the truncated (dark green empty circles) and the exponentially declining (dark green filled circles) SFHs are shown with a time step of 1 Myr within the first 10 Myr after quenching, $\sim$ 20 Myr from 10 to 100 Myr after quenching, and 100 Myr even further. For the exponentially declining SFH, gold small stars mark the values of the emission line ratios corresponding to 10, 80, and 200 Myr after the SF quenching, from top to bottom. Orange downward arrows are the 10 extreme quenching candidates with S/N([O III]) < 2.

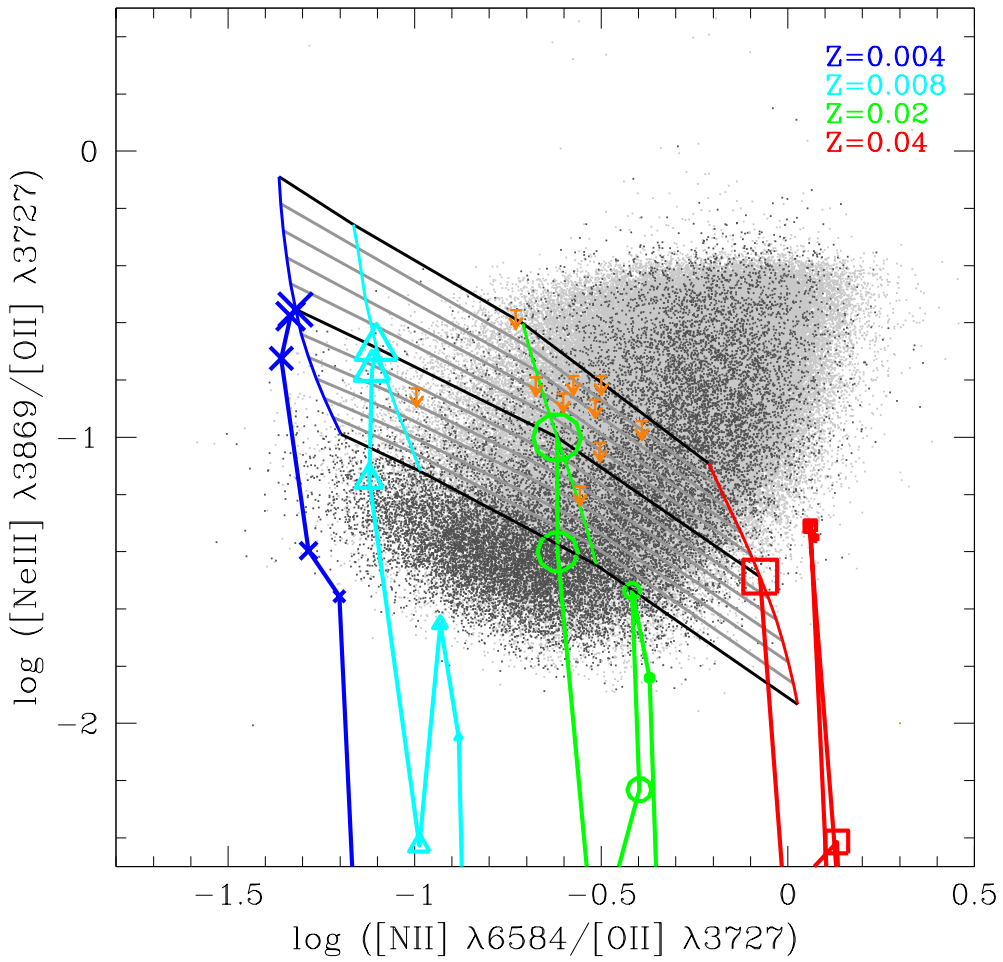

Figure 3.19: Quenching candidates within the [Ne III]/[O II] vs. [N II]/[O II] plane. Dark grey points are galaxies extracted from the SDSS DR8 with S/N(Hα) > 5, S/N(Hβ) > 3, and S/N([N II]), S/N([O II]), S/N([Ne III]) > 2, while light grey points are galaxies with S/N([Ne III])< 2. Colours and symbols are defined as in Fig. 3.5. Orange downward arrows are the 10 extreme quenching candidates with S/N([O III]) < 2.

3.8.1 Properties of the quenching candidates

In this section we illustrate the main properties of the 10 selected quenching galaxies, verifying if they are compatible with a recent quenching of the SF.
Figs. 3.20 and 3.21 illustrate the candidate spectra, corrected for dust extinction adopting the Calzetti extinction curve (Calzetti et al., 2000) and the Hα/Hβ ratio to estimate the nebular colour excess E(B − V). In particular, we applied the same correction for both the continuum and the emission lines. Spectra lack of strong absorption Balmer lines, which are characteristic of the post-starburst phase. This indicates that the candidates may have been caught in an earlier evolutionary phase with respect to the post-starburst (E+A, K+A) one (e.g. Dressler & Gunn, 1983, Couch & Sharples, 1987, Poggianti et al., 2008). Moreover, they have strong Hα and [O II] lines, in agreement with our predictions that low-ionization lines decrease by a small factor with respect to high-ionization ones in just quenched objects (cfr Sect. 3.6). Fig. 3.21 shows the median stacked spectrum of the 10 candidates obtained by stacking the individual spectra before and after applying the correction for dust extinction. In this latter case we assumed the Calzetti et al. (2000) extinction curve and the same nebular colour excess E(B − V) for both emission lines and continuum. The 10 candidates have $0.2 \lesssim \mathrm{E(B-V)} \lesssim 0.8$, with a mean $\mathrm{E(B-V)} \sim 0.5 \pm 0.2$. The large E(B − V) of some of them explain why the stacked spectrum derived from individual spectra corrected for dust extinction is significantly bluer than the one derived from dust-extincted spectra. We find that, even after the stacking, which increases the S/N of the individual spectra, the stacked spectrum has very faint high-ionization lines in both cases. This confirms that the absence of the high-ionization emission lines is a real feature and not an artifact due to low signal in the individual spectra.
The 10 candidates have high Hα luminosities L(Hα) (as expected from the evolution described in Sect. 3.6), ranging from 10^{40} to 10^{42} erg/s/Å, and a median SFR $\sim 1.4 \pm 1.7\ M_{\odot}\ yr^{-1}$. However, we remind that the usual recipes to convert L(Hα) into SFR cannot be applied to our galaxies because most O stars are missing compared to a galaxy where star-formation is still ongoing. Therefore, the L(Hα)-derived SFRs represent the past SFRs (i.e. the ones before the quenching) and thus should be considered as upper limits. We also find that the 10 candidates have Elliptical and S0 morphologies. We refer to Quai et al. (2017, submitted) for a detailed discussion about the typical morphologies of complete samples of quenching candidates and how they relate to the parent population of SF galaxies.
The nature of the 10 quenching candidates is also shown in Fig. 3.22, which illustrates the $(u-r)$ – mass diagram for our sample. Following Schawinski et al. (2014), we corrected colours for dust extinction assuming the colour excess of the stellar continuum, defined as $\mathrm{E_s(B-V)} = 0.44 \times \mathrm{E(B-V)}$, where E(B − V) is the nebular continuum adopted so far (Calzetti et al., 2000). Colours are compatible with the evolution discussed in Sect. 3.6.5 at early times after the SF halt, and are bluer than the green valley $(u-r)$ colours (corrected for dust extinction) derived by Schawinski et al. (2014). This suggests that the 10 galaxies may be at the beginning of the quenching process, not being yet as red as green valley galaxies. Furthermore, it is interesting to note that they have $\log(\mathrm{M/M_{\odot}}) \sim 10$, compatible with the mass of the passive galaxy population building up at low-intermediate redshifts (e.g. Pozzetti et al., 2010).

Since the [O III]/Hα and the [N II]/[O II] emission line ratios are affected by dust extinction, we verified if our results are influenced by the choice of the extinction law assumed to correct our data.We adopt the Allen (1976) extinction curve, comparing the

results with the ones obtained so far using the Calzetti et al. (2000) one. We quantify the effect of the two extinction laws on the emission line ratios [O III]/Hα and [N II]/[O II] by calculating the median extinction differences ($A_{[NII]} - A_{[OII]}$) and ($A_{[OIII]} - A_{H\alpha}$) for both cases. We find that ($A_{[OIII]} - A_{H\alpha}$) is $\sim$ 0.35 in both cases, while ($A_{[NII]} - A_{[OII]}$) differs by $\sim$ 0.03 mag, with the Allen (1976) extinction curve producing slightly higher [N II]/[O II]. This very small discrepancy leads us to conclude that our approach is not influenced by the choice of the extinction curve.

We also investigated if our results are valid when dust-free diagnostic diagrams are used, which would have the advantage of producing results not relying on the assumption of an extinction law. Fig. 3.23 shows the 10 quenching candidates within the [O III]/Hβ vs. [N II]/[S II] plane, which involves ratios between emission lines closer in wavelength, and thus is basically unaffected by dust extinction. Although the discrepancy between models and data at the highest metallicities is still present, within this plane the 10 galaxies are located at the lowest edge of the data distribution, suggesting that the [O III]/Hβ can be used as a dust-free, quenching diagnostic, similarly to [O III]/Hα. However, the [N II]/[S II] ratio, although being appropriate to avoid the uncertainties related to dust extinction, involves weaker lines like [S II] and is less efficient in separating different metallicities compared to [N II]/[O II], also producing larger errors relative to the covered range in metallicity.

Since the 10 selected objects are just an example of quenching candidates, they do not represent a complete sample of just quenched galaxies and cannot be used to derive reliable quenching candidate fractions (see Sect. 3.6.6). We refer to Quai et al (2017, submitted) for a detailed discussion about them.

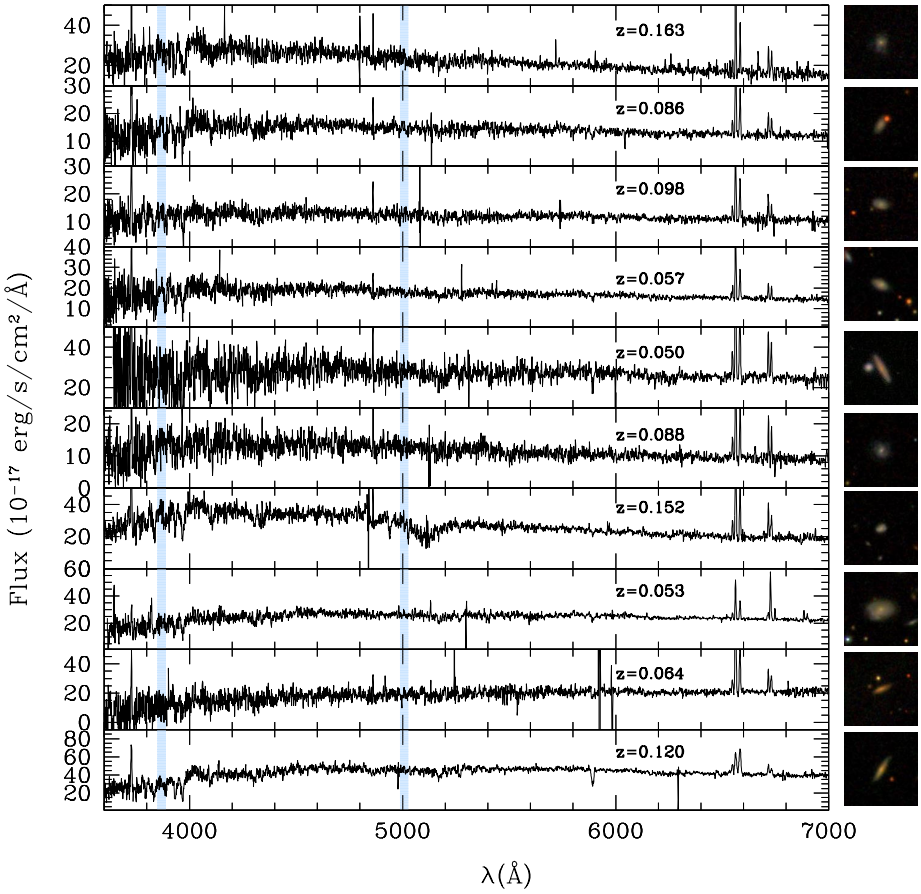

Figure 3.20: Spectra of the 10 extreme quenching candidates corrected for dust exinction using the nebular colour excess $\mathrm{E(B-V)}$. *The black curves are spectra corrected for dust extinction. The emission lines discussed in this Chapter are indicated on the top of the figure (from left to right: [O II], [Ne III], [O III], H*α*, [N II], [S II]), and light blue shaded regions mark the not-detected [Ne III] and [O III] lines. Redshifts are reported for each object and morphologies are shown on the right side of each spectrum.*

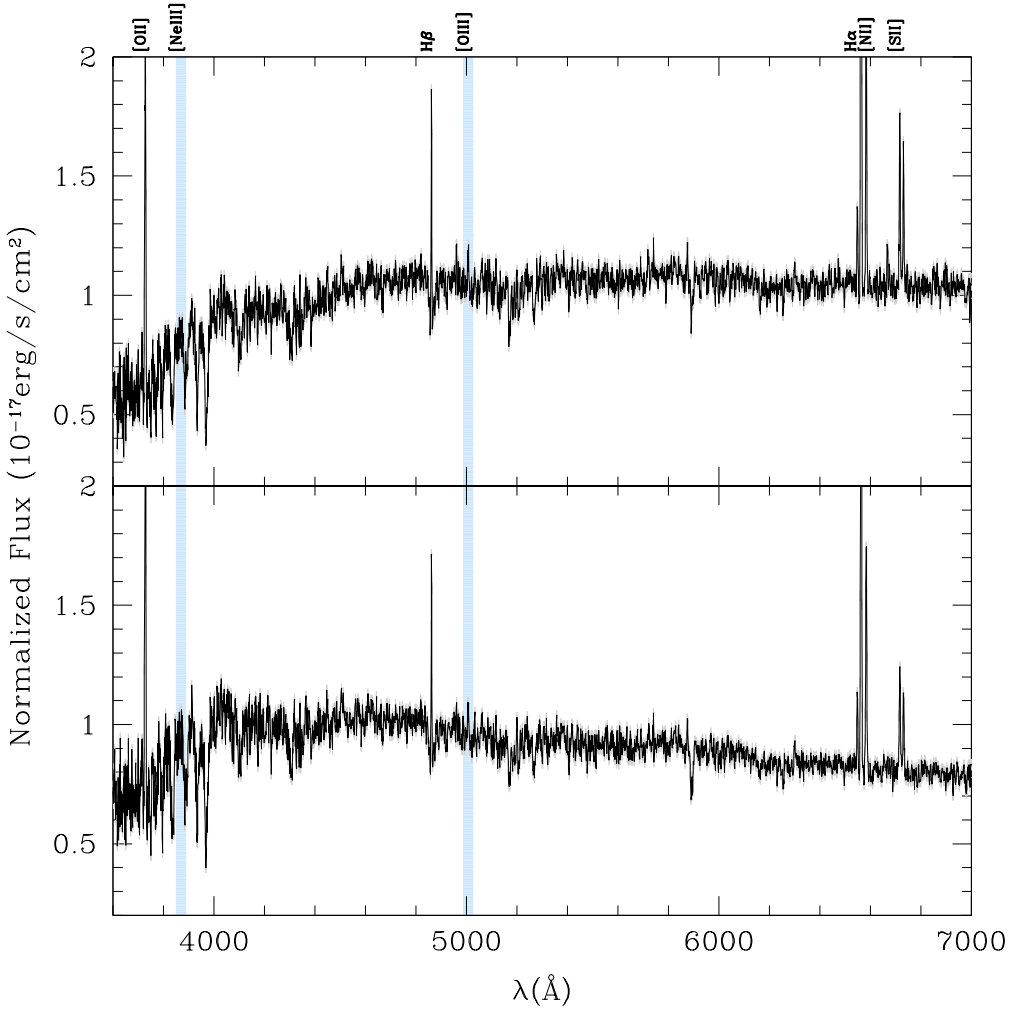

Figure 3.21: Median stacked spectrum of the 10 extreme quenching candidates. The top panel illustrates the median stacked spectrum (black curve) obtained from the dust-extincted quenching candidate spectra. The bottom panel shows the median stacked spectrum (black curve) obtained correcting the quenching candidates spectra for dust extinction, adopting the nebular $\mathrm{E(B-V)}$ *(Calzetti et al., 2000) for both continuum and emission lines. Errors are shown in grey. The emission lines discussed in this Chapter are indicated on the top of the figure (from left to right: [O II], [Ne III], [O III],* $\mathrm{H}\alpha$*, [N II], [S II]). Light blue shaded regions mark the not-detected [Ne III] and [O III] lines.*

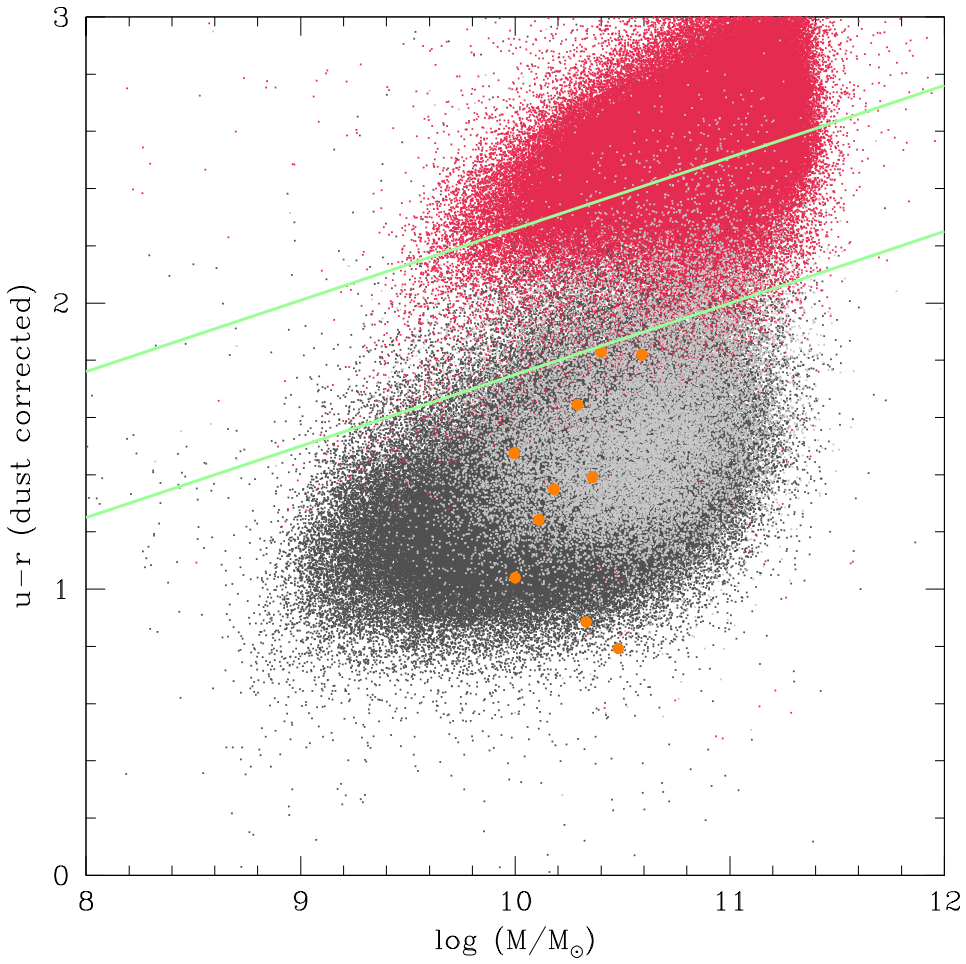

Figure 3.22: colour – mass diagram for our galaxy sample ($(u-r)$ colours are corrected for dust extinction). Dark grey points are galaxies extracted from the SDSS DR8 with S/N(Hα) > 5, S/N(Hβ) > 3 and with S/N([N II]), S/N([O II]) and S/N([O III]) > 2, while light grey points are galaxies with S/N([O III]) < 2. Red points are galaxies with S/N (Hα) < 5 and/or EW(Hα) > 0 (see Quai et al. 2017, submitted for further details). Orange circles are the 10 extreme quenching candidates with S/N([O III]) < 2. Green lines mark the green valley defined by Schawinski et al. (2014). This is taken as reference since it was derived from a sample of low-redshift galaxies, as ours.

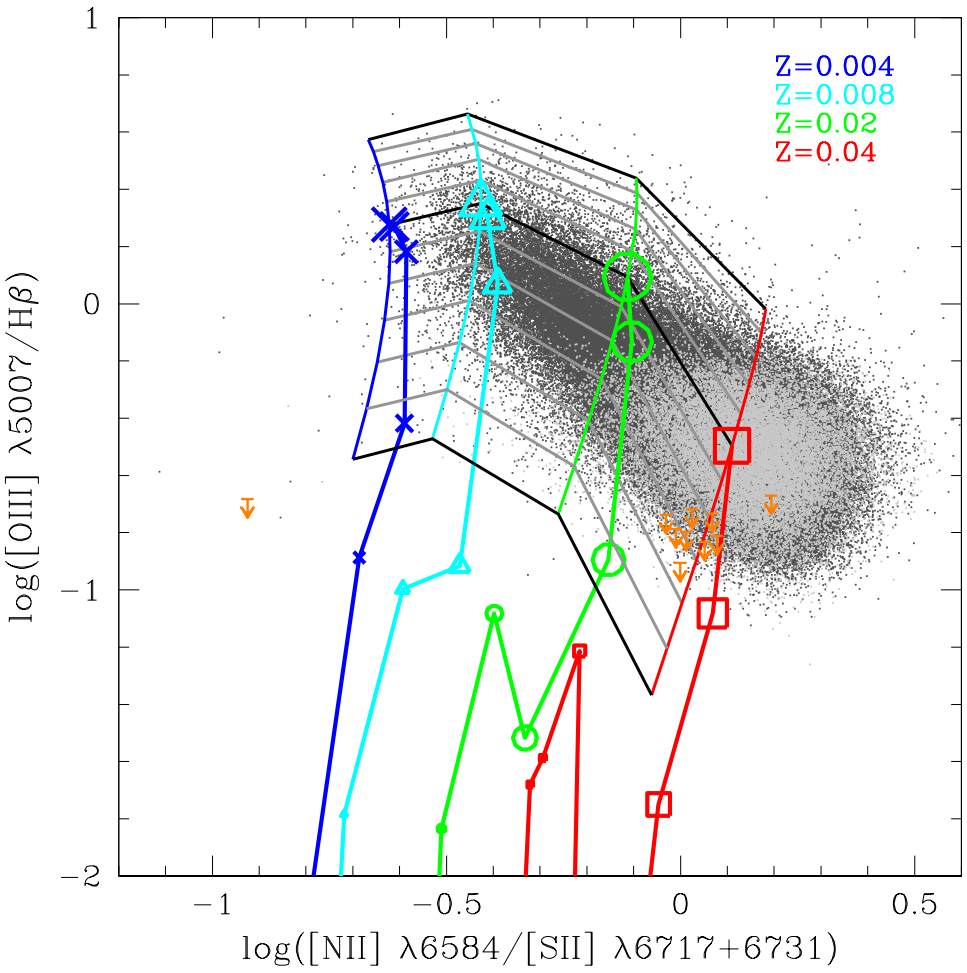

Figure 3.23: Quenching candidates within the [O III]/Hβ vs. [N II]/[S II] plane. Dark grey points are galaxies extracted from the SDSS DR8 with S/N(Hβ) > 3 and S/N([N II]), S/N([S II]), S/N([O III]) > 2, while light grey points are galaxies with S/N([O III]) < 2. Colours and symbols of the grid are defined as in Fig. 3.5. Orange arrows are the 10 extreme quenching candidates with S/N([O III]) < 2.

3.9 Summary of Chapter 3

In this Chapter, we propose a methodology aimed at identifying galaxies in the phase which immediately follows the quenching of the star formation, under the assumption of a fast quenching (shorter than 200 Myr), both for an extreme sharp case and for a more realistic, smoother SF decline. Our approach is based on the use of specific emission line ratios involving high- and low-ionization lines, which are expected to be strongly affected by quenching, rapidly dropping when the most massive O stars able to produce high-ionization lines, disappear. Our main findings can be summarized as follows.

- We focus in particular on the [O III]/Hα and [Ne III]/[O II] emission line ratios, modelling them by means of the CLOUDY (Ferland et al., 2013) photoionization code. We find that they are able to trace the phase just after the SF quenching, decreasing even by more than a factor 10 after its occurrence. The time-scales of this decline depend on the SFH adopted to characterize the ionizing stellar population. In particular, if the extreme case of a sharp quenching is assumed, the emission line ratios definitively drop on time-scales of $\sim$ 10 Myr after the SF quenching, while, if a smoother and more realistic quenching is considered (e.g. an exponentially declining SFR with an e-folding time τ = 200 Myr) they decline by a factor $\sim$ 2 within the time interval needed by the star-forming region to become quiescent (i.e. $\sim$ 80 Myr);

- Our methodology is valid even when different synthetic stellar spectra are assumed to characterize the central ionizing source. In particular, in the case of a sharp quenching, we find a good agreement between Starburst99 and BC03 models: the decline of the two emission line ratios occurs in both cases and happens on similar time-scales, at each metallicity. This is an interesting result, since BC03 models are generally used to describe more advanced phases of galaxy evolution;

- We find that our approach is influenced by the ionization – metallicity degeneracy, since more metallic ionizing sources, being characterized by a low number of hard UV ionizing photons, can produce the same low values of the analysed emission line ratios as quenching ionizing sources. We find that this degeneracy can be reduced using pairs of independent emission line ratios, separately related to metallicity and ionization. In particular, due to its strong dependence on metallicity and weak dependence on ionization parameter, we propose the [N II]/[O II] ratio as metallicity diagnostic to mitigate the degeneracy, and alternatively the [N II]/[S II] one, less affected by dust attenuation but involving weaker lines like [S II];

- We compare our models to a sample of $\sim$ 174,000 SDSS DR8 star-forming galaxies, in order to verify if objects characterized by low values of [O III]/Hα and [Ne III]/[O II] are indeed present in the global galaxy population and if their properties are compatible with a recent SF quenching. We mainly use the [O III]/Hα vs. [N II]/[O II] diagnostic diagram, since it is able to separate metallicity effects from ionization ones. Within this plane, we identify 10 objects with extremely low [O III]/Hα ratios and S/N([O III]) < 2. We find that their spectra are characterized by the absence of the [Ne III] line but rather strong Hα and [O II]. All these properties

agree with the hypothesis that they may have quenched their SF in the recent past;

- Within the dust-corrected $(u-r)$ – mass diagram, the 10 candidates lie outside the green valley, due to the bluer colours. These latter are compatible with the evolution predicted by our models after $\sim$ 10 – 100 Myr from the SF quenching, further suggesting that the 10 objects may be at the beginning of the quenching process;

- We find that our methodology is independent from the dust extinction curve adopted to correct the data. Moreover, the [O III]/Hβ ratio is similar to [O III]/Hα in identifying quenching candidates, while [N II]/[S II], although being unaffected by dust extinction, has the disadvantage to involve the weaker [S II] line and of being less efficient in separating metallicities with respect to [N II]/[O II], also producing larger errors relative to the covered range in metallicity;

- We verify that our approach is valid also when dust-free diagnostic diagrams, such as the [O III]/Hβ vs. [N II]/[S II] one, are used. Indeed, the 10 quenching candidates lie at the lowest edge of the data distribution also in this plane.

The proposed methodology suggests that emission line ratios involving high- and low-ionization lines are powerful tools to identify galaxies in the quenching phase. Moreover, this kind of approach has the advantage of being applicable also at higher redshifts, once that suitable pairs of emission lines are chosen. Therefore, our methodology can be used for the analysis of large spectroscopic surveys data such as JWST (Gardner et al., 2006), WFIRST (Spergel et al., 2013) and Euclid (Laureijs et al., 2011), which identify a large number of Hα emitters at $z > 1$ (e.g. Pozzetti et al., 2016). Since the 10 candidates identified in this Chapter are just examples of quenching galaxies, they cannot be used to derive reliable quenching fractions. However, our results indicate that, once that a complete sample of quenching candidates is identified within a SF galaxy sample, their observed fraction, compared to the global population of star-forming galaxies, could be used to disentangle what is the quenching mechanism at Chapter and what are its typical time-scales. We refer to Quai et al. (2017, submitted) both for this purpose and for the investigation of the detailed properties of complete samples of quenching candidates.

Chapter 4

Spectral analysis of high-redshift galaxies

A comprehensive view on how galaxies form and assemble their mass can be certainly obtained by studying galaxy populations at high-redshift, when a substantial fraction of galaxy mass assembly took place (e.g. Madau & Dickinson, 2014). In addition, in the past decades, it has been shown that the precursors of local massive ETGs at $z \sim 0$ have to be searched among the high-redshift star-forming systems (e.g. Daddi et al., 2004, Wiklind et al., 2008, Brammer et al., 2011, Finkelstein et al., 2013, Marsan et al., 2015, Williams et al., 2015). Therefore, linking high- to low-redshift studies can help to better constrain the evolutionary path of galaxies across cosmic time.
The evolutionary and physical properties of high-redshift star-forming galaxies, in terms of both stellar populations and gas, are generally inferred from their rest-frame Ultraviolet (rest-UV) spectra, which have become accessible from several ground-based facilities at $z > 1$ in recent times. Estimates of ages, metallicities, stellar masses, extinction and SFRs are derived from fitting galaxy SEDs or investigating the slope of the UV continuum (e.g. Calzetti et al., 1994, Talia et al., 2015). Moreover, some of the prominent spectral features visible in the UV range in absorption or emission (e.g. Lyα) can be used as tracers of the high-z galaxy properties. In this Chapter, we apply the full-spectrum fitting and the spectral decomposition described in Chapter 2 to a sample of high-redshift star-forming galaxies at $2 < z < 3$ from the on-going ESO-VLT public spectroscopic survey VANDELS (PIs: Ross McLure, Laura Pentericci). Our ultimate purpose is to derive the evolutionary properties (i.e. ages, metallicities, dust extinction) and the SFHs of the analyzed sample. This latter represents a step forward with respect to many literature works which rely on the a-priori assumption of the SFHs to derive galaxy evolutionary properties from the UV continuum and features. The Chapter is organized as follows: in Sect. 4.1 and 4.2 we review the most important properties of UV spectra and the challenges linked to fit them with the full-spectrum fitting method, in Sect. 4.3 we discuss the reliability of the full-spectrum fitting applied to UV simulated spectra, while in Sect. 4.4 and 4.5 we apply the full-spectrum fitting to VANDELS spectra. Sect. 4.6 summarizes our main results.

The results shown in this Chapter will be described and further developed in *Citro et al. 2018, in prep.*

4.1 Extracting evolutionary information from rest-ultra violet spectra

The UV spectra of star-forming galaxies exhibit numerous spectral signatures which enclose information on the underlying stellar populations. In the following Sections, we briefly recall which are the most important among these features and which are the physical and evolutionary galaxy properties that can be inferred from them.

4.1.1 Individual spectral features and Ultra-Violet continuum

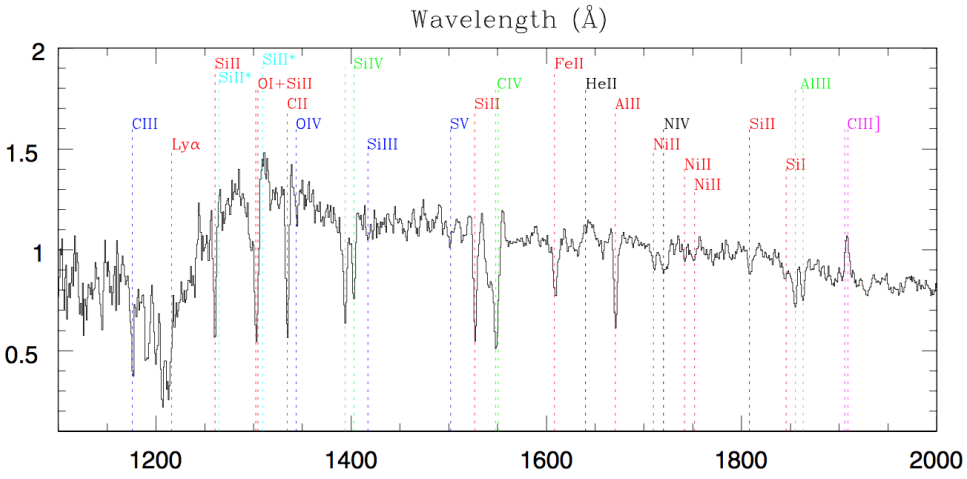

Figure 4.1: Main rest-UV spectral features (From Talia et al., 2012). Blue: absorption stellar photospheric lines; red: interstellar absorption low-ionization lines; green: interstellar absorption high-ionization lines; black: emission nebular lines; black: emission and absorption lines associated with stellar winds; cyan: interstellar fine-structure emission lines.

The main individual features characterizing galaxy rest-frame-UV-spectra are illustrated in Fig. 4.1 (from Talia et al., 2012, back to Leitherer et al., 1999, Shapley et al., 2003, Leitherer et al., 2011), and can be classified into three different types: *photospheric absorption lines* (which also include stellar-wind P-Cygni lines), *interstellar absorption lines*, and *nebular emission lines* emitted by the ISM.
The UV absorption lines which are produced in the stellar photospheres enclose information on stellar ages, metallicities and initial mass function (IMF) in galaxies. The most important of them are: Si IV $\lambda\lambda$1393.76, 1402.77, C IV $\lambda\lambda$1548.20,1550.78, O IV $\lambda\lambda$1032, 1038, C II $\lambda\lambda$1036, 1037 and NV $\lambda\lambda$1238.82,1242.80 (e.g. Pettini et al., 2000, Mehlert et al., 2006, Leitherer et al., 2011, Talia et al., 2012). Some of these lines, such as Si II λ1260.42, O I λ1302.17, Si II λ1304.37, C II λ1334.53 and Si IV λ1400 and C IV λ1550.78 lines, are also strongly affected by stellar winds.
The interstellar absorption lines are instead generally used to infer the gas chemical composition, the dust and large-scale kinematics of the ionized and neutral ISM. The strongest among them are: Si II λ1260.42, Si IV $\lambda\lambda$1393.76, 1402.77, Si II λ1526.71, but also Fe II λ1608.45, Al II λ1670.79, Fe II λ2344.21 and Fe II λ2382.76 (e.g. Pettini et al., 2000, Shapley et al., 2003, Steidel et al., 2010, Leitherer et al., 2011, Talia et al., 2012, James et al., 2014).

Nebular emission lines also trace the physical properties of gas (or AGN activity), and the strongest among them are C IV $\lambda\lambda$1548.20, 1550.78, He II λ1640.42, the semi-forbidden O II] $\lambda\lambda$1661, 1666, the forbidden [Si III] λ1883+Si II] λ1892 and c III] λ1906.68+C III] λ1908.68 (e.g. Erb et al., 2010, Stark et al., 2014).
Another notable line linked to the ISM is the Lyα (at $\lambda = 1215.67$), which can be seen both in emission or in absorption and whose strength in emission mainly depend on dust attenuation, but is also related to metallicity, geometry of the ISM, age and resonant scattering (Taniguchi et al., 2005, Gronwall et al., 2007, Kornei et al., 2010, Talia et al., 2012).
However, it is important to note that the observations of rest-UV spectral features can be hampered by the low SNRs usually characterizing high-redshift spectra. Stacked spectra are therefore often used to analyze them. In the following, we follow this approach to analyze VANDELS spectra.

The rest-UV continuum and its slope have also been demonstrated to be linked to galaxy stellar and gas properties (Meurer et al., 1999, Shapley et al., 2005, Rogers et al., 2014 and has been proved to be particularly useful to measure the dust obscuration whereas the Balmer decrement is not easily measurable (i.e. at high-redshifts, e.g. Bouwens et al., 2009, Wilkins et al., 2011, Dunlop et al., 2012). In general, the UV slope β is determined by fitting the continuum to the function f(λ) $\propto \lambda\beta$. f(λ) is the flux density in a specified wavelength range, usually chosen so that strong spectral features are avoided (e.g. Calzetti et al., 2000, Talia et al., 2015).

4.2 Applying the full-spectrum fitting to Ultraviolet spectra

Since several information is enclosed in both the individual spectral features and the UV continuum of high-redshift galaxies, the full-spectrum fitting technique (see Chapt. 2) would potentially be a very powerful tool to analyze rest-UV spectra. The drawback is that the current evolutionary synthesis models, on which the full-spectrum fitting relies, do not account for the contamination of photospheric absorption lines by the same lines sometimes present in the ISM. In the past past two decades significant progress has been made in the ultraviolet spectral models of galaxies, which have been improved by libraries of theoretical stellar atmospheres or by the modelling of stellar wind effects (e.g. Hauschildt & Baron, 1999, Hillier & Miller, 1999, Pauldrach et al., 2001, Puls et al., 2005, Leitherer et al., 2010). However, a proper treatment of the interstellar absorption is still lacking. In this context, understanding the age and metallicity trends of the pure photospheric absorptions can help to better interpret the spectral fitting results. In the following, we investigate the behaviour of some of the most important UV absorption features. To carry on these investigations, we adopt the Charlot & Bruzual 2016 models (BC16 hereafter, See Bruzual & Charlot, 2003). These evolutionary synthesis models extend to the UV wavelengths (i.e. downward 911 Å), have a high resolution (i.e. 1 Å) in the range 911 – 3540.5 Å (Hubeny & Lanz, 1995), and cover a wide range of ages (from 0.1 Myr to 20 Gyr) and metallicities (form $Z = 0.005\ Z_{\odot}$ to $Z = 5\ Z_{\odot}$). The large coverage of the parameter space will also allow a more accurate analysis of real data analyzed further on.

In Fig. 4.2 we show the evolution of BC16 models as a function of time, for $Z = 0.2\ Z_{\odot}$ and ages going from 0.1 Myr to 2 Gyr (this limits was chosen not to exceed the age of the Universe at the redshifts of the real spectra analyzed further on, see Sect. 4.4). It also illustrates their evolution for different metallicities and an age of 0.05 Gyr. As it is possible to note, the continuum UV shape gets redder as age increases, since the most massive stars contributing to the UV flux depart from the main sequence. At ages older than 1.5 Gyr, the UV flux increases again due to the contribution of post-AGB stars and White Dwarfs. A sharp increase of the flux at wavelengths longer than $\sim$ 1700 Å is also visible for ages older than $\sim$ 1 Gyr. Furthermore, higher metallicities imply redder continua, due to the increased opacity of the stellar atmospheres which absorb the UV flux. Fig. 4.3 and 4.4 illustrate instead a zoom of the region 1320 – 1420 Å and show the evolution of O IVλ1343.35 and C IIλ 1334.53, and Si IV $\lambda\lambda$1393.76,1402.77 as a function of the age and metallicity. We remind that C II λ1334.35 and Si IV$\lambda\lambda$ 1393.76,1402.77 are strongly affected by the ISM in real galaxies.

The O IVλ1343.35 absorption line (which is a high ionization potential line) is visible only at very young ages (i.e. $\lesssim$ 10 Myr), when the photons provided by the stellar interiors are energetic enough to ionize the oxygen three times. A similar trend characterize the photospheric absorption doublet Si IV$\lambda\lambda$ 1393.76,1402.77. The photospheric absorption line C II λ1334.35 (which is a low-ionization potential line) is absent at very young ages, strengthens at intermediate ages, and decreases again at older ages. This behaviour is due to the fact that, at ages < 0.05 Gyr, all the Carbon ions are in higher ionization states than C^{+}. On the contrary, at older ages, the only available photons are too soft even to create Carbon ions in the first ionization state.

In general, regardless of their nature, the absorption lines tend to get stronger for higher metallicities, due to the fact that higher metallicities increase the number of metal ions in the stellar atmospheres. All the illustrated trends confirm what found by Vidal-García et al. (2017).

From the previous discussion, we argue that stellar absorptions are non negligible in UV spectra, especially at young ages and high metallicities. This implies that all the fitting methods relying on stellar population synthesis models (which do not account for the ISM contribution), can provide untrue young ages and high metallicities for the fitted spectra, interpreting the strong lines as pure stellar absorptions. Starting from this, we devote the first part of this Chapter to verify if the evolutionary properties and the SFHs of star-forming high-redshift galaxies are reliably retrieved by the full-spectrum fitting also when the photospheric lines including ISM contributions (ISM lines, hereafter) are excluded from the fits of their UV spectra. Moreover, we investigate the extreme case in which also pure photospheric absorption lines are not considered in the spectral fit. In this last case, the full-spectrum fitting basically relies only on the continuum shape of the observed spectra.

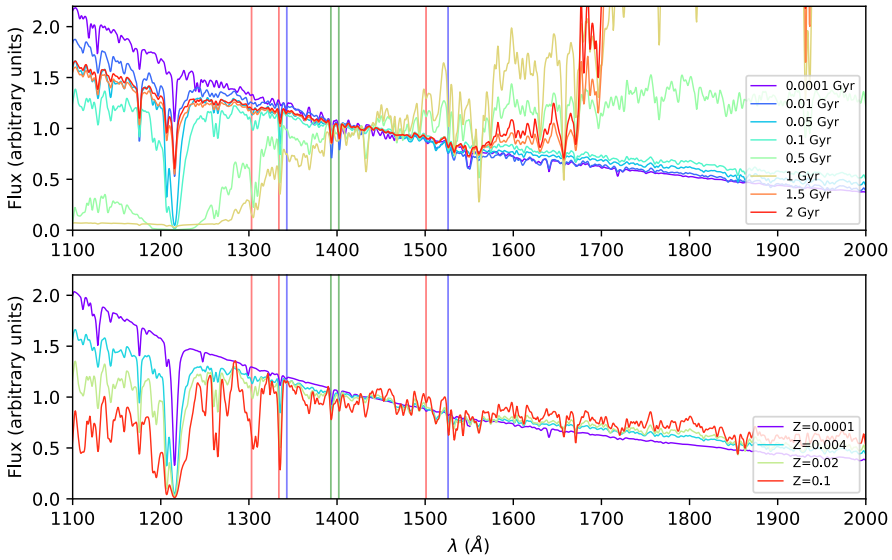

Figure 4.2: Comparison among BC16 SSP models at different ages and metallicities. Top panel: BC16 SSPs for ages going from 0.0001 to 2 Gyr, as labeled, and $Z = 0.2Z_{\odot}$. Bottom panel: BC16 SSPs for metallicities ranging from 0.0001 to 0.1, as labeled, and an age of 0.05 Gyr.

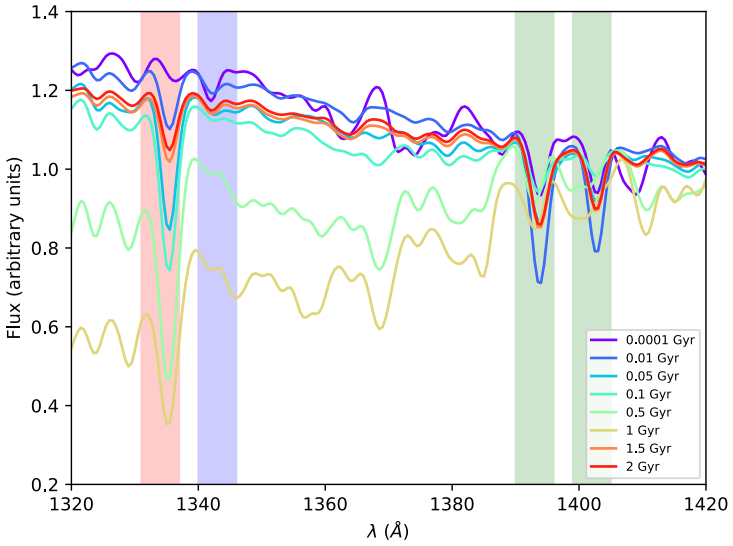

Figure 4.3: Comparison among BC16 SSPs at different ages and metallicities in the wavelength range 1320 – 1420 Å. Ages range from 0.0001 to 2 Gyr, as labeled, and the metallicity is fixed at $Z = 0.2Z_{\odot}$. The shaded regions mark the most prominent absorption features in the considered range, and are color-coded as in Fig. 4.1.

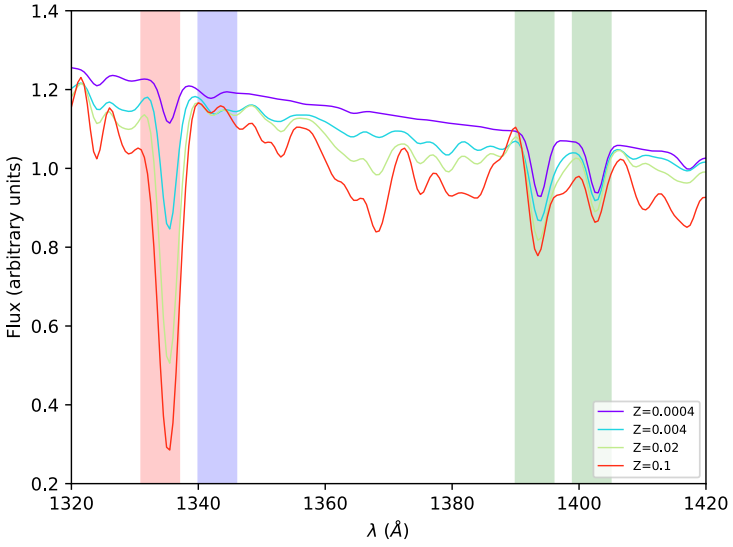

Figure 4.4: Comparison among BC16 models at different ages and metallicities in the wavelength range 1320 – 1420 Å. Metallicities range from 0.0001 to 0.1, as labeled, and the age is fixed at 0.05 Gyr. The shaded regions mark the most prominent absorption features in the considered range, and are color-coded as in Fig. 4.1.

4.3 Simulations

To verify if the full-spectrum fitting is able to reliably retrieve the evolutionary properties (i.e. ages, metallicities, dust extinctions) and the SFHs of star-forming, high-redshift galaxies also when ISM lines are excluded from the fit, we create simulated spectra resembling the properties (i.e. SNR, resolution and wavelength coverage) of VANDELS (see Sect. 4.4) galaxies at $z \sim 3.5$ (which will be one of the subjects of our future investigations). To create the simulated spectra, we adopt the BC16 models described above (see Sect. 4.2). In particular, we create a grid of models assuming an exponentially declining SFH with two different e-folding times (i.e. 0.5 and 2 Gyr) and ages going from 0.05 to 2 Gyr. This latter limit is chosen not to exceed the age of the Universe at $z \sim 3.5$, according to the assumed cosmology (which is the one already adopted in Chapt. 2). We redden our simulated spectra using the Calzetti et al. (2000) attenuation curve, assuming $A_V = 0.5$, 1, 1.5 mag. Finally, to resemble the spectral resolution of VANDELS spectra, we downgrade the BC16 resolution to 2.5 Å (FWHM) (see Sect. 4.4). Note that in these models we do not introduce a velocity dispersion σ. In fact, if also pure photospheric absorption lines are excluded from the fit, the full-spectrum fitting has basically no absorption features to rely on to derive σ.
To simulate different SNRs for the simulated spectra, we apply an error to the BC16 models, following the procedure described in Chapter 2. For each simulated spectrum, we define a median error in the wavelength window 1420 – 1500 Å as the ratio between the median flux in this window and a grid of pre-defined SNRs = 3, 5, 7, 10, 20, 50. Then we apply this flat error to the whole spectrum. Moreover, in order to verify the accuracy of our results, we re-simulate each spectrum 4 times.
We verify that the defined models actually resemble the data which will be analyzed further on, by comparing the data and model distributions of the spectral color c_r, defined by eq. 4.1:

$$c_r = \frac{F_\lambda(1650-1750)}{F_\lambda(1250-1350)} \quad . \tag{4.1}$$

We find that all the models have colors in agreement with data (see Fig. 4.5), whose c_r colors extend from ~ 0.5 to ~ 1.2.
From this ensamble of simulated spectra, we randomly select 19 models, performing our further analysis on this subsample. Table 4.1 summarizes the main properties of the selected 19 models.

To test if the results from the full-spectrum fitting are deteriorated when ISM lines are excluded from the fit, we define three different sets of fitting parameters, basing on the spectral features excluded from the fit: (i) we only mask the most prominent emission lines (case 1, hereafter); (ii) we mask both the emission lines and all the ISM lines (case 2, hereafter), (iii) we mask emission lines, ISM lines and pure photospheric absorption lines (case 3, hereafter). This latter represents the extreme case in which the full-spectrum fitting will rely on the UV continuum shape only. Among the three cases, we consider case 2 as the most reliable one, since it contains as much spectral information as possible about the underlying stellar populations. The emission/absorption lines which are excluded from the fit in the three cases are listed in Table 4.3. Note that, for the high and the low redshift subsamples, we mask the emission/ISM/pure stellar absorption lines included in the wavelength ranges $1222 - 2000$ Å and $1400 - 2600$ Å ,

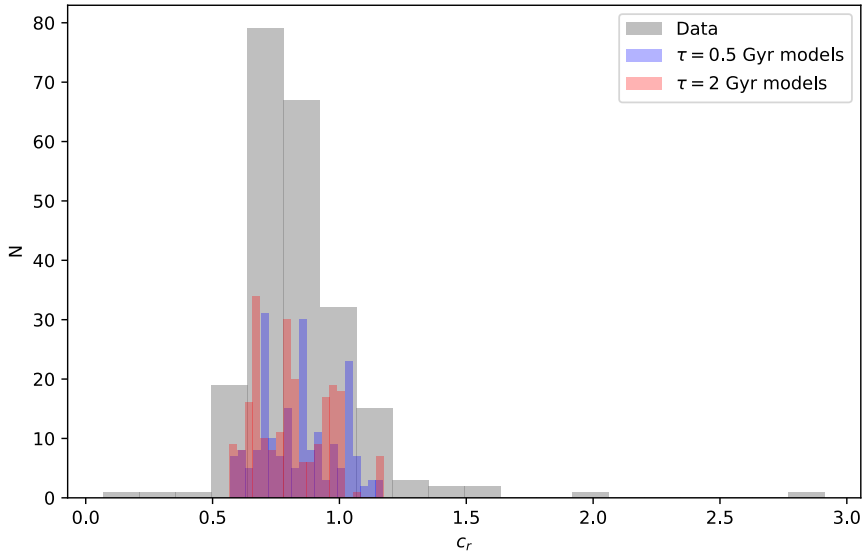

Figure 4.5: Distribution of the c_r colors for data (see Sect.4.4) and simulated models. The grey histogram refers to data, while the colored ones refer to exponentially declining simulated models with $\tau = 0.5$ Gyr (blue) and $\tau = 2$ Gyr (red).

respectively (see Sect. 4.5).

Concerning the other fitting parameters, we fit the simulated spectra between 1222 and 2000 Å (which is the wavelength range also adopted for real data further on), and we assume a normalization wavelength which is the median within the 1420 – 1500 Å window. As explained before, in these fits we are not interested to retrieve the velocity dispersion, which is fixed at 0 km s^{-1}. Finally, we adopt a Calzetti et al. (2000) attenuation curve to derive the visual extinctions A_V.

Table 4.1: Properties of the 19 simulated spectra investigated in this Chapter.

A_V (mag)	Z	τ (Gyr)	age (Gyr)	mass-weighted age (Gyr)	c_r
0.5	0.004	0.5	0.1	0.06	0.6195
0.5	0.02	0.5	1	0.64	0.6961
0.5	0.1	0.5	1	0.64	0.8088
1.5	0.0001	0.5	0.05	0.033	0.8356
1.5	0.1	0.5	0.05	0.033	1.017
1	0.0001	0.5	1.5	1.073	0.8751
1	0.004	0.5	0.1	0.06	0.7456
1	0.02	0.5	1	0.64	0.8512
1	0.1	0.5	1.5	1.07	0.9935
0.5	0.0001	2	2	1.30	0.6404
0.5	0.004	2	0.1	0.06	0.6182
0.5	0.02	2	1	0.6	0.6752
0.5	0.1	2	0.01	0.006	0.6324
1.5	0.0001	2	0.05	0.033	0.8352
1.5	0.02	2	0.5	0.3	1.003
1.5	0.1	2	0.05	0.033	1.015
1	0.004	2	2	1.3	0.8006
1	0.02	2	2	1.3	0.8259
1	0.1	2	2	1.3	0.9569

Table 4.2: Spectral lines masked in case 1 (emission lines only), case 2 (emission lines + ISM lines) and case 3 (emission lines + ISM lines + pure photospheric absorption lines).

emission lines		ISM lines		pure phot. abs. lines	
Ion	λ [Å]	Ion	λ [Å]	Ion	λ [Å]
He II	1640.42	O I - Si II	1302.17,1304.37	C III	1175.71
C III]	1906.68,1908.68	C II	1334.53	O IV	1343.35
C II]	2326.00	Si IV	1393.76	Si III	1417.24
		Si IV	1402.77	S V	1501.76
		Si II	1526.71	N IV	1718.55
		C IV	1548.20,1550.78		
		Fe II	1608.45		
		Al II	1670.79		
		Al III	1854.72		
		Al III	1862.79		
		Fe II	2365.66		
		Fe II	2374.46		

4.3.1 Results

The first results obtained from the simulations are shown in Figs. 4.6, 4.7 and 4.8, which illustrate the case of an SNR ~ 50 simulated spectrum, with $\tau = 0.5$ Gyr, age $= 1.5$ Gyr and $Z = 0.0001$. As it is possible to note, in all the three cases the best fit model is able to reproduce the observed spectrum, and no significant differences among the three best fit models are visible (the χ^2 obtained for the three cases are comparable and $\sim$ 1.5). Moreover, there is qualitative agreement between the input and the output shape of the SFH in all the three cases. These results suggest that no significant biases are introduced in the best fit model when ISM lines (and pure photospheric absorption lines) are excluded from the fit.

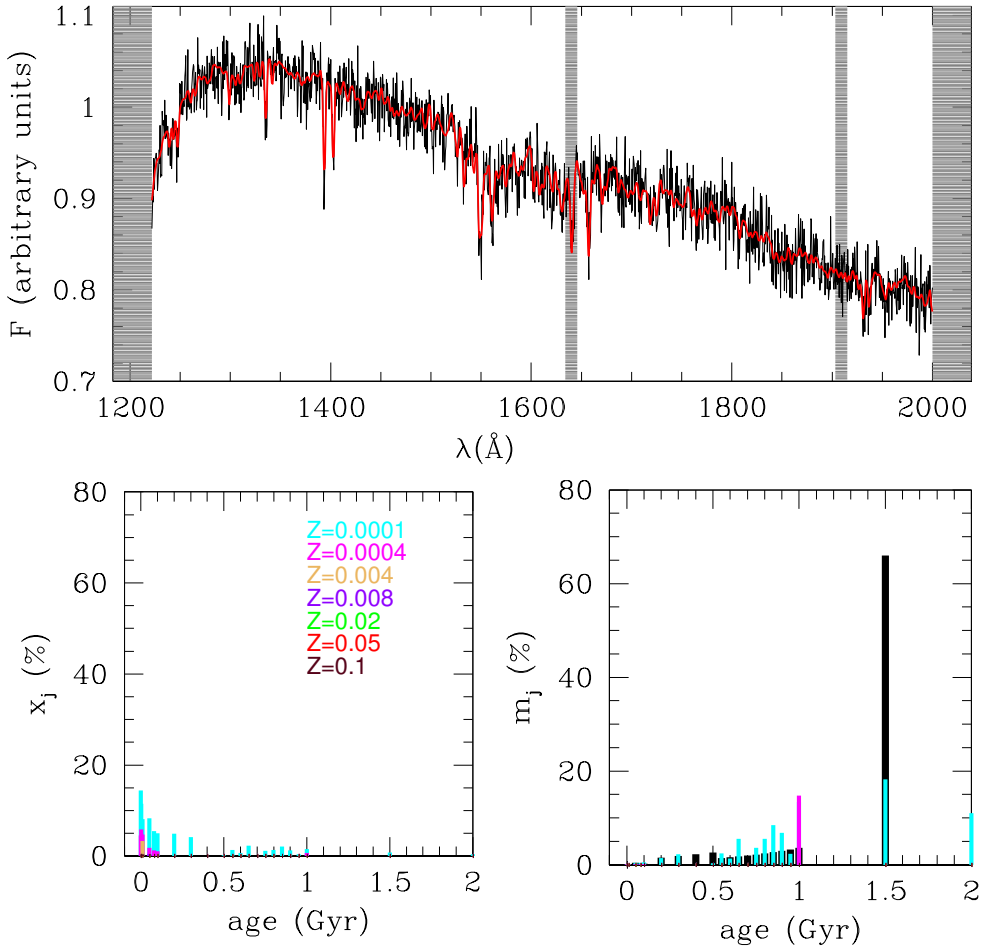

Figure 4.6: Typical full-spectrum fitting output for case 1 and a simulated spectrum with SN=50, $\tau = 0.5$ Gyr, age $= 1.5$ Gyr and $Z = 0.0001$. Top panel: observed spectrum (black), best-fit model (red), masked regions (grey shaded regions). Bottom panels: light- (left) and mass- (right) contributions (in percentages) of the library models derived to fit the simulated spectrum. Different colors stand for different metallicities, as labeled. The black vertical lines are the SFH for $\tau = 0.5$ Gyr and an age of 1.5 Gyr.

Fig. 4.9 illustrates instead the median shifts and dispersions between the output and

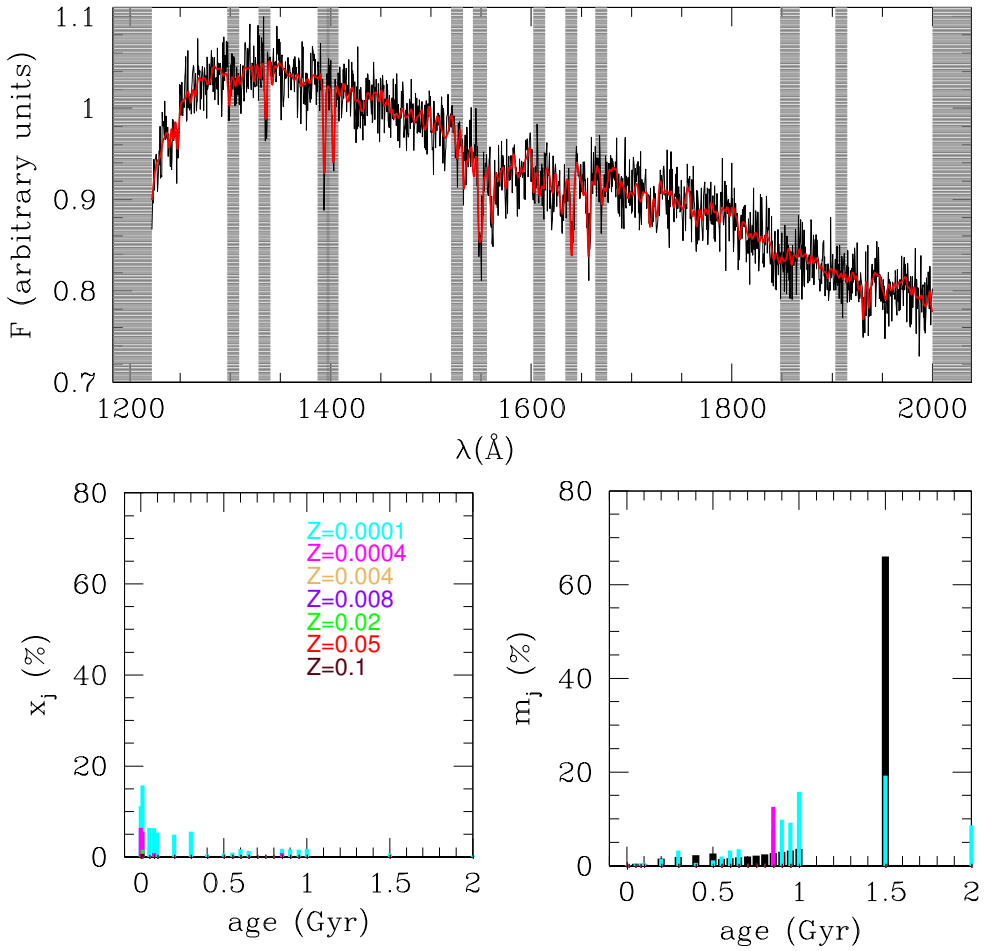

Figure 4.7: Typical full-spectrum fitting output for case 2 and a simulated spectrum with SN=50, $\tau = 0.5$ Gyr, age $= 1.5$ Gyr and $Z = 0.0001$. Top panel: observed spectrum (black), best-fit model (red), masked regions (grey shaded regions). Bottom panels: light- (left) and mass- (right) contributions of the library models derived to fit the simulated spectrum. Different colors stand for different metallicities, as labeled. The black vertical lines are the true SFH for $\tau = 0.5$ Gyr and an age of 1.5 Gyr.

the input mass-weighted ages, metallicities and dust extinctions obtained for the three cases, as a function of the SNR of the input spectrum[1]. The values of shifts and dispersions are also summarized in Table 4.3 as the median values obtained with SNR=20 and 50 (SNR_{20-50}). As it is possible to note, there is good agreement between output and input quantities starting from SNRs $\sim 10-20$. Moreover, comparing the three cases, we find that, for SNR_{20-50}:

- Mass-weighted ages are retrieved with median shifts $\sim 0.12 - 0.15$ for the three cases, with dispersion increasing from ~ 0.37 Gyr (case 1) to ~ 0.49 Gyr (case 2) (and to ~ 0.56 Gyr for case 3).

[1]We computed 76 different simulations for each SNR.

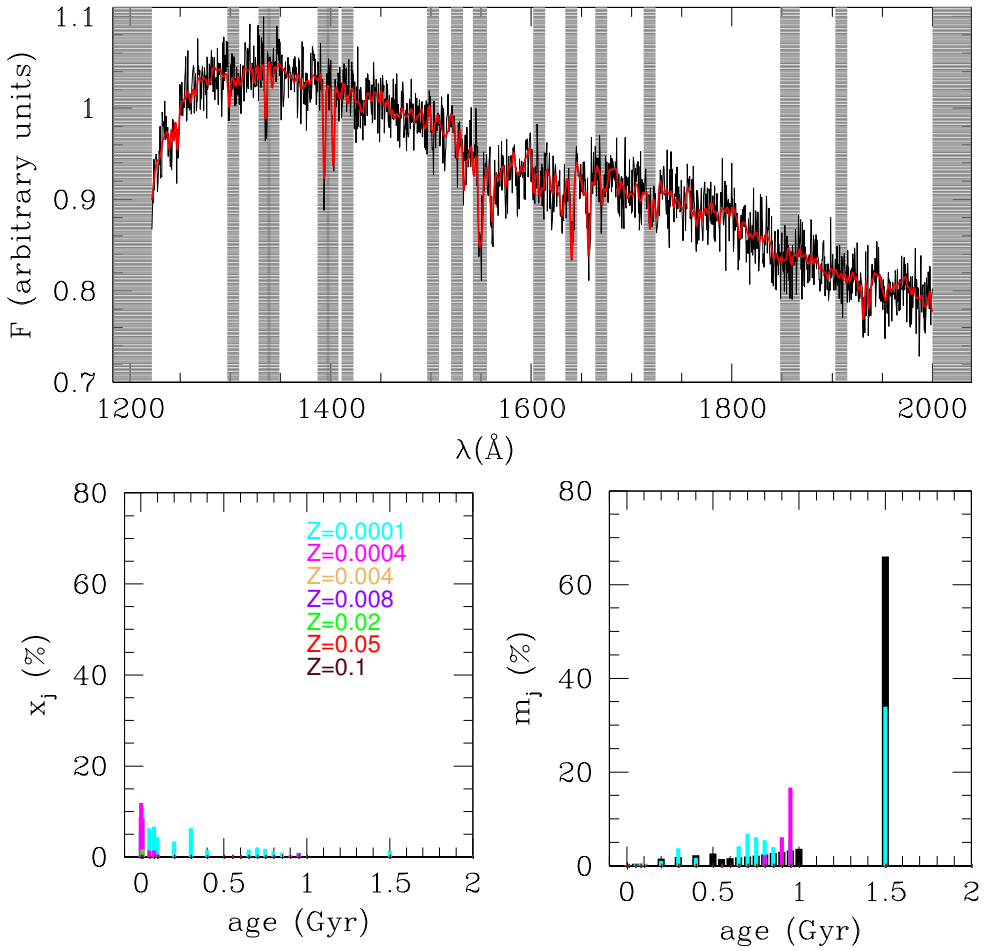

Figure 4.8: Typical full-spectrum fitting output for case 3 and a simulated spectrum with SN=50, $\tau = 0.5$ Gyr, age $= 1.5$ Gyr and $Z = 0.0001$. Top panel: observed spectrum (black), best-fit model (red), masked regions (grey shaded regions). Bottom panels: light- (left) and mass- (right) contributions of the library models derived to fit the simulated spectrum. Different colors stand for different metallicities, as labeled. The black vertical lines are the true SFH for $\tau = 0.5$ Gyr and an age of 1.5 Gyr.

- mass-weighted metallicities are retrieved with median shifts $\sim 2 \times 10^{-4} - 10^{-3}$ and dispersion increasing from ~ 0.026 (case 1) to ~ 0.031 (case 2) (and to ~ 0.036 in case 3).
- Dust extinctions are more stable in terms of dispersion, which amounts to $\sim 0.035-0.042$ mag for the three cases.

These results suggest that, excluding ISM lines from the spectral fit still allows to retrieve the input properties, although with a slightly larger dispersion and thus lower accuracy. The situation gets worse in case 3, as expected since, in this case, the full-spectrum fitting has a lower number of wavelengths to rely on to provide the best fit model.
These trends are also visible in Fig. 4.10, which shows the distribution of the differences

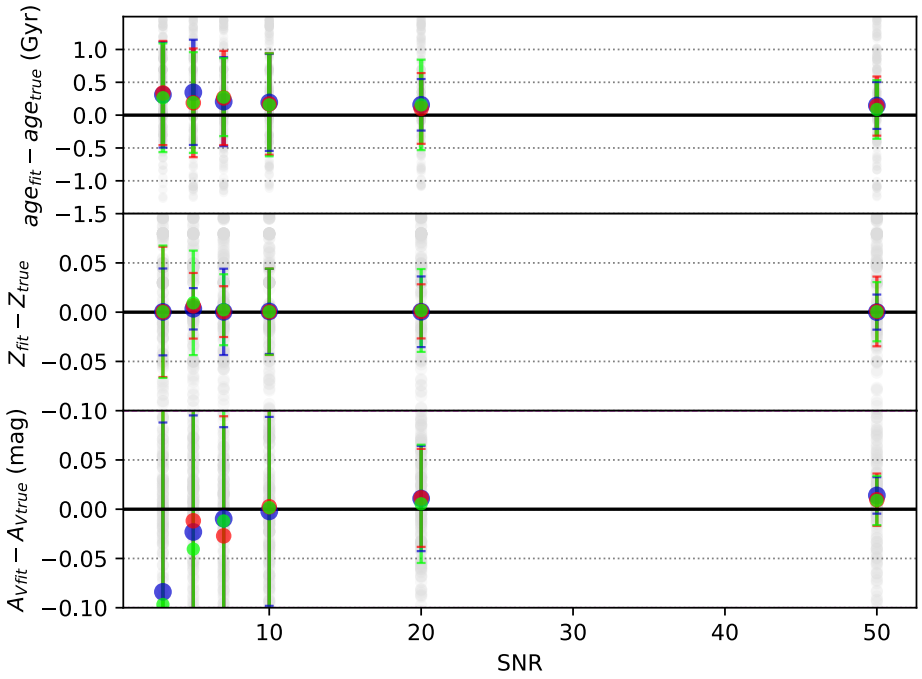

Figure 4.9: Differences between output and true mass-weighted ages (top panel), mass-weighted metallicities (middle panel) and visual extinctions (bottom panel) as a function of the SNR of the simulated spectra. Filled circles and vertical bars are the median shifts and dispersions (blue: case 1; red: case 2, green: case 3) derived at each SNR, respectively.

between the output and the input properties for SNR $\geq$ 20. Here it is also evident that, while the mass-weighted age and the A_V distributions are symmetric, there is a clear tendency for the mass-weighted metallicities to be overestimated by the fit.

Table 4.3: Median shifts and dispersions obtained for VANDELS UV simulated spectra and SNR_{20-50}

case	$\langle t \rangle_{mass}$ (Gyr)		Z		A_V (mag)	
	shift	disp	shift	disp	shift	disp
1	0.15	0.37	$\lesssim 10^{-3}$	0.026	0.012	0.035
2	0.12	0.49	$\lesssim 10^{-3}$	0.031	0.01	0.038
3	0.12	0.56	0.001	0.036	0.007	0.042

Complementary information about the capabilities of the full-spectrum fitting to retrieve galaxy evolutionary properties against the three assumed sets of parameters can be obtained from Fig. 4.11, which shows the differences between the retrieved and true

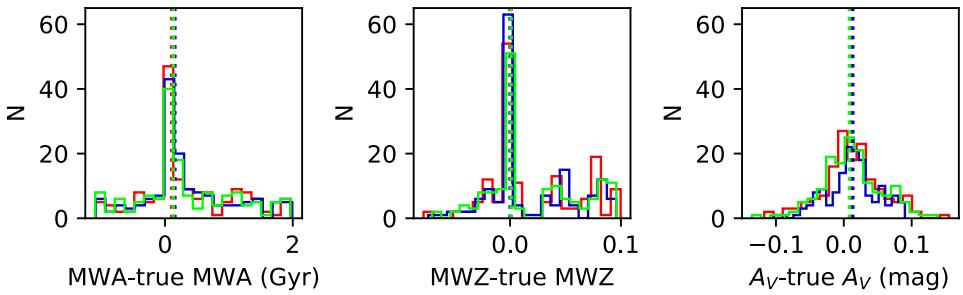

Figure 4.10: Distribution of the retrieved mass-weighted ages (MWA), mass-weighted metallicities (MWZ) and dust extinctions for SNR $\geq$ 20. Dotted vertical lines mark the median of the distributions (blue: case 1; red: case 2, green: case 3).

mass-weighted ages, mass-weighted metallicities and visual extinctions as a function of their true values for SNR $\gtrsim$ 20.
As it is possible to note, the visual extinction A_V is robustly retrieved regardless of its input value, with median shifts and dispersions lower than 0.037 mag and 0.034 mag, respectively. Moreover, the age and the metallicity of the models with the youngest age and the lowest metallicity of our grid are well retrieved. In fact, the steep UV slope and the absence of strong spectral features characterizing spectra at very young ages and low metallicities, reduce the degeneracies which could provide less accurate results. Older ages and higher metallicities are instead characterized by more significant biases. In particular, the observed age overestimations could be due to the fact that, at each true age, we are putting together models with different values of visual extinction. This implies that the simulated spectra with the largest dust extinction can be redder than the SSPs library models used to fit them, leading the full-spectrum fitting to choose older SSPs to reproduce the input spectra color. On the contrary, when dust extinction has a weaker effect on the shape of the input spectra (i.e. at older ages), mass-weighted ages tend to be underestimated, since the SSPs library models around 1 Gyr are redder than the simulated spectra. Furthermore, the sharp increase of the flux at wavelengths longer than $\sim$ 1700 Å (see Fig. 4.2) can contribute to this effect.
However, it is important to note that, at subsolar metallicities and ages younger than $\sim$ 0.3 Gyr (which are the values of ages and metallicities generally found for high-redshift, star-forming galaxies – e.g. Sommariva et al. (2012), see also our following discussion on VANDELS spectra) lower shifts are provided by the spectral fit for both ages (i.e. $\lesssim 0.7$ Gyr) and metallicities (i.e. $\lesssim 0.002$).

The simulations described in these sections should be considered as preliminary and serve to understand the general trends of the full-spectrum fitting results against the three considered sets of fitting parameters. Further investigations are needed to confirm the obtained results (median shifts and dispersions), which will be described in more detail in Citro et al. (2018, in prep).

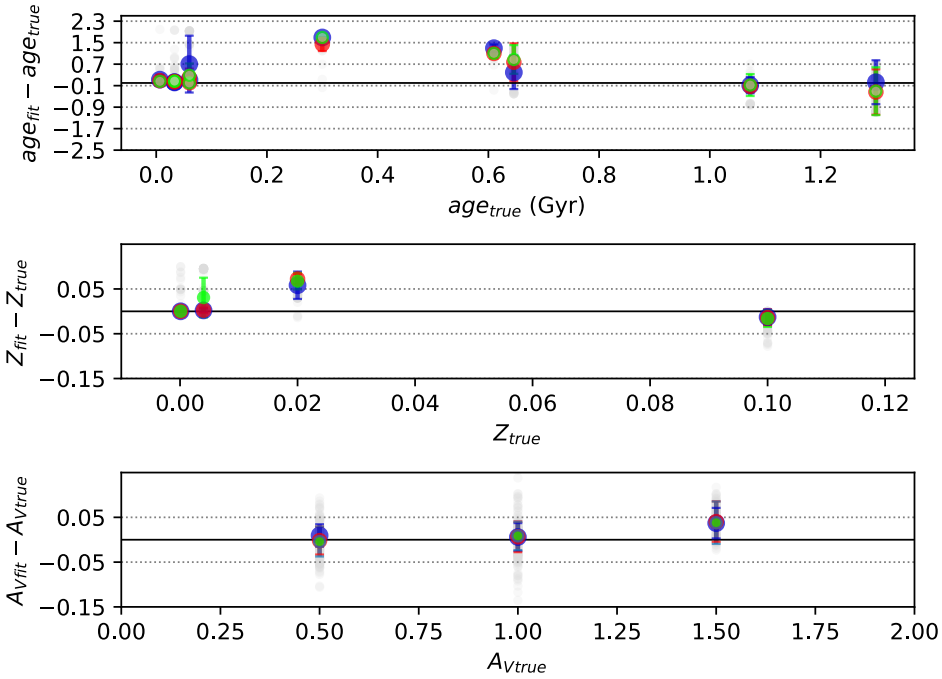

Figure 4.11: Differences between output and true mass-weighted ages (top panel), metallicities (middle panel) and dust extinctions (bottom panel) as a function of their true values (only SNRs ≥ 20 are considered). Filled circles and vertical bars are the median shifts and dispersions (blue: case 1; red: case 2, green: case 3) derived at each true value of the considered quantities, respectively.

4.4 Applying the full-spectrum fitting to real data

In this Section, we apply the full-spectrum fitting to a sample of high-redshift star-forming and Lyman break galaxies at $2 \leq z \leq 4$ from the on-going ESO VLT public spectroscopic survey VANDELS (see Sect. 4.4.1). We derive the evolutionary properties (i.e. ages, metallicities and dust extinctions) and SFHs of these galaxies, assuming the three sets of fitting parameters described above.

4.4.1 The Survey VANDELS

VANDELS (A deep VIMOS survey of the CANDELS UDS and CDFS fields, PIs: R.J. McLure, L. Pentericci)[2] is a on-going ESO-VLT survey, which is targeting 8 overlapping VIMOS pointings over an area of ~ 0.2 deg^2, in the United Kingdom InfraRed Telescope (UKIRT) Infrared Deep Sky Survey (UKIDSS), Ultra Deep Survey (UDS) and Chandra Deep Fiels Survey (CDFS). Observations are performed by means of the medium resolution (MR) grism+GG475 order-sorting filter, which provides spectra with a resolution R $\sim$ 580 in the wavelength range 4800 – 10000 Å , with a sampling of 2.5 Å pixel^{-1}. Spectra are obtained by means of a long on-source integration starting from a minimum of 20 hours up to a maximum of 80 hours per individual objects. Some of the primary targets of the VANDELS survey are star-forming galaxies at $2.4 < z < 5.5$ and Lyman Break galaxies at $3 < z < 7$. The spectroscopic observations are complemented with photometric ones: the WFC3/IR deep imaging provided by CANDELS, the ultra-deep imaging with the Spitzer Space Telescope and Y+K-band imaging from the HAWK-I Ultra Deep Survey (Fontana et al., 2014).

4.4.2 The sample of high-redshift star-forming galaxies

As discussed before, we analyze a sample of VANDELS star-forming and Lyman break galaxies in the redshift range $2 \leq z \leq 4$. In order to study the evolutionary properties and the SFHs of the sample as a function of redshift, we divide it into two subsamples at $2 \leq z < 3$ and $3 \leq z \leq 4$, containing 66 and 224 objects, respectively. These objects are the ones so far available out of the total VANDELS star-forming sample, which will amount to $\sim$ 800 spectra. Fig. 4.12 illustrates the distribution of the two subsamples within the SFR-mass plane. The stellar masses of the two subsamples are $8 \lesssim \log(\mathrm{M}/\mathrm{M}_{\odot}) \lesssim 11.5$ for the $3 \leq z \leq 4$ subsample, and $9 \lesssim \log(\mathrm{M}/\mathrm{M}_{\odot}) \lesssim 10.8$ for the $2 \leq z < 3$ one, while the SFRs are in the range 2.5 – 1000 $\mathrm{M}_{\odot}$ yr^{-1} and 3 – 350 $\mathrm{M}_{\odot}$ yr^{-1} at high and low redshift, respectively. The SFRs and stellar masses exploited here are obtained by SED fitting to the photometry adopting BC03, solar metallicity, models and using a wide range of exponentially declining models for the SFH, with $\tau > 0.3$ Gyr (Wuyts et al., 2011).
Comparing the two samples with some of the literature main sequences of star-forming galaxies (i.e. their ridge lines) at different redshifts, we find that the lower-redshift subsample lies slightly above the Daddi et al. (2009) relation at $z \sim 2$, while the high-redshift one is more in agreement with the relations predicted at higher redshift, especially at lower masses. This is what expected due to the decreasing of the SFR density with cosmic time at $z \gtrsim 2$ (e.g. Madau & Dickinson, 2014). In this Figure we also show a comparison between our two subsamples and the evolving SFR-mass curves illustrated in Fig.

[2]More informations are available on the website: *http://vandels.inaf.it*

2.24. These curves are the reconstructed SFHs obtained for the most massive and passive local ETGs studied in Chapter 2. As it is possible to note, the most massive SF galaxies overlap with the evolving curves at $z \lesssim 4$, and could therefore be the high-redshift progenitors of the passive local galaxies analyzed in Chapter 2. However, since in the previous Chapter we focused only on the most massive (i.e. $log(M/M_{\odot}) \gtrsim 10^{10.75}$) population, the star-forming VANDELS galaxies analyzed here could rather be the progenitors of less massive ETGs. This is shown by shifting the SFR-mass evolving curve relative to the lowest mass bin to even lower masses (in the hypothesis of similar SFHs).

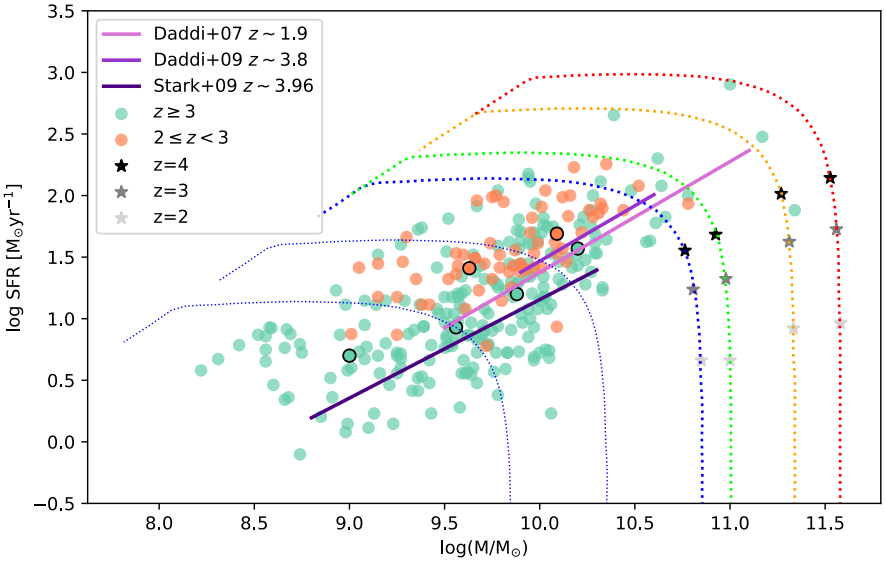

Figure 4.12: Analyzed VANDELS spectra in the SFR-mass plane. Green and orange circles mark the higher and lower redshift subsamples. Green and orange circles with black border are the median stacked spectra obtained for the two subsamples (see Sect. 4.4.3). Dotted colored curves are the evolving SFR-mass relations illustrated in Fig. 2.24. Thin blue dotted curves are the blue SFR-mass curve shifted to lower masses. Grey stars mark the redshifts $z = 2$, $z = 3$, $z = 4$, which include the redshift range of the analyzed sample.

4.4.3 The signal-to-noise ratios of the observed spectra

Since the reliability of the full-spectrum fitting is related to the SNR of the input spectra (see Chapt. 2), in this Section we investigate in more detail the SNR of the galaxies in the analyzed sample. In particular, since the error spectra provided by the VANDELS survey is slightly underestimated (Ross Mclure, private communication) we re-define the SNR of the individual spectra following eq. 4.2 (which holds for the $3 \leq z \leq 4$ subsample) and 4.3 (which holds for the $2 \leq z < 3$ subsample), in order to have a more reliable estimate of the SNRs:

$$\mathrm{SNR}_{1420-1500} = \frac{\mathrm{median}(1420-1500)}{\mathrm{MAD}(1420-1500)} \ , \tag{4.2}$$

$$\mathrm{SNR}_{2100-2180} = \frac{\mathrm{median}(2100-2180)}{\mathrm{MAD}(2100-2180)} \ . \tag{4.3}$$

In these two equations, the wavelength windows 1420 – 1500 Å and 2100 – 2180 Å are chosen to avoid strong individual spectral features. The obtained SNRs per pixel are illustrated in Fig. 4.13. When eq. 4.2 and 4.3 are used, the SNRs range from ~ 1 to ~ 8 for the two subsamples (these values double if resolution elements instead of pixels are considered).

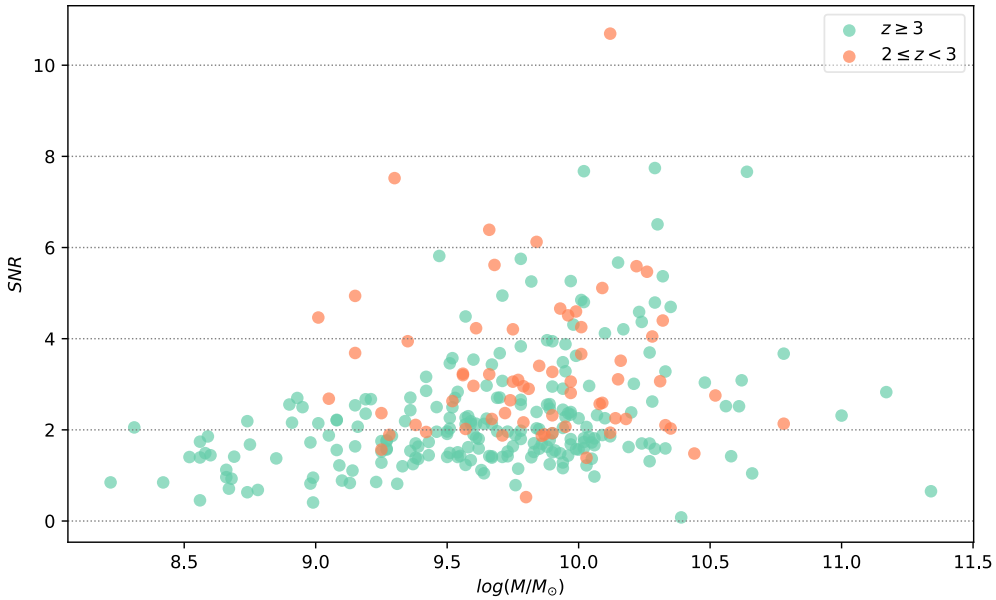

Figure 4.13: SNR of the individual stacked spectra of the two subsamples derived from eq. 4.2 and 4.3. Green and orange circles are the higher and the lower redshift subsamples, respectively.

Given the low SNRs of the individual spectra, which are lower than the ones needed by the full-spectrum fitting to break the degeneracy among different parameters (i.e. SNRs $\sim$ 10 – 20), we increase the SNRs stacking the individual spectra together as a function of mass, preserving the number of objects included in each mass bin. In particular, to maximize the SNRs, we divide the subsample at $3 \leq z \leq 4$ into 4 mass bins, each containing 56 objects, and the subsample at $2 \leq z < 3$ into 2 mass bins, each containing 33 objects.
The properties of the individual spectra in each mass bin are illustrated in more detail in Fig. 4.14. In particular, we show the ratio MAD/S for the higher and the lower redshift subsamples, calculated within the ranges 1420 – 1500 Å and 2100 – 2180 Å , respectively. This number basically provides the dispersion of the individual spectra in each mass bin, with respect to the medium signal in each bin. We note that the stacked spectra in the more massive bins are less dispersed than the ones in the less massive bins, suggesting that the individual spectra included in the stack are more similar between each other at higher masses. Fig. 4.15 shows instead a comparison between the error defined as MAD/$\sqrt{N}$ (where N is the number of the individual objects included within the stack), which we generally associate to the median stacked spectra (see Sect. 2.4.2), and the error defined following eq. 4.2 and 4.3, for the two subsamples. We note that the two error estimates are very similar between each other, with a median difference of ~ 1.8 for both the subsamples. In our further analyses, we associate the error MAD/$\sqrt{N}$ to the analyzed spectra.

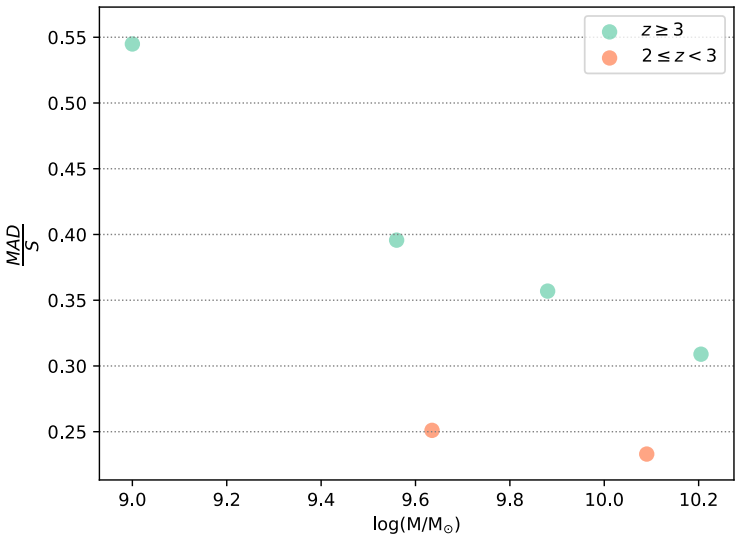

Figure 4.14: MAD/S ratio for the higher (green) and the lower (orange) redshift subsamples.

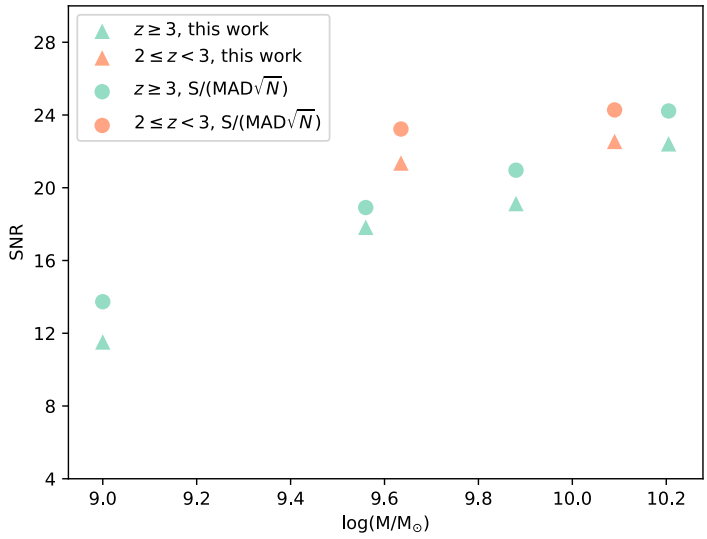

Figure 4.15: SNR of the analyzed median stacked spectra in the lower (orange) and the higher (green) redshift subsamples. Circles represent the SNRs defined as MAD/$\sqrt{N}$. Triangles are the SNRs derived by means of eq. 4.2 and 4.3.

4.4.4 The properties of the median stacked spectra

Fig. 4.16 and Fig. 4.20 (top panel) show the trend of the median stacked spectra obtained for the higher redshift subsample as a function of stellar mass (a zoom on the most important spectral features is illustrated in Fig. 4.17). The overall UV shape of the stacked spectra gets redder for increasing mass. The strongest pure photospheric absorption features (i.e. C III λ1175.71, Si III λ1417.24, S V λ1501.76, C III λ2297.58) get weaker for increasing mass, while it is evident that the Lyα emission decreases for increasing stellar mass. As explained in Sect. 4.1, these trends are consequences of the mutual effects of dust extinction, age and metallicity. In particular, more massive galaxies are expected to be more metallic (Tremonti et al., 2004) and to have higher dust masses, since the dust in the ISM basically originates from the accretion of the enriched gas processed by stars (Dwek, 1998). Dust in turn produces a decrease of the Lyα photons escape fraction, reducing the strength of the Lyα line in emission. However, recent studies have suggested that also older ages and higher metallicities can be responsible of redder UV continuum slopes. Moreover, some authors argue that weaker Lyα emission can be provided by younger ages or by the absence of supernovae-induced outflows, since they both increase the dust covering fraction (Finkelstein et al., 2009, Kornei et al., 2010).
The two stacked spectra of the lower-redshift subsample are illustrated in Fig. 4.18 and Fig. 4.20 (bottom panel) as a function of mass (a zoom on the most important spectral features is illustrated in Fig. 4.19). The higher mass spectrum is slightly redder than the lower mass one. The pure photospheric absorption lines included in the considered spectral range (i.e. SV λ1501.76 and C III λ2297.58) get weaker for increasing mass. Moreover, interstellar absorption lines such as Fe II λ2344.21, Fe II λ2374.46 and Fe II λ2382.76, are more prominent at higher masses, while nebular lines, such as C III] $\lambda\lambda$1906.68,1908.68, decrease with mass. The knowledge about what are the main dependences of these lines on the stellar/ISM properties is still lacking, however, Stark et al. (2014) Rigby et al. (2015) suggest that high C III] can be produced, at a first order, by lower metallicities, while Leitherer et al. (2011) argue that larger absorption equivalent width for Fe II can be produced especially by larger ISM covering factors.

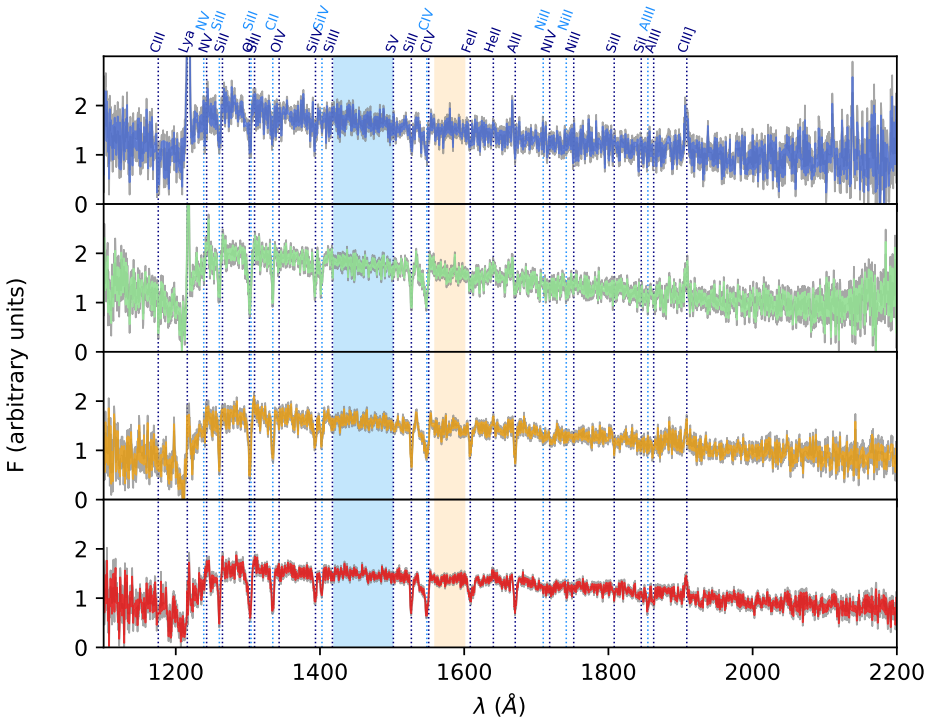

Figure 4.16: Median stacked spectra as a function of mass for the high-redshift subsample. Mass increases from blue to red, error is shown in grey. The light-blue shaded region marks the wavelength window in which we define the SNRs of the spectra (i.e. 1420 – 1500 Å), while the yellow shaded region marks the wavelength window in which the individual spectra are normalized before stacking them together (i.e. 1560 – 1600 Å). Two distinct wavelength windows are chosen to avoid biases due to the decrease of the error close to the normalization region. Note that here the median stacked spectra are normalized in the wavelength window 1930-1970 Å, in order to make them directly comparable with the lower redshift spectra illustrated in Fig. 4.18 below. Dark- and light-blue dotted vertical lines mark the most important spectral features in the considered wavelength range (different colors are used for easier distinction of lines very close in wavelength).

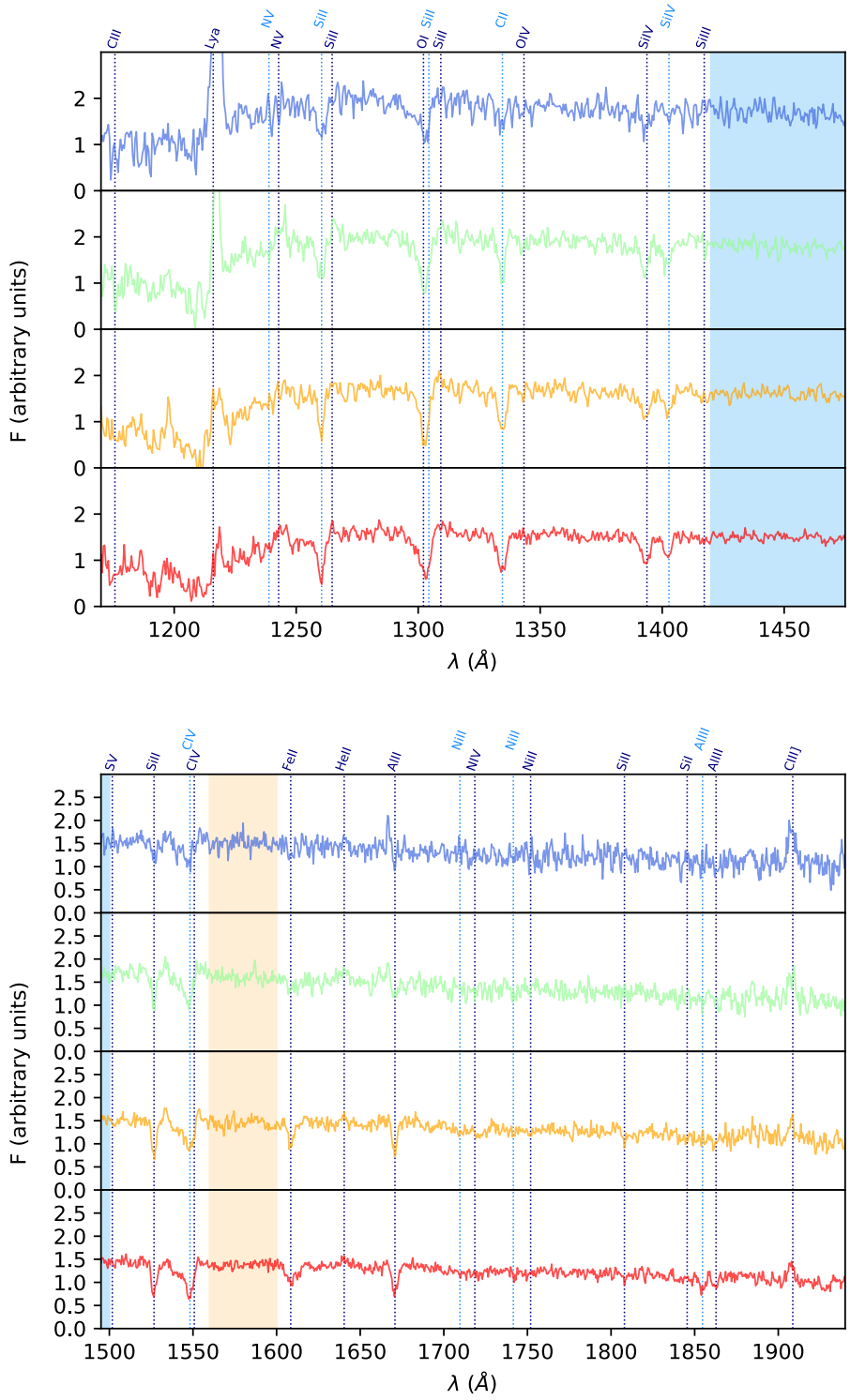

Figure 4.17: Median stacked spectra as a function of mass for the high-redshift subsample. The top panel shows a zoom on the wavelength window 1170 – 1475 Å , while the bottom panel shows a zoom on the wavelength window 1495 – 1940 Å . Errors are not plotted in order to visualize the trends of the most important spectral features more clearly. Colors are coded as in Fig. 4.16.

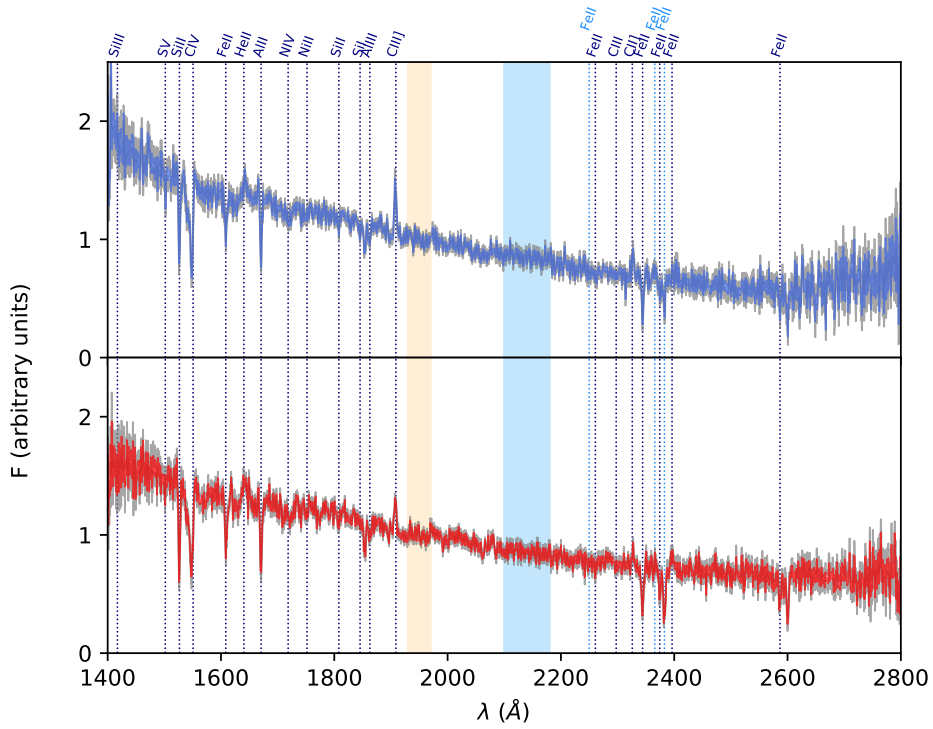

Figure 4.18: Median stacked spectra as a function of mass for the lower redshift subsample. Mass increases from blue to red, error is shown in grey. The light-blue shaded region marks the wavelength window in which we define the error and thus the SNRs of the spectra (i.e. 2100 – 2180 Å), while the yellow shaded region marks the wavelength window in which the individual spectra are normalized to stack them together (i.e. 1930-1970 Å). Dark- and light-blue dotted vertical lines mark the most important spectral features in the considered wavelength range (different colors are used for easier distinction of lines very close in wavelength).

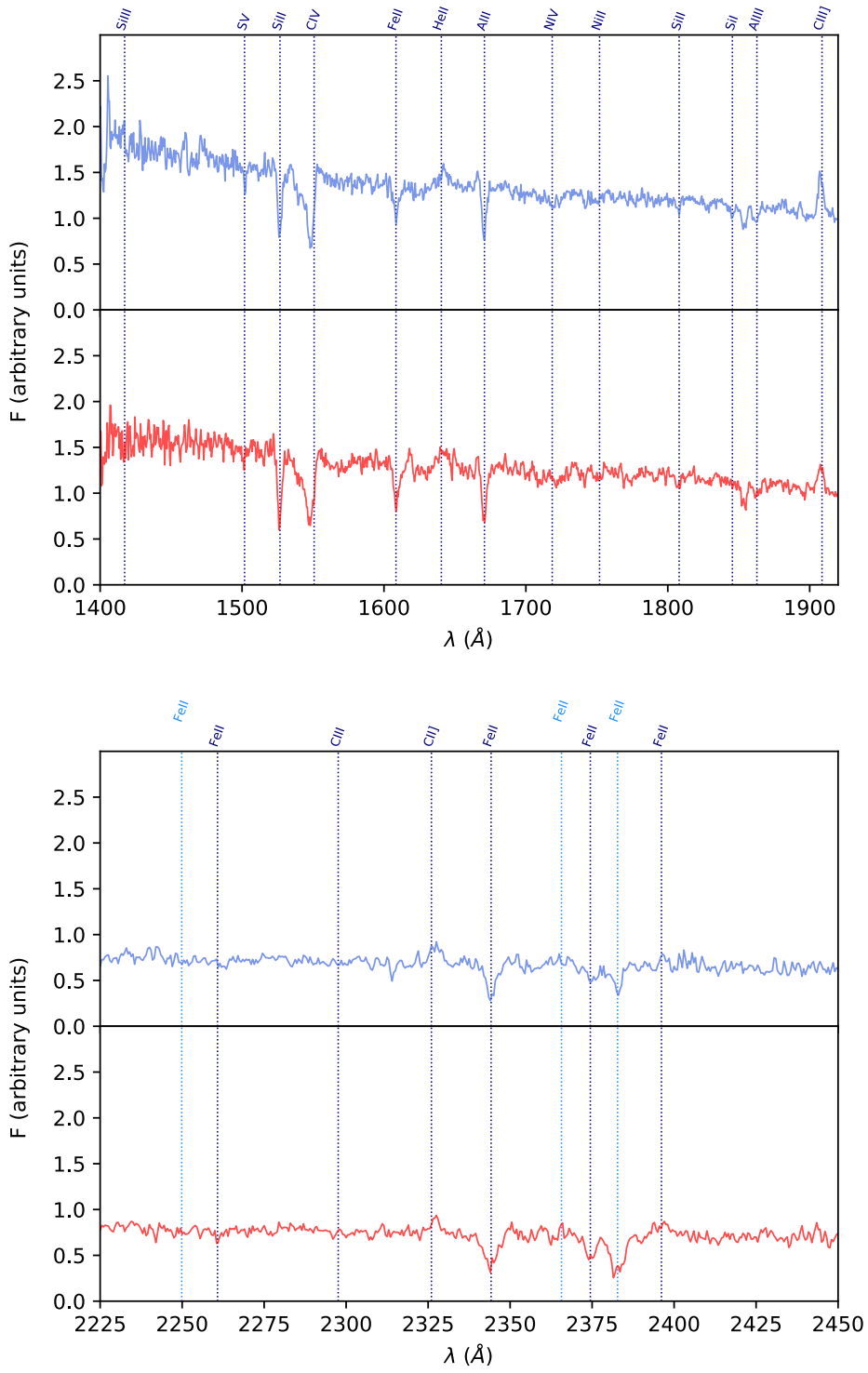

Figure 4.19: Median stacked spectra as a function of mass for the low redshift subsample. The top panel shows a zoom on the wavelength window 1400 – 1920 Å , while the bottom panel shows a zoom on the wavelength window 2225 – 2450 Å . Errors are not plotted in order to visualize the trends of the most important spectral features more clearly. The y-axis scale is the same used in Fig. 4.17, in order to facilitate the comparison. Colors are coded as in Fig. 4.18.

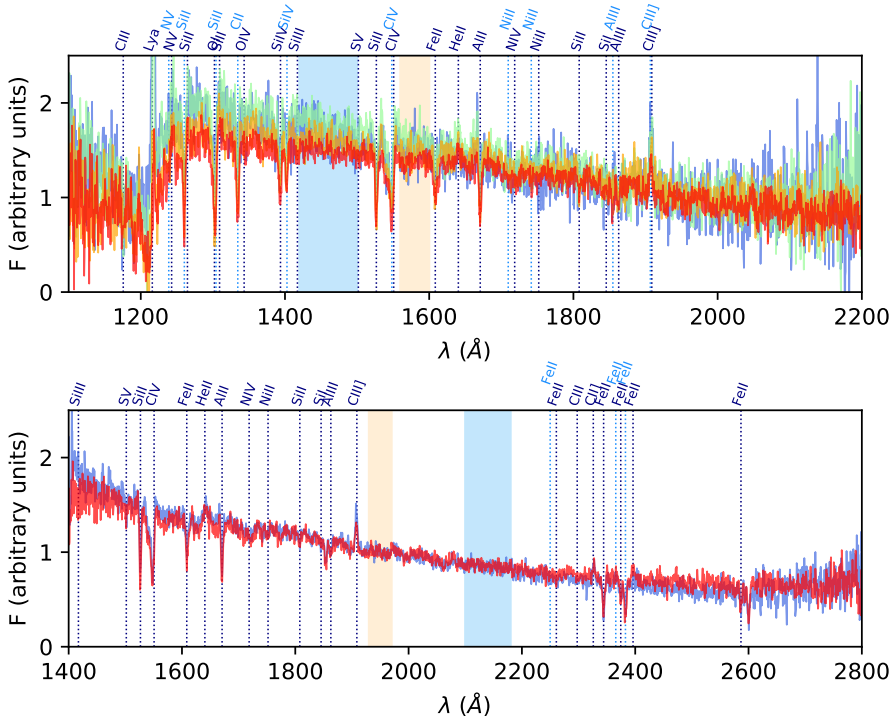

Figure 4.20: Median stacked spectra as a function of mass for the higher (top panel) and lower (bottom panel) redshift subsamples. Mass increases from blue to red. Light-blue and yellow shaded regions are defined as in Figs. 4.16 and 4.18. Dark- and light-blue dotted vertical lines mark the most important spectral features in the considered wavelength range (different colors are used for easier distinction of lines very close in wavelength). The high-redshift median stacked spectra are, also in this case, normalized in the wavelength window 1930-1970 Å.

4.5 Fitting the median stacked spectra

In this Section we show the results obtained by fitting the median stacked spectra of the two subsamples using the fitting parameters defined in case 1, case 2 and case 3.
We fit the stacked spectra with the same BC16 library used for the simulations, with ages going from 0.1 Myr to 2 Gyr.
For both the subsamples, we exclude from the spectral fit the two regions at the edges of the spectra (at short wavelengths these regions also include the Lyα emission line), since they are characterized by a larger noise (MAD/$\sqrt{N}$, in our case). Eventually, the fitted wavelength ranges are 1222 – 2000 Å for the higher redshift subsample, and 1400 – 2600 Å for the lower redshift one. Starting from the VANDELS observed-frame spectral resolution R, we derived the rest-frame spectral resolution $\Delta\lambda$ (FWHM) for our two subsamples applying the following equation 4.4:

$$\Delta\lambda\ (FWHM) = \lambda_{central}/R/(1+z)\ \ , \tag{4.4}$$

where R $\sim$ 580 is the resolution of the VIMOS spectrograph and $\lambda_{central}$ = 7000 Å is the central wavelength of the adopted grism. Considering median redshifts of $\sim$ 2.5 and $\sim$ 3.5 for the two subsamples, we obtain $\Delta\lambda$ (FWHM) $\sim$ 2.5 Å and $\sim$ 3.4 Å respectively. Using these rest-frame spectral resolutions, we downgrade the library spectra to match the observed values before fitting the spectra.

In these spectral fits, we fix the velocity dispersion to a value of 0 km s^{-1}. This choice is made since, especially in case 3, the absorption features on which the spectral fit could rely to derive σ, are excluded from the fit. Moreover, we tested that, if the full-spectrum fitting is allowed to fit the velocity dispersion, very large values of σ are provided. This is probably due to the fact that the full-spectrum fitting broadens the ISM lines trying to fit them as pure photospheric absorptions. This effect is even more pronounced when stacked spectra are considered, since in this case absorption lines are already broadened by the combined effect of the interpolation required by the staking procedure and potential errors in the de-redshifting process of individual spectra. However, we also verified that the retrieving of the evolutionary properties (ages, metallicities, dust extinction) is not affected by the σ assumed for the fit (we compared the cases $\sigma = 0$ km s^{-1}, $\sigma = 100$ km s^{-1} and $\sigma = 300$ km s^{-1}.)

Figs. 4.21, 4.22 and 4.23 show the main results for the high-redshift subsample. We find that the median differences between case 2 and 3, which are the most reliable cases, amount to $\Delta_{med_{[2-3]}}(age) \sim 0.007$ Gyr, $\Delta_{med_{[2-3]}}(Z) < 4 \times 10^{-3}$ and $\Delta_{med_{[2-3]}}(A_V) \sim 0.05$ mag. Apart from dust extinction, these values are consistent with the dispersions derived from the simulations. The differences between case 2/3 and case 1 are instead larger, i.e. $\Delta_{med_{[2,3-1]}}(age) \sim 0.16$ Gyr, $\Delta_{med_{[2,3-1]}}(Z) < 0.15$ and $\Delta_{med_{[2,3-1]}}(A_V) \sim 0.3$ mag. However, we remind that the younger ages and higher metallicities provided by case 1 are due to the fact that it is misinterpreting the absorption lines as pure interstellar absorptions, which are deeper for young ages and high metallicities (see Fig. 4.2). This effect is clearly visible also in Fig. 4.24, which illustrates a comparison among the best fit models obtained in case 1, 2, 3 for the least and the most massive stacked spectra of the $3 \leq z \leq 4$ subsample.

For the lower-redshift subsample, the full-spectrum fitting provides instead the results illustrated in Figs. 4.25, 4.26 and 4.27. Despite the fact that case 1 is not reliable, the retrieved evolutionary properties are more stable among the three cases, probably due to the larger number of wavelengths available for the spectral fit. At these redshifts, the

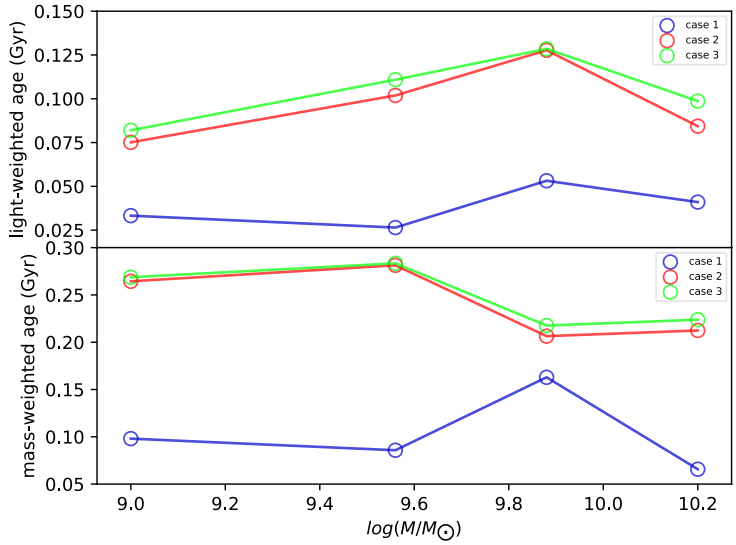

Figure 4.21: Retrieved light- and mass-weighted ages as a function of mass for the higher redshift bin. The results obtained for case 1, 2 and 3 are illustrated with different colors, as labeled.

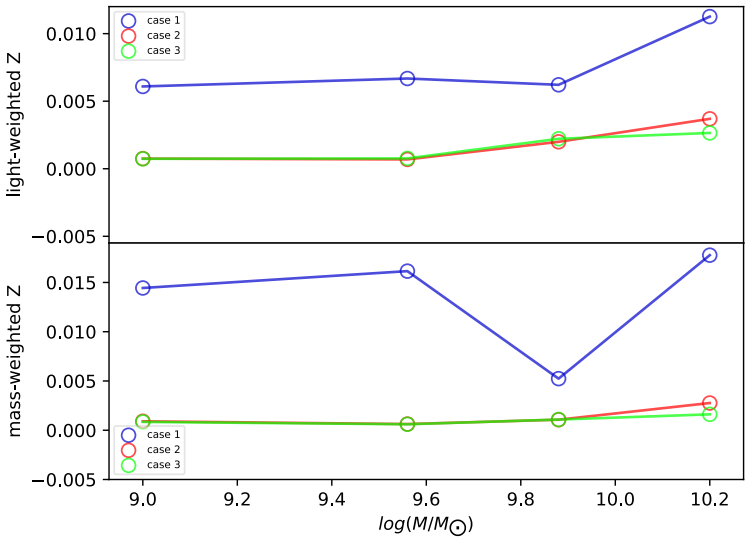

Figure 4.22: Retrieved light- and mass-weighted metallicities as a function of mass for the higher redshift bin. The results obtained for case 1, 2 and 3 are illustrated with different colors, as labeled.

differences among the three cases are always included within the dispersion predicted by simulations.

As already explained, cases 2 and 3 should be considered as the most reliable ones, since they provide ages, metallicities, dust extinctions and SFHs which are related only

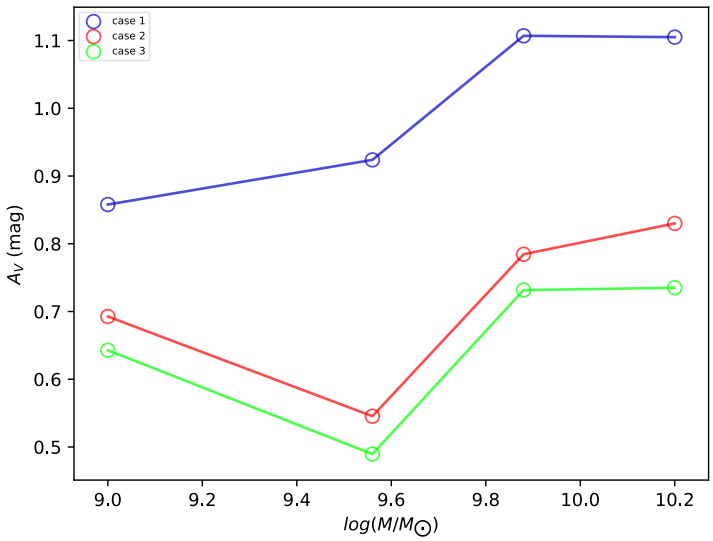

Figure 4.23: Retrieved A_V as a function of mass for the higher redshift bin. The results obtained for case 1, 2 and 3 are illustrated with different colors, as labeled.

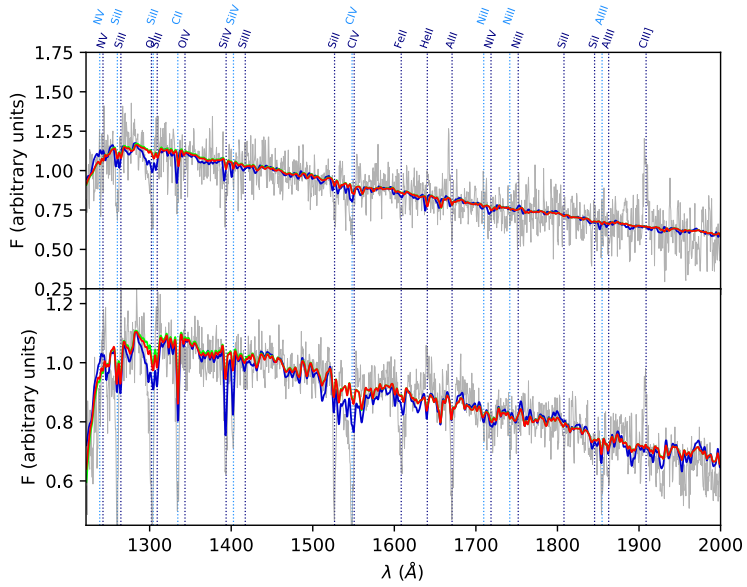

Figure 4.24: Comparison among the best fit models obtained for the least (top panel) and most (bottom panel) massive median stacked spectra in the high-redshift subsample. The spectra are shown within the wavelength range used for the fit (i.e. 1222-2000 Å). The observed spectra are shown in grey in both panels. The best fit models for cases 1,2 and 3 are also illustrated and color-coded as in Fig. 4.23.

to the galaxy stellar populations. For these two cases, we find that ages decrease from low to high masses, while metallicities and dust extinctions increase with mass. This last result is in agreement with the well-known stellar mass-stellar metallicity-dust re-

lation, which has been inferred in the literature by means of SED fitting (Gallazzi et al., 2005, Panter et al., 2008) or UV absorption lines (Leitherer et al., 2001, Rix et al., 2004, Sommariva et al., 2012). Moreover, these trends are in qualitative agreement with the trends derived by studying individual spectral features. In general, we find that the the full-spectrum fitting provides higher metallicities and lower dust extinctions for the lower redshift subsample, regardless of the mass.

We find that the median value of the mass-weighted ages derived from case 2 and case 3 is ~ 0.24 Gyr, while the median A_V is ~ 0.71 mag. The median stellar metallicity is instead $\sim 0.1 Z_{\odot}$. This value is slightly lower than the ones derived by Sommariva et al., 2012 and Mehlert et al. (2006) from FORS SF galaxies at $z \sim 3$, which were $\sim 0.2 - 0.3 Z_{\odot}$. The lower redshift subsample has instead higher median metallicities of $Z \sim 0.5 Z_{\odot}$. This is in agreement with the scenario in which galaxies at lower redshift are more evolved and thus have enriched their interstellar medium more then higher redshift ones. Moreover, the decrease of dust extinction as a function of redshift agrees with the results found by Marchesini et al. (2010), who analyzed a sample of SF galaxies with stellar masses similar to the ones of our sample, and with the ones by Cucciati et al. (2012) and Burgarella et al. (2013).
However, further analyses will be performed in order to confirm the observed trends and place them into a more general evolutionary context.

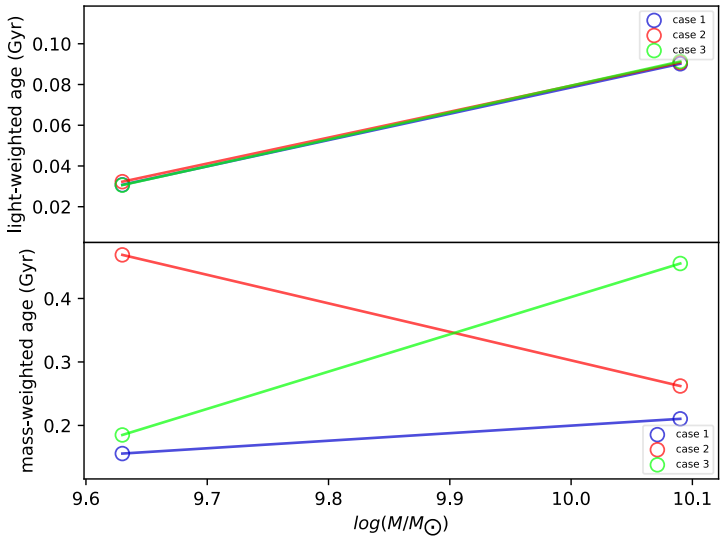

Figure 4.25: Retrieved light- and mass-weighted ages as a function of mass for the lower redshift bin. The results obtained for case 1, 2 and 3 are illustrated with different colors, as labeled.

Our last result concerns the retrieved SFHs, which are illustrated in Figs. 4.28 and 4.29. In particular, we show a sketch of the median stacked spectra and their SFHs within the SFR-mass plane, when case 2 is applied, . We find that, for both the two subsamples, the SFHs appear to be more prolonged going towards higher masses. In particular, at $3 \leq z \leq 4$, the mass percentages retrieved within $\Delta t = 0.2 - 1$ Gyr are $\sim 83\%$, $\sim 92\%$, $\sim 75\%$, $\sim 60\%$ from lower to higher masses. At $2 \leq z < 3$, the mass

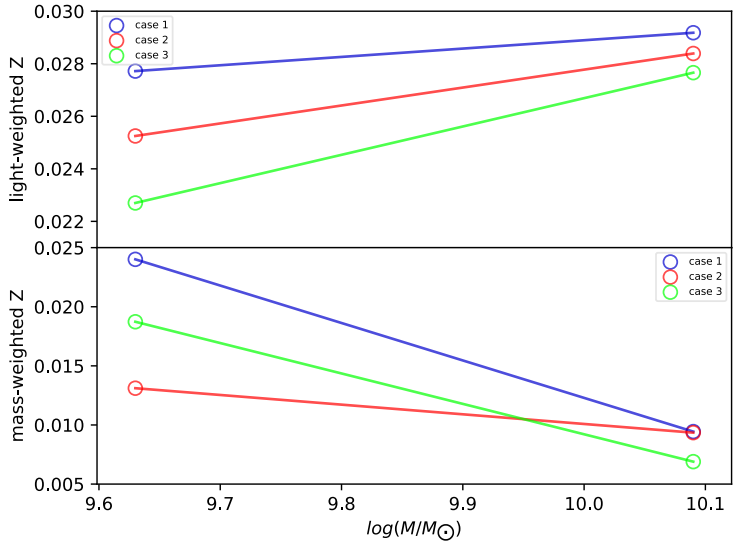

Figure 4.26: Retrieved light- and mass-weighted metallicities as a function of mass for the lower redshift bin. The results obtained for case 1, 2 and 3 are illustrated with different colors, as labeled.

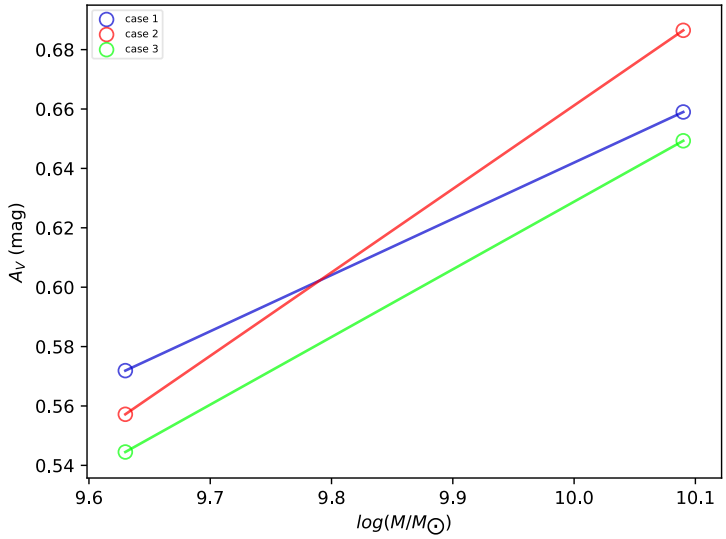

Figure 4.27: Retrieved A_V as a function of mass for the lower redshift bin. The results obtained for case 1, 2 and 3 are illustrated with different colors, as labeled.

percentages within the same Δt decreases instead from $\sim$ 70% to $\sim$ 62% from low to high mass. However, these are preliminary results and further analyses on the complete sample of VANDELS star-forming galaxies will be performed to confirm them.

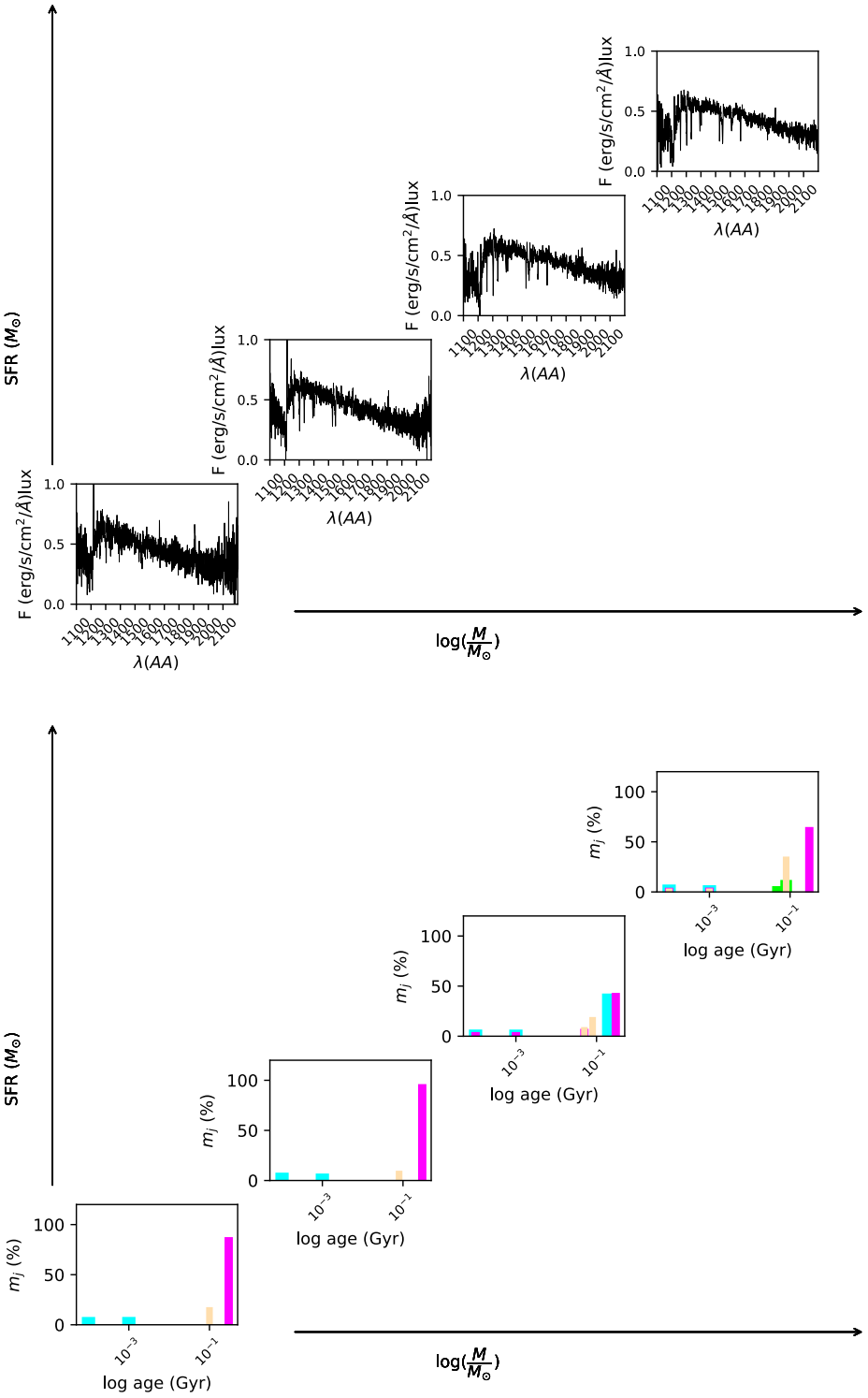

Figure 4.28: Sketch of the median stacked spectra of the higher redshift subsample (top panel) and of their SFHs obtained assuming case 2 (bottom panel) within the SFR-mass plane. Colors are coded as in Fig. 4.6.

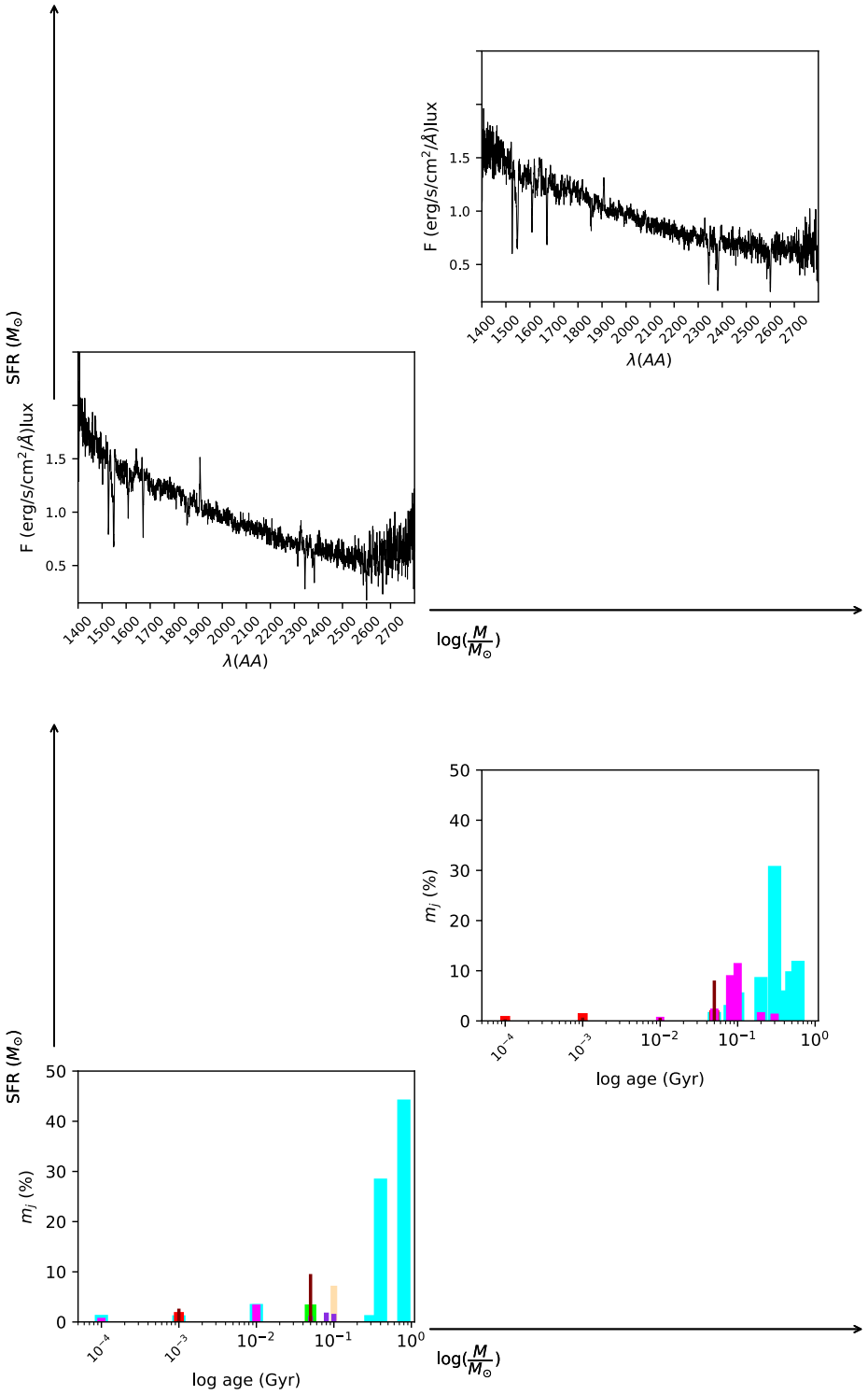

Figure 4.29: Sketch of the median stacked spectra of the lower redshift subsample (top panel) and of their SFHs obtained assuming case 2 (bottom panel) within the SFR-mass plane. Colors are coded as in Fig. 4.6.

4.6 Summary of Chapter 4

In this Chapter, we focused on the study of the so far available sample of high-redshift star-forming galaxies from the ESO-VLT public spectroscopic survey VANDELS. Our ultimate goal is to derive the evolutionary properties (i.e. ages, metallicities, dust extinctions) and the SFHs of these galaxies, in order to place them into a more general evolutionary context and link them to the ETG archaeological study performed in Chapter 2. Before applying the full-spectrum fitting to real data, we verified if the full-spectrum fitting results are reliable also when, besides the strongest emission lines (case 1), also the stellar absorption lines which have ISM contributions (ISM lines) are excluded from the spectral fit (case 2). This is an interesting test since the current evolutionary synthesis models needed to perform the full-spectrum fitting do not model the ISM absorption. Moreover, we also investigated the extreme case in which pure photospheric absorption lines are excluded from the fit (case 3). Our main results can be summarized as follows:

- By means of specifically derived simulated spectra resembling VANDELS star-forming UV spectra at $3 \leq z \leq 4$, we found that the full-spectrum fitting is able to retrieve the evolutionary properties (i.e. ages, metallicities, dust extinctions) and the SFHs (qualitatively) of the simulated spectra starting from SNRs $\gtrsim 10 - 20$, with small shifts (i.e. $\lesssim 0.012$ mag for A_V, $\lesssim 0.15$ Gyr for ages and $\lesssim 10^{-3}$ for metallicities) between the output and the input properties, both including (case 1) or excluding (case 2) ISM lines;

- We found that, for an SNR between 20 and 50, the dispersions of the results are $\lesssim 0.042$ mag for dust extinction, and very similar regardless of the setting parameters used for the fit. The median age dispersion increases instead from ~ 0.37 Gyr to ~ 0.49 Gyr from case 1 to 2 (which is the most reliable one), while the median metallicity dispersion increases from ~ 0.026 to ~ 0.031 from case 1 to case 2. This means that the full-spectrum fitting is still able to retrieve the input quantities when ISM lines are excluded, but the accuracy of the results slightly worsen, especially for ages and metallicities. However, these simulations are preliminary and serve to understand the general trends of the results against the three cases assumed. Further analyses are needed to confirm the obtained results;

- We found that A_V are robustly retrieved regardless of their input values, while mass-weighted ages and metallicities have larger biases, which however decrease when the typical ages (i.e. < 0.3 Gyr) and metallicities (i.e. subsolar metallicities) of star-forming, high-redshift galaxies are considered;

- The differences among case 1, 2 and 3 are confirmed also when the median stacked spectra of two real subsamples of VANDELS star-forming galaxies at $2 \leq z < 3$ and $3 \leq z \leq 4$ are fitted. However, we found that, in most cases, these differences are compatible with the dispersions predicted by the simulations;

- The preliminary results obtained from case 2 and 3 (which are the only ones related only to galaxy stellar populations) suggest that more massive galaxies have larger dust extinctions and younger ages with respect to less massive ones, while no clear mass trend is present in metallicity. These results agree with the stellar mass-stellar metallicity-dust relation observed in the literature and with some literature studies focused on the behaviour of individual spectral features;

- Our preliminary results concerning SFHs (for the most reliable case 2) are that they appear to be more prolonged in more massive galaxies than in less massive ones, with the mass percentage formed within $\Delta t = 0.2 - 1$ Gyr decreasing from $\sim 80 - 70\%$ to $\sim 60\%$ from low to high masses.
  However, all these results are preliminary, and further analyses on the complete sample of VANDELS spectra will be performed to confirm the retrieved trends;

Chapter 5

Conclusions and future prospects

In this thesis work, we addressed some debated questions in the field of galaxy evolution concerning the mechanisms regulating the formation of stars in galaxies, the links between galaxy evolutionary properties and stellar masses/star-formation rates, and the processes suppressing star formation and their timescales.
These open questions have been tackled analyzing and studying galaxy evolution back in cosmic time. In particular, we started from the archaeological analysis of passive local galaxies, reconstructing their past star formation histories. Then we took a step back towards the star formation quenching phase, defining a new methodology able to identify the quenching progenitors of passive galaxies. Finally, we moved to the star-forming phase, investigating the properties of high-redshift galaxies which could be the star-forming progenitors of the passive local ones.
Our investigations mainly relied on the spectral analysis of galaxies. In particular, we studied both the passive and star-forming phase by exploiting the information contained in the galaxy full-spectra, whose shape and features are related to the properties of the underlying stellar populations. The quenching phase has been instead investigated by means of emission line ratios, which are associated to the ISM and its ionization state during or just after the star formation has stopped. Our most important results are reviewed in the following.

- *Local Passive Galaxies*

  Concerning passive local galaxies, we analyzed the median stacked spectra of $\sim$ 25000 massive ($\log(\mathrm{M}/\mathrm{M}_{\odot}) > 10.75$) and passive Sloan Digital Sky Survey (SDSS) DR4 early-type galaxies at $z < 0.3$. In particular, we derived their evolutionary and physical properties (i.e. ages, metallicities, dust extinctions, velocity dispersion) and star-formation histories from the full-spectrum fitting performed with the STARLIGHT public code (Cid Fernandes et al., 2005). Our most important results can be summarized as follows:

  – Using specifically derived simulations, we found that the full-spectrum fitting is able to retrieve the age, metallicity, dust extinction, star-formation history and the velocity dispersion of the analyzed galaxies with a percentage accuracy higher than 10 $\%$ for signal-to-noise ratios $\gtrsim$ 10 – 20;
  – We found that the analyzed galaxies are very old, with mass-weighted ages increasing with cosmic time from $\sim$ 10 to $\sim$ 13 Gyr. This suggests that most massive and passive ETGs represent the oldest galaxies in the present-day

Universe, with ages close to the age of the Universe itself in the most extreme cases.
Ages also show a clear tendency to increase with mass despite the rather limited mass leverage of our sample ($\log(\mathrm{M}/\mathrm{M}_{\odot}) > 10.75$), in agreement with the downsizing scenario, according to which more massive galaxies form earlier and on shorter timescales than less massive galaxies;

- Mass-weighted metallicities are slightly supersolar, with a median $Z \sim 0.029 \pm 0.0015$ ($Z \sim 0.027 \pm 0.0020$ for MS11 models), increase with stellar mass, and do not show any significant trends with redshift. This supports the interpretation that the analyzed galaxies are very old objects which formed the bulk of their stars much earlier and did not enrich significantly their interstellar medium with new metals at later epochs;
- The SFHs inferred with the full-spectrum fitting suggest that the star formation occurred during an extended period of time. The best analytical shape to describe the star formation histories of the analyzed galaxies is an exponentially declining model of the form $\mathrm{SFR(t)} \propto \tau^{-(c+1)}\mathrm{t}^{c}\exp(-\mathrm{t}/\tau)$, where the typical value of τ and c are always short, with τ decreasing from ~ 0.8 to ~ 0.6 Gyr (with a dispersion of $\pm$ 0.1) from lower to higher masses and $c \sim 0.1$ (with a dispersion of $\pm$ 0.05) regardless of mass, reproducing the fast rise of the SFR at the beginning of the SFH. This trend is also in agreement with the downsizing scenario;
- Based on the SFHs, we reconstructed the mass assembly history and the properties of the progenitors of the analyzed ETGs. We found that they should have been vigorously forming stars and assembled large stellar masses ($\gtrsim$ 75 % of the total stellar mass) by $z \sim 4-5$, with SFR up to $50 - 370$ $\mathrm{M}_{\odot}$ yr^{-1}, and quiescent by $z \sim 1.5 - 2$. Moreover, the R_e of our sample ETGs are significantly smaller than those of the parent sample of SDSS DR4 ETGs with $\log(\mathrm{M}/\mathrm{M}_{\odot}) > 10.75$. This implies higher stellar mass densities and suggests that they should have formed from high density progenitors.

- *Galaxies in the quenching phase*

  Concerning the star-formation quenching phase, we developed a new methodology aimed at finding galaxies which have just entered the quenching phase, based on emission line ratios involving high- and low-ionization potential lines. This represents a step forward with respect to the other literature works in this field, where quenching galaxies are usually identified at later epochs of the quenching process. Our most important results can be summarized as follows:

  - We focused on the use of the [O III] λ5007/Hα and [Ne III] λ3869/[O II] λ3727 emission line ratios, modelling them by means of the CLOUDY (Ferland et al., 2013) photoionization code. We found that they are able to trace the phase just after the SF quenching, decreasing even by more than a factor 10 after 6 Myr from its occurence in the extreme case of a sharp quenching, and by a factor $\sim$ 2 in $\sim$ 80 – 90 Myr from its occurrence in the case of a smoother quenching (i.e. an exponentially declining star-formation history with e-folding time τ = 200 Myr);
  - We found that our approach is influenced by the ionization – metallicity degeneracy, since more metallic ionizing sources, being characterized by a low

number of hard UV ionizing photons, can provide the same low values of the analyzed emission line ratios as quenching ionizing sources. We found that this degeneracy can be reduced using pairs of independent emission line ratios, separately related to metallicity and ionization. Starting from this, we introduced the new diagnostic diagram [O III] λ5007/Hα vs. [N II] λ3869/[O II] λ3727. Using a sample of SDSS DR8 star-forming galaxies for comparison, we selected the 10 most extreme objects in this plane, verifying whether they could actually be just quenched galaxies. We found that they are characterized by blue continua and have $(u-r)$ colors bluer than the Green Valley ones. These results are consistent with the hypothesis that they just quenched their star formation;

- The 10 identified galaxies can potentially be the quenching precursors of the ETGs studied earlier on, which are expected to be quiescent at $z \lesssim 2$. Moreover, it is important to remind that this proposed methodology has been further exploited to identify a complete sample of quenching candidates among the SDSS DR8 star-forming sample mentioned above, with the aim of studying its properties and investigating the quenching mechanism at work and its time-scales (see Quai et al. 2017, submitted to MNRAS).

- *High-redshift star-forming galaxies*. Concerning the star-forming high-redshift phase, we analyzed 6 UV median stacked spectra obtained from a sample of star-forming galaxies at high redshift. In particular, we studied the 290 star-forming and Lyman break galaxies so far available from the on-going ESO-VLT public spectroscopic survey VANDELS (PIs: Ross McLure, Laura Pentericci), where I am involved. These galaxies have $2 \leq z \leq 4$ and $8 < \log(\mathrm{M/M_{\odot}}) < 11.5$. As a first step, we verified if the full-spectrum fitting results are reliable also when, besides the strongest emission lines (case 1), absorption lines with ISM contributions (ISM lines) are excluded from the spectral fit (case 2). This is an interesting test, since the ISM contributions are usually not modelled by the current stellar population synthesis models. Moreover, we studied the extreme case in which also pure photospheric absorptions are excluded from the fit (case 3). Then, we applied the full-spectrum fitting to real galaxies, deriving their evolutionary properties (i.e. ages, metallicities, dust extinctions) and SFHs. Our most important results can be summarized as follows:

  - By means of specifically derived simulated spectra resembling VANDELS star-forming UV spectra at $3 \leq z \leq 4$, we found that the full-spectrum fitting is able to retrieve the evolutionary properties (i.e. ages, metallicities, dust extinctions) and – qualitatively – the SFHs of the simulated spectra starting from SNRs $\gtrsim$ 10 – 20, with small shifts (i.e. $\lesssim 0.012$ mag for A_V, $\lesssim 0.15$ Gyr for ages and $\lesssim 10^{-3}$ for metallicities) between the output and the input properties, both including (case 1) or excluding (case 2) ISM lines;
  - We found that for a median SNR between 20 and 50, the dispersions of the results are $\lesssim 0.042$ mag for dust extinction, and very similar among case 1, 2 and 3. The median age dispersion increases instead from ~ 0.37 Gyr to ~ 0.49 Gyr from case 1 to 2 (which is the most reliable one), while the median metallicity dispersion increases from $\sim$ 0.026 to $\sim$ 0.031 from case 1 to case 2. This means that the full-spectrum fitting is still able to retrieve the input quantities when ISM lines are excluded from the fit, but with lower accuracy,

especially for ages and metallicities. These simulations serve to understand the general trends of the results against the three cases assumed. Further analyses are needed to confirm the derived results;

- We found that dust extinctions are robustly retrieved regardless of their input values. Mass-weighted ages and metallicities have larger biases, which however decrease when the typical ages (i.e. < 0.3 Gyr) and metallicities (i.e. subsolar metallicities) of star-forming, high-redshift galaxies are considered;
- We applied the full-spectrum fitting to the median stacked spectra of VANDELS galaxies, which overlap with the star formation histories reconstructed for the local massive ETGs studied earlier on, especially at the highest masses. This makes them their potential star-forming progenitors at high redshift. The differences among case 1, 2 and 3 are confirmed also in the case of real data. However, we found that, in most cases, the differences are compatible with the dispersions predicted by the simulations;
- We found that, in case 2 and 3 (which are the only ones related only to galaxy stellar populations), more massive galaxies have larger dust extinctions and younger ages with respect to less massive ones, while no clear mass trend is present in metallicity. These results agree with the stellar mass-stellar metallicity-dust relation inferred by the literature and also with some literature studies focused on the behaviour of individual spectral features;
- We found that the SFHs predicted by the most reliable case 2 appear to be more prolonged in more massive galaxies than in less massive ones, with the mass percentage relative to $\Delta t = 0.2 - 1$ Gyr decreasing from $\sim 80 - 70\%$ to $\sim 60\%$ from low to high masses. Further analyses on the complete sample of VANDELS spectra will be performed to confirm the retrieved trends;
- An interesting development of this study could be to subtract the best fit model obtained by masking ISM lines from real spectra. This would allow to derive the "ISM excess" in correspondence of each absorption feature, and to separate the contributions of photospheric absorptions from the ones of the interstellar medium.

5.0.1 Future prospects

The full-spectrum fitting and emission line ratios have been proved to be valid methods to infer clues on the evolutionary stages of galaxies, on the basis of galaxy stellar population or interstellar medium properties. Starting from this, additional developments of these two approaches can be performed to further exploit them.
From a more technical point of view, it would be interesting to supplement the full-spectrum fitting with photometry, following the approach introduced by López Fernández et al. (2016), also verifying whether the reliability of the former improves if complemented with photometry.
Furthermore, it would be useful to employ programs which are designed to handle both spectra and photometry, such as the new-generation BEAGLE tool (Chevallard & Charlot, 2016).
Another step forward would be to fit spectral emission lines together with the stellar continuum, in order to derive at the same time stellar and gas properties, especially in the case of star-forming galaxies.
The CLOUDY photoionization code alone could be also adopted to derive gas properties, gas metallicities, galaxy ionization states and dust properties. Finally, the CLOUDY models used in this thesis could be extended to the UV range in order to identify other emission lines/line ratios able to disentangle the ionization mechanism at the work in galaxies and to learn more about the star-formation quenching and its time-scales.

Bibliography

Allard F., Hauschildt P. H., 1995, ApJ, 445, 433
Allen C. W., 1976, Astrophysical Quantities
Allen M. G., Groves B. A., Dopita M. A., Sutherland R. S., Kewley L. J., 2008, ApJS, 178, 20
Alongi M., Bertelli G., Bressan A., Chiosi C., Fagotto F., Greggio L., Nasi E., 1993, A&AS, 97, 851
Andredakis Y. C., Peletier R. F., Balcells M., 1995, MNRAS, 275, 874
Andrews B. H., Martini P., 2013, ApJ, 765, 140
Arimoto N., Yoshii Y., 1987, A&A, 173, 23
Asplund M., Grevesse N., Sauval A. J., 2005, in Barnes III T. G., Bash F. N., eds, Astronomical Society of the Pacific Conference Series Vol. 336, Cosmic Abundances as Records of Stellar Evolution and Nucleosynthesis. p. 25
Bañados E., et al., 2014, AJ, 148, 14
Baldry I. K., Glazebrook K., Brinkmann J., Ivezić Ž., Lupton R. H., Nichol R. C., Szalay A. S., 2004, ApJ, 600, 681
Baldry I. K., Glazebrook K., Driver S. P., 2008, MNRAS, 388, 945
Baldwin J. A., Phillips M. M., Terlevich R., 1981, PASP, 93, 5
Balogh M. L., Navarro J. F., Morris S. L., 2000, ApJ, 540, 113
Balogh M. L., et al., 2011, MNRAS, 412, 2303
Barber T., Meiksin A., Murphy T., 2007, MNRAS, 377, 787
Barrientos L. F., Lilly S. J., 2003, ApJ, 596, 129
Behroozi P. S., Wechsler R. H., Conroy C., 2013, ApJ, 770, 57
Bekki K., 2009, MNRAS, 399, 2221
Bell E. F., de Jong R. S., 2001, ApJ, 550, 212
Bell E. F., et al., 2004, ApJ, 600, L11
Belli S., Newman A. B., Ellis R. S., 2015, ApJ, 799, 206
Bender R., Burstein D., Faber S. M., 1992, ApJ, 399, 462
Bender R., Ziegler B., Bruzual G., 1996, ApJ, 463, L51
Benson A. J., 2012, New A, 17, 175
Bernardi M., et al., 2003, AJ, 125, 1817
Bernardi M., Nichol R. C., Sheth R. K., Miller C. J., Brinkmann J., 2006, AJ, 131, 1288
Bessell M. S., Brett J. M., Wood P. R., Scholz M., 1989, A&AS, 77, 1
Béthermin M., et al., 2015, A&A, 573, A113
Bezanson R., van Dokkum P. G., Tal T., Marchesini D., Kriek M., Franx M., Coppi P., 2009, ApJ, 697, 1290
Blanton M. R., et al., 2003, ApJ, 594, 186
Blanton M. R., et al., 2005, AJ, 129, 2562
Blumenthal G. R., Faber S. M., Primack J. R., Rees M. J., 1984, Nature, 311, 517
Bouché N., et al., 2007, ApJ, 671, 303

Bouwens R. J., et al., 2009, ApJ, 705, 936
Bower R. G., Lucey J. R., Ellis R. S., 1992, MNRAS, 254, 601
Boylan-Kolchin M., Springel V., White S. D. M., Jenkins A., Lemson G., 2009, MNRAS, 398, 1150
Brammer G. B., et al., 2009, ApJ, 706, L173
Brammer G. B., et al., 2011, ApJ, 739, 24
Bressan A., Chiosi C., Fagotto F., 1994, ApJS, 94, 63
Brinchmann J., Charlot S., White S. D. M., Tremonti C., Kauffmann G., Heckman T., Brinkmann J., 2004, MNRAS, 351, 1151
Brinchmann J., Charlot S., Kauffmann G., Heckman T., White S. D. M., Tremonti C., 2013, MNRAS, 432, 2112
Brodie J. P., Huchra J. P., 1991, ApJ, 379, 157
Brooks A. M., Governato F., Booth C. M., Willman B., Gardner J. P., Wadsley J., Stinson G., Quinn T., 2007, ApJ, 655, L17
Bruzual G., Charlot S., 2003, MNRAS, 344, 1000
Bruzual A. G., Kron R. G., 1980, ApJ, 241, 25
Bundy K., et al., 2006, ApJ, 651, 120
Burgarella D., et al., 2013, A&A, 554, A70
Burstein D., Faber S. M., Gaskell C. M., Krumm N., 1984, ApJ, 287, 586
Busarello G., Capaccioli M., Capozziello S., Longo G., Puddu E., 1997, A&A, 320, 415
Calura F., Pipino A., Chiappini C., Matteucci F., Maiolino R., 2009, A&A, 504, 373
Calzetti D., 2001, PASP, 113, 1449
Calzetti D., Kinney A. L., Storchi-Bergmann T., 1994, ApJ, 429, 582
Calzetti D., Armus L., Bohlin R. C., Kinney A. L., Koornneef J., Storchi-Bergmann T., 2000, ApJ, 533, 682
Cappellari M., Emsellem E., 2004, PASP, 116, 138
Caputi K. I., et al., 2015, ApJ, 810, 73
Caputo F., Marconi M., Musella I., Pont F., 2001, A&A, 372, 544
Carollo C. M., Danziger I. J., 1994, MNRAS, 270, 743
Carollo C. M., Danziger I. J., Buson L., 1993, MNRAS, 265, 553
Carpineti A., Kaviraj S., Darg D., Lintott C., Schawinski K., Shabala S., 2012, MNRAS, 420, 2139
Cassisi S., Castellani M., Castellani V., 1997, A&A, 317, 108
Cattaneo A., Woo J., Dekel A., Faber S. M., 2013, MNRAS, 430, 686
Cenarro A. J., Trujillo I., 2009, ApJ, 696, L43
Ceverino D., Dekel A., Bournaud F., 2010, MNRAS, 404, 2151
Chabrier G., 2003, PASP, 115, 763
Charlot S., Longhetti M., 2001, MNRAS, 323, 887
Chen X. Y., Liang Y. C., Hammer F., Prugniel P., Zhong G. H., Rodrigues M., Zhao Y. H., Flores H., 2010, A&A, 515, A101
Cheung E., et al., 2012, ApJ, 760, 131
Chevallard J., Charlot S., 2016, MNRAS, 462, 1415
Choi J., Conroy C., Moustakas J., Graves G. J., Holden B. P., Brodwin M., Brown M. J. I., van Dokkum P. G., 2014, ApJ, 792, 95
Cicone C., et al., 2014, A&A, 562, A21
Cid Fernandes R., Mateus A., Sodré L., Stasińska G., Gomes J. M., 2005, MNRAS, 358, 363
Ciesla L., et al., 2016, A&A, 585, A43
Cimatti A., et al., 2004, Nature, 430, 184

Cimatti A., Daddi E., Renzini A., 2006, A&A, 453, L29
Cimatti A., et al., 2008, A&A, 482, 21
Cimatti A., Nipoti C., Cassata P., 2012, MNRAS, 422, L62
Cimatti A., et al., 2013, ApJ, 779, L13
Concas A., Pozzetti L., Moresco M., Cimatti A., 2017, MNRAS, 468, 1747
Conroy C., 2013, ARA&A, 51, 393
Conroy C., van Dokkum P., 2012, ApJ, 747, 69
Conroy C., Graves G. J., van Dokkum P. G., 2014, ApJ, 780, 33
Couch W. J., Sharples R. M., 1987, MNRAS, 229, 423
Cowie L. L., Songaila A., Hu E. M., Cohen J. G., 1996, AJ, 112, 839
Cresci G., Mannucci F., Maiolino R., Marconi A., Gnerucci A., Magrini L., 2010, Nature, 467, 811
Cristiani S., et al., 2004, ApJ, 600, L119
Cucciati O., et al., 2012, A&A, 539, A31
Cullen F., Cirasuolo M., McLure R. J., Dunlop J. S., Bowler R. A. A., 2014, MNRAS, 440, 2300
Daddi E., et al., 2004, ApJ, 600, L127
Daddi E., et al., 2005, ApJ, 626, 680
Daddi E., et al., 2007, ApJ, 670, 156
Daddi E., Dannerbauer H., Elbaz D., Dickinson M., Morrison G., Stern D., Ravindranath S., 2008, ApJ, 673, L21
Daddi E., et al., 2009, ApJ, 694, 1517
Damjanov I., et al., 2009, ApJ, 695, 101
Dannerbauer H., Lehnert M. D., Lutz D., Tacconi L., Bertoldi F., Carilli C., Genzel R., Menten K. M., 2004, ApJ, 606, 664
Dasyra K. M., et al., 2006, ApJ, 651, 835
Davies R. L., Sadler E. M., Peletier R. F., 1993a, MNRAS, 262, 650
Davies R. L., Sadler E. M., Peletier R. F., 1993b, MNRAS, 262, 650
De Lucia G., Blaizot J., 2007, MNRAS, 375, 2
De Lucia G., Springel V., White S. D. M., Croton D., Kauffmann G., 2006, MNRAS, 366, 499
De Rossi M. E., Theuns T., Font A. S., McCarthy I. G., 2015, MNRAS, 452, 486
Dekel A., Birnboim Y., 2006, MNRAS, 368, 2
Dekel A., et al., 2009a, Nature, 457, 451
Dekel A., et al., 2009b, Nature, 457, 451
Denicoló G., Terlevich R., Terlevich E., 2002, MNRAS, 330, 69
Diemand J., Kuhlen M., Madau P., 2007, ApJ, 667, 859
Dietrich M., Hamann F., Shields J. C., Constantin A., Heidt J., Jäger K., Vestergaard M., Wagner S. J., 2003, ApJ, 589, 722
Djorgovski S., Davis M., 1987, ApJ, 313, 59
Domínguez Sánchez H., et al., 2011, MNRAS, 417, 900
Dopita M. A., Kewley L. J., Heisler C. A., Sutherland R. S., 2000, ApJ, 542, 224
Dopita M. A., et al., 2006, ApJS, 167, 177
Draine B. T., 2011, ApJ, 732, 100
Draine B. T., et al., 2007, ApJ, 663, 866
Dressler A., Gunn J. E., 1983, ApJ, 270, 7
Dressler A., Lynden-Bell D., Burstein D., Davies R. L., Faber S. M., Terlevich R., Wegner G., 1987, ApJ, 313, 42

Dunlop J., Peacock J., Spinrad H., Dey A., Jimenez R., Stern D., Windhorst R., 1996, Nature, 381, 581
Dunlop J. S., et al., 2004, MNRAS, 350, 769
Dunlop J. S., McLure R. J., Robertson B. E., Ellis R. S., Stark D. P., Cirasuolo M., de Ravel L., 2012, MNRAS, 420, 901
Dwek E., 1998, ApJ, 501, 643
Edmunds M. G., 1990, MNRAS, 246, 678
Efstathiou G., Silk J., 1983, Fund. Cosmic Phys., 9, 1
Eggen O. J., Lynden-Bell D., Sandage A. R., 1962, ApJ, 136, 748
Eisenstein D. J., et al., 2011, AJ, 142, 72
Elbaz D., et al., 2011, A&A, 533, A119
Ellis R. S., Smail I., Dressler A., Couch W. J., Oemler Jr. A., Butcher H., Sharples R. M., 1997, ApJ, 483, 582
Erb D. K., 2008, ApJ, 674, 151
Erb D. K., Shapley A. E., Pettini M., Steidel C. C., Reddy N. A., Adelberger K. L., 2006, ApJ, 644, 813
Erb D. K., Pettini M., Shapley A. E., Steidel C. C., Law D. R., Reddy N. A., 2010, ApJ, 719, 1168
Faber S. M., Worthey G., Gonzales J. J., 1992, in Barbuy B., Renzini A., eds, IAU Symposium Vol. 149, The Stellar Populations of Galaxies. p. 255, http://adsabs.harvard.edu/abs/1992IAUS..149..255F
Faber S. M., et al., 2007, ApJ, 665, 265
Fabian A. C., 2012, ARA&A, 50, 455
Fagotto F., Bressan A., Bertelli G., Chiosi C., 1994a, A&AS, 104, 365
Fagotto F., Bressan A., Bertelli G., Chiosi C., 1994b, A&AS, 105, 29
Fan X., et al., 2003, AJ, 125, 1649
Feldmann R., Carollo C. M., Mayer L., Renzini A., Lake G., Quinn T., Stinson G. S., Yepes G., 2010a, ApJ, 709, 218
Feldmann R., Carollo C. M., Mayer L., Renzini A., Lake G., Quinn T., Stinson G. S., Yepes G., 2010b, ApJ, 709, 218
Ferland G. J., 2003, ARA&A, 41, 517
Ferland G. J., Korista K. T., Verner D. A., Ferguson J. W., Kingdon J. B., Verner E. M., 1998, PASP, 110, 761
Ferland G. J., et al., 2013, Rev. Mexicana Astron. Astrofis., 49, 137
Ferreras I., Lisker T., Carollo C. M., Lilly S. J., Mobasher B., 2005, ApJ, 635, 243
Finkelstein S. L., Rhoads J. E., Malhotra S., Grogin N., 2009, ApJ, 691, 465
Finkelstein S. L., et al., 2013, Nature, 502, 524
Finlator K., Davé R., 2008, MNRAS, 385, 2181
Fontana A., et al., 2004, A&A, 424, 23
Fontana A., et al., 2009, A&A, 501, 15
Fontana A., et al., 2014, A&A, 570, A11
Fontanot F., De Lucia G., Monaco P., Somerville R. S., Santini P., 2009, MNRAS, 397, 1776
Förster Schreiber N. M., et al., 2014, ApJ, 787, 38
Foster C., et al., 2012, A&A, 547, A79
Franx M., et al., 2003, ApJ, 587, L79
Fraser-McKelvie A., Brown M. J. I., Pimbblet K. A., Dolley T., Crossett J. P., Bonne N. J., 2016, MNRAS, 462, L11
Freudling W., Corbin M. R., Korista K. T., 2003, ApJ, 587, L67

Gallazzi A., Charlot S., Brinchmann J., White S. D. M., Tremonti C. A., 2005, MNRAS, 362, 41
Gardner J. P., et al., 2006, Space Sci. Rev., 123, 485
Garnett D. R., Shields G. A., 1987, ApJ, 317, 82
Geha M., Blanton M. R., Yan R., Tinker J. L., 2012, ApJ, 757, 85
Genel S., et al., 2008, ApJ, 688, 789
Genzel R., Tacconi L. J., Rigopoulou D., Lutz D., Tecza M., 2001, ApJ, 563, 527
Girardi L., Bressan A., Chiosi C., Bertelli G., Nasi E., 1996, A&AS, 117, 113
Girardi L., Bressan A., Bertelli G., Chiosi C., 2000, A&AS, 141, 371
Gladders M. D., López-Cruz O., Yee H. K. C., Kodama T., 1998, ApJ, 501, 571
Glazebrook K., et al., 2004, Nature, 430, 181
Gobat R., et al., 2012, ApJ, 759, L44
Gobat R., et al., 2013, ApJ, 776, 9
Gonzalez A. S., 1993, in Klare G., ed., Astronomische Gesellschaft Abstract Series Vol. 8, Astronomische Gesellschaft Abstract Series. p. 9
Goto T., Utsumi Y., Furusawa H., Miyazaki S., Komiyama Y., 2009, MNRAS, 400, 843
Graves G. J., Schiavon R. P., 2008, ApJS, 177, 446
Grazian A., et al., 2015, A&A, 575, A96
Greggio L., 1997, MNRAS, 285, 151
Greis S. M. L., Stanway E. R., Davies L. J. M., Levan A. J., 2016, MNRAS, 459, 2591
Gronwall C., et al., 2007, ApJ, 667, 79
Gunn J. E., Gott III J. R., 1972, ApJ, 176, 1
Guo Q., White S. D. M., 2008, MNRAS, 384, 2
Guzmán R., Gallego J., Koo D. C., Phillips A. C., Lowenthal J. D., Faber S. M., Illingworth G. D., Vogt N. P., 1997, ApJ, 489, 559
Harrington J. P., 1968, ApJ, 152, 943
Hauschildt P. H., Baron E., 1999, Journal of Computational and Applied Mathematics, 109, 41
Hayashi M., et al., 2015, PASJ, 67, 80
Heavens A. F., Jimenez R., Lahav O., 2000, MNRAS, 317, 965
Heavens A., Panter B., Jimenez R., Dunlop J., 2004, Nature, 428, 625
Henriques B. M. B., White S. D. M., Thomas P. A., Angulo R. E., Guo Q., Lemson G., Springel V., 2013, MNRAS, 431, 3373
Henriques B. M. B., White S. D. M., Thomas P. A., Angulo R., Guo Q., Lemson G., Springel V., Overzier R., 2015, MNRAS, 451, 2663
Hibbard J. E., van Gorkom J. H., 1996, AJ, 111, 655
Hillier D. J., Miller D. L., 1998, ApJ, 496, 407
Hillier D. J., Miller D. L., 1999, ApJ, 519, 354
Hilz M., Naab T., Ostriker J. P., Thomas J., Burkert A., Jesseit R., 2012, MNRAS, 425, 3119
Hirschmann M., Naab T., Somerville R. S., Burkert A., Oser L., 2012, MNRAS, 419, 3200
Hirschmann M., De Lucia G., Wilman D., Weinmann S., Iovino A., Cucciati O., Zibetti S., Villalobos Á., 2014, MNRAS, 444, 2938
Hoaglin D. C., Mosteller F., Tukey J. W., 1983, Understanding robust and exploratory data anlysis
Hodge J., Riechers D. A., Decarli R., Walter F., Carilli C. L., Daddi E., Dannerbauer H., 2015, in American Astronomical Society Meeting Abstracts. p. 251.11
Hopkins P. F., Hernquist L., Cox T. J., Di Matteo T., Martini P., Robertson B., Springel V., 2005, ApJ, 630, 705
Hopkins P. F., et al., 2010, ApJ, 724, 915

Hubeny I., Lanz T., 1995, ApJ, 439, 875
Ilbert O., et al., 2006, A&A, 457, 841
Ilbert O., et al., 2010, ApJ, 709, 644
Ilbert O., et al., 2013, A&A, 556, A55
Issa M. R., MacLaren I., Wolfendale A. W., 1990, A&A, 236, 237
James B. L., Aloisi A., Heckman T., Sohn S. T., Wolfe M. A., 2014, ApJ, 795, 109
Jogee S., et al., 2009, ApJ, 697, 1971
Johansson J., Thomas D., Maraston C., 2012a, MNRAS, 421, 1908
Johansson P. H., Naab T., Ostriker J. P., 2012b, ApJ, 754, 115
Jørgensen I., 1999, MNRAS, 306, 607
Juarez Y., Maiolino R., Mujica R., Pedani M., Marinoni S., Nagao T., Marconi A., Oliva E., 2009, A&A, 494, L25
Juneau S., et al., 2005, ApJ, 619, L135
Kahn F. D., 1954, Bull. Astron. Inst. Netherlands, 12, 187
Karim A., et al., 2011, ApJ, 730, 61
Kashino D., et al., 2016, preprint, (arXiv:1604.06802)
Kauffmann G., Colberg J. M., Diaferio A., White S. D. M., 1999, MNRAS, 303, 188
Kauffmann G., et al., 2003, MNRAS, 341, 33
Kaviraj S., 2010, MNRAS, 408, 170
Kelson D. D., Illingworth G. D., Franx M., van Dokkum P. G., 2001, ApJ, 552, L17
Kereš D., Katz N., Weinberg D. H., Davé R., 2005, MNRAS, 363, 2
Kewley L. J., Dopita M. A., 2002, ApJS, 142, 35
Kewley L. J., Ellison S. L., 2008, ApJ, 681, 1183
Kewley L. J., Dopita M. A., Sutherland R. S., Heisler C. A., Trevena J., 2001, ApJ, 556, 121
Kewley L. J., Dopita M. A., Leitherer C., Davé R., Yuan T., Allen M., Groves B., Sutherland R., 2013, ApJ, 774, 100
Khochfar S., Silk J., 2006, ApJ, 648, L21
Knudsen K. K., van der Werf P. P., Kneib J.-P., 2008, MNRAS, 384, 1611
Kobayashi C., Springel V., White S. D. M., 2007, MNRAS, 376, 1465
Koleva M., Prugniel P., Bouchard A., Wu Y., 2009, A&A, 501, 1269
Köppen J., Weidner C., Kroupa P., 2007, MNRAS, 375, 673
Korn A. J., Maraston C., Thomas D., 2005, A&A, 438, 685
Kornei K. A., Shapley A. E., Erb D. K., Steidel C. C., Reddy N. A., Pettini M., Bogosavljević M., 2010, ApJ, 711, 693
Kriek M., et al., 2006, ApJ, 649, L71
Kriek M., van der Wel A., van Dokkum P. G., Franx M., Illingworth G. D., 2008, ApJ, 682, 896
Kroupa P., 2001, MNRAS, 322, 231
Krumholz M. R., Matzner C. D., 2009, ApJ, 703, 1352
Kuntschner H., 2000, MNRAS, 315, 184
Kuntschner H., et al., 2001, in Schielicke E. R., ed., Astronomische Gesellschaft Meeting Abstracts Vol. 18, Astronomische Gesellschaft Meeting Abstracts.
Labbé I., et al., 2005, ApJ, 624, L81
Lackner C. N., Cen R., Ostriker J. P., Joung M. R., 2012, MNRAS, 425, 641
Larson R. B., 1975, MNRAS, 173, 671
Laureijs R., et al., 2011, preprint, (arXiv:1110.3193)
Le Borgne J.-F., et al., 2003, A&A, 402, 433
Le Borgne D., et al., 2006, ApJ, 642, 48
Leitherer C., et al., 1999, ApJS, 123, 3

Leitherer C., Leão J. R. S., Heckman T. M., Lennon D. J., Pettini M., Robert C., 2001, ApJ, 550, 724
Leitherer C., Ortiz Otálvaro P. A., Bresolin F., Kudritzki R.-P., Lo Faro B., Pauldrach A. W. A., Pettini M., Rix S. A., 2010, ApJS, 189, 309
Leitherer C., Tremonti C. A., Heckman T. M., Calzetti D., 2011, AJ, 141, 37
Lejeune T., Cuisinier F., Buser R., 1997, A&AS, 125
Lequeux J., Peimbert M., Rayo J. F., Serrano A., Torres-Peimbert S., 1979, A&A, 80, 155
Levesque E. M., Kewley L. J., Larson K. L., 2010, AJ, 139, 712
Li Z., Han Z., 2007, A&A, 471, 795
Lisenfeld U., Ferrara A., 1998, ApJ, 496, 145
Longhetti M., et al., 2007, MNRAS, 374, 614
Lonoce I., et al., 2015, preprint, (arXiv:1509.04000)
López Fernández R., et al., 2016, MNRAS, 458, 184
Lotz J. M., Jonsson P., Cox T. J., Primack J. R., 2008, MNRAS, 391, 1137
Lu Y., Mo H. J., Weinberg M. D., Katz N., 2011, MNRAS, 416, 1949
Lu Y., Blanc G. A., Benson A., 2015, ApJ, 808, 129
Ma X., Hopkins P. F., Faucher-Giguère C.-A., Zolman N., Muratov A. L., Kereš D., Quataert E., 2016, MNRAS, 456, 2140
Madau P., Dickinson M., 2014, ARA&A, 52, 415
Madau P., Pozzetti L., Dickinson M., 1998, ApJ, 498, 106
Magoulas C., et al., 2012, MNRAS, 427, 245
Magris G., Mateu P. J., Mateu C., Bruzual A. G., Cabrera-Ziri I., Mejía-Narváez A., 2015, PASP, 127, 16
Maiolino R., et al., 2008, A&A, 488, 463
Mancini C., Matute I., Cimatti A., Daddi E., Dickinson M., Rodighiero G., Bolzonella M., Pozzetti L., 2009, A&A, 500, 705
Mannucci F., et al., 2009, MNRAS, 398, 1915
Mannucci F., Cresci G., Maiolino R., Marconi A., Gnerucci A., 2010, MNRAS, 408, 2115
Maraston C., Strömbäck G., 2011, MNRAS, 418, 2785
Maraston C., Daddi E., Renzini A., Cimatti A., Dickinson M., Papovich C., Pasquali A., Pirzkal N., 2006, ApJ, 652, 85
Maraston C., Strömbäck G., Thomas D., Wake D. A., Nichol R. C., 2009, MNRAS, 394, L107
Maraston C., Pforr J., Renzini A., Daddi E., Dickinson M., Cimatti A., Tonini C., 2010, MNRAS, 407, 830
Marchesini D., et al., 2010, ApJ, 725, 1277
Marchesini D., et al., 2013, Unveiling the Most Massive Galaxies in the Universe: IRAC Mapping of the NMBSII/CFHTLS Fields, Spitzer Proposal
Marchesini D., et al., 2014, ApJ, 794, 65
Marsan Z. C., et al., 2015, ApJ, 801, 133
Martig M., Bournaud F., Teyssier R., Dekel A., 2009, ApJ, 707, 250
Martin D. C., et al., 2007, ApJS, 173, 342
McCarthy P. J., et al., 2004, ApJ, 614, L9
McDermid R. M., et al., 2015, MNRAS, 448, 3484
McIntosh D. H., et al., 2014, MNRAS, 442, 533
Mehlert D., Thomas D., Saglia R. P., Bender R., Wegner G., 2003, A&A, 407, 423
Mehlert D., Tapken C., Appenzeller I., Noll S., de Mello D., Heckman T. M., 2006, A&A, 455, 835
Mendel J. T., Simard L., Ellison S. L., Patton D. R., 2013, MNRAS, 429, 2212

Meurer G. R., Heckman T. M., Calzetti D., 1999, ApJ, 521, 64
Meynet G., Maeder A., Schaller G., Schaerer D., Charbonnel C., 1994, A&AS, 103
Meza A., Navarro J. F., Steinmetz M., Eke V. R., 2003, ApJ, 590, 619
Mobasher B., et al., 2005, ApJ, 635, 832
Mobasher B., et al., 2009, ApJ, 690, 1074
Mok A., et al., 2013, MNRAS, 431, 1090
Moresco M., Jimenez R., Cimatti A., Pozzetti L., 2011, J. Cosmology Astropart. Phys., 3, 45
Moresco M., et al., 2013, A&A, 558, A61
Morisset C., 2017, in Liu X., Stanghellini L., Karakas A., eds, IAU Symposium Vol. 323, Planetary Nebulae: Multi-Wavelength Probes of Stellar and Galactic Evolution. pp 43–50 (arXiv:1612.04242), doi:10.1017/S1743921317001004
Morisset C., et al., 2016, A&A, 594, A37
Mouhcine M., Gibson B. K., Renda A., Kawata D., 2008, A&A, 486, 711
Moustakas J., Kennicutt Jr. R. C., Tremonti C. A., 2006, ApJ, 642, 775
Moustakas J., Kennicutt Jr. R. C., Tremonti C. A., Dale D. A., Smith J.-D. T., Calzetti D., 2010, ApJS, 190, 233
Moustakas J., et al., 2013, ApJ, 767, 50
Muzzin A., et al., 2012, ApJ, 746, 188
Muzzin A., et al., 2013a, ApJ, 777, 18
Muzzin A., et al., 2013b, ApJ, 777, 18
Naab T., Khochfar S., Burkert A., 2006, ApJ, 636, L81
Naab T., Johansson P. H., Ostriker J. P., Efstathiou G., 2007, ApJ, 658, 710
Naab T., Johansson P. H., Ostriker J. P., 2009, ApJ, 699, L178
Naab T., et al., 2014, MNRAS, 444, 3357
Nagao T., Maiolino R., Marconi A., 2006, A&A, 459, 85
Nagao T., Maiolino R., Grazian A., 2008, in Kodama T., Yamada T., Aoki K., eds, Astronomical Society of the Pacific Conference Series Vol. 399, Panoramic Views of Galaxy Formation and Evolution. p. 272
Nakajima K., Ouchi M., 2014, MNRAS, 442, 900
Nelan J. E., Smith R. J., Hudson M. J., Wegner G. A., Lucey J. R., Moore S. A. W., Quinney S. J., Suntzeff N. B., 2005, ApJ, 632, 137
Nelson E., et al., 2014, Nature, 513, 394
Newman A. B., Belli S., Ellis R. S., 2015, preprint, (arXiv:1509.04345)
Nipoti C., Treu T., Bolton A. S., 2009a, ApJ, 703, 1531
Nipoti C., Treu T., Auger M. W., Bolton A. S., 2009b, ApJ, 706, L86
Nipoti C., Treu T., Leauthaud A., Bundy K., Newman A. B., Auger M. W., 2012, MNRAS, 422, 1714
Noeske K. G., et al., 2007, ApJ, 660, L43
Ocvirk P., Pichon C., Lançon A., Thiébaut E., 2006a, MNRAS, 365, 46
Ocvirk P., Pichon C., Lançon A., Thiébaut E., 2006b, MNRAS, 365, 74
Onodera M., et al., 2012, ApJ, 755, 26
Onodera M., et al., 2015, ApJ, 808, 161
Onodera M., et al., 2016, ApJ, 822, 42
Oser L., Ostriker J. P., Naab T., Johansson P. H., Burkert A., 2010, ApJ, 725, 2312
Ouchi M., et al., 2009, ApJ, 696, 1164
Pacifici C., Kassin S. A., Weiner B., Charlot S., Gardner J. P., 2013, ApJ, 762, L15
Panter B., Jimenez R., Heavens A. F., Charlot S., 2007, MNRAS, 378, 1550
Panter B., Jimenez R., Heavens A. F., Charlot S., 2008, MNRAS, 391, 1117

Papovich C., Dickinson M., Ferguson H. C., 2001, ApJ, 559, 620
Parkinson D., et al., 2012, Phys. Rev. D, 86, 103518
Pauldrach A. W. A., Hoffmann T. L., Lennon M., 2001, A&A, 375, 161
Peng Y.-j., et al., 2010, ApJ, 721, 193
Pérez-Montero E., et al., 2013, A&A, 549, A25
Perlmutter S., et al., 1999, ApJ, 517, 565
Pettini M., Pagel B. E. J., 2004, MNRAS, 348, L59
Pettini M., Steidel C. C., Adelberger K. L., Dickinson M., Giavalisco M., 2000, ApJ, 528, 96
Pforr J., Maraston C., Tonini C., 2012, MNRAS, 422, 3285
Pickles A. J., 1985, ApJS, 59, 33
Pickles A. J., 1998, PASP, 110, 863
Pilyugin L. S., 2001, A&A, 369, 594
Poggianti B. M., Bridges T. J., Komiyama Y., Yagi M., Carter D., Mobasher B., Okamura S., Kashikawa N., 2004, ApJ, 601, 197
Poggianti B. M., et al., 2008, ApJ, 684, 888
Poggianti B. M., et al., 2013, ApJ, 762, 77
Pozzetti L., et al., 2003, A&A, 402, 837
Pozzetti L., et al., 2010, A&A, 523, A13
Pozzetti L., et al., 2016, A&A, 590, A3
Pozzi F., et al., 2015, ApJ, 803, 35
Proctor R. N., Sansom A. E., 2002, MNRAS, 333, 517
Proctor R. N., Forbes D. A., Beasley M. A., 2004, MNRAS, 355, 1327
Prugniel P., Koleva M., Ocvirk P., Le Borgne D., Soubiran C., 2007, in Vazdekis A., Peletier R., eds, IAU Symposium Vol. 241, Stellar Populations as Building Blocks of Galaxies. pp 68–72 (arXiv:astro-ph/0703130), doi:10.1017/S1743921307007454
Puls J., Urbaneja M. A., Venero R., Repolust T., Springmann U., Jokuthy A., Mokiem M. R., 2005, A&A, 435, 669
Quintero A. D., et al., 2004, ApJ, 602, 190
Ragone-Figueroa C., Granato G. L., 2011, MNRAS, 414, 3690
Rauch T., 2002, in Henney W. J., Franco J., Martos M., eds, Revista Mexicana de Astronomia y Astrofisica Conference Series Vol. 12, Revista Mexicana de Astronomia y Astrofisica Conference Series. pp 150–151
Ravindranath S., et al., 2004, ApJ, 604, L9
Renzini A., 2006, ARA&A, 44, 141
Renzini A., Buzzoni A., 1986, in Chiosi C., Renzini A., eds, Astrophysics and Space Science Library Vol. 122, Spectral Evolution of Galaxies. pp 195–231, doi:10.1007/978-94-009-4598-2_19
Renzini A., Peng Y.-j., 2015, ApJ, 801, L29
Riechers D. A., et al., 2013, Nature, 496, 329
Riechers D. A., et al., 2015, IAU General Assembly, 22, 55781
Riess A. G., et al., 1998, AJ, 116, 1009
Rigby J. R., Rieke G. H., 2004, ApJ, 606, 237
Rigby J. R., Bayliss M. B., Gladders M. D., Sharon K., Wuyts E., Dahle H., Johnson T., Peña-Guerrero M., 2015, ApJ, 814, L6
Rix S. A., Pettini M., Leitherer C., Bresolin F., Kudritzki R.-P., Steidel C. C., 2004, ApJ, 615, 98
Rodighiero G., Cimatti A., Franceschini A., Brusa M., Fritz J., Bolzonella M., 2007, A&A, 470, 21

Rodighiero G., et al., 2011, ApJ, 739, L40
Rogers A. B., et al., 2014, MNRAS, 440, 3714
Rothberg B., Joseph R. D., 2004, AJ, 128, 2098
Rubin R. H., 1968, ApJ, 153, 761
Saglia R. P., Maraston C., Greggio L., Bender R., Ziegler B., 2000, A&A, 360, 911
Salim S., 2014, Serbian Astronomical Journal, 189, 1
Salim S., et al., 2007, ApJS, 173, 267
Salmon B., et al., 2015, ApJ, 799, 183
Sánchez-Blázquez P., et al., 2006, MNRAS, 371, 703
Sanders D. B., Soifer B. T., Elias J. H., Madore B. F., Matthews K., Neugebauer G., Scoville N. Z., 1988, ApJ, 325, 74
Sanders R. L., et al., 2015, ApJ, 799, 138
Saracco P., et al., 2005, MNRAS, 357, L40
Saracco P., Longhetti M., Andreon S., 2009, MNRAS, 392, 718
Sargent M. T., Béthermin M., Daddi E., Elbaz D., 2012, ApJ, 747, L31
Savaglio S., et al., 2005, ApJ, 635, 260
Savedoff M. P., Greene J., 1955, ApJ, 122, 477
Schaefer A. L., et al., 2017, MNRAS, 464, 121
Schaller G., Schaerer D., Meynet G., Maeder A., 1992, A&AS, 96, 269
Schawinski K., Thomas D., Sarzi M., Maraston C., Kaviraj S., Joo S.-J., Yi S. K., Silk J., 2007, MNRAS, 382, 1415
Schawinski K., et al., 2014, MNRAS, 440, 889
Schiavon R. P., Rose J. A., Courteau S., MacArthur L. A., 2004, ApJ, 608, L33
Schinnerer E., et al., 2008, ApJ, 689, L5
Schinnerer E., Capak P., Carilli C. L., Scoville N. Z., COSMOS Collaboration 2009, in American Astronomical Society Meeting Abstracts #214. p. 708
Schmutz W., Leitherer C., Gruenwald R., 1992, PASP, 104, 1164
Schweizer F., Seitzer P., 1992, AJ, 104, 1039
Sersic J. L., 1968, Atlas de galaxias australes. http://adsabs.harvard.edu/abs/1968adga.book.....S
Shankar F., Bernardi M., 2009, MNRAS, 396, L76
Shapley A. E., Steidel C. C., Pettini M., Adelberger K. L., 2003, ApJ, 588, 65
Shapley A. E., Steidel C. C., Erb D. K., Reddy N. A., Adelberger K. L., Pettini M., Barmby P., Huang J., 2005, ApJ, 626, 698
Shen S., Mo H. J., White S. D. M., Blanton M. R., Kauffmann G., Voges W., Brinkmann J., Csabai I., 2003, MNRAS, 343, 978
Shields J. C., Kennicutt Jr. R. C., 1995, ApJ, 454, 807
Shirazi M., Brinchmann J., Rahmati A., 2014, ApJ, 787, 120
Skillman E. D., Kennicutt R. C., Hodge P. W., 1989, ApJ, 347, 875
Sommariva V., Mannucci F., Cresci G., Maiolino R., Marconi A., Nagao T., Baroni A., Grazian A., 2012, A&A, 539, A136
Spergel D., et al., 2013, preprint, (arXiv:1305.5422)
Spinrad H., Taylor B. J., 1971, ApJS, 22, 445
Spitoni E., Calura F., Matteucci F., Recchi S., 2010, A&A, 514, A73
Springel V., et al., 2005, Nature, 435, 629
Stanford S. A., Eisenhardt P. R., Dickinson M., 1998, ApJ, 492, 461
Stark D. P., Ellis R. S., Bunker A., Bundy K., Targett T., Benson A., Lacy M., 2009, ApJ, 697, 1493
Stark D. P., et al., 2014, MNRAS, 445, 3200

Stasińska G., Cid Fernandes R., Mateus A., Sodré L., Asari N. V., 2006, MNRAS, 371, 972
Stefanon M., Marchesini D., Rudnick G. H., Brammer G. B., Whitaker K. E., 2013, ApJ, 768, 92
Steidel C. C., Erb D. K., Shapley A. E., Pettini M., Reddy N., Bogosavljević M., Rudie G. C., Rakic O., 2010, ApJ, 717, 289
Steinhardt C. L., Capak P., Masters D., Speagle J. S., 2015, preprint (arXiv:1506.01377)
Straatman C. M. S., et al., 2014, ApJ, 783, L14
Strateva I., et al., 2001, AJ, 122, 1861
Strömgren B., 1939, ApJ, 89, 526
Tacconi L. J., et al., 2006, ApJ, 640, 228
Tacconi L. J., et al., 2008, ApJ, 680, 246
Tal T., van Dokkum P. G., Nelan J., Bezanson R., 2009, AJ, 138, 1417
Talia M., et al., 2012, A&A, 539, A61
Talia M., et al., 2015, A&A, 582, A80
Tanaka M., Kodama T., Arimoto N., Okamura S., Umetsu K., Shimasaku K., Tanaka I., Yamada T., 2005, MNRAS, 362, 268
Taniguchi Y., et al., 2005, PASJ, 57, 165
Taniguchi Y., et al., 2015, ApJ, 809, L7
Taranu D. S., Hudson M. J., Balogh M. L., Smith R. J., Power C., Oman K. A., Krane B., 2014, MNRAS, 440, 1934
Tarter C. B., Salpeter E. E., 1969, ApJ, 156, 953
Tasca L. A. M., et al., 2015, A&A, 581, A54
Terlevich A. I., Forbes D. A., 2002, MNRAS, 330, 547
Thomas D., Maraston C., Bender R., 2002, in Schielicke R. E., ed., Reviews in Modern Astronomy Vol. 15, Reviews in Modern Astronomy. p. 219 (arXiv:astro-ph/0202166)
Thomas D., Maraston C., Bender R., 2003, MNRAS, 343, 279
Thomas D., Maraston C., Korn A., 2004, MNRAS, 351, L19
Thomas D., Maraston C., Bender R., Mendes de Oliveira C., 2005, ApJ, 621, 673
Thomas D., Maraston C., Schawinski K., Sarzi M., Silk J., 2010, MNRAS, 404, 1775
Thomas D., et al., 2013, MNRAS, 431, 1383
Tielens A. G. G. M., 2010, The Physics and Chemistry of the Interstellar Medium
Tinker J. L., Wechsler R. H., Zheng Z., 2010, ApJ, 709, 67
Tinsley B. M., 1978, ApJ, 222, 14
Toft S., et al., 2007, ApJ, 671, 285
Tojeiro R., Heavens A. F., Jimenez R., Panter B., 2007, MNRAS, 381, 1252
Tojeiro R., et al., 2013, MNRAS, 432, 359
Tomczak A. R., et al., 2016, ApJ, 817, 118
Toomre A., 1974, in Shakeshaft J. R., ed., IAU Symposium Vol. 58, The Formation and Dynamics of Galaxies. pp 347–363
Toomre A., 1977, in Tinsley B. M., Larson D. Campbell R. B. G., eds, Evolution of Galaxies and Stellar Populations. p. 401
Toomre A., Toomre J., 1972, in Bulletin of the American Astronomical Society. p. 214
Trager S. C., Worthey G., Faber S. M., Burstein D., González J. J., 1998, ApJS, 116, 1
Trager S. C., Faber S. M., Worthey G., González J. J., 2000, AJ, 120, 165
Tran K.-V. H., van Dokkum P., Franx M., Illingworth G. D., Kelson D. D., Schreiber N. M. F., 2005, ApJ, 627, L25
Tremonti C. A., et al., 2004, ApJ, 613, 898
Treu T., et al., 2005, ApJ, 633, 174
Tripicco M. J., Bell R. A., 1995, AJ, 110, 3035

Trujillo I., Conselice C. J., 2008, in Knapen J. H., Mahoney T. J., Vazdekis A., eds, Astronomical Society of the Pacific Conference Series Vol. 390, Pathways Through an Eclectic Universe. p. 416
Trujillo I., et al., 2006, MNRAS, 373, L36
Trujillo I., Ferreras I., de La Rosa I. G., 2011, MNRAS, 415, 3903
Turnrose B. E., 1976, ApJ, 210, 33
Ueda Y., Akiyama M., Ohta K., Miyaji T., 2003, ApJ, 598, 886
Vassiliadis E., Wood P. R., 1993, ApJ, 413, 641
Vassiliadis E., Wood P. R., 1994, ApJS, 92, 125
Vazdekis A., Arimoto N., 1999, ApJ, 525, 144
Vazdekis A., Ricciardelli E., Cenarro A. J., Rivero-González J. G., Díaz-García L. A., Falcón-Barroso J., 2012, MNRAS, 424, 157
Veilleux S., Osterbrock D. E., 1987, ApJS, 63, 295
Verdolini S., Yeh S. C. C., Krumholz M. R., Matzner C. D., Tielens A. G. G. M., 2013, ApJ, 769, 12
Vergani D., et al., 2008, A&A, 487, 89
Vidal-García A., Charlot S., Bruzual G., Hubeny I., 2017, MNRAS, 470, 3532
Walter F., et al., 2012, Nature, 486, 233
Wetzel A. R., Tinker J. L., Conroy C., van den Bosch F. C., 2013, MNRAS, 432, 336
Whitaker K. E., et al., 2014, ApJ, 795, 104
White S. D. M., Frenk C. S., 1991, ApJ, 379, 52
Wiklind T., Dickinson M., Ferguson H. C., Giavalisco M., Mobasher B., Grogin N. A., Panagia N., 2008, ApJ, 676, 781
Wild V., Walcher C. J., Johansson P. H., Tresse L., Charlot S., Pollo A., Le Fèvre O., de Ravel L., 2009, MNRAS, 395, 144
Wilkins S. M., Bunker A. J., Stanway E., Lorenzoni S., Caruana J., 2011, MNRAS, 417, 717
Williams R. J., Quadri R. F., Franx M., van Dokkum P., Toft S., Kriek M., Labbé I., 2010, ApJ, 713, 738
Williams C. C., et al., 2015, ApJ, 800, 21
Wise M. W., Silva D. R., 1996, ApJ, 461, 155
Worthey G., 1994, ApJS, 95, 107
Worthey G., Ottaviani D. L., 1997, ApJS, 111, 377
Worthey G., Faber S. M., Gonzalez J. J., 1992, ApJ, 398, 69
Worthey G., Faber S. M., Gonzalez J. J., Burstein D., 1994, ApJS, 94, 687
Wu P.-F., Gal R. R., Lemaux B. C., Kocevski D. D., Lubin L. M., Rumbaugh N., Squires G. K., 2014, ApJ, 792, 16
Wu X.-B., et al., 2015, IAU General Assembly, 22, 51223
Wuyts S., et al., 2011, ApJ, 738, 106
Wyder T. K., et al., 2007, ApJS, 173, 293
Yamada T., et al., 2005, ApJ, 634, 861
Yates R. M., Kauffmann G., Guo Q., 2012, MNRAS, 422, 215
Yeh S. C. C., Matzner C. D., 2012, ApJ, 757, 108
Younger J. D., et al., 2007, ApJ, 671, 1531
Zabludoff A. I., Zaritsky D., Lin H., Tucker D., Hashimoto Y., Shectman S. A., Oemler A., Kirshner R. P., 1996, ApJ, 466, 104
Zahid H. J., Kewley L. J., Bresolin F., 2011, ApJ, 730, 137
Zahid H. J., Geller M. J., Kewley L. J., Hwang H. S., Fabricant D. G., Kurtz M. J., 2013, ApJ, 771, L19

Zaritsky D., Kennicutt Jr. R. C., Huchra J. P., 1994, ApJ, 420, 87
Ziegler B. L., Bender R., 1997, MNRAS, 291, 527
da Cunha E., Eminian C., Charlot S., Blaizot J., 2010, MNRAS, 403, 1894
de Propris R., Stanford S. A., Eisenhardt P. R., Dickinson M., Elston R., 1999, AJ, 118, 719
van Dokkum P. G., 2005, AJ, 130, 2647
van Dokkum P. G., Franx M., 1996, MNRAS, 281, 985
van Dokkum P. G., et al., 2008, ApJ, 677, L5
van Zee L., Salzer J. J., Haynes M. P., O'Donoghue A. A., Balonek T. J., 1998, AJ, 116, 2805
van de Sande J., et al., 2011, ApJ, 736, L9
van der Wel A., Holden B. P., Zirm A. W., Franx M., Rettura A., Illingworth G. D., Ford H. C., 2008, ApJ, 688, 48
van der Wel A., et al., 2014, ApJ, 788, 28